Continuous Hydrothermal Synthesis of Pseudocapacitive Nanomaterials for High-Power Electrochemical Energy Storage

Dustin Bauer, MSc BSc

A thesis submitted to UCL for the degree of *Doctor of Philosophy*

Department of Chemistry

University College London

December 2018

I, Dustin Bauer, confirm that the work presented in this thesis is my own. Where information has been derived from other sources, I confirm that this has been indicated in the thesis.

London, 10th December 2018

Abstract

In this thesis, the synthesis of nanosized transition metal oxides, which exhibit pseudocapacitive charge storage in Li-ion and Na-ion chemistries, is explored via a “green” continuous hydrothermal flow synthesis (CHFS) process. The materials are characterised, and their electrochemical properties evaluated, as active materials in anodes for Li-ion batteries (LIBs), Na-ion batteries (NIBs), Li-ion hybrid electrochemical capacitors (Li-HECs), and Na-ion hybrid electrochemical capacitors (Na-HECs).

Chapter 1 gives a background on electrochemical energy storage, including a description of different active materials for energy storage devices. In Chapter 2, the experimental methods and materials employed are discussed.

Chapters 3 and 4 explore how doping an insertion material such as TiO_2 (anatase) with molybdenum, vanadium, and niobium can improve electrochemical performance and which synergistic and antagonistic effects can be achieved by co-doping. The role of pre-lithiation/sodiation on the performance of Li-HECs and Na-HECs, respectively, is explored in Section 3.4.2.3.

In Chapter 5, the co-precipitation of conversion active materials (MoO_2, $NiCo_2O_4$) with TiO_2 is explored and the benefits of the inclusion of the more stable TiO_2 (anatase) phase on cycling stability and rate performance in LIB anodes is discussed. Chapter 6 explores how mixed molybdenum/vanadium oxides can provide a route to high-power and high-energy active materials for LIBs by highly pseudocapacitive charge storage, which is faster than diffusion-limited charge storage.

Impact Statement

Climate change is one of the most serious issues currently facing humanity. Concerns over greenhouse gas emissions leading to increasing sea levels, a higher frequency of extreme weather patterns, and rising temperatures have increased investments in renewable energy generation. However, the intermittency of renewable energy sources has put a focus on the development of high-energy and high-power energy storage devices.

This work is one of the first to investigate high-performance hybrid electrochemical capacitor (HEC) negative electrodes made using active materials synthesised using a green and scalable method. By covering the whole cycle of synthesis, physical characterisation, electrochemical characterisation of Li/Na-ion battery (LIB/NIB) half-cells, and electrochemical characterisation of Li/Na-HECs, this research has helped to fill a gap in the literature and has opened new potential avenues for research, both regarding negative electrode materials and Li/Na-HEC analysis.

The findings have shown the potential of a green and scalable continuous hydrothermal flow synthesis (CHFS) process for producing negative electrode materials for LIBs, NIBs, Li-HECs, and Na-HECs. This work has already led to further research in the areas covered in this thesis within my research group and a grant proposal with a hybrid capacitor start-up.

I presented parts of my work at conferences both in Europe and in Japan. Nationally, I presented the results both at UCL and at the UK Energy Storage Conference (UKES) at Birmingham University. During my time researching in Japan, I presented my research at the Society of Polymer Science Japan’s annual conference. The work in Chapter 5 was presented at the Advanced Inorganic Materials 2018 conference in Padova, Italy. Furthermore, part of the work has already been published or is under review in peer-reviewed journals.

Acknowledgements

I have many people to thank for getting me through this PhD. First and foremost, I would like to thank my supervisor, Prof. Jawwad A Darr, for his encouragement, ideas, and support. Whilst spending a year away during your PhD can easily make it feel like you are not really part of any group, Jawwad and the entire CMTG always made sure I remained a member of the group. I would also like to thank Prof Noriyoshi Matsumi, who kindly hosted me in his laboratory at JAIST for a year and gave me the opportunity to experience another country and its research environment.

I would like to thank Dr Emma Kendrick, Dr Raman Vedajaran, and most especially Dr Alexander Roberts for their help with my research on Na-ion batteries, EIS, and hybrid capacitors, respectively.

My group at UCL was immensely helpful, not just because of their continued academic support, but also because people were always ready and willing to whinge about how frustrating academic life can be. I’d like to thank (in no particular order [we all know it is a popularity ranking]): Liam, Pete, Marco, Tom, Carlos, Chris, Ian, Clement, Meggi, Kalyani, Dougal, Chalres, Adrian, Alex, and Yiana.

Furthermore, I’d like to thank everyone else who feels like they deserve thanks, I couldn’t have done it without you.

Thanks to my family (Mutti, Vati, Charlie, Lulu, Oma) and my siblings (David, Joschka, Niklas, Roman, Nora) for feigning interest when I talked about batteries and capacitors, and for your encouragement to stick with it.

Lastly, Jodie, thank you for taking my ranting about how difficult life as a PhD student was after you spent your day getting peed on by patients. You are a star.

Table of Contents

Aims & Objectives

The aim of this work was to explore whether certain metal oxide nanoparticles, which show significant pseudocapacitive contributions to charge storage in Li-ion and Na-ion battery (LIBs/NIBs) half-cells, could be used as negative electrode materials for Li-ion and Na-ion hybrid electrochemical capacitors (Li-HECs/Na-HECs). The chosen method of synthesis for these nanoparticles was continuous hydrothermal flow synthesis (CHFS), as it offers small particle size, some size and morphology control, a narrow size distribution, reproducibility, and scalability (see Section 1.6.2).

In Chapter 3, the electrochemical performance of molybdenum-, vanadium-, or niobium-doped anatase (TiO_2) samples was investigated. Their electrochemical performance was analysed as negative electrodes in LIB and NIB half-cells; Mo(VI), V(V), and Nb(V) were chosen as dopants. This was to study if the fact that the electrochemical potential windows versus Li/Li^+ of the dopants align well with the ideal potential window for negative electrodes for Li-HECs improved their performance.

For Chapter 4, CHFS was used in a high-throughput combinatorial study of anatase doped with a variety of concentrations and combinations of molybdenum, vanadium and niobium, to investigate the influence of co-doping and dopant concentrations on performance and potential synergetic and antagonist effects.

In Chapter 5, the aim was to investigate if the co-precipitation of a conversion material with a more stable insertion material such as anatase would improve the electrochemical performance of said conversion material. The materials studied were TiO_2/MoO_2, for which a variety of concentrations was probed to analyse the best concentration of TiO_2 and a $TiO_2/NiCo_2O_4$ system, which was studied to analyse the best concentration and its dependence on the conversion material.

In Chapter 6, a range of mixed molybdenum/vanadium oxides in a variety of concentrations was studied, to see if pseudocapacitive contributions to charge storage can be improve. Finally, in Chapter 7, conclusions were drawn for the work presented herein and potential future avenues of research in this area were suggested.

1. Introduction to Electrochemical Energy Storage

1.1. Background

Rechargeable Li-ion batteries (LIBs) are the energy storage technology of choice in personal electronics and are becoming more common in electric vehicles.[1] Energy storage systems that are capable of storing a large among of energy and of releasing that energy quickly (high power) are essential to solve the current concerns over air

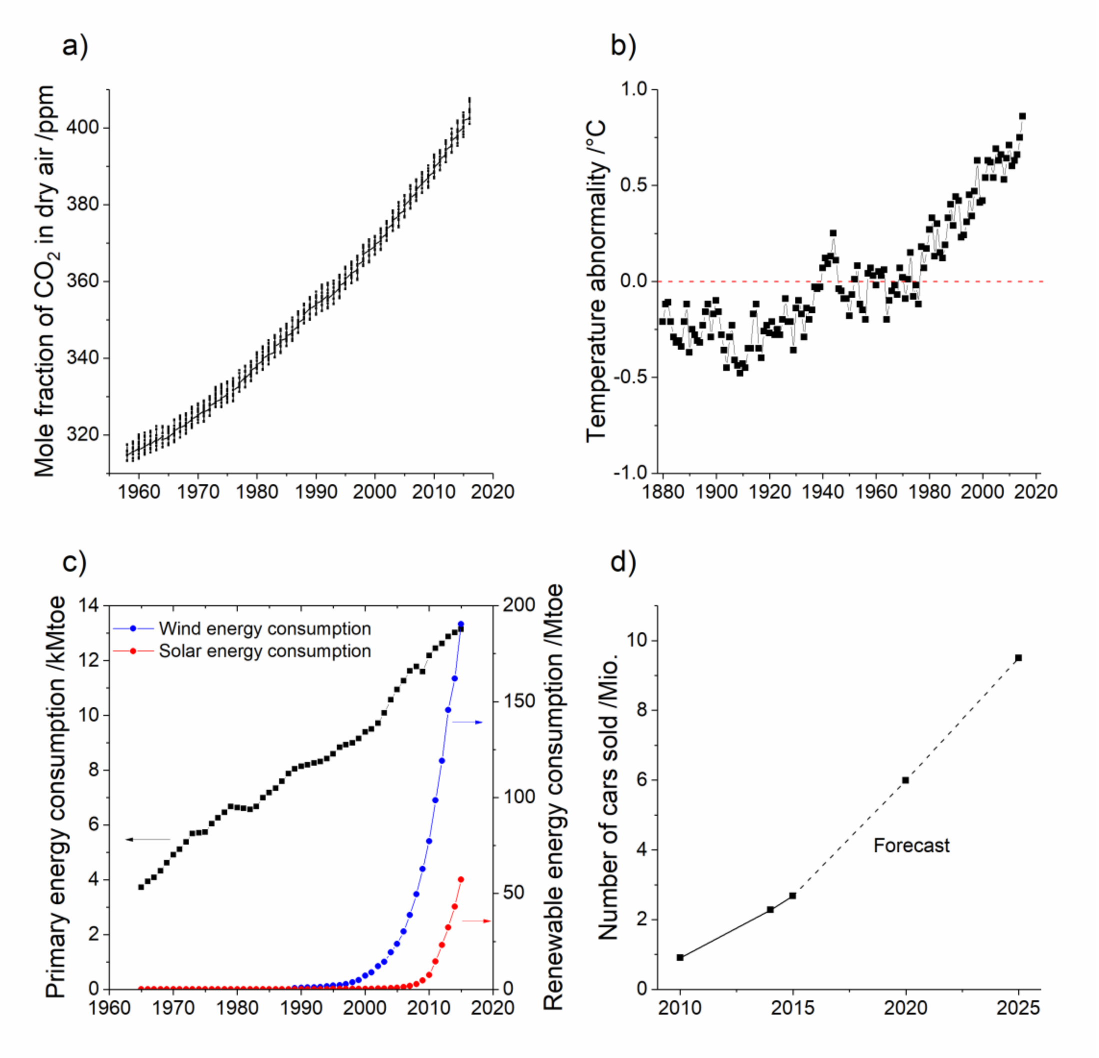

Figure 1-1: a) Mole fraction of CO_2 in dry air in ppm over time, data taken from [2]. b) Temperature deviations from the global long-term trend since the 1970s, data taken from [3]. c) Increase in primary energy consumption as well as the more recent increase in renewable energy consumption of wind and solar renewable energy, data taken from [4]. d) The number of electric vehicles (EVs, HEVs and PHEVs) sold per year, with forecasts taken from [6], which were based on the assumption of continuing subsidies in China.

pollution, dwindling fossil fuel supplies, global warming, and energy security, which have led to a push for the increased application of renewable energy sources. Carbon dioxide (CO_2) levels in the atmosphere have risen in the last 55 years, from ca. 320 parts per million (ppm) in 1962 to over 400 ppm in 2017 (see Figure 1-1a, data from [2]). Emissions of CO_2 and other greenhouse gases have increased sharply since industrialisation began and are linked to anthropic climate change. There have been significant positive temperature anomalies (deviations from the global long-term average) since the 1990s (see Figure 1-1b, data from [3]). The rise in greenhouse gas emissions stems from an increasing global energy consumption (see Figure 1-1c, data from [4]). However, the anxieties about global warming and its consequences have also led to investments in renewable energy sources, of which especially solar and wind have seen expanded use in the past 20 years (see Figure 1-1c). Due to the intermittency of wind and solar energy generation, better energy storage systems have become more important.[5] Besides energy generation, personal transportation is seen as one of the key areas to combat increasing greenhouse gas emissions.

In LIBs, which consist of an anode, a cathode, an electrolyte and a separator, lithium ions are released from the cathode and stored via Faradaic reactions in the anode during charging. Upon discharging, lithium ions are stored in the cathode and released from the anode. The demand for LIBs will continue to increase because of the progressing dissemination of portable electronics and the sharply rising demand for electric vehicles (electric vehicles [EV], hybrid electric vehicles [HEV] and plug-in hybrid electric vehicles [PHEV]), as can be seen in Figure 1-1d, created with data from [6]. LIBs combine various positive attributes, including a high energy density and low self-discharge. Nevertheless, they are not ideally suited for applications that require fast charge storage, such as regenerative braking.

Electrochemical double layer capacitors (EDLCs), which store charge on the basis of the non-Faradaic formation of Helmholtz double layers on the surface of the electrodes, tend to be more suited to tasks such as grid smoothing and regenerative braking because of their higher power densities.[7] However, EDLCs suffer from significantly lower energy densities than LIBs and are not competitive for applications such as personal electronics.[8]

A possible way to combine the merits of both alkali metal-ion batteries and EDLCs is the design of hybrid electrochemical capacitors (HECs), which employ both a high energy density redox electrode, which exhibits Faradaic charge storage, and an EDLC cathode, which exhibits non-Faradaic double layer charge storage, typically using an organic electrolyte solution.[9]

More generally, the storage of electrical energy, which is becoming ever more important due to the increasing installation of wind and solar farms and the intermittency of these energy sources, can be achieved in four ways: as kinetic energy (e.g. flywheels), as potential energy (e.g. pumped water storage), as electrical charge via charge separation in capacitors, or as chemical energy (in batteries).[7]

Chemical energy storage will be the focus of this thesis.

1.2. Electrochemical Foundations

Devices capable of electrochemical energy storage are typically called electrochemical cells, a basic diagram of which can be seen in Figure 1-2. They comprise a positive and a negative electrode, which are referred to as cathode and anode, respectively. The two electrodes are separated by a separator and an electrolyte. Electrolytic electrochemical cells convert electrical energy into chemical energy, whereas galvanic electrochemical cells convert chemical energy into electrical energy. The anode is defined as the electrode which is oxidised, the cathode as the electrode which is reduced.[10]

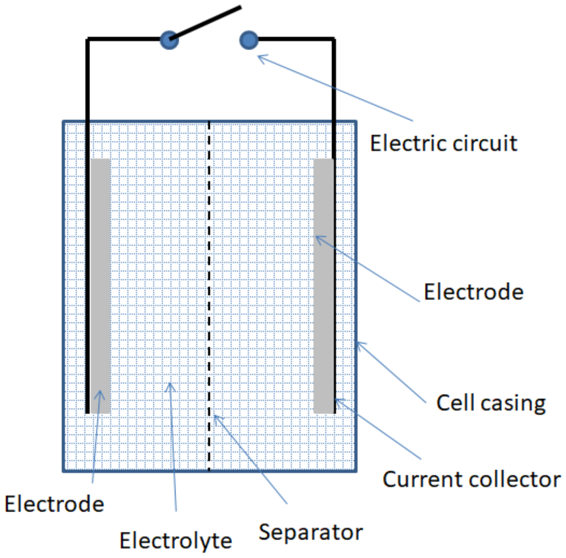

Figure 1-2: Diagram of a basic electrochemical cell.

Often, half-cells are constructed, using a reference electrode (RE) of a known potential and a working electrode (WE). Electrochemistry is regularly concerned with the study of the reactions which occur on only one electrode (the WE). Generally, REs are expected to be nonpolarizable, reliable, and reproducible, so that the ohmic drop (IR drop) is small and does not lead to complications in interpreting measurements. When the ohmic drop is large, a counter electrode (CE) is used to reduce the current that passes through the RE.[11]

The voltage of an electrochemical cell can be calculated using Equation 1.1:

$$\Delta E = E_{cell} = E_{cathode} - E_{anode} \tag{1.1}$$

$E_{cathode}$ and E_{anode} are the active (half-cell) potentials of the cathode and anode materials vs. the RE.

The maximum free energy storable in an electrolytic electrochemical cell or available from a galvanic electrochemical cell is equal to the Gibbs free energy change for the cell, which is dependent on both the number of electrons transferred (n) and the cell voltage (ΔE). Equation 1.2 allows for the calculation of the change in Gibbs free energy (ΔG) of an electrochemical cell using the Faraday constant (F: 96485 C mol^{-1}):

$$\Delta G = -nF\Delta E \tag{1.2}$$

The change in Gibbs free energy of the cell and other cell parameters can be correlated with the chemical and electrochemical potentials of the redox reactions which occur. For a given redox reaction, the Gibbs free energy change can be calculated using the chemical potentials (Equation 1.3):

$$\Delta G = \sum \mu_{products} - \sum \mu_{reactants} \tag{1.3}$$

$\mu_{products}$ and $\mu_{reactants}$ are the chemical potentials of the products and reactants, respectively. Therefore, a negative ΔG indicates a spontaneously occurring redox reaction, because the most energetically favourable state has not been achieved (not considering activation energies). A positive ΔG, however, means that no reaction will occur. The chemical potential is the change of Gibbs free energy upon an infinitesimal deviation from the chemical equilibrium between different species. The chemical potential relates to the activity of the species (a), its standard potential (μ^0), the gas constant (R), and the temperature (T) in K according to Equation 1.4:

$$\mu = \mu^0 + RTln(a) \tag{1.4}$$

The electrochemical potential accounts for the electrostatic Galvani potentials between a species ($\Phi_{species}$) and an ion containing electrolyte ($\Phi_{electrolyte}$). Due to the build-up of charge on the interface between the species and the electrolyte, the Galvani potential difference ($\Delta\Phi$) can be calculated using Equation 1.5:

$$\Delta\phi = \phi_{species} - \phi_{electrolyte} \tag{1.5}$$

The electrochemical potential can therefore be expressed by combining Equations 1.4 and 1.5 into Equation 1.6:

$$\bar{\mu} = \mu^0 + RTln(a) + nF\Delta\phi \tag{1.6}$$

An electrochemical cell of the type shown in Figure 1-2, with electrodes of different potentials and species with different activities, both of which follow Equation 1.6, is therefore governed by Equation 1.7:

$$\Delta\bar{\mu} = \bar{\mu}_+ - \bar{\mu}_- = RT \times \left(\frac{a^+}{a^-}\right) + nF\Delta\phi \tag{1.7}$$

The Nernst equation expresses the influence of the chemical and electrochemical potentials on the Gibbs free energy change and, therefore, the cell voltage E_{cell} as shown in Equation 1.8:

$$E_{cell} = E^0 - \frac{RT}{nF} \times ln\left(\frac{a^+}{a^-}\right) \tag{1.8}$$

E_{cell} is the same cell potential expressed in Equation 1.1, but here E_0 is the measured half-cell potential of an electrode, and a_+ and a_- are the activities of the different active species. However, measuring E^0 of a single electrode is a practical impossibility. Therefore, potentials of electrodes are measured against standard electrodes. Whilst standard hydrogen electrodes (SHE) are most common, in Li-ion and Na-ion battery research reference is usually made to the potential vs. Li/Li^+ and Na/Na^+, respectively.

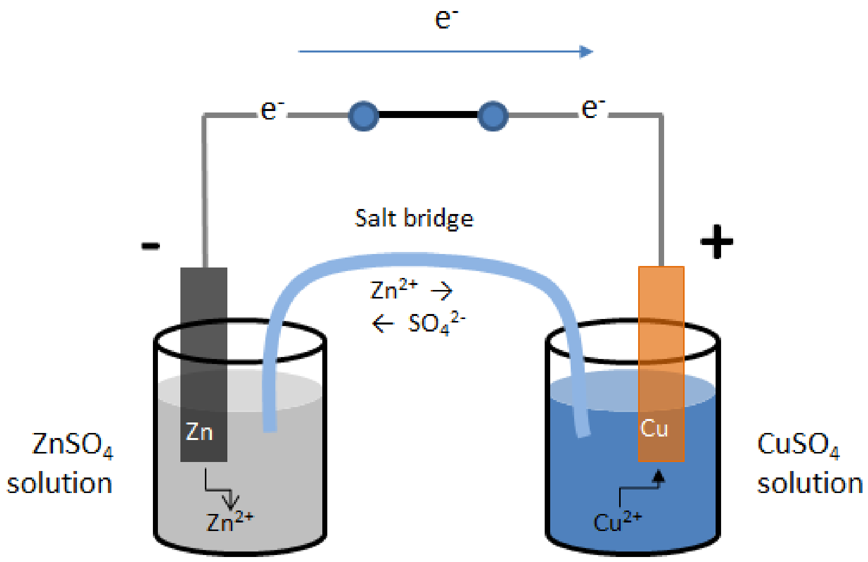

$$\mathrm{Zn(s)} \rightarrow \mathrm{Zn^{2+}(aq)} + 2\mathrm{e^-} \qquad \mathrm{Cu^{2+}(aq)} + 2\mathrm{e^-} \rightarrow \mathrm{Cu(s)}$$

Figure 1-3: Diagram of a Daniell cell with the corresponding redox-reactions.

An early example of a current-generating electrochemical cell is the Daniell cell,[12] a diagram of which can be seen in Figure 1-3. The overall reaction for this cell can be expressed as Equation 1.9:

$$\mathrm{Zn(s)} + \mathrm{Cu^{2+}(aq)} \rightarrow \mathrm{Zn^{2+}} + \mathrm{Cu(s)} \qquad (1.9)$$

Using the standard potential for the Daniell cell of 1.10 V and considering two electrons are transferred in the reaction, the cell potential at any concentration ratio can be expressed using the Nernst equation (Equation 1.8) in Equation 1.10:

$$E_{cell} = 1.10V - \frac{149\ x\ R}{F} ln\left(\frac{Zn^{2+}}{Cu^{2+}}\right) \qquad (1.10)$$

The theoretical specific capacity (Q_{th}, often in mAh g^{-1}) of an electrochemical cell is given by Equation 1.11:

$$Q_{th} = \frac{nF}{M_w} \qquad (1.11)$$

M_w is the molecular weight of the active material (g mol^{-1}). The specific capacity and cell voltage can be used to calculate the theoretical energy density (*ED*) as per Equation 1.12:

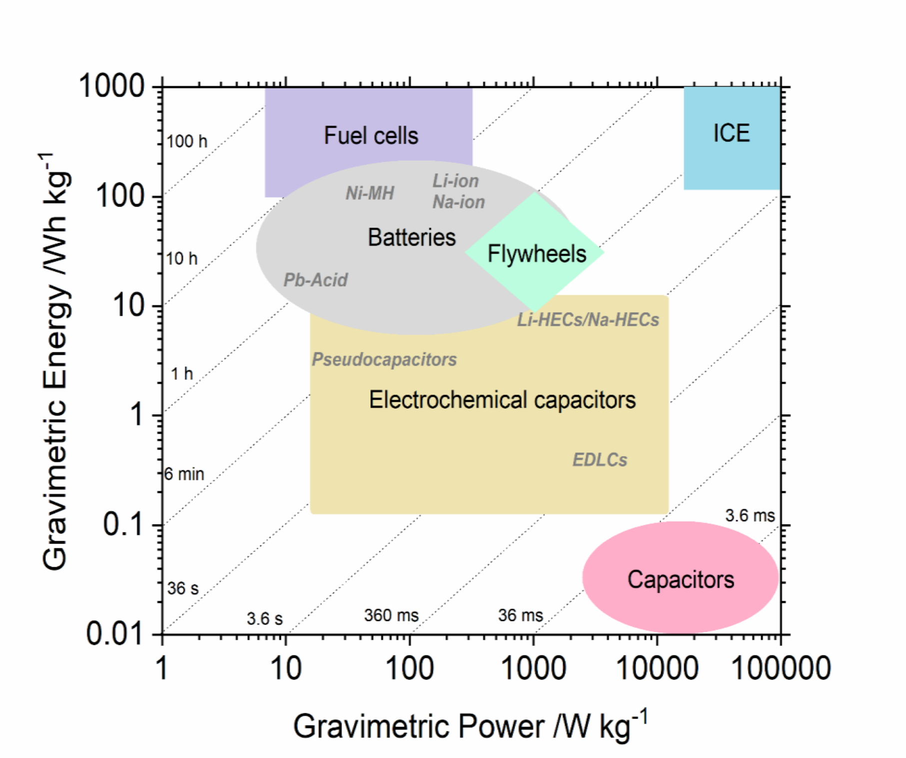

Figure 1-4: Ragone plot of different energy storage technologies along with energy generation devices such as fuel cells and internal combustion engines (ICE). Data taken from the literature.[50,170]

$$ED = \frac{nF}{M_w} \times E_{cell} = Q_{th} \times \Delta E \tag{1.12}$$

Maximizing the cell voltage ΔE can, therefore, increase the Gibbs free energy ΔG of the reaction and, by extension, the theoretical energy density.

1.3. Electrochemical Energy Storage

Whilst LIBs are currently employed in most mobile energy storage applications, due to their high energy density and acceptable power density (see Figure 1-4), they are yet to accomplish the goal of ca. 120 Wh kg^{-1} at a power density of ca. 600 W kg^{-1}, which would give high energy density and a charge or discharge time of ca. 12 minutes.[13] Different energy storage technologies as well as different battery chemistries are often compared in Ragone plots. Ragone plots consist of logarithmic axes for both specific power and specific energy (gravimetric or volumetric) and allow for quick comparison of these metrics as well as an easy understanding of charging/discharging times.

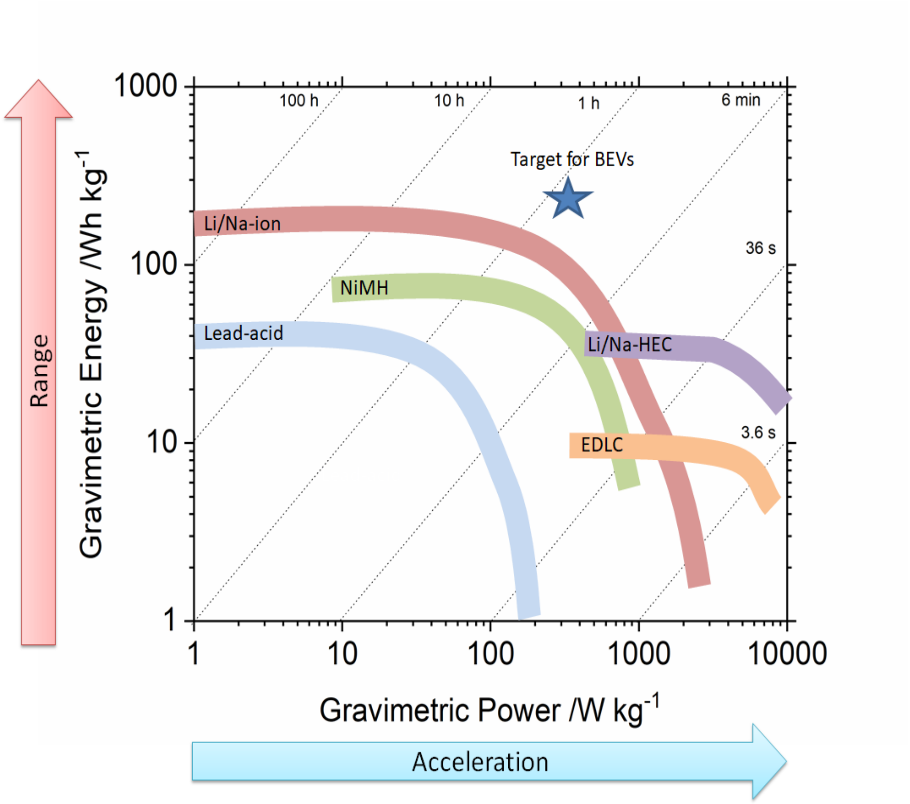

Figure 1-5: Ragone plot comparing different battery and (hybrid) capacitor technologies.

There are also some concerns about the limited supply, geographic concentration in politically unstable countries, and possibly increasing price of lithium, as the demand for LIBs increases further.[14] When considering stationary applications such as grid storage, NIBs have gained importance both in academic and commercial research and development due to the widespread availability of sodium because of its abundance in sea water.[15] Since it is often possible to adopt knowledge gained from Li-ion research, progress on Na-ion technology is expected to be made more quickly compared to LIBs.[16]

1.3.1. Design of Batteries

1.3.1.1. Li-ion Batteries (LIBs)

Commercial LIBs were introduced by Sony in 1991; the first commercial cell used graphite as intercalation anode (2-dimensional diffusion pathways) and $LiCoO_2$ (LCO) as insertion cathode (3-dimensional diffusion pathways).[17] As previously described, LIBs have higher energy densities than many other available battery chemistries (see Ragone plot in Figure 1-5). This means that in a typical application for LIBs such as in an EV, the available energy gives an indication of the range of the EV, whereas the specific power gives an indication of the possible acceleration.[18] A diagram of a LIB, as commercialised by Sony, can be seen in Figure 1-6.

Generally, upon charging, lithium ions transfer from the positive electrode into the electrolyte and intercalate from the electrolyte into the graphite layers. Lithium ions also diffuse through the electrolyte and the separator towards the negative electrode, due to the local concentration gradients created by the interactions of lithium ions with cathode and anode active materials. The reverse occurs upon discharge. Because of the reversibility of insertion from and deinsertion into the electrolyte of alkali metal-ions, this type of cell has been referred to as a "rocking-chair" cell by its inventor J. B. Goodenough.[19] For the first commercial cell, the "rocking-chair" reactions can be described by Equations 1.13 and 1.14:

$$\mathrm{LiCoO_2} \leftrightarrow \mathrm{Li_{1-x}CoO_2} + \mathrm{xLi^+} + \mathrm{xe} \quad (1.13)$$

$$\mathrm{6C} + \mathrm{xLi^+} + \mathrm{xe} \leftrightarrow \mathrm{Li_xC_6} \quad (1.14)$$

The electrolytes most commonly used consist of dimethyl carbonate (DMC) and ethylene carbonate (EC) (often 1:1) with 1 M lithium hexafluorophosphate ($LiPF_6$). In general, mixtures of a high dielectric constant solvent (EC, propylene carbonate [PC], etc., but high viscosity) with solvents of low viscosity (DMC, diethyl carbonate [DEC], etc., but low dielectric constant) are most beneficial.[20] This is to achieve both a low viscosity in the required temperature window[20] as well as allowing for high concentrations (> 1 M) of Li-ion salts to be dissolved.[21] Often, the formation of a solid electrolyte interphase (SEI, see Section 1.4.5), a solid, Li-ion conducting layer of decomposition products from the electrolyte, is essential for the reversibility and stability of cycling. In such cases, EC is an essential part of the electrolyte: it reduces on the surface of the anode at potentials of ca. 0.8 V vs. Li/Li^+ on the first cycle, creating a layer of protective decomposition products on the electrode's surface.[1,22]

For a LIB, the reactions during charging and discharging occur due to a potential difference between the two electrodes, which fundamentally shows that it is more energetically favourable for one of the electrodes to be oxidised and for the other

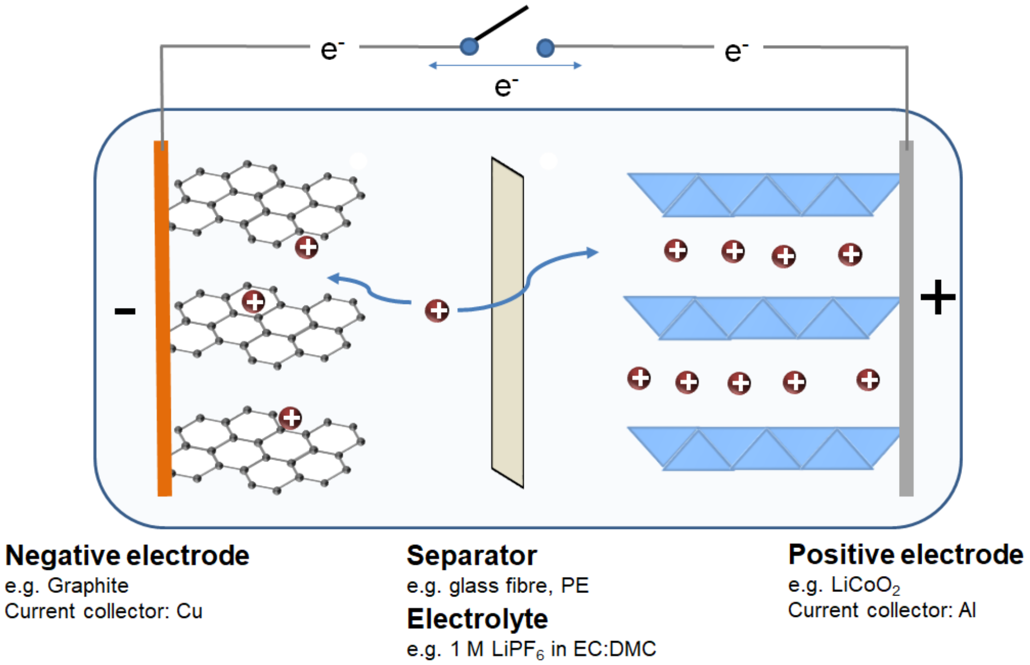

Figure 1-6: Diagram of a commercial Li-ion battery consisting of an intercalation negative electrode (e.g. $LiCoO_2$) and an intercalation positive electrode (e.g. graphite), a separator doused in electrolyte (e.g. 1 M $LiPF_6$), a casing, and an external circuit connection.

to be reduced. The reaction dynamics of a LIB are shown in Figure 1-7a. As can be determined from Equation 1.1, the electrochemical potentials of anode (μ_a) and cathode (μ_c) determine the open circuit voltage (V_{OC}), as shown in Equation 1.15:

$$V_{OC} = \mu_A - \mu_c \tag{1.15}$$

It is therefore important to consider suitable pairings of anode and cathode materials, to maximise the difference in electrochemical potentials of anode and cathode species and thereby the energy density (as seen from Equation 1.12).

E_g is the energy difference between the highest occupied molecular orbital (HOMO) and lowest unoccupied molecular orbital (LUMO) of the electrolyte, giving the electrochemical stability window of the electrolyte system. Therefore, thermodynamic and electrochemical stability of the electrolyte is achieved when both μ_a and μ_c lie within this window; otherwise, the electrolyte will be preferentially reduced/oxidised rather than the active materials in the electrodes.[23–25]

As previously described, current commercial LIBs almost exclusively employ graphite anodes. As can be seen in Figure 1-7b, whilst using graphite is beneficial due to its low electrochemical potential versus Li/Li$^+$ compared to, for example, TiO$_2$, its electrochemical potential μ_a is lower than the LUMO of the electrolyte. Therefore, during the first charge, the electrolyte is reduced.[26] The same is true for cathode materials such as nickel manganese cobalt oxide (NMC), which have a higher electrochemical potential than the HOMO, resulting in oxidation of the electrolyte. However, if the difference in electrochemical potential between the electrode material and the LUMO or HOMO of the electrolyte is only relatively small, a passivation layer (SEI, solid electrolyte interphase) can be formed, which can act to prevent additional electrolyte decomposition.[27]

Another possibility to avoid electrolyte reduction/oxidation and retain a large operating potential is to develop novel electrolyte systems with larger stability windows, thereby increasing E_g (see Figure 1-7c).

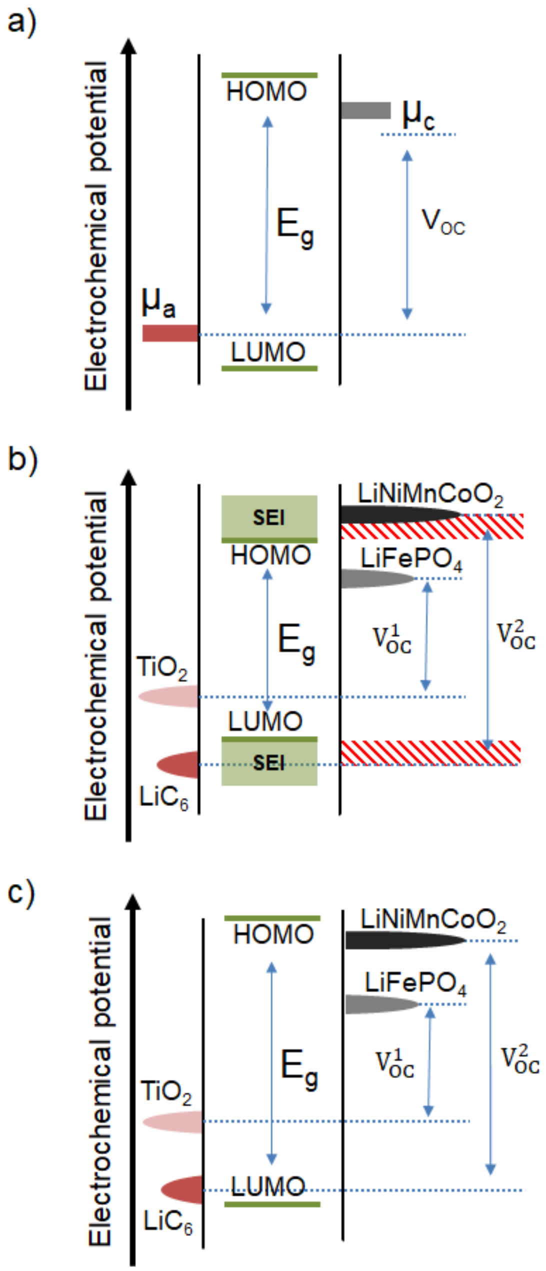

Figure 1-7: Energy levels of a Li-ion battery with a standard organic electrolyte with anode and cathode potentials (μ_a and μ_c, respectively) a) both within the electrolyte's stability window, b) outside the electrolyte's stability window (requiring SEI formation). c) Energy levels of an electrolyte with extended potential window, with anode and cathode outside the stability window of a standard electrolyte.

1.3.1.2. *Na-ion Batteries (NIBs)*

Because of the much lower price of sodium carbonate compared to lithium carbonate,[28] along with the much higher abundance of sodium compared to lithium in the earth's crust (23600 compared to 20 ppm),[29,30] Na-ion batteries (NIBs) are a promising alternative to LIBs in large-scale applications. Whilst many of the insights gained from Li-ion research can be applied in Na-ion research, there are several significant differences between LIBs and NIBs:

- Na-ions do not intercalate into graphite (unless under high pressure), therefore hard carbons are typically used as anode materials instead of graphite.[31]
- Because of the higher half-cell potential of Na/Na$^+$ compared to Li/Li$^+$, cheaper electrolytes with lower requirements for the potential window can be used.[31]
- Due to the higher half-cell potential of Na compared to Li, and because there is no alloying between Na and aluminium, cheaper and lighter aluminium foil can be used as current collector for the negative electrode compared to copper in LIB.[32]
- Because of the higher half-cell potential of Na compared to Li, the overall energy density will be lower for NIBs compared to equivalent LIBs.[33]
- The larger ionic radius and higher weight of Na$^+$ compared to Li$^+$ can result in more sluggish diffusion and intercalation, therefore suggesting a limited power capability for NIBs. However, in some layered frameworks, diffusion of Na-ions can be higher than Li-ion diffusion in spite of the larger ionic radius.[34]

1.3.2. Design and Operation of Capacitors

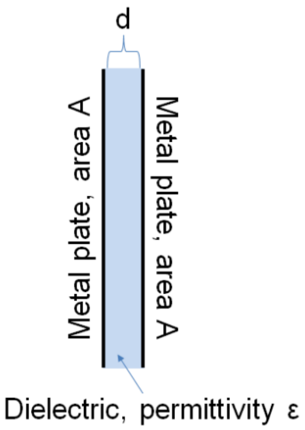

Figure 1-8: Diagram of a basic capacitor.

In its most basic form, a capacitor is a passive two-terminal electrical component which allows for the storage of electrical energy in its electrical field.[35] Capacitors consist of two conducting plates separated by an insulting dielectric.[35,36] The amount of charge (q) stored in a capacitor is directly related to the applied voltage (V) as well as its capacitance (C), which is calculated using the permittivity (ε) of the dielectric, the surface area of the metal plates (A), and the distance (d) between the two electrodes (see Equation 1.16):

$$q = V \times C = V \times \frac{(\varepsilon A)}{d} \tag{1.16}$$

1.3.2.1. Electrochemical Capacitors

In contrast to basic capacitors, electrochemical supercapacitors, which were first commercialised by Nippon Electric Company, store charge physically or electrochemically via one of two mechanisms:[36]

- Electrostatic build-up of charge on the electrode/electrolyte interface called electric double layer capacitance (EDLC)
- Highly reversible, surface-near Faradaic reactions called pseudocapacitance.

Due to the charge being stored physically in EDLCs, they show significantly better cycling stability and higher specific power than alkali metal-ion batteries. There are many applications in which high power and reliability are essential, including defibrillators, load smoothing for the electricity grid, electric buses, and container trains in harbours.[37] Because of the charge storage at the interface, charge storage in EDLCs is highly dependent on the specific surface area (SSA) and pore volume of the active material.[38]

A high surface area carbon EDLC was patented as early as 1957.[39] The high capacitance of these devices can be explained by the formation of a Helmholtz double layer on the surface of a high SSA carbon electrode (see Figure 1-9). Helmholtz' theory was the first theory on double layers. It is assumed that counterions neutralise the charge of an electrode by aggregating on the electrode's surface to a distance of *d*. In this theory, the potential of the surface charge dissipates linearly.

The higher the SSA of the electrode, the higher the stored charge in the Helmholtz double layer. There are no chemical reactions between ionic species in the electrolyte and the electrode, which allows for a very long cycle life. The Helmholtz model assumed that the potential drop between electrode and electrolyte occurred only in the adsorbed layer of counterions.

The Gouy-Chapman theory added a diffuse double layer to the theoretical foundation of double layers: the theory describes a layer of counterions on a charged electrode, in which the concentration of counterions decreases with increasing distance from the electrode's surface. The Boltzman distribution can be used to calculate the gradient in concentration. The potential drop between the electrode and the electrolyte is expected to be exponential. The Gouy-Chapman theoy did not account for the fact that electrolytes consist of both anions and cations, and that with an increasing distance from a charged electrode, the concentration of ions of the same charge as the electrode increases.

Stern improved upon this model by considering diffusion and electrostatics. Stern's theory modified the diffuse double layer theorised by Gouy-Chapman. It considers that because ions are not infinitesimally small, they cannot be on the surface of the electrode but will rather be some distance away from the surface. It is assumed that some ions, however, become specifically adsorbed onto the surface (to form a Stern layer). Therefore, there will be a potential drop over the Stern layer, and a further potential drop over the diffuse layer.[40] This combines the linear potential drop of Helmholtz' theory (within the Stern layer) with the exponential potential drop of Gouy-Chapman's theory in the diffuse layer. It is important to realise, however, that none of these theories perfectly mirror the practical workings of a double layer.

More recently, *in situ* NMR spectroscopy has been used to quantify cationic and anionic species in double layers on capacitor electrodes. It was found that the quantities of cationic and anionic species in double layers depended on the polarisation of the electrodes. There was evidence that the double layer was not composed of just one counter-ion species, but that micropores were filled with a significant number of co-ions over almost all relevant potential ranges.[41]

As for standard capacitors, the capacitance (C) arising from double layer capacitance can be calculated using the dielectric constant of electrolyte (ε_r) and

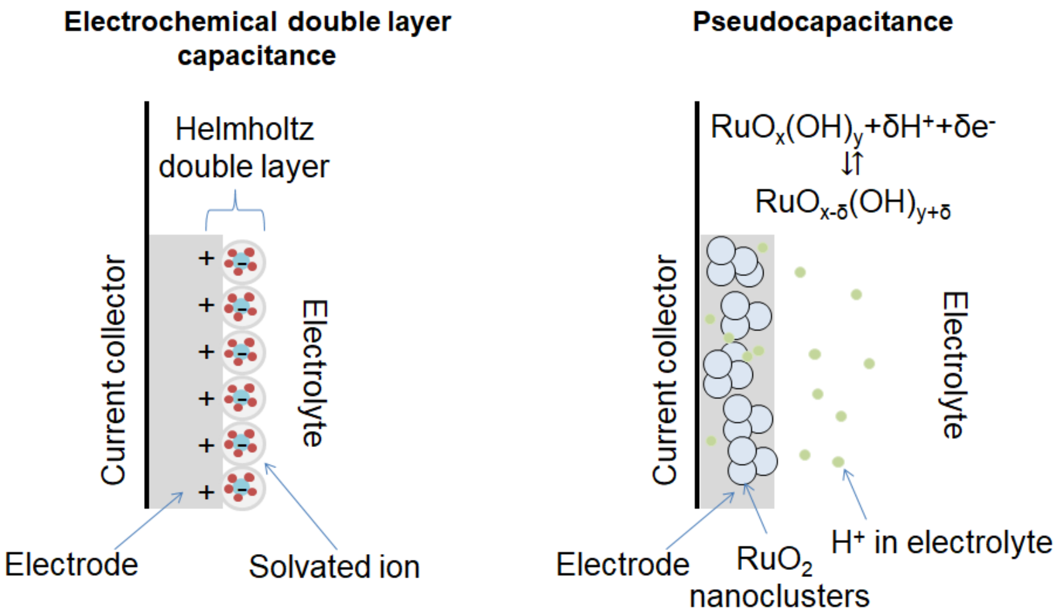

Figure 1-9: Diagram showing the distinction between non-Faradaic capacitance in EDLC and Faradaic pseudocapacitance in RuO_2.[49]

vacuum (ε_0) as well as the surface area (A) of the electrode and the effective thickness of the double layer (d) in Equation 1.17:

$$C = \frac{\epsilon_r \epsilon_0 A}{d} \tag{1.17}$$

The high surface area of some activated carbons (ACs, up to 3200 m^2 g^{-1}), their low cost and excellent electrical conductivity have made ACs the most widely used active material in EDLCs.[42–44] As for standard capacitors, specific energy and specific power of EDLCs depend on the cell voltage (V). The series resistance R, which comprises the resistance of the electrolyte, the resistance between active particles, and the resistance between active material and current collector, is directly related to the maximum specific power (P_{max}) of an EDLC as shown in Equation 1.18:[45]

$$P_{max} = \frac{V^2}{4R} \tag{1.18}$$

The maximum specific energy (E_{max}) can be calculated using Equation 1.19, which uses the specific capacitance (C) and the maximum cell voltage (V):[45,46]

$$E_{max} = 0.5 \times CV^2 \tag{1.19}$$

Owing to the significant influence of the voltage window on E_{max}, systems employing ionic liquid electrolytes, which are comparatively stable to electrolyte reduction or oxidation (with a voltage window up to ca. 3 V), can outperform those using aqueous (voltage window ~1.2 V)[47] or organic electrolytes.[43,44]

A relatively recent type of electrochemical capacitors are transition metal oxide capacitors, which can store charge via quick faradaic reactions (e.g. materials such as Nb_2O_5, $RuO_2 \cdot H_2O$, TiO_2). These reactions require the exchange of electrons with ions in the electrolyte. This has been called pseudocapacitance and pseudocapacitive materials are often capable of significantly higher charge storage (up to 100 times higher) than EDLC active materials.[37,48]

1.3.2.2. Pseudocapacitance

Pseudocapacitive materials tend to show significantly higher capacitance than materials for ELDCs, which store charge via Helmholtz double layers.[49] Pseudocapacitance stems from highly reversible Faradaic reaction between ions in the electrolyte and the active material, which typically occur on or near the surface of the active material particles. One of the first materials shown to exhibit pseudocapacitive behaviour was RuO_2, which has since received much interest because of its high theoretical capacitance of up to 1300 F g^{-1}.[50]

Whilst double layer charge storage in EDLCs depends on the Helmholtz double layer of solvated ions and charged electrodes (see Figure 1-9), quick pseudocapacitive charge storage requires the Faradaic exchange of electrons. For RuO_2 specifically, hydration plays an important role in the valence state change of ruthenium from Ru^{4+} to Ru^{3+}.[51] Protons interact with the hydroxy groups in hydrated RuO_2, as shown in Figure 1-9 and in Equation 1.20:

$$\mathrm{Ru(IV)O_x(OH)_y + \delta H^+ + \delta e^- \rightleftharpoons Ru(III)_\delta Ru(IV)_{1-\delta}O_{x-\delta}(OH)_{y+\delta}} \qquad (1.19)$$

Pseudocapacitance has since been shown to occur in many active materials for LIB negative electrodes such as various nanosized TiO_2 polymorphs (anatase TiO_2,[52] Nb-doped anatase TiO_2,[53] Mo-doped anatase,[54] TiO_2(B),[55] and TiO_2 bronze[56]) as well as for nanosized MoO_2.[57] For negative electrodes for NIBs, amorphous TiO_2 nanotubes,[58] anatase TiO_2/TiO_2(B)-graphene

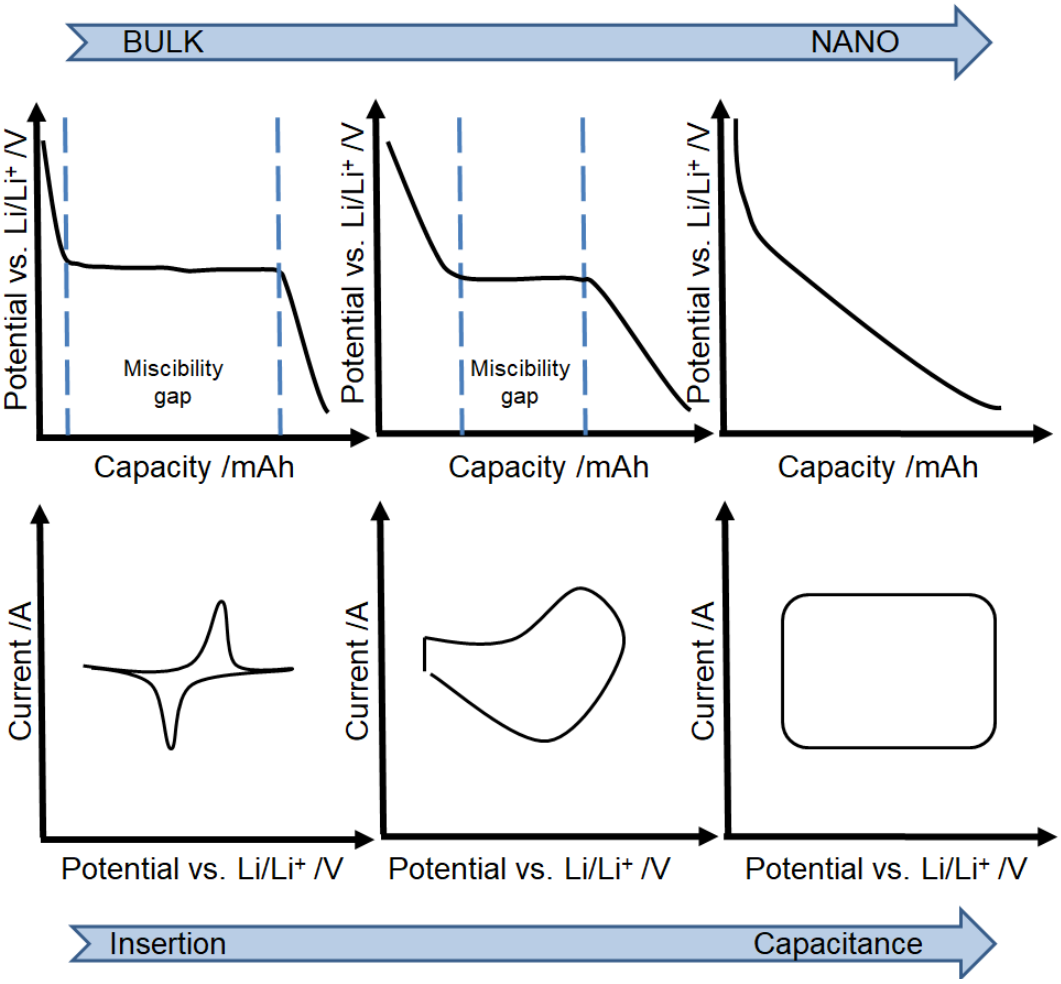

Figure 1-10: Galvanostatic charge/discharge curves and cyclic voltammograms of materials exhibiting battery-type insertion/intercalation behaviour (left), pseudocapacitive oxide supercapacitors-type behaviour (middle), and capacitive EDLC-type behaviour (right).

composites,[59] and anatase TiO_2 mesocages[60] have been shown to exhibit pseudocapacitance.

It is important, however, to distinguish between intrinsic, extrinsic, and intercalation pseudocapacitance. Intrinsically pseudocapacitive materials such as hydrated RuO_2[37,61–65] and MnO_2[66,67] experience pseudocapacitance independently of electrode design. In contrast, extrinsic pseudocapacitance occurs only due to design of the electrode/material and occurs due to diffusion on very small timescales.[66] Once crystallite size falls below a certain size, surface sites for Li^+ or Na^+ become available for fast Faradaic reactions in a range of energies.[68,69] This can be interpreted as the surface of the nanomaterial acting as solid solution host for insertion, because the free energy of the surface varies with the concentration of the active cations.[55] This critical crystallite size for solid solution host behaviour has been demonstrated, amongst others, for $LiMn_2O_4$,[70] V_2O_5,[71] $LiCoO_2$,[72] and TiO_2.[52] Extrinsic pseudocapacitance leads to broadened intercalation peaks in cyclic voltammograms and a sloping charge/discharge profile from galvanostatic measurements (see Figure 1-10).

The differences of cyclic voltammograms and charge/discharge curves between active materials for EDLCs, batteries, and pseudocapacitors can be seen in Figure 1-10. The cyclic voltammogram (see Section 1.5.1) of a double layer capacitor is rectangular, because the capacitance is linearly related to the current at a set scan rate. For (insertion) active materials in batteries, there are distinct peaks indicating the two-phase transition as lithium ions are inserted into the lattice and a phase transition occurs. Pseudocapacitive materials have CVs that still show peaks, but they are much broader than for battery materials. The charge/discharge profile of an EDLC electrode is a straight line, indicating that the amount of charge stored is relative to the potential window the EDLC is cycled in. For battery electrodes, at a certain potential, there is a plateau indicating a two-phase transition due to a miscibility gap. Pseudocapacitive materials can still show a limited two-phase transition plateau, but it is much smaller than for materials where insertion occurs exclusively.

Lastly, intercalation pseudocapacitance can be described as the intercalation into a crystal structure through two-dimensional channels without significant changes to the crystal structure that can be achieved quickly because of limitless solid-state diffusion characteristics.[73,74] It has been described for orthorhombic Nb_2O_5 (T-Nb_2O_5),[73–75] $H_xTi_yO_z$,[76] V_2O_5,[77] and $VOPO_4$,[78] amongst others. The requirements for such intercalation pseudocapacitance have been described as:[75]

- Interconnected crystal layers with adsorption sites of varying energies
- Local charge-transfer at all adsorption sites
- Solid-state diffusion limitation-free intercalation pathways
- No phase transformation upon intercalation.

The surface or surface-near, Faradaic, highly-reversible redox reactions which are the basis of extrinsic pseudocapacitance allow for much faster charge storage than diffusion-controlled intercalation.[68] Nanoparticles show a reduced (or no) miscibility gap when accommodating Li^+/Na^+ on their surface/into their structure because of their crystallite size (see Figure 1-10). This can be explained in part by the free energy of the lattice strain due to the intercalated ion, which can more easily be accommodated for by nanoparticles.[79]

1.3.2.3. Hybrid Electrochemical Capacitors

Hybrid electrochemical capacitors (HECs) use an EDLC electrode and a battery-type electrode. They are referred to as Li-ion hybrid electrochemical capacitors (Li-HECs) or Na-ion hybrid electrochemical capacitors (Na-HECs), depending on the active cation in the electrolyte used. During charging of a Li/Na-HEC, lithium/sodium insertion into the anode active material occurs, whereas hexafluorophosphate anions are adsorbed onto the surface of the activated carbon in the cathode (see Figure 1-11). PF_6^- desorption and Li^+/Na^+ extraction are observed during discharge.[80] In contrast to conventional metal-ion batteries, in HECs, the driving forces for both cations and anions to opposite electrodes during charge and discharge are symmetrical.[81] This

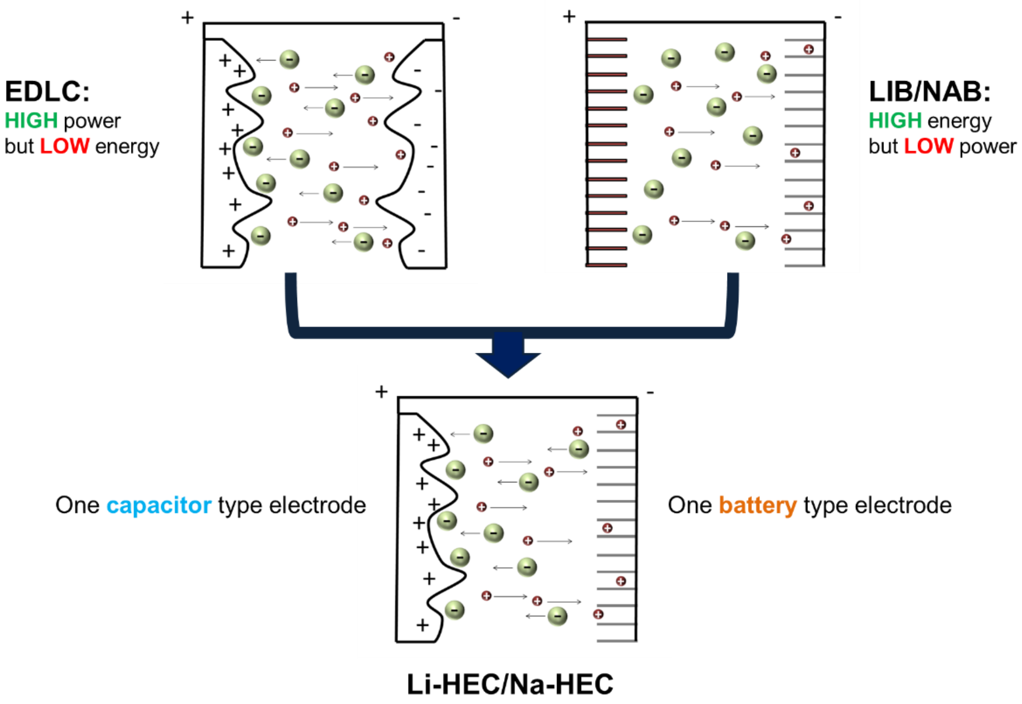

Figure 1-11: Diagram showing the combination of an EDLC positive electrode and a (pseudocapacitive) LIB/NIB negative electrode in a Li/Na-HEC. Li/Na-HECs typically use an organic electrolyte with 1 M $LiPF_6/NaPF_6$.

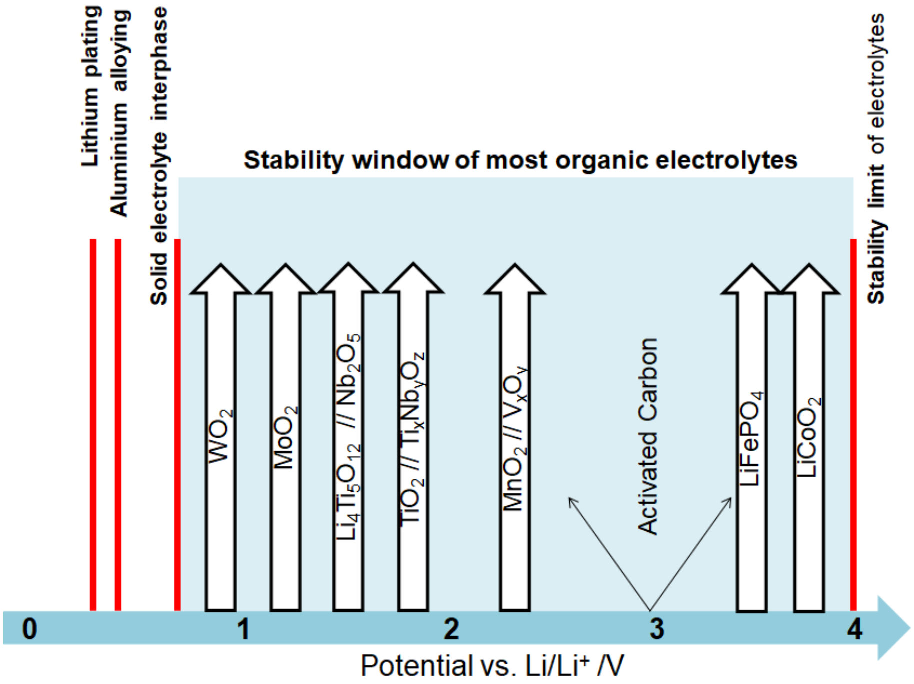

Figure 1-12: Diagram showing potential materials for Li-HECs including their typical potential vs. Li/Li$^+$.

reduces concentration gradients and leads to superior high power performance for Li/Na-HECs compared to LIBs/NIBs.[82] Thus, HECs use both non-Faradaic charge storage as well as Faradaic reactions.[82]

Another way of combining the positive attributes of capacitor and battery-type materials is the development of hybrid electrodes. Naoi et al. first developed such a system using $Li_4Ti_5O_{12}$ anchored on carbon nanofibers (CNF), which showed excellent charge storage properties even at very high applied currents.[83,84] Similar approaches have been taken for supercapacitor electrodes[85–87] and other Li-HECs[74,81,88] and Na-HECs.[59]

Activated carbons (ACs) are used as EDLC electrode because of their high specific surface areas and relatively high specific capacitances. Because of their favourable potential combined with that of AC vs. Li/Li$^+$ (or Na/Na$^+$), various materials have been proposed as insertion-type electrode materials for HECs (see Figure 1-12). However, many other kinds of materials have been studied as negative electrode active materials for Li/Na-HECs, including carbonaceous (e.g. graphite), alloying (e.g. Si), MXenes (e.g. Ti_3C_2), sulphides (e.g. MoS_2), and nitrides (e.g. VN).[89]

Ideally, an oxide capacitor negative electrode for a Li-HEC using an AC positive electrode should have a potential of > 0.8 V vs. Li/Li^+ to avoid lithium plating, to enable the use of inexpensive aluminium as current collector rather than copper, and to avoid the formation of a solid electrolyte interphase (SEI).[9] Active materials should also have a potential < 4.0 V vs. Li/Li^+ because that is the upper limit of the stable voltage window for most organic electrolyte.

1.4. Anode Materials for Batteries and HEC

The energy density of LIBs/NIBs can be improved by higher capacity active materials or a higher cell voltage. The cell voltage depends on the potentials vs. Li/Li^+ at which the anode and cathode materials are active (see Equation 1.1). Minimising the potential of the negative electrode and maximising the potential of the positive electrode result in a maximisation of the potential window. Efforts to maximise cell potential have been severely hampered by a lack of electrolytes that are capable of electrochemical stability at high potentials vs. Li/Li^+. Such properties are required for the use of positive electrode active materials such as lithium cobalt oxide (LCO), nickel cobalt manganese oxide (NMC), or nickel cobalt aluminium oxide (NCA).[90]

For this reason, maximising specific capacity is an attractive pathway to improved energy densities. Positive electrode materials with high theoretical capacity include materials such as (lithium) vanadium oxides (~ 350 mAh g^{-1}). In contrast, negative electrodes with significantly higher specific capacities have been developed using a variety of materials.[91] These include insertion, alloying and conversion materials (see Figure 1-13 and Figure 1-14).

Commercially used graphite is an insertion material with a specific capacity of up to 372 mAh g^{-1}. For insertion materials, lithium insertion (or intercalation in 2D materials like graphite) into the crystal structure does not change the crystal structure significantly. Volume changes are typically limited, e.g. to ca. 10 vol.% for graphite and ca. 1 vol.% for lithium titanium oxide ($Li_4Ti_5O_{12}$).[92] Because of the limited volume change on lithiation/delithiation, insertion materials show the best stability.

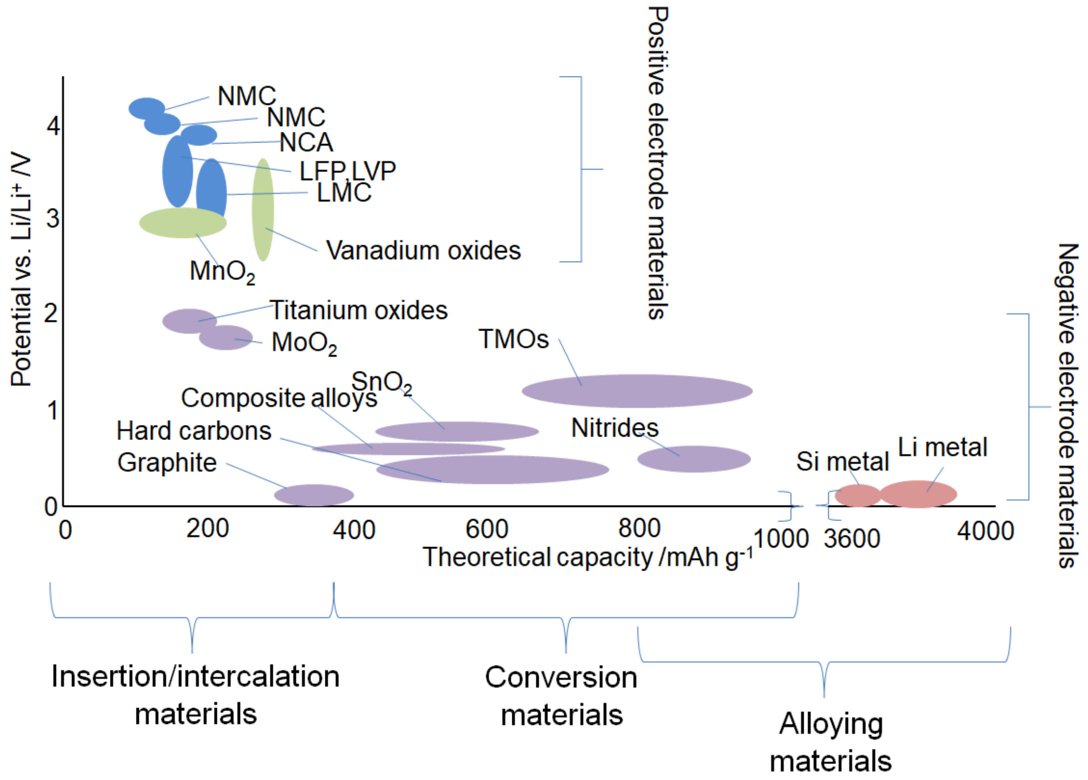

Figure 1-13: Graph of potential electrode materials for both negative and positive electrodes, comprising insertion, conversion, and alloying materials. Adapted from [91] with permission. ©2001 Springer Nature.

Alloying materials such as Si are interesting because they have very high theoretical capacities of up to 3572 mAh g^{-1}.[93] Other alloying materials including Sn (theoretical capacity of 993 mAh g^{-1}), SiO and Al have also been studied due to their high theoretical specific capacities.[94] High capacities can also be obtained for conversion materials such as Fe_2O_3 (1007 mAh g^{-1}), Fe_3O_4 (926 mAh g^{-1}),[93] and MoO_2 (838 mAh g^{-1}).[95] The main disadvantage of both conversion and alloying materials, however, is a significantly limited cycle life due to expansion of up to 300 vol% upon lithiation, which results in cracking and mechanical stress. This can lead to the loss of active material from the electrode.[94,96,97]

Generally, high energy negative electrode materials are alloying or conversion materials. They can store significantly higher charge (more Li-ions) per unit of mass. They normally have a lower operating potential vs. Li/Li$^+$ compared to insertion materials. However, where high power negative electrode materials are of interest, the ability to store charge rapidly becomes relevant. Because both alloying and conversion

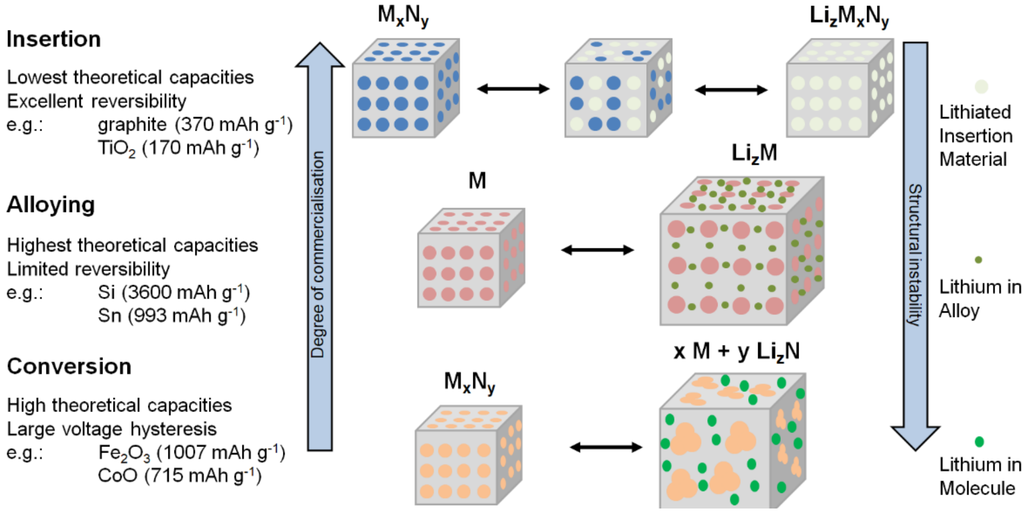

Figure 1-14: Differences in structural changes, stage of commercialisation, structure, and lithiation mechanisms between insertion, alloying, and conversion materials.

reactions involve significant structural reorganisation (which is typically slow due to diffusion limitation), neither type of active material is suited for high power applications. Insertion materials, in contrast, are typically capable of much faster charge storage due to lower diffusion limits to intercalation versus structural reorganisation.

The theoretical specific capacity Q of an electrode active material can be calculated using the number of electrons transferred in the reaction n, its molecular mass M, and Faraday constant F according to Equation 1.20:

$$Q_{th} = \frac{n \times F}{3600 \times M} \tag{1.20}$$

1.4.1. Nanosizing of Battery Active Materials

When high power is a requirement for a battery or a HEC, active materials must be capable of quickly storing and releasing charge. The rate at which an active material can store charge determines its high power properties.[98] Whilst an ideal high power material would be capable of storing the same amount of charge at any rate, physical and electrochemical limitations generally result in a decrease in storable charge with increasing applied currents.

Nanosizing has emerged as one of the most promising ways of producing high power active materials for LIBs and NIBs, because it shortens diffusion path lengths

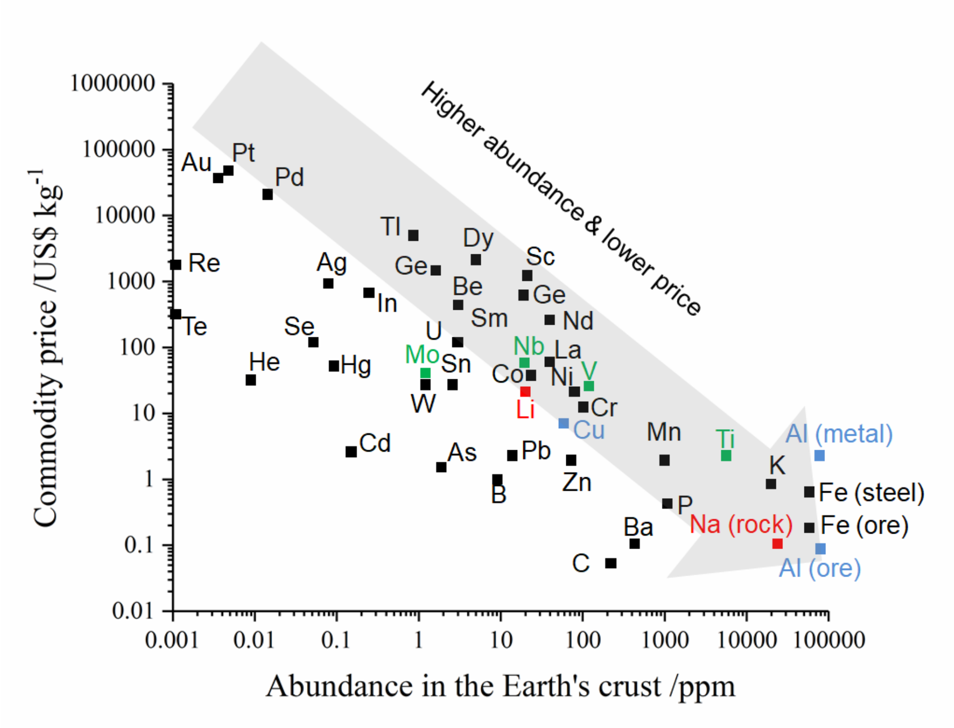

Figure 1-15: Abundance of elements in the Earth's crust and commodity prices of different elements. With data from 2013.[30]

compared to bulk materials and increases the interfacial area between electrolyte and electrode due to the increased specific surface area of smaller particles. For most commercially available cells, internal resistances and diffusion limitations result in only very low available specific capacities at 10 C (which corresponds to a charge or discharge cycle taking six minutes) or higher rates.[98]

An ideal electrode material for high power batteries (or pseudocapacitors) should possess the following properties:[98]

- High Li/Na$^+$ diffusion coefficients
- Short Li/Na$^+$ diffusion and e$^-$ conduction pathways
- High electronic conductivity
- A large interfacial area between electrode and electrolyte (see Figure 1-16).

For extrinsic pseudocapacitors, the proportion of charge stored via bulk-insertion, pseudocapacitance, and non-Faradaic double layer capacitance can be separated (see Section 1.5.1.1). With increased applied currents, the proportion of charge stored via pseudocapacitance typically increases, whilst that stored via

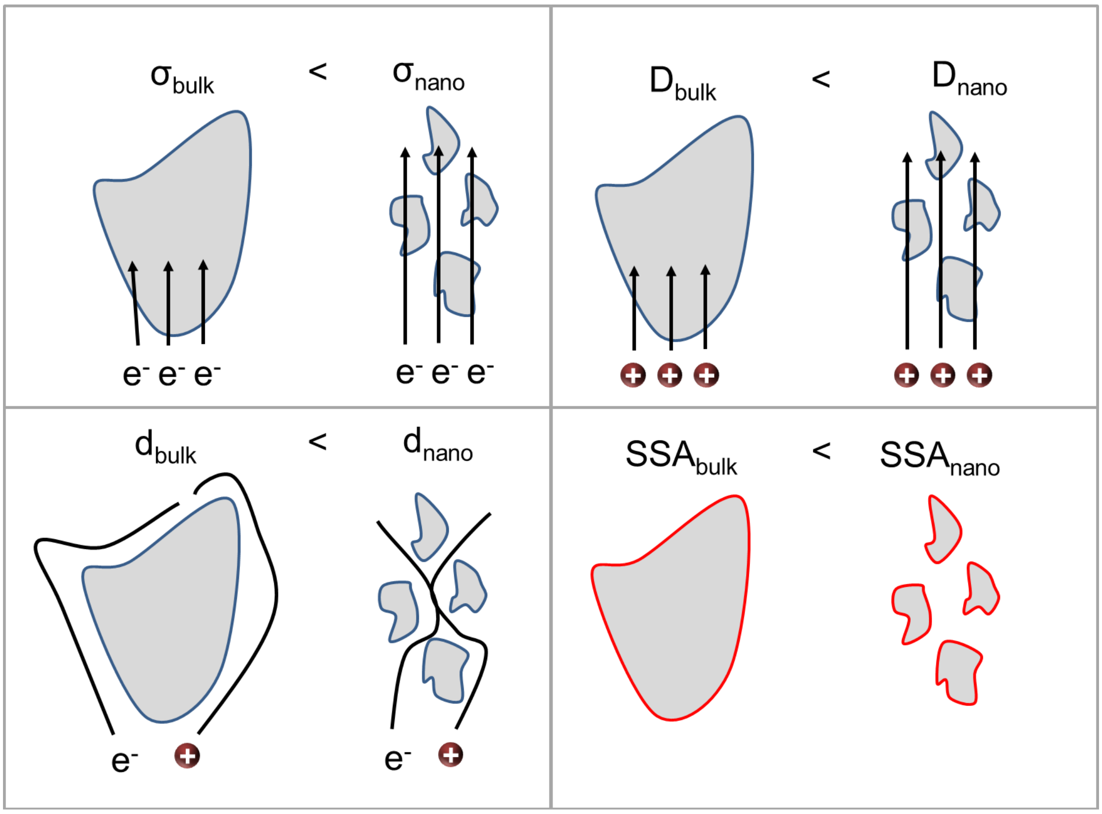

Figure 1-16: Advantages of nanosizing, which include (clockwise from top left): higher electronic conductivity, higher Li/Na-ion diffusion coefficients, higher specific surface areas, and shorter diffusion paths.

diffusion-limited insertion into the bulk decreases.[77] The higher the specific surface area (due to decreased particle size), the higher the pseudocapacitive contributions.[52,99]

Another benefit of using nanoparticles as pseudocapacitive active materials in electrodes is the reduction of two-phase reactions, which results in a sloped voltage profile for charge and discharge, and has been described in Section 1.3.2.2 as the active material acting as solid-solution host.[55,79] Further advantages of nano-sizing include the improved accommodation of strain due to intercalation and potential beneficial reactions that do not occur in micron-sized particles. An oft-cited example for this is mesoporous, nanosized rutile β-MnO_2, which can reversibly store many lithium ions per molecule, whereas the bulk material shows no reversibility at all for this reaction.[100]

1.4.1.1. Disadvantages of Nanoparticles in Energy Storage Devices

There are, however, several disadvantages to using nanoparticles as active material in electrodes. The potential toxicity of nanoparticles is a major concern. Both the environmental impact[101–103] of nanoparticles and the possible danger posed to humans and animals [104–106] have been studied.

The increased complexity, reduced reliability and size control, small scale, as well as higher cost of many synthesis methods for nanoparticles are also detrimental for commercialisation.[107] Some of these issues can be addressed by using a continuous hydrothermal process, as will be discussed later (see Section 1.6.2).

Whilst a high surface area is advantageous for quick charge storage, it also leads to significantly increased side reactions with the electrolyte, catalysed by the lower coordination of surface atoms.[8,108,109] Finally, a lower packing density of nanosized powders compared to micron-sized powders is another concern because it directly influences volumetric power and energy densities.

1.4.2. Research of Insertion Materials

Most currently employed active materials for anodes and cathodes in metal-ion batteries are insertion/intercalation materials. Redox reactions typically follow Equation 1.21, the insertion of cation *C* (Li^+ or Na^+) into sites via 1-, 2-, or 3-dimensional pathways:

$$\mathrm{M^{x+}O_y + zC^+ + ze^- \rightleftharpoons C_zM^{(x-z)+}O_y} \tag{1.21}$$

A larger number of diffusion pathways and low solid-state diffusion limitations for these pathways greatly enhance high power performance of active materials.[110] The three types of intercalation and insertion pathways are shown in Figure 1-17. During lithiation and delithiation (or sodiation and desodiation), the additional charge from Li^+ (or Na^+) is compensated by the reduction or oxidation of the transition metal, respectively. The advantage of insertion materials is the limited volume change during lithiation and delithiation (or sodiation and desodiation). Intercalation/insertion materials should ideally be both ionic and electronic conductors, otherwise, highly conductive carbons or other additives are needed to make conductive electrodes.

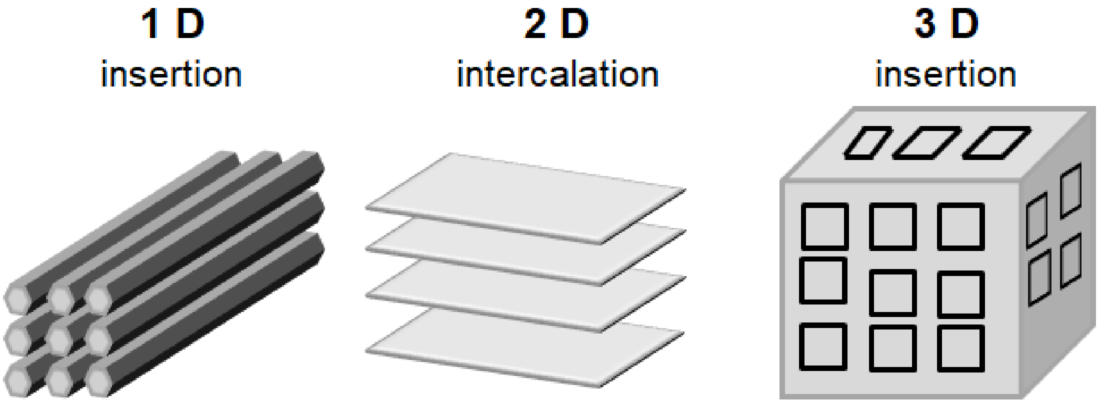

Figure 1-17: Diagram showing the three possible pathway geometries for insertion materials, comprising 1-, 2-, and 3-dimensional diffusion pathways.

For LIBs, graphite is by far the most commonly used active material for the anode, and is capable of intercalating one Li^+ per six carbon atoms, as seen in Equation 1.14.[5] Graphite has a low intercalation/deintercalation potential vs. Li/Li^+ and high cycling stability. Intercalation results in an expansion of interlayer distance of the graphene layers by 10 vol.%.[92,111] There are various issues with graphite as active material, however, including poor rate properties,[108,112,113] the necessity for the formation of a solid electrolyte interphase (SEI) for stable cycling,[108,113] and safety issues due to lithium plating and dendrite formation, which can cause catastrophic cell failure.[114]

Titanium-based oxides have been considered as potential alternatives to graphite. Among these, $Li_4Ti_5O_{12}$ (LTO, theoretical specific capacity of 175 mAh g^{-1}) and TiO_2 (for example, anatase, 170 mAh g^{-1}) have received widespread attention due to very good cycle life,[115] inherent safety because of their high operating potential vs. Li/Li^+ of 1.2 to 2.3 V,[116] environmental benignness,[117] high elemental abundance (see Figure 1-15),[30,118] low capacity loss, good high power characterisitics and relatively small structural changes during cycling.[119] However, as can be seen from Equation 1.11, the high operating potential vs. Li/Li^+ severely reduces the achievable energy density.[117,120]

Anatase TiO_2 has received considerable attention.[121–126] The body centred crystal structure (space group $I4_1/amd$) of anatase consists of TiO_6 octahedra in planar double chains,[127] allowing for Li-ion diffusion paths to form from the octahedra interstitial sites (“octahedral holes”).[119] Charge neutrality is maintained via Equation 1.22:[119]

$$\mathrm{Ti^{4+}O_2 + zLi^+ + ze^- \rightleftharpoons Li_z(Ti^{3+}_zTi^{4+}_{1-z})O_2} \qquad (1.22)$$

The transition between Ti^{4+} and Ti^{3+} (and the reverse) takes place in the range of 1.6 to 2.1 V vs. Li/Li^+. Whilst the theoretical capacity can be as high as 330 mAh g^{-1} assuming the reversible intercalation of one Li^+ ($z = 1$) per molecule of TiO_2,[94] only 0.5 Li^+ can usually be reversibly stored per molecule of TiO_2, which is accompanied by the reversible transformation to orthorhombic crystal structure (space group *Imma*).[128,129] The resultant increase of lattice parameters a and b (from 3.784 to 3.808 and 4.077 Å, respectively) and decrease in c (from 9.515 to 9.053 Å) suggest an increase in volume by ca. 3 %.[129]

Newer additions to titanium based negative electrode materials include work on titanium niobium mixed oxides such as $TiNb_6O17$,[130] $Ti_2Nb_{10}O_{29}$,[131,132] $Ti_2Nb_{10}O_{27.1}$,[133] and $TiNb_2O_7$.[113,134–138] For example, $TiNb_2O_7$ has been shown to exhibit a working potential of ca. 1.6 V vs. Li/Li^+ and a specific capacity of 285 mAh g^{-1} at 0.2 C.[137]

Due to its small interlayer distance of 3.2 Å, graphite cannot reversibly intercalate the larger Na-ions (95 pm) in the same way as seen for Li-ions (68 pm).[139] Hard carbon, on the other hand, with its larger interlayer distances (ca. 3.9 Å) and disordered structures,[140] has commonly been used as an anode in Na-ion batteries because it can intercalate sodium ions.[29]

Various polymorphs of TiO_2 have also been investigated as active material for anodes in NIBs. Micrometre-sized anatase has been shown to be electrochemically inactive in NIBs,[141] although first-principle calculations have indicated that diffusion coefficients in anatase should be similar for both Na- and Li-ions.[142] As described above, nanosized particles show extrinsic pseudocapacitive charge storage once the crystallite size falls below a critical limit (typically > 20 nm) and surface sites for Li^+ (or Na^+) accommodation become available in a range of energies for Faradaic reactions.[68,69]

1.4.3. Research of Conversion Materials

Compounds of transition metals (M) like Cu, Ni, Co and Fe with anions A (e.g. O, F, S, N or P) of the formula M_xA_y can undergo a conversion reaction upon lithiation.[94] Metal oxides were shown by Poizot et al. to be fully converted into the metallic state.[143] These materials follow the reaction in Equation 1.23:

$$M_xA_y + zLi^+ + ze^- \rightleftharpoons Li_zA_y + xM \tag{1.23}$$

Whilst for graphite one Li-ion can be stored per six carbon atoms, these conversion reactions can involve up to six Li^+ in the reaction (*z*) per formula unit. Because of this, the theoretical capacity of conversion materials can be up to ~1000 mAh g^{-1}.[5,92]

Because of low cost, non-toxicity, and the large natural abundance of iron, the iron oxides Fe_2O_3 and Fe_3O_4 are of special interest as conversion active materials in LIBs.[144] γ-Fe_2O_3 and Fe_3O_4 are promising materials for higher specific energy LIBs because of their theoretical capacities of 926 and 1007 mAh g^{-1}, respectively. However, large volume changes during cycling can result in structural instability of the electrode, which manifests in significant capacity fading.[1] Voltage hysteresis is another issue associated with conversion materials; the delithiation of the active material occurs at much higher potentials vs. Li/Li^+ compared to the lithiation.[145] This results in a significant lowering of energy efficiency, which makes the commercial application of these materials infeasible.[146] Similar caveats apply to the use of conversion active materials for anodes of NIBs.[147]

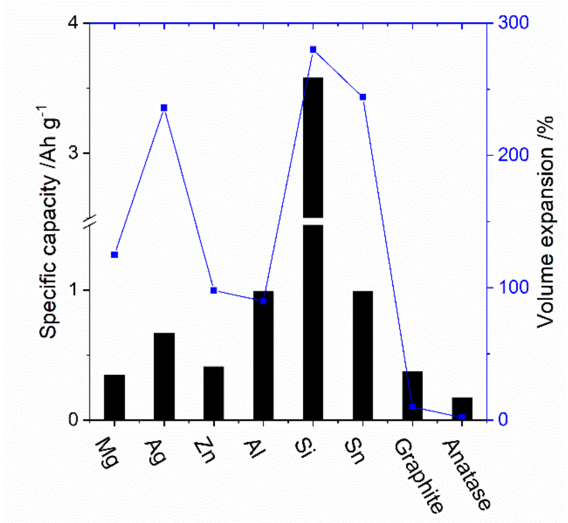

Figure 1-18: Specific capacities and volume expansion of various alloying materials upon full lithiation, using data from the literature.[155]

The significant expansion/shrinking during lithiation and delithiation for alloying materials can lead to cracking of particles or the electrode.[148,149] High applied currents can also be a contributing factor to electrode cracking because of the enrichment of lithium-ions on the electrode surface resulting from diffusion limitations in the electrode.[150] To mitigate the negative effects of large volume expansion in alloying and conversion materials, various strategies have been developed. These include providing voids capable of accommodating volume changes: reduced graphene oxide composites with Fe_2O_3,[151] MoO_2 @ carbon hollow microspheres[152], or layer-by-layer MoO_2-graphene composite films.[148] Another strategy has used the chemical and structural stability of anatase to improve the stability of other active materials such as $TiO_2@Fe_2O_3$ arrays[153] and $Fe_3O_4@TiO_2$ clusters.[154]

1.4.4. Research of Alloying Materials

Alloying materials such as Sn, Ge, Al, and Si have gained interest due to their high specific capacities[94] of up to 3572 mAh g^{-1} (for silicon).[93] The theoretical specific capacities for alloying materials and intercalation materials such as graphite and anatase have been plotted with the respective volume expansion upon full lithiation in Figure 1-18.[155]

Alloying reactions in LIBs follow Equation 1.24:

$$\mathrm{M} + \mathrm{zLi}^{+} + \mathrm{ze}^{-} \rightleftharpoons \mathrm{Li_zM} \qquad (1.24)$$

It describes the formation of an alloy between Li and the alloying material M. The high specific capacities of these materials can be explained by the fact that, for example, a single Si atom can alloy with up to 15 Li-ions ($z = 15$). The lithiation of some alloying materials such as ZnO involves both the conversion reaction of the metal oxide and the alloying process of the metal described in Equation 1.23 and 1.24.[156]

1.4.5. The Solid Electrolyte Interphase (SEI) and its Role

As mentioned above, the formation of a stable SEI is a key requirement for the use of graphite in LIBs. This is also true for alloying and conversion materials, which show significantly higher specific capacities than graphite. Because they are active at low potentials vs. Li/Li^{+}, organic electrolytes become unstable. The formation of an SEI on graphite electrodes both represses the exfoliation of graphite[157] and the

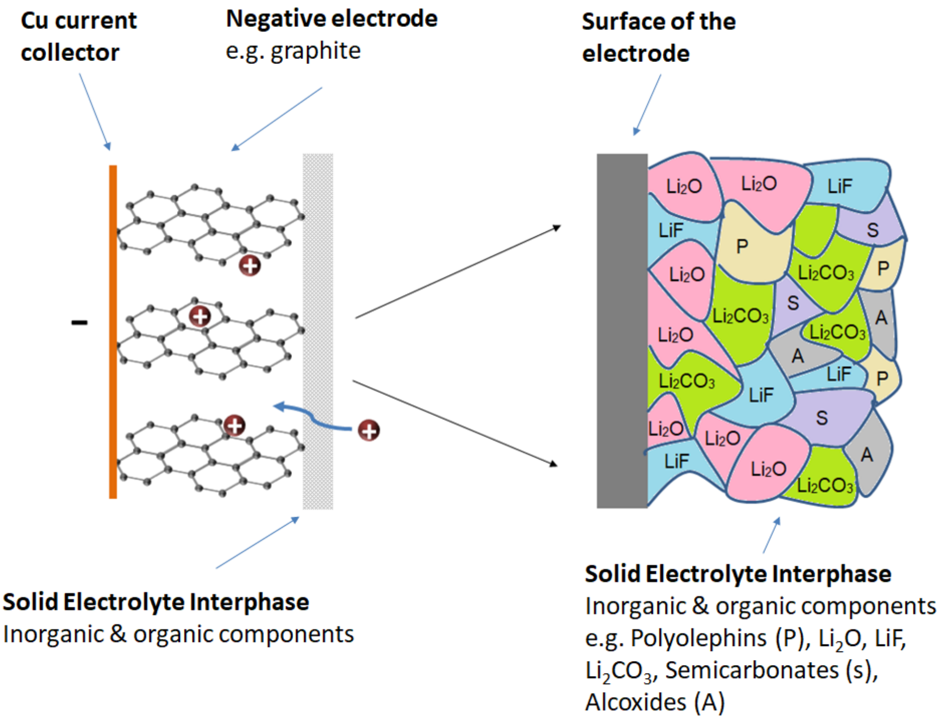

Figure 1-19: Diagram showing the inhomogeneous SEI layer formed on a standard graphite LIB anode, consisting of a mixture of inorganic & organic components.

continued decomposition of the organic solvents and Li-ion containing salt at low potentials.[158] The requirements for an ideal SEI are the same in LIBs and NIBs:[27]

- Electronic insulation (to prevent continued electrolyte decomposition)
- High ionic conductivity for the active cation
- Insolubility (to allow for a stable, inert chemical environment).

The electrolytes used herein, as those used in nearly all commercial LIBs, contain EC, because in combination with the commonly employed PF_6^- anion it allows for the formation of stable, complex, inhomogeneous SEIs on most electrodes.[158–164] An SEI consists of a variety of different components in various layers/clusters (see Figure 1-19). The components of SEIs include LiF, Li_2O, Li_2C_2, Li_2CO_3 as well as various organic components such as alcoxides, semicarbonates, and polyolephines.[163]

For NIB anode materials such as sodium titanate, a similarly composed array of decomposition products of carbonates (Na_2CO_3, $NaCO_3$-R), NaF, NaCl and NaO-R has been identified.[26] The formation of SEI in NIBs usually occurs at potentials < 1.0 V vs. Na/Na^+.

However, it has been shown that the stability of SEIs in NIBs depend on the materials used in the electrode, both the binder and active material. Studies of the SEI formation on electrodes with $Na_2Ti_3O_7$ active material and PVDF as binder using 1M $NaClO_4$ electrolyte have revealed that even before cycling, Na-ions reacted via a dehyrdo-fluorination with PVDF. Muñoz-Márquez et al. concluded that current electrode formulations for Na-ion electrodes using PVDF as binder and $NaClO_4$ as Na-ion salt in the electrolyte are not viable. The increased reactivity of sodium over lithium can be considered a key factor in the need for different binders in NIBs.[26]

Typically, the higher the surface area of an active material, the larger the irreversible capacity loss in the first cycle due to the formation of SEI.[165] This is often considered as one of the prime disadvantages of using nanoparticles as anode materials in LIBs and NIBs. The balancing of full cells becomes significantly more difficult with increased formation of SEI on high surface area nanoparticles.

There is a wide range of additives for LIB and NIB electrolytes that can improve the cycling stability of full-cells and half-cells by promoting the formation of a stable SEI. During cycling, vinylene carbonate (VC) and similar additives are polymerized electrochemically, forming insoluble polyolefin nuclei, which stabilize the SEI.[165]

1.5. Electrochemical Measurements of Batteries and Hybrid Capacitors

1.5.1. Potentiodynamic Methods for Batteries and Hybrid Capacitors

In potentiodynamic electrochemical measurements, the potential of the working electrode versus the reference electrode is changed by a set potential (the scan rate) per time interval. Most commonly used is cyclic voltammetry, in which the potential is changed linearly with time from a minimum (V_{min}) to a maximum potential V_{max} and then back to V_{min} (see Figure 1-20). The resulting current is measured. The measurement can be used to determine the active potential range of a material, in which charge can be stored/discharged via redox, pseudocapacitive and/or capacitive processes. The specific discharge capacity Q_{dis} for a half-cell in mAh g^{-1} can be

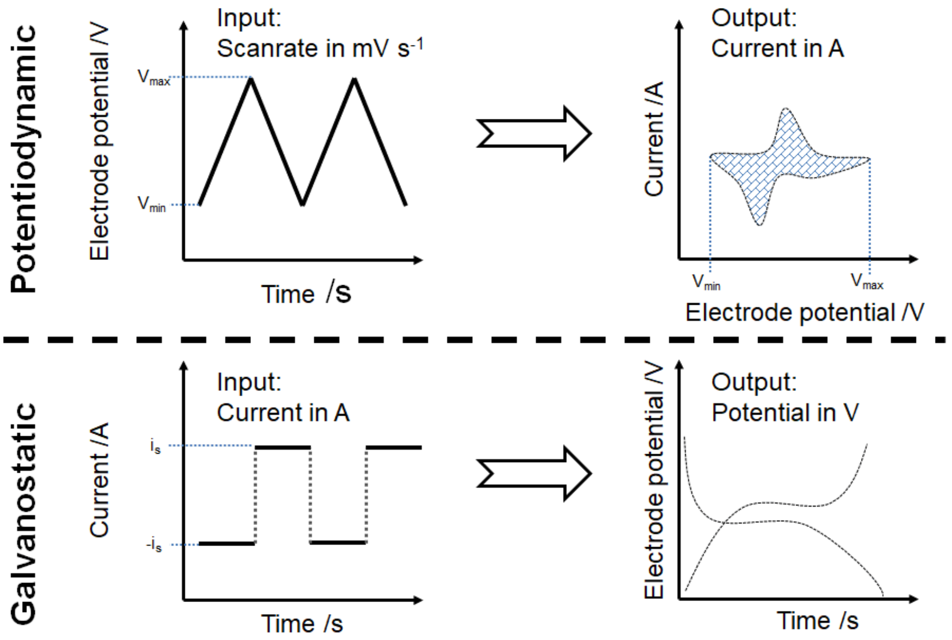

Figure 1-20: Diagram of input and output for both potentiodynamic and galvanostatic electrochemical measurement techniques.

calculated using the integral of current *I* and the potential *V* (area of the CV, see shaded area of the CV on the top right in Figure 1-20), divided by the scan rate *v* and the mass of active material (*m*) as shown in Equation 1.25:

$$Q_{dis} = \int_{V_{min}}^{V_{max}} I(V)\, dV\, \nu^{-1}\ m^{-1} \tag{1.25}$$

Cyclic voltammograms can also be recorded for hybrid capacitors. For these, the specific capacitance of the full cell C_{cell} can be calculated from the integral area of the cyclic voltammograms, divided by 2, the potential window ($V_{max} - V_{min}$), the scan rate *v* and the total mass of active material in both anode and cathode (*m*) via Equation 1.26:

$$C_{cell} = \int_{V_{min}}^{V_{max}} I(V)\, dV\, 2^{-1}\, (V_{max} - V_{min})^{-1}\, \nu^{-1}\ m^{-1} \tag{1.26}$$

1.5.1.1. Charge Storage Mechanism

There are various methods to separate diffusion-limited and (pseudocapacitive) contributions to charge storage (and currents). All methods employ the power law relationship between the current *i* and the scan rate *v* in Equation 1.27:

$$i = a \times \nu^{b} \tag{1.27}$$

A method first described by Trasatti et al. uses the fact that the total charge (q_T) can be expressed as the sum of the charge stored via capacitive (q_s) and via diffusion-limed processes (q_d) as in Equation 1.28:[64]

$$q_T = q_s + q_d \tag{1.28}$$

Herein, q_T is the total voltammetric charge, which measures the total charge exchanged between electrode active material and electrolyte. q_s is the charge stored in the outer, easily accessible surface area, which is related to fast pseudocapacitive charge storage. q_d is the charge related to the slower, diffusion-limited processes.

An estimated percentage for the pseudocapacitive contribution to charge storage (PCS) can therefore be calculated by rearranging Equation 1.28 into Equation 1.29:

$$PCS = q_s / q_T \tag{1.29}$$

Using the power law relationship in Equation 1.27 and considering that pseudocapacitive charge storage is linearly related to ν^{1}, whereas the diffusion-limited processes are linearly related to $\nu^{0.5}$, q_d can be replaced in Equation 1.28 as seen in Equation 1.30, where c is a constant:[68]

$$q_T = q_s + c\nu^{-0.5} \tag{1.30}$$

Hence, q_s can be determined from the intercept and the constant c from the slope by plotting $\nu^{-0.5}$ against the total charge q_T. This means that when $\nu \rightarrow \infty$, at a theoretical, infinitely fast scan rate, the intercept q_s gives the pseudocapacitive charge. Deviations from the linear plot indicated polarization effects, which were discounted.[64,73,80]

For a method based on a (simplified) Cottrell equation which is the basis for the power law relationship in Equation 1.27, a relationship can be expressed for a constant a (which is a collection of constants in the Cottrell equation) that connects the current i with charge/discharge time t for diffusion limited processes in Equation 1.31:

$$i = a\, t^{-0.5} \tag{1.31}$$

In this relationship, time t can be replaced with the reciprocal of the scan rate v, which gives Equation 1.32 for diffusion-limited processes:

$$i = a\, v^{0.5} \tag{1.32}$$

As discussed above, the current response for capacitive processes follows Equation 1.33:

$$i = a\, v^{1} \tag{1.33}$$

Hence, currents measured via cyclic voltammetry follow Equation 1.27, where a and b are adjustable parameters. b gives an indication of the ratio of diffusion-limited and capacitive charge storage. Therefore, one can plot a graph of Equation 1.34:

$$log\, i \;=\; log\, a \;+\; b\, log\, v \tag{1.34}$$

This allows to calculate the parameter b from the slope of such a plot at different potentials. For b = 0.5, the charge storage is assumed to be completely diffusion-limited, and the closer b is to 1.0, the more (pseudo)capacitive contributions to charge storage come into effect.

A further way of calculating contributions to the currents uses the fact that the power law relationship in Equation 1.27 can also be expressed as the sum of the current due to capacitive processes (i_s) and the current due to diffusion-limed processes (i_d) as in Equation 1.35:

$$i = i_s + i_d \tag{1.35}$$

Therefore, using Equation 1.32 and 1.33 leads to Equation 1.36:[71]

$$i = a_1\, v + a_2\, v^{0.5} \tag{1.36}$$

Rewriting this relationship yields Equation 1.37:

$$\frac{i(V)}{v^{0.5}} = a_1\, v^{0.5} + a_2 \tag{1.37}$$

The values for a_1 and a_2 can be calculated from CVs for different potential from a range of scan rates by plotting a graph of the relationship in Equation 1.37. The slope and intercept give the parameters a_1 and a_2, respectively. These parameters can then be used to calculate the contributions from diffusion-limited and capacitive charge storage at each individual potential. Furthermore, these contributions can then be multiplied with the measured currents to yield a cyclic voltammogram of the capacitive part of the charge storage. The charge can be calculated for both the measured CV and the calculated pseudocapacitive CV and compared to yield the contributions to charge storage from pseudocapacitive processes.

1.5.1.2. Diffusion Coefficient

A method described by Randles-Sevcik[166–168] was used to calculate Li/Na$^+$ diffusion coefficients from CVs. The peak current (I_p) relates to the number of electrons transferred (n), the (geometric) area of the electrode (A), the ion concentration (C), the scan rate (v), and the diffusion coefficient (D) as per Equation 1.38. The slopes obtained from a plot using this equation was used to calculate the diffusion coefficient.

$$I_p = 2.69 \times 10^5 n^{\frac{3}{2}} A D^{\frac{1}{2}} C v^{\frac{1}{2}} \tag{1.38}$$

It is important to note that the Randles-Sevcik equation was developed for theoretical redox reactions with perfect reversibility. Reactions such as the ferrocene/ferrocenium redox reaction depend on the concentration, diffusion properties, and scan rate as described by Equation 1.38. Therefore, it is important to note that the apparent diffusion coefficients calculated using the Randles-Sevcik equation are not true diffusion values, but rather apparent diffusion values mostly useful for comparisons between samples.

1.5.2. Galvanostatic Methods for Batteries and Hybrid Capacitors

Galvanostatic charge/discharge measurements were used to determine high power cycling properties and cycling stability of the active materials and HECs. In galvanostatic measurements, a constant positive current (during charge) and a constant negative current with equal value (during discharge) are applied alternately, until a maximum (V_{max}) or minimum (V_{min}) cut-off potential are reached, respectively (see Figure 1-20). The change in potential over time is recorded. The discharge capacity (Q_{dis} in As g^{-1}) of a half-cell can be calculated from the current (I in A), charge/discharge time (t in s) and mass of active material (m in g) using Equation 1.39:

$$Q_{dis} = I \times t \times m^{-1} \tag{1.39}$$

From both charge and discharge capacity, the Coulombic efficiency η_{Coul} can be calculated using Equation 1.40:

$$\eta_{Coul} = 100 \times \frac{Q_{dis}}{Q_{char}} \tag{1.40}$$

It describes how much of the charge capacity is retained during discharge. It should be high (> 99 %) in most cases.

For the Li-HECs/Na-HECs, the cell capacitance (C_{cell} in C g^{-1}) was calculated using the current (I in A), discharge time (t in s), the potential window during discharge (ΔV in V), and the mass of active material in both anode and cathode (m in g) in Equation 1.41:

$$C_{cell} = (I \times t)\ (\Delta V \times m)^{-1} \tag{1.41}$$

Similarly, the specific capacity for Li/Na-HECs can be calculated using Equation 1.39, where m is the mass of active material in both anode and cathode.

1.5.2.1. *Power & Energy Density*

Galvanostatic charge/discharge measurements are also used to calculate power (P in W kg^{-1}) and energy densities (E in Wh kg^{-1}) for Li/Na-HECs using Equations 1.42 and 1.43:

$$P = \Delta V \times (I/m) \tag{1.42}$$

$$E = P \times (t/3600) \tag{1.43}$$

ΔV is the average potential during discharge, I the current (in A), m the mass of the active materials in both anode and cathode (in kilograms) and t is the discharge time (in seconds).

Using these values, a Ragone plot can be constructed by plotting energy density and power density on logarithmic scales, which allows for the comparison of energy and power properties for a wide variety of energy storage technologies.[36,169,170]

1.5.2.2. *Balancing Masses of Active Materials in Anode and Cathode*

To achieve a good performance for full cells such as Li/Na-HECs, the total charge of anode Q_{anode} and cathode $Q_{cathode}$ should follow Equation 1.44:

$$Q_{anode} = Q_{cathode} \tag{1.44}$$

Therefore, if q_{anode} and $C_{cathode}$ are the specific capacity of the negative electrode active material and specific capacitance of the positive electrode active material, respectively, the mass ratio between the mass of active material in anode (m_{anode}) and cathode ($m_{cathode}$) should follow Equation 1.45:

$$m_{anode} \times q_{anode} = m_{cathode} \times C_{cathode} \times \Delta V/3.6 \tag{1.45}$$

$$\rightarrow\ m_{anode}/m_{cathode} = C_{cathode} \times \Delta V/(3.6 \times q_{anode})$$

For example, if the specific discharge capacity of a material is 100 mAh g^{-1} at a certain specific current, and the specific capacitance of an AC electrode is 60 F g^{-1} with an expected potential window of 1.5 V, the resulting mass ratio of active material in anode and cathode is ca. 1:4. This mass loading ratio “optimization” is only valid for one current, unless the rate properties of both materials are equal.

1.5.2.3. *C-rate*

Although galvanostatic charge/discharge measurements in this thesis will be referred to by specific current values, C-rate is a common concept when analysing the performance of battery materials.

A C-rate is defined via the theoretical capacity of a material. A C-rate of 1 C indicates the current required to charge (or discharge) an electrode fully in 1 hour. Hence, a C-rate of ½ C equals a full charge or discharge within 2 hours and a C-rate of 2 C equals a charge or discharge within ½ hour. For a material with a theoretical capacity of 170 mAh g^{-1} and an electrode with an active mass loading of 2 mg, the current that needs to be applied for a C-rate of 1 C would be 0.34 mA.

1.5.2.4. Differential Capacity

Differential capacity analysis can make use of electrochemical results from galvanostatic charge/discharge measurements to monitor properties such as lifetime and phase transitions.[171] The differential capacity (dQ/dV) can be calculated using the capacity increase per change in potential, plotted over the potential range. Peaks in different capacity plots correspond to specific lithiation and delithiation processes.

1.5.2.5. Galvanostatic Intermittent Titration Technique (GITT)

Galvanostatic Intermittent Titration Technique (GITT) can be used to determine the chemical diffusion coefficient of electrode materials. An understanding of the thermodynamics of active materials enables a further analysis of the electrochemical behaviour. The GITT procedure can provide an insight into the kinetics.

In GITT measurements, current pulses are followed by relaxation periods after each pulse. During lithiation, a current pulse will quickly decrease the cell potential (proportional to the iR drop due to resistance), after which the cell potential will slowly decrease as in a normal lithiation process due to concentration gradients. During the relaxation step, the lithium concentration in the electrode will slowly homogenize via Li-ion diffusion. Firstly, the cell potential will rapidly increase by a value proportional to the iR drop and second, the cell potential will increase slowly until the electrode reaches equilibrium. At equilibrium, the change in cell potential becomes zero.

Diffusion coefficients can be calculated using Equation 1.46:[172,173]

$$D = \frac{4}{\pi}\left(\frac{iV_m}{z_A F S}\right)^2 \left[\frac{\frac{dE}{d\delta}}{\frac{dE}{d\sqrt{t}}}\right] \tag{1.46}$$

In Equation 1.46, i is the current, V_m the molar volume of the electrode, z_A the number of electrons transferred, F is the Faraday constant, S is the area of the electrode, $\frac{dE}{d\delta}$ is the slope of the titration curve and $\frac{dE}{d\sqrt{t}}$ is the slope of the linearized potential curve during the current pulse of duration t.

If small currents are applied for sufficiently short times, both the linearized potential curve as well as the titration curve will be linear, so that Equation 1.46 can be simplified to Equation 1.47:[174]

$$D = \frac{4}{\pi\tau}\left(\frac{n_m V_m}{S}\right)^2 \left[\frac{\Delta E_s}{\Delta E_t}\right] \tag{1.47}$$

In Equation 1.47, τ is the duration of each pulse, ΔE_s is the voltage change due to the electrochemical relaxation, and ΔE_t is the voltage change during the current pulse.

1.5.3. Electrochemical Impedance Spectroscopy (EIS) of Batteries and Hybrid Capacitors

In electrochemical impedance spectroscopy (EIS), an AC voltage is applied to an electrochemical cell. The frequency of the signal is varied over a wide range (usually from 10s of mHz to 100s of kHz). The real and imaginary components of the current response are combined with an equivalent circuit model to fit the data. Impedance is the equivalent of resistance in AC circuits, extending the definition from just a magnitude to include a phase. Following Ohm's law (Equation 1.48), resistance (R) can be calculated by the division of voltage $U(t)$ and current $I(t)$.

$$R = \frac{U(t)}{I(t)} \tag{1.48}$$

Because the impedance Z requires the complex division of voltage and current, however, this is only valid for single element circuits with an ideal resistor (see Figure 1-21a). The complex behaviour of a real resistor must be taken into account by expressing the dependence of voltage and current on frequency.[175] Considering an AC excitation signal of $U(t)$ at time t, U_0 is the amplitude of the excitation signal, ω the frequency following Equation 1.49, and assuming the equivalent for $I(t)$, I_0 is the current amplitude shifted by the phase shift φ. Therefore, Equations 1.50 and 1.51 describe the complex potential and current responses:

$$\omega = 2\pi f \tag{1.49}$$

$$U(t) = U_0 sin(\omega t) \tag{1.50}$$

$$I(t) = I_0 sin(\omega t + \phi) \tag{1.51}$$

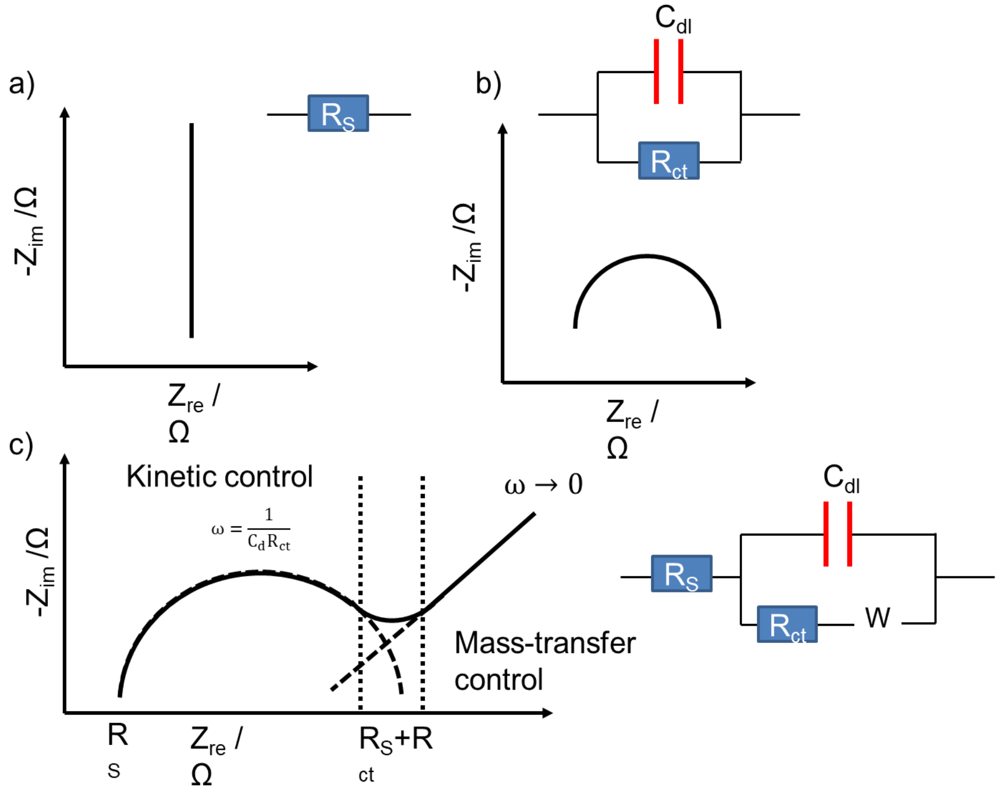

Figure 1-21: Typical response (Nyquist plot of real and imaginary parts of impedance) to Electrochemical Impedance Spectroscopy (EIS) for a) a perfect resistor, b) a Randall circuit and c) the model of a simplified Li/Na-ion half-cell.

Hence, *Z* can be expressed using Ohm's law (Equation 1.48) as magnitude Z_0 and the phase φ in Equation 1.52:

$$Z = \frac{U_0 sin(\omega t)}{I_0 sin(\omega t + \phi)} = Z_0 \frac{sin(\omega t)}{sin(\omega t + \phi)} \tag{1.52}$$

Using Euler's formula (Equation 1.53) allows for the conversion of Equation 1.52 into the complex impedance $Z(\omega)$ in Equation 1.54:

$$exp(i\phi) = cos(\phi) + j\ sin(\phi) \tag{1.53}$$

$$Z(\omega) = Z_0\ exp(i\phi) = Z_0(cos(\phi) + j\ sin(\phi)) \tag{1.54}$$

Complex impedance responses for typical elements, with both real and imaginary parts, and combinations thereof, are shown in Figure 1-21b and c. In Nyquist plots such as these, the real part of the complex impedance is plotted on the abscissa and the inverse of the imaginary part on the ordinate. The Randles circuit[176] in Figure 1-21c describes an equivalent circuit in which R_s is the series resistance of the electrolyte, C_{dl} the double-layer capacitance, and R_{ct} the charge-transfer resistance. The Warburg element W represents mass-transfer impedance. This can be considered a good equivalent circuit for Li-ion and Na-ion half-cells.[142,177–180]

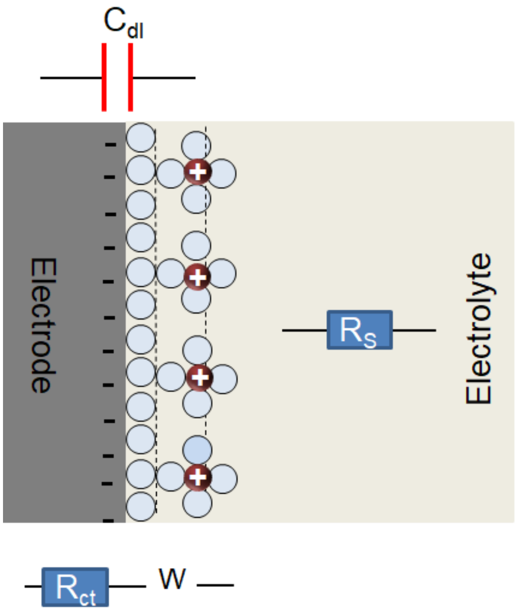

Figure 1-22: Figure representing a Randles circuit of an electrode in a Li/Na-ion half-cell.

Figure 1-22 shows a diagram of the double layer capacitance and the charge transfer and mass-transfer resistance in an electrode, along with the series resistance of the electrolyte, as represented by a Randles circuit. As can be seen from Figure 1-22, this is only valid for electrode materials that do not undergo significant structural changes upon cycling which lead to the breakup of the electrode structure, or electrodes after the formation of a SEI (see 1.4.5)

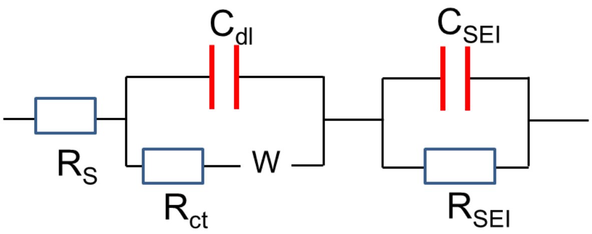

Figure 1-23: An equivalent circuit that includes the formation of a solid electrolyte interphase (SEI) forming on the anode pf a Li-ion or Na-ion half-cell.

Therefore, for systems that develop a SEI (typically ones cycled to low potentials vs. Li/Li$^+$ and Na/Na$^+$, where organic electrolytes become unstable), additional elements need to be introduced into equivalent circuits to account for addition impedance. An example for such an equivalent circuit is shown in Figure 1-23.

The Warburg impedance can be determined from the low frequency (diffusion-limited) region of a Nyquist plot. The Warburg impedance is the slope of a plot of the real impedance versus the reciprocal square root of the angular frequency as calculated by Equation 1.49. It can be used to calculate the lithium-ion diffusion coefficient using the molar volume (V_M), the geometric area of the electrode (A), Faraday constant (F), and the slope of the galvanostatic charge/discharge curve ($\frac{\delta E}{\delta x}$) as shown in Equation 1.55:

$$D_{Li^+} = 0.5\left[\left(\frac{V_M}{AF\sigma_{WARBURG}}\right)\frac{\delta E}{\delta x}\right] \qquad (1.55)$$

1.5.3.1. Staircase Potentio-Electrochemical Impedance Spectroscopy (SPEIS)

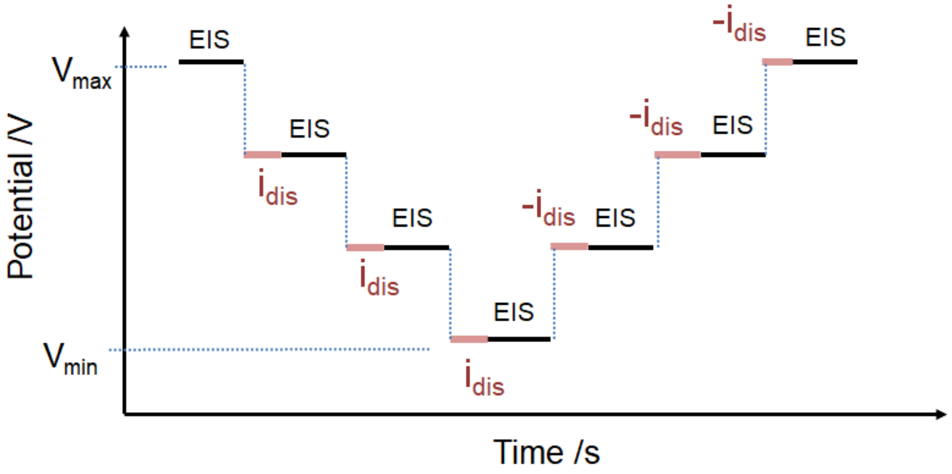

Figure 1-24: Diagram of a plot of potential versus time during a Staircase potentio-electrochemical impedance spectroscopy (SPEIS) measurement. At various set potentials, EIS is performed. After each potential jump from one potential to the next, the current dissipates until the next EIS at the new potential is conducted.

Staircase potentio-electrochemical impedance spectroscopy is a type of EIS experiment: instead of measuring an EIS at OCV or just at one set potential, impedance spectra are collected at various potentials between a maximum (V_{max}) and minimum potential (V_{min}). In between the EIS at each potential, the current i_{dis} resulting from the potential steps was allowed to dissipate below a minimum value I to allow for electrochemical relaxation processes in the cell to complete (see Figure 1-24). This type of EIS allows for the study of trends in impedance at various stages during a charge storage process, which enables for the observation of changes in e.g. charge transfer resistance with level of lithiation/delithiation.

1.6. Synthesis of Transition Metal Oxide Nanoparticles

The synthesis of nanomaterials (at least one dimension < 100 nm) can either start from ions/atoms/molecules via bottom-up synthesis or from bulk materials via top-down synthesis (see Figure 1-25). In top-down methods, a bulk material is broken down stepwise (e.g. via grinding) into smaller constituent parts. In contrast, bottom-up approaches use ions, atoms, or molecules to build up nanoparticles from smaller constituents.

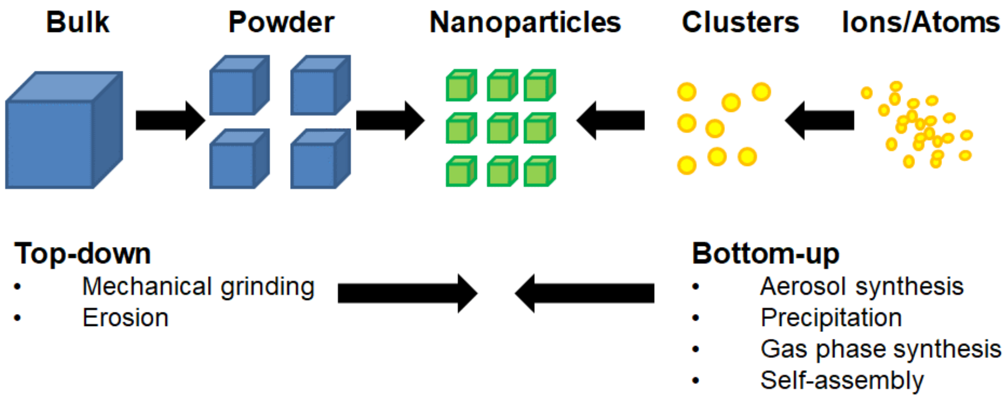

Figure 1-25: Difference between Top-down and Bottom-up synthesis of nanoparticles.

The synthesis of nanoparticles from bottom-up approaches is generally favoured because of greater control of size, morphology and compositions. As for larger particles, nucleation and particle growth are the two essential steps of any synthesis process. Synthesis methods can be divided into gas-phase, liquid-phase and solid-phase methods. Among the liquid-phase methods, solvothermal methods have been extensively studied; they allow for the synthesis of nanoparticles in a solvent at elevated temperatures, with some control over particle size, morphology, and size distributions. Of these, hydrothermal methods use water as the solvent, making them comparatively environmentally friendly synthesis techniques.[181,182]

1.6.1. Hydrothermal Synthesis & Supercritical Water

Hydrothermal synthesis offers some advantages for the preparation of nanoparticles compared to other more conventional synthesis methods. It can facilitate the control of crystal phase, morphology and, to some extent, particle size because the density, dielectric constant and other properties of (supercritical) water can be tuned with pressure and temperature.[183,184]

Hydrothermal synthesis can be used for the synthesis of nanopowders, fibres, coatings, polymers, and metallic nanoparticles.[185,186] Because the solvent is non-toxic and sealed reactors are used for the synthesis, volatilization of reagents/products is not a major concern.[187] High yields and some degree of size control (via surfactants) as well as high purity are further advantages.[185,188,189] Because energy consumption is comparatively low and secondary heat-treatment steps are often not necessary, the energy demand for the synthesis of nanomaterials via batch hydrothermal methods has the potential to be lower than for other synthesis methods such as solid state routes. Although hydrothermal synthesis is generally only defined as a heterogenous reaction in an aqueous solvent under high pressure and temperature,[186] it typically uses sub-critical water temperatures in the range of 100 and 220 °C due to the limits of Teflon liners and in order to reduce possible corrosion of the vessel.[183]

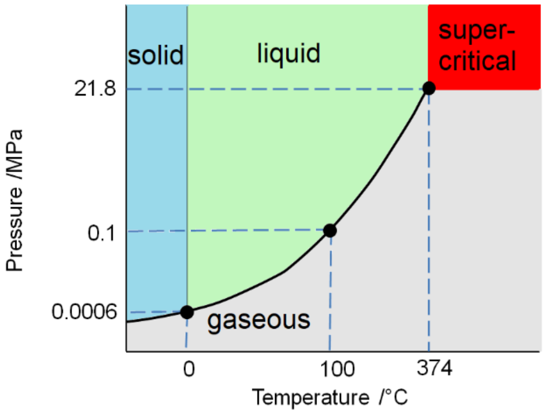

Figure 1-26: Phase diagram of water, highlighting the supercritical state above the critical point of water.

The phase diagram of water is plotted in Figure 1-26. Above its critical point (T_c = 374 °C and P_c = 22.1 MPa),[190] the supercritical state of water offers a significant change in solvent properties such as dielectric constant and solubility.[183] The supercritical state implies that solvent properties can be adjusted between gas-like and liquid-like properties, which offers significant flexibility in conditions.[191] Supercritical water in particular becomes largely non-polar, resulting in the

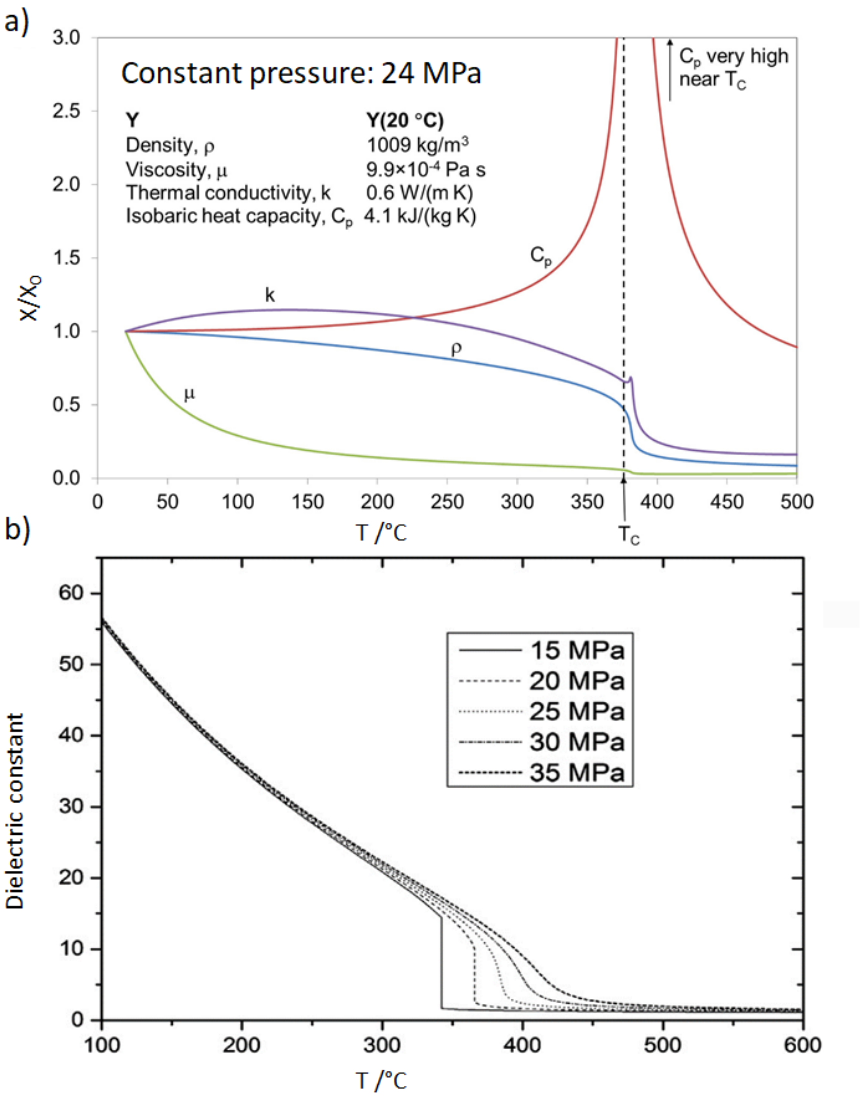

Figure 1-27: a) Dependence of density, viscosity, thermal conductivity, and heat capacity of water on the temperature at a constant pressure of 24 MPa, compared to the value at a temperature of 300 K, showing the massive change in these properties around the supercritical point. Reprinted with permission from [181]. ©2017 American Chemical Society. b) Dependence of the dielectric constant of water on temperature and pressure. Reprinted with permission from [201]. ©2013 Elsevier.

insolubility of aqueous salts.[187] Reaction rate, solubility, and the equilibrium of chemical species are influenced and controlled by the dielectric constant, which is variable at these conditions (see Figure 1-27a).[192] This variability of the dielectric constant at and around the critical point of water has been shown to allow the formation of a large number of nuclei of metal oxide nanoparticles due to supersaturation.[193] As shown in Figure 1-27a, the dielectric constant and density of water decrease (at constant pressure) with temperature. The same is true for the ionic product *Kw* of water. *Kw* can be described in terms of Equation 1.56:

$$\mathrm{K_w} = [\mathrm{H^+}][\mathrm{OH^-}] \quad (1.56)$$

At room temperature, both the concentration of protons and hydroxide ions are 1 x 10^{-7} mol L^{-1}. However, the value of *Kw* varies with temperature. *pKw* can be defined according to Equation 1.57:

$$pK_w = -\,log_{10}\, K_w \quad (1.57)$$

The *pKw* value decreases from 14 at room temperature to 11 under supercritical conditions. Using Eq. 1.56, this means a 30-fold increase in concentration from 1 x 10^{-7} to ca. 3.16 x 10^{-6} mol L^{-1} for both [H^+] and [OH^-], leading to an increasingly hydrolysing environment.[181]

Many batch hydrothermal synthesis methods are time-intensive (taking between several hours and a few days). The nucleation and particle growth mechanisms in hydrothermal synthesis are shown according to a theory developed by LaMer in Figure 1-28.[194] As the concentration builds up, the reaction becomes metastable, and eventually reaches $C_{nucleation}$. The emergence of nuclei does not stop

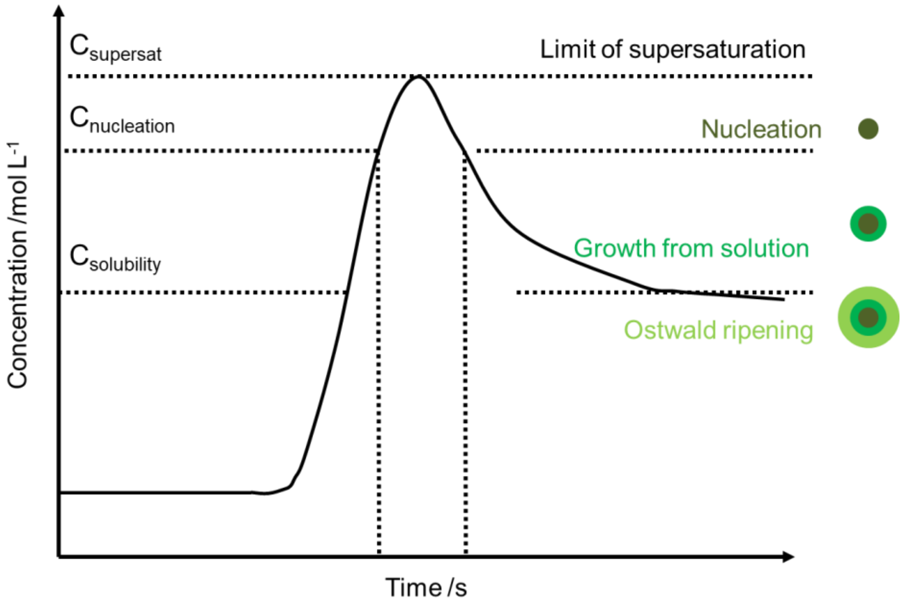

Figure 1-28: Diagram of LaMer's theory of nucleation and particle growth via growth from solution and Ostwald ripening.

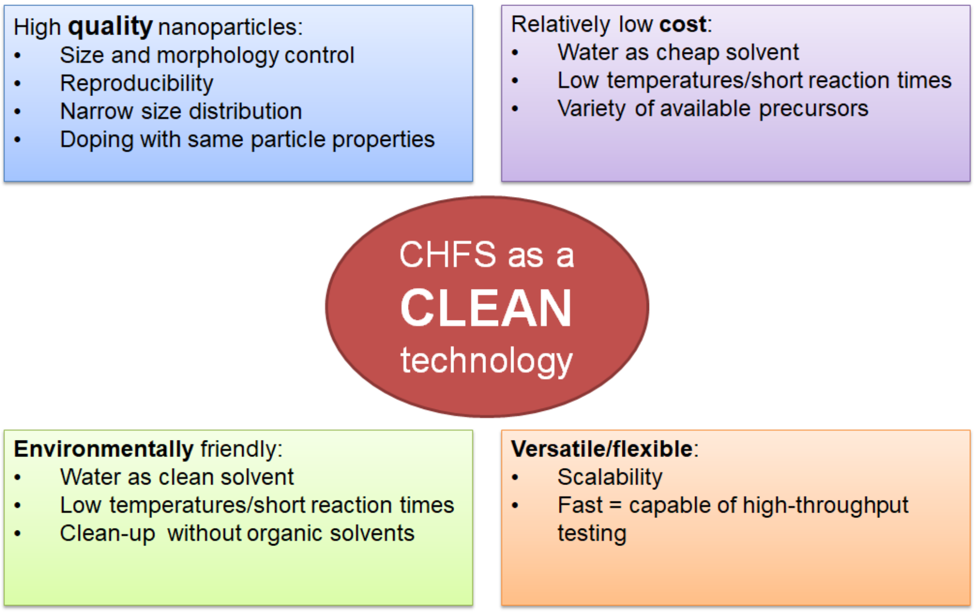

Figure 1-29: Diagram showing the advantages of Continuous Hydrothermal Flow Synthesis (CHFS) as synthesis method for nanoparticles.

the increase in concentration until a limiting supersaturation $C_{supersat}$ is reached, at which point the concentration quickly falls below $C_{nucleation}$, stopping nucleation. Following this, as long as the concentration is above the limit of solubility $C_{solubility}$, growth from solution occurs, whilst below $C_{solubility}$, Ostwald ripening dominates.[195] The longer a reaction, the stronger is the growth from solution and Ostwald ripening, hence the more pronounced particle growth becomes.

Therefore, it seems sensible to assume that a hydrothermal process with short reaction times, such as continuous hydrothermal flow synthesis (CHFS), should enable nucleation driven nanoparticle synthesis and avoid significant particle growth.

1.6.2. Continuous Hydrothermal Flow Synthesis (CHFS)

Scalable, environmentally benign, and reproducible synthesis techniques are necessary for nanoparticles to be economically viable in commercial applications. Continuous hydrothermal flow synthesis (CHFS) uses short reaction times (of a few seconds) and allows for the control of particle parameters such as morphology, size, and size distribution, which can be very narrow.[181,185,196] Materials synthesised via CHFS include metal oxides, metal hydroxides, metal oxyhydroxides, sulphides, and phosphates, as well as doped and composite materials.[181] High yields,[53,54] scalability,[197] comparatively low synthesis temperatures (ca. 450 °C) and water as environmentally benign solvent make CHFS a promising green technology (see Figure 1-29).[198]

Because CHFS is fast and capable of increasing dopant levels without changing other properties of the produced particles, screening for optimised dopant concentrations is a promising application.[199,200]

In a typical CHFS process, water is heated to above its critical point ($T_c = 374$ °C and $P_c = 22.1$ MPa), which reduces its dielectric constant and the solubility of ionic species significantly (see Figure 1-27).[201] The reduced solubility can lead to the precipitation of metal hydroxide nanoparticles, which then undergo quick dehydration according to Equations 1.58 and 1.59 (on the example of a metal nitrite precursor):[181,202]

$$\mathrm{M(NO_3)_{x\,(aq)} + x\,H_2O \rightarrow M(OH)_{x\,(s)} + xHNO_3} \qquad (1.58)$$

$$\mathrm{M(OH)_{x\,(s)} \rightarrow M(O)_{0.5x\,(s)} + 0.5H_2O} \qquad (1.59)$$

However, decomposition of nitrates can also occur, so this reaction mechanism is only a general guide. Particles are typically less than 10 nm and show a narrow size distribution, due to rapid and homogenous nucleation and short reaction times, which limit growth from solution and Ostwald ripening seen in autoclave batch hydrothermal processes according to LaMer's theory (see Figure 1-28).[183] Yields are typically high (> 90 %) and the nanoparticle-laden aqueous slurries are environmentally benign due to water as a solvent.[203–205]

Because of the highly hydrolysing environment provided by supercritical water and the rapid change in density, solubility, and temperature upon mixing, which result in nucleation driven reaction conditions, the design of the mixer is very important. Various designs are possible (see Figure 1-30), including co-current, counter-current, T-shaped, +-shaped and Y-shaped.[206] In this thesis, however, only the co-current, +-shaped mixer used will be described in detail in Section 2.1.

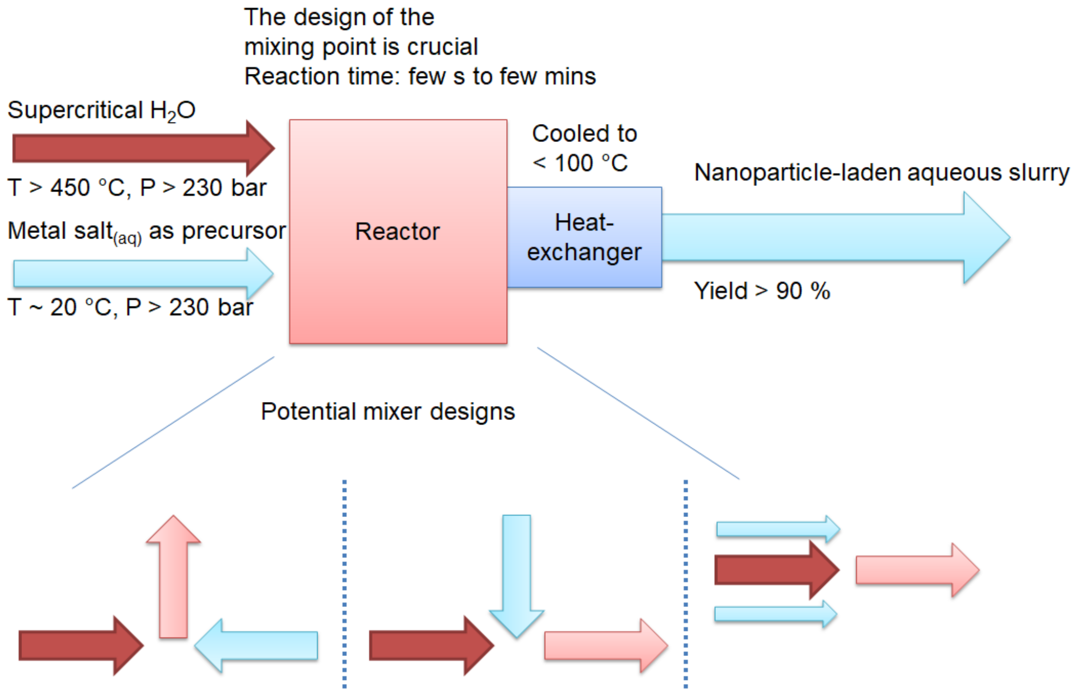

Figure 1-30: Diagram showing a Continuous Hydrothermal Flow Synthesis (CHFS) process and possible flow designs for the mixing point.

1.7. Conclusions

This review of the relevant literature has shown that there is interest in improving the high-power performance of electrochemical energy storage devices such as LIBs and NIBs. By combining electrodes with good capacities at high specific currents used in such devices with high specific surface area carbon electrodes typically used in EDLCs, high-power and high-energy Li/Na-HECs can be created. These devices can be used to bridge the gap between high-power EDLCs and high-energy LIBs/NIBs.

The methods used to synthesise nanomaterials for such Li/Na-HEC devices and the characterisation techniques used to study them will be discussed in Chapter 2.

2. Materials and Methods

As discussed in the review of the relevant literature above, the synthesis and study of nanomaterials to be used in negative electrodes for high-power LIBs/NIBs is of interest. The methods used to synthesise nanomaterials for Li/Na-HEC devices and the characterisation technique used to study them will be discussed in this chapter.

2.1. Materials Synthesis

The continuous hydrothermal flow synthesis (CHFS) process used in this thesis incorporates a patented co-current Confined Jet Mixer (CJM)[207,208] made from “off the shelf” Swagelok^{TM} parts (see Figure 2-1). The CJM allows for efficient mixing of a supercritical water stream with a flow of an ambient temperature aqueous metal salt solution.[207] It has been reported that on the pilot scale, a CHF process is capable of producing more than 1 kg of nanoparticles per hour.[198] A diagram of a typical CHFS reactor with a single mixer, as used in this thesis, can be seen in Figure 2-2.

Nanomaterials produced via CHFS have previously been studied as active materials for LIBs in both cathodes and anodes.[181] Nanoparticles synthesised via

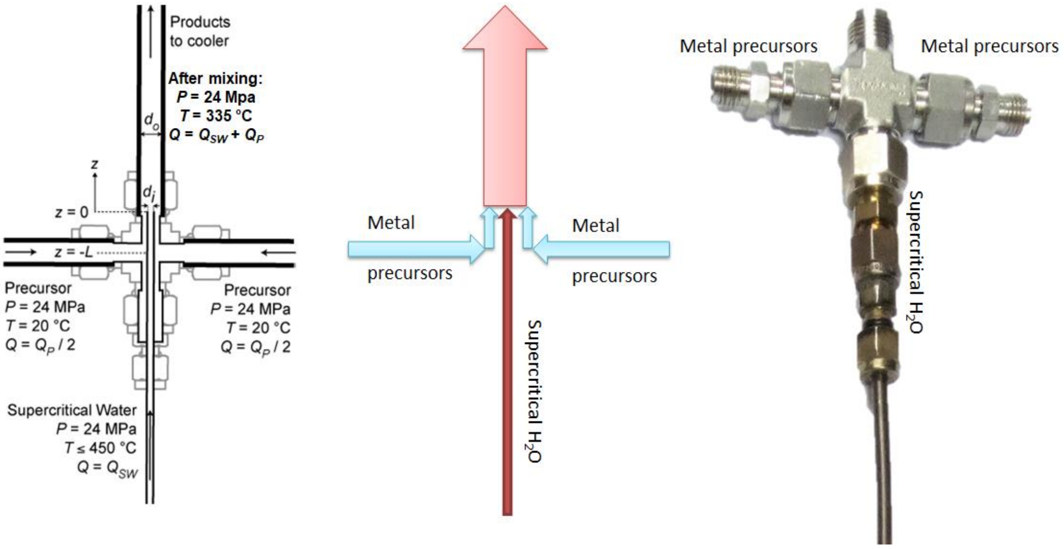

Figure 2-1: Diagram of the patented Confined Jet Mixer (CJM) allowing for co-current mixing of supercritical water and precursor solutions (adapted with permission from [208]. ©2015 Elsevier B.V.), diagram of the flows of aqueous metal precursors and supercritical water, and a photograph of a mixer employed for the work in this thesis.

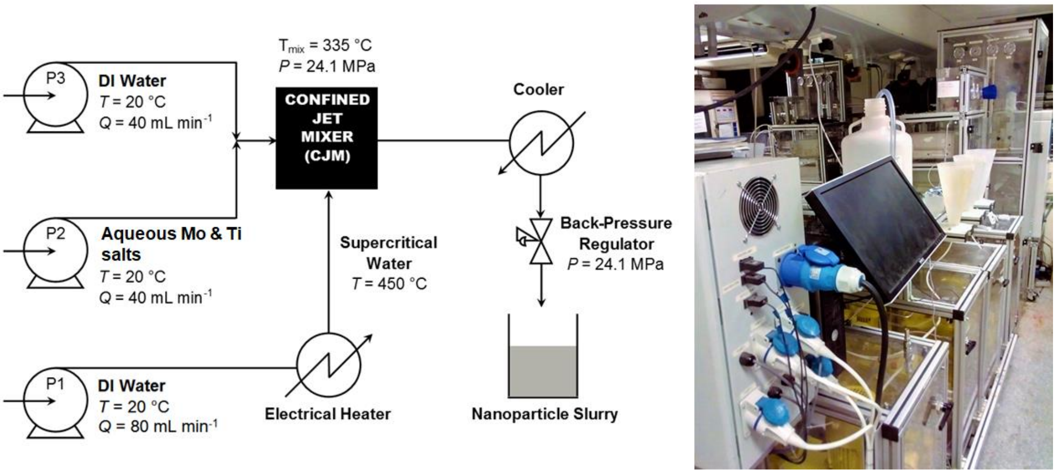

Figure 2-2: a) Diagram of the Continuous Hydrothermal Flow Synthesis (CHFS) reactor used by the author. Adapted with permission from [200]. ©2017 American Chemical Society. b) Photo of the CHFS reactor (lab-scale).

CHFS have, however, not previously been used as active materials in the electrodes of Li-HECs, Na-HECs, or NIBs.

The CHFS reactor used for this thesis used three (standard setup) or four (quench setup) Primeroyal K (Milton Roy, France) diaphragm pumps, which were pressurized to 24.1 MPa. They were used to supply three feeds; Pump 1 supplied deionised water (DI water) at a flow rate of 80 mL min^{-1}. The DI water was heated in flow to above the critical temperature of water (critical temperature T_c = 374 °C) using a custom-made 7 kW electrical water heater. Aqueous metal salt precursors were supplied by Pump 2 at a flow rate of 40 mL min^{-1} and Pump 3 supplied either KOH (aq.) or further DI water, at a flow rate of 40 mL min^{-1}. The feeds from Pumps 2 and 3 were combined in flow in a tee-piece at room temperature, before being mixed with the supercritical water stream inside the CJM. A pipe-in-pipe cooler was used to cool the nanoparticle-laden slurry to ca. 40 °C, before it passed through a back-pressure regulator.[205] The wet nanoparticles were allowed to settle and cleaned via dialysis in DI water.

When a quench was used, Pump 4 supplied a stream of DI water at room temperature. After the first mixer, the nanoparticle slurry entered via the inner tube of another CJM and was mixed with a flow of DI water at room-temperature (see Figure

2-3). This diluted and cooled the nanoparticle slurry to 181 °C, before the slurry was further cooled in the pipe-in-pipe cooler.[205]

2.1.1. Pseudocapacitive Mo, V, or Nb-doped TiO_2

TiO_2, $Mo_{0.1}Ti_{0.9}O_2$, $V_{0.2}Ti_{0.8}O_2$ and $Nb_{0.25}Ti_{0.75}O_2$ nanoparticles were synthesized using a lab-scale continuous hydrothermal flow synthesis (CHFS) reactor as described in Section 2.1.

Table 2-1: Synthesis conditions for the four different samples.

	Pump 2	Pump 3	T_{heater} [°C]	T_{mix} [°C]
TiO_2	0.3 M TiBALD	DI water	400	305
$Mo_{0.1}Ti_{0.9}O_2$	0.45 M TiBALD 0.05 M $(NH_4)_6Mo_7O_{24}\cdot 4H_2O$	0.3 M KOH	450	335
$V_{0.2}Ti_{0.8}O_2$	0.16 M TiBALD 0.04 M NH_4VO_3	0.3 M KOH	450	335
$Nb_{0.25}Ti_{0.75}O_2$	0.4 M TiBALD 0.1 M $C_4H_4NNbO_9$.	0.3 M KOH	450	335

The precursors used were TiBALD [titanium(IV) bis(ammonium lactato)dihydroxide solution, 50 wt.% in H_2O, Sigma Aldrich, Dorset, UK], ammonium heptamolybdate tetrahydrate (99.98 %, Sigma Aldrich, Dorset, UK), ammonium metavanadate (99.8 %, Sigma Aldrich, Dorset, UK), ammonium niobate(V) oxalate hydrate (>99.99 %, Sigma Aldrich, Dorset, UK), and KOH (Fisher Scientific, Loughborough, UK). The syntheses of nano-TiO_2 and $Nb_{0.25}Ti_{0.75}O_2$ have been described previously.[53]

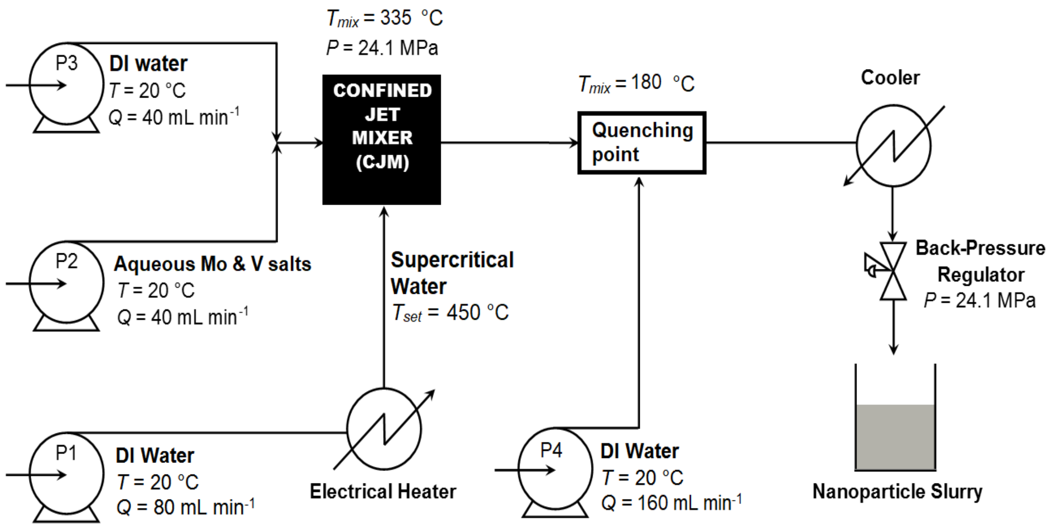

Figure 2-3: Diagram of a continuous hydrothermal flow synthesis (CHFS) reactor with a quench feed. Adapted with permission from [200]. ©2017 American Chemical Society.

The synthesis conditions for the four materials, including precursor concentrations, the temperature of the heater, and calculated mixing temperature were recorded in Table 2-1. The residence time before the pipe-in-pipe cooler was ca. 5 s for all samples.

The wet nanoparticles were cleaned by dialysis in DI water for at least 48 h, before being dried by freeze drying (see Section 2.1.5). All powders were then used without further treatment.

2.1.2. Combinatorial Synthesis of Mo-, V-, and Nb-(co-)doped Anatase TiO_2

A range of titania samples doped with up to 15 at.% of molybdenum, vanadium, and niobium were synthesised using the same reactor and precursors as for the doped titania discussed above (see Section 2.1.1). For all samples, the flow rates were 80, 40, and 40 mL min^{-1} for Pumps 1, 2, and 3, respectively. The supercritical water was heated to 450 °C, the mixing temperature was 335 °C, and the calculated residence time ca. 5 s. The wet nanoparticles were cleaned via dialysis in DI water for 48 hours before being freeze dried. All nanopowders were used without further treatment. Pump 2 supplied 0.2 M KOH solution for all samples except the undoped TiO_2 sample, for which Pump 2 supplied a flow of DI water.

The concentrations of the precursors, along with the nominal concentrations of the titania samples, are given in Table 2-2. The concentrations of the precursors are given in mM. The precursors were abbreviated using the metals' chemical symbols. The preparation of precursors and the synthesis were achieved in a single day. In total, the reaction time for all 35 samples was ca. 6 hours. The samples were dialysed in DI water for at least 48 hours and then freeze-dried.

Table 2-2: Concentrations of precursors for the range of different molybdenum, niobium, and vanadium (co-)doped TiO_2 (anatase) samples in mM.

TiO_2 200 Ti	**$Mo_{0.04}Ti_{0.96}O_2$** 192.5 Ti, 7.5 Mo	**$Nb_{0.04}Mo_{0.11}Ti_{0.85}O_2$** 170 Ti, 7.5 Nb, 22.5 Mo	**$Nb_{0.11}V_{0.04}Ti_{0.85}O_2$** 170 Mo, 22.5 Nb, 7.5 V
$Nb_{0.04}Ti_{0.96}O_2$ 192.5 Ti, 7.5 Nb	**$Nb_{0.15}Ti_{0.85}O_2$** 170 Ti, 30 Nb	**$Mo_{0.04}V_{0.04}Nb_{0.04}Ti_{0.89}O_2$** 177.5 Ti, 7.5 Nb, 7.5 V, 7.5 Mo	**$Nb_{0.08}V_{0.04}Mo_{0.04}Ti_{0.85}O_2$** 170 Ti, 7.5 Mo, 7.5 V, 15 Nb
$Nb_{0.08}Ti_{0.92}O_2$ 185 Ti, 15 Nb	**$Nb_{0.08}V_{0.04}Ti_{0.89}O_2$** 185 Ti, 15 Nb, 7.5 V	**$Nb_{0.04}Vo_{0.08}Ti_{0.89}O_2$** 177.5 Ti, 7.5 Nb, 15 V	**$Nb_{0.04}V_{0.11}Ti_{0.85}O_2$** 185 Ti, 7.5 Nb, 22.5 V
$Nb_{0.11}Ti_{0.89}O_2$ 177.5 Ti, 22.5 Nb	**$Nb_{0.04}V_{0.04}Ti_{0.92}O_2$** 185 Ti, 7.5 Nb, 7.5 V	**$Nb_{0.11}Mo_{0.04}Ti_{0.85}O_2$** 170 Ti, 22.5 Nb, 7.5 Mo	**$Mo_{0.08}V_{0.08}Ti_{0.85}O_2$** 170 Ti, 15 Mo, 15 V
$V_{0.04}Ti_{0.96}O_2$ 192.5 Ti, 7.5 V	**$Mo_{0.04}V_{0.04}Ti_{0.92}O_2$** 185 Ti, 7.5 Mo, 7.5 V	**$Mo_{0.04}Vo_{0.08}Ti_{0.89}O_2$** 177.5 Ti, 7.5 Mo, 15 V	**$Nb_{0.08}Mo_{0.08}Ti_{0.85}O_2$** 185 Ti, 15 Nb, 15 Mo
$V_{0.08}Ti_{0.92}O_2$ 185 Ti, 15 V	**$V_{0.15}Ti_{0.85}O_2$** 170 Ti, 30 V	**$Mo_{0.04}V_{0.11}Ti_{0.85}O_2$** 170 Ti, 7.5 Mo, 22.5 V	**$Nb_{0.04}Mo_{0.04}Ti_{0.92}O_2$** 185 Ti, 7.5 Nb, 7.5 Mo
$Mo_{0.15}Ti_{0.85}O_2$ 170 Ti, 30 Mo	**$Nb_{0.08}V_{0.08}Ti_{0.85}O_2$** 185 Ti, 15 Nb, 15 V	**$Mo_{0.08}V_{0.04}Ti_{0.89}O_2$** 177.5 Ti, 15 Mo, 7.5 V	**$Nb_{0.04}Mo_{0.08}Ti_{0.89}O_2$** 177.5 Ti, 15 Mo, 7.5 Nb
$Mo_{0.11}Ti_{0.89}O_2$ 177.5 Ti, 22.5 Mo	**$V_{0.11}Ti_{0.89}O_2$** 177.5 Ti, 22.5 V	**$Mo_{0.08}V_{0.04}Nb_{0.04}Ti_{0.89}O_2$** 170 Ti, 7.5 Nb, 7.5 V, 15 Mo	**$Mo_{0.04}V_{0.08}Nb_{0.04}Ti_{0.89}O_2$** 170 Ti, 7.5 Nb, 15 V, 7.5 Mo
$Mo_{0.08}Ti_{0.92}O_2$ 185 Ti, 15 Mo	**$Mo_{0.12}V_{0.04}Ti_{0.85}O_2$** 170 Ti, 22.5 Mo, 7.5 V	**$Nb_{0.08}Mo_{0.04}Ti_{0.89}O_2$** 185 Ti, 15 Nb, 7.5 Mo	

2.1.3. TiO_2 Co-precipitated with Conversion Materials

2.1.3.1. TiO_2/MoO_2

MoO_2 nanoparticles and various TiO_2/MoO_2 nanocomposites were synthesised using the lab-scale CHFS reactor with a single mixer, as described in Section 2.1. The precursors used were TiBALD (50 wt.% in H_2O, Sigma Aldrich, Dorset, UK), ammonium heptamolybdate tetrahydrate (99.98 %, Sigma Aldrich, Dorset, UK), and oxalic acid ($C_6H_8O_6$, Sigma Aldrich, Dorset, UK). The synthesis conditions for all materials, including precursor concentrations, heater temperature, and calculated mixing temperature are shown in Table 2-3. The samples were denoted MoO_2, TiO_2/MoO_2-1, TiO_2/MoO_2-2, TiO_2/MoO_2-3, TiO_2/MoO_2-4, and TiO_2/MoO_2-5 for nominal ratios of MoO_2 to TiO_2 of 100:0, 95:5, 90:10, 80:20, 67:33, and 50:50. Because the oxidation state of molybdenum in the precursor was VI, it was pre-mixed with $C_6H_8O_6$ under vigorous stirring for 20 minutes, which resulted in the solution changing colour from yellow to blue as Mo(VI) was reduced to Mo(IV).

Table 2-3: Synthesis conditions for the MoO_2 and TiO_2/MoO_2 composite samples.

	Mo^{4+} [M]	Ti^{4+} [M]	T_{heater} [°C]	T_{mix} [°C]
MoO_2	0.300	0.000	450	335
TiO_2/MoO_2-1	0.190	0.010	450	335
TiO_2/MoO_2-2	0.180	0.020	450	335
TiO_2/MoO_2-3	0.160	0.040	450	335
TiO_2/MoO_2-4	0.133	0.067	450	335
TiO_2/MoO_2-5	0.100	0.100	450	335

The nanoparticles were recovered by the addition of NaCl and the wet nanoparticles were cleaned by dialysis in DI water for at least 48 h, before being dried by freeze-drying. All powders were then used without further treatment.

2.1.3.2. $NiCo_2O_4$, $Ni_{1.5}Co_{1.5}O_4$, Co_2TiO_4, and $TiO_2/NiCo_2O_4$

$NiCo_2O_4$, $Ni_{1.5}Co_{1.5}O_4$, and Co_2TiO_4 nanoparticles and a range of $TiO_2/NiCo_2O_4$ nanocomposites were synthesised using the lab-scale CHFS reactor with a single mixer described in Section 2.1. The precursors used were TiBALD (50 wt.% in H_2O, Sigma Aldrich, Dorset, UK]), Co(II) nitrate [$Co(NO_3)_2 \cdot 6H_2O$, > 99 %, Sigma Aldrich, Dorset, UK), Ni(II) nitrate [$Ni(NO_3)_2 \cdot 6H_2O$, > 99 %, Sigma Aldrich, Dorset, UK), and KOH (Fisher Scientific, Loughborough, UK). The precursor concentrations are shown in Table 2-4. The calculated rate of synthesis was ca. 110 g h^{-1} for the $TiO_2/NiCo_2O_4$ composites and Co_2TiO_4. The heater was set to heat the supercritical water to 450 °C, which resulted in a mixing temperature of 335 °C.

Table 2-4: Synthesis conditions for the cobalt/nickel/titanium samples.

	Co [M]	Ni [M]	Ti [M]	KOH [M]
Co_2TiO_4	0.4	-	0.2	0.3
$NiCo_2O_4$	0.2	0.1	-	-
$Ni_{1.5}Co_{1.5}O_4$	0.15	0.15	-	-
$NiCo_2O_4/TiO_2$-1	0.19	0.095	0.015	-
$NiCo_2O_4/TiO_2$-2	0.18	0.09	0.03	-
$NiCo_2O_4/TiO_2$-3	0.16	0.08	0.06	-
$NiCo_2O_4/TiO_2$-4	0.133	0.067	0.1	-

The calculated residence time was ca. 5 s for all samples. The nanoparticles were recovered from solution by addition of NaCl and the wet nanoparticles were cleaned by dialysis in DI water for at least 48 h, before being dried by freeze drying. All powders were then used without further treatment.

2.1.4. Mixed Molybdenum/Vanadium Oxides

VO_2, MoO_2, and mixed molybdenum/vanadium oxide nanoparticles were synthesised using the lab-scale CHFS reactor with a quench setup (a normal single mixer & a second mixer) described in Section 2.1 (see Figure 2-3). This was to retard growth from solution, hence synthesising smaller particles by using a quench. The supercritical water supplied by Pump 1 was heated to 450 °C for all syntheses. The precursors used were ammonium heptamolybdate tetrahydrate (99.98 %, Sigma Aldrich, Dorset, UK), ammonium metavanadate (99.8 %, Sigma Aldrich, Dorset, UK), and oxalic acid ($C_6H_8O_6$, Sigma Aldrich, Dorset, UK). The calculated residence time before the quench was less than one second. The synthesis conditions for the samples can be found in Table 2-5, including the concentration of precursors and mixing temperatures after the first mixing and after the quench. Because of the oxidation states of the metals in the metal salts, the initially yellow metal precursor solutions were stirred vigorously overnight with oxalic acid. This resulted in the reduction of molybdenum and vanadium to their respective (IV) oxidation states, indicated by the solution turning blue. The freeze-dried powders were collected as free flowing powders and were analysed without any further treatment.

Table 2-5: Synthesis conditions for the mixed molybdenum/vanadium oxide samples.

	T_{mix} [°C]	T_{quench} [°C]	Pump 2	Pump 3
MoO_2	335	181	0.1 M Mo, 0.1 M $C_6H_8O_6$	DI water
$Mo_{0.67}V_{0.33}O_2$	335	181	0.067 M Mo, 0.033 M V, 0.1 M $C_6H_8O_6$	DI water
$Mo_{0.5}V_{0.5}O_2$	335	181	0.05 M Mo, 0.05 M V, 0.1 M $C_6H_8O_6$	DI water
$Mo_{0.33}V_{0.67}O_2$	335	181	0.033 M Mo, 0.067 M V, 0.1 M $C_6H_8O_6$	DI water
$Mo_{0.1}V_{0.9}O_2$	335	181	0.01 M Mo, 0.09 M V, 0.1 M $C_6H_8O_6$	DI water
$Mo_{0.05}V_{0.95}O_2$	335	181	0.005 M Mo, 0.095 M V, 0.1 M $C_6H_8O_6$	DI water
VO_2	335	181	0.1 M V, 0.1 M $C_6H_8O_6$	DI water

2.1.5. Freeze-drying

To retain the maximum specific surface area, water was removed via freeze-drying. Freeze-drying is a method which is used in food processing, for pharmaceutical products and nanoparticle drying.[209] As can be seen from the phase diagram of water in Figure 1-26, at very low pressures, frozen water sublimes into vapour at low temperatures. For nanoparticles, this allows for the removal of water without reducing the specific surface area.[210,211] This requires the freezing of the wet nanoparticles to < −40 °C, the application of a vacuum of 13.3 Pa and then the heating back to room temperature over the course of 22 hours.

All particles were freeze-dried using a Virtis Genesis 35XL freeze-drier by cooling samples to 213 K and slow heating back to room-temperature under a vacuum of 13.3 Pa.

2.2. Physical Characterisation

2.2.1. Powder X-ray Diffraction (XRD)

(Powder) X-ray diffraction (PXRD) is a non-destructive technique used for phase identification of crystalline & semi-crystalline materials, crystallite size estimations, and to determine crystal lattice parameters. PXRD uses the order of (partly) crystalline materials, which leads to preferential diffraction of incident radiation at certain angles. The relationship between the angle of the radiation θ and the distance between lattice planes *d* was first described by Bragg et al. in 1913.[212] This relationship (see Figure 2-4) is described by Equation 2.1:

$$2d \times sin(\theta) = n \times \lambda \tag{2.1}$$

n is the number of lattice planes and λ the constant wavelength of the incident radiation. Reflection only occurs when this condition is met.

The Scherrer equation (2.2) can be used to estimate a crystallite domain size of particles:[213]

$$d = \frac{K \times \lambda}{\beta \times cos\theta} \tag{2.2}$$

d is the crystallite domain size in nm, λ is the radiation source’s wavelength (here Mo, 0.7107 Å), β the full width at half-maximum (FWHM) of the peak and θ the Bragg angle. The shape factor k can range from 0.86 to 0.98, and if unknown, was approximated to 0.9.[214]

Visualization for Electronic and Structural Analysis (VESTA) Version 3.4.4 (© Koichi Momma and Fujio Izumi) was used to create structural models of the various materials as well as doped materials.

PXRD of all powders was performed to collect diffraction patterns in various 2θ ranges, typically with a step size of 0.5° and a step time of 20 s on a STOE StadiP diffractometer (Darmstadt, Germany) using Mo-Kα radiation (λ = 0.7107 Å).

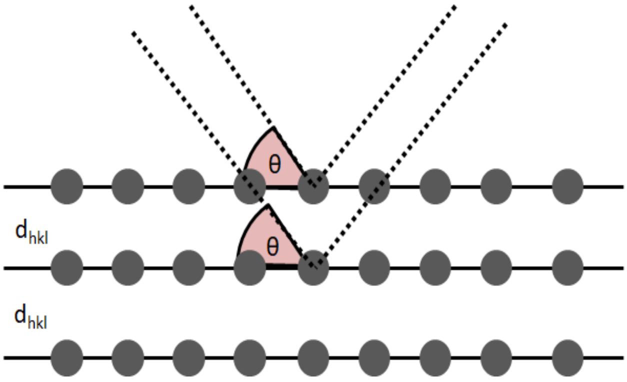

Figure 2-4: Diagram showing the interaction of the incident X-ray beams and a crystalline material with special attention to the Bragg angle θ.

X-ray diffraction of electrochemically lithiated and delithiated electrodes was carried out using a Rigaku MiniFlex 600 diffractometer (Tokyo, Japan) in various 2θ ranges, with a rotational velocity of 10° min^{-1} using Cu-Kα radiation (λ = 1.5406 Å). Phase identification was carried out using Match! Software (CRYSTAL IMPACT, Bonn, Germany) with a PDF-2 database by the International Centre for Diffraction Data (ICDD). Peak fitting of patterns was carried out using Fityk (Version 0.9.8).

2.2.2. X-ray Photoelectron Spectroscopy (XPS)

X-ray photoelectron spectroscopy (XPS) is a quantitative technique used to measure the elemental composition of chemical species on the surface of materials. Chemical state, electronic state, and elemental compositions can be determined. Because XPS relies on an X-ray beam to penetrate the material to excite electrons and quantify excited electrons emitted by the material, the technique only captures signals to a maximum distance of about 1 to 10 nm from the surface of the sample (see Figure 2-5). The limited sampling depth does not stem from a limitation to the penetration of the sample by the incident X-ray, but rather from the much lower probability of photoelectron escape below the surface.[215] The binding energy ($E_{binding}$) of the collected electrons can be calculated using the energy of the incident X-ray used for excitation (E_{photon}, typically 1486.6 eV for Al-Kα), the measured kinetic energy of the electron ($E_{kinetic}$), and the work function Φ in Equation 2.3. The work function is the minimum energy required to release an electron from a solid into a vacuum immediately above the solid's surface.[216]

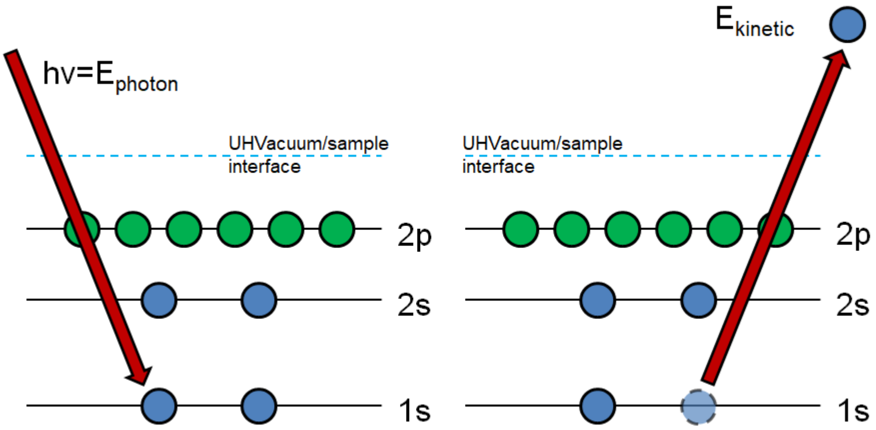

Figure 2-5: Diagram showing the expulsion process of electrons from the inner shells of a sample analysed via X-ray photoelectron spectroscopy.

$$E_{binding} = E_{photon} - E_{kinetic} - \Phi \tag{2.3}$$

Since the binding energy of core electrons is influenced by the oxidation state of an ion, slight shifts in binding energy of core electrons due to changes to outer shells can be used to determine oxidation states.

The valence states of metal ions were determined using XPS collected using a Thermo Scientific K-alpha™ spectrometer, which used Al-Kα radiation. High-resolution regional scans for the different metal ions, including molybdenum, titanium, vanadium, niobium, nickel, and cobalt, were conducted at 50 eV. Processing of the XPS data was performed using CasaXPS™ software (version 2.3.19). All spectra were calibrated to the C 1s peak for the carbon tape at 284.8 eV.

For electrochemically lithiated and delithiated electrodes, XPS was carried out using an Axis-Ultra DLD (Kratos Analytical Ltd, Manchester, UK) using Al-Kα radiation.

2.2.3. X-ray Absorption Spectroscopy (XAS)

When X-ray radiation interacts with a sample, X-ray absorption and scattering are possible outcomes. The quantity of X-rays absorbed at specific wavelengths can illuminate the electronic structure of the atoms in the sample. The difference between the transmitted and incident radiations, I and I_0, respectively, is related to the linear absorption coefficient μ and the thickness of the sample d (see Equation 2.4):

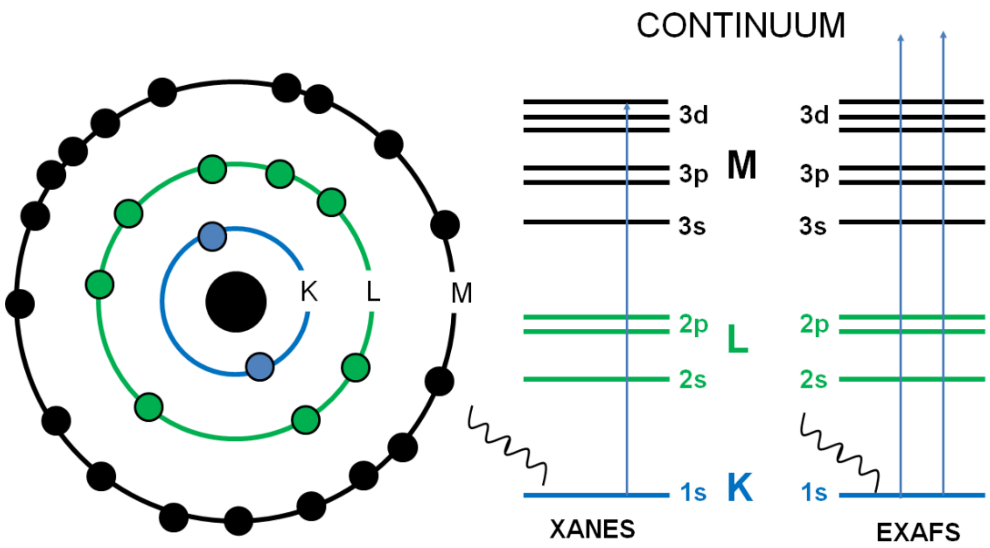

Figure 2-6: Bohr’s atomic model, showing the electron levels K, L, and M. Core electrons in X-ray absorption are referred to by the electronic levels.

$$\mu \times \mathrm{d} = \ln\left(\frac{I_0}{I}\right) \tag{2.4}$$

Atoms absorb a large amount of incident radiation at certain photon energies. Because the absorbed radiation increases rapidly, these photon energy levels are referred to as absorption edges. The absorption edge occurs at the energy level at which an atom absorbs sufficient energy to expel an electron from one of its ground states (K, L, M; see Figure 2-6a) into the continuum. The plot of an absorption edge is not a step, but rather an incline, because electrons can rest in many p-states and relax back to their previous states (see Figure 2-6b). For the purposes of this thesis, only K-edge XAS of vanadium, molybdenum, and titanium was considered.

X-ray absorption spectra typically consist of one or more features constituting the edge; pre-edge features (see Figure 2-7, Number 1) and a steep incline (see Figure 2-7, Number 2). Pre-edge features are the result of photons with energies lower than the edge energy exciting electrons into unoccupied states (such as 3d in transition metal oxides).

The energy of the entire absorption spectrum can shift depending on the oxidation state of the atom being studied, although charge environment and coordination number play an important role as well, so that the relationship between the shift and oxidation states is non-linear.[217] As the oxidation state increases, the

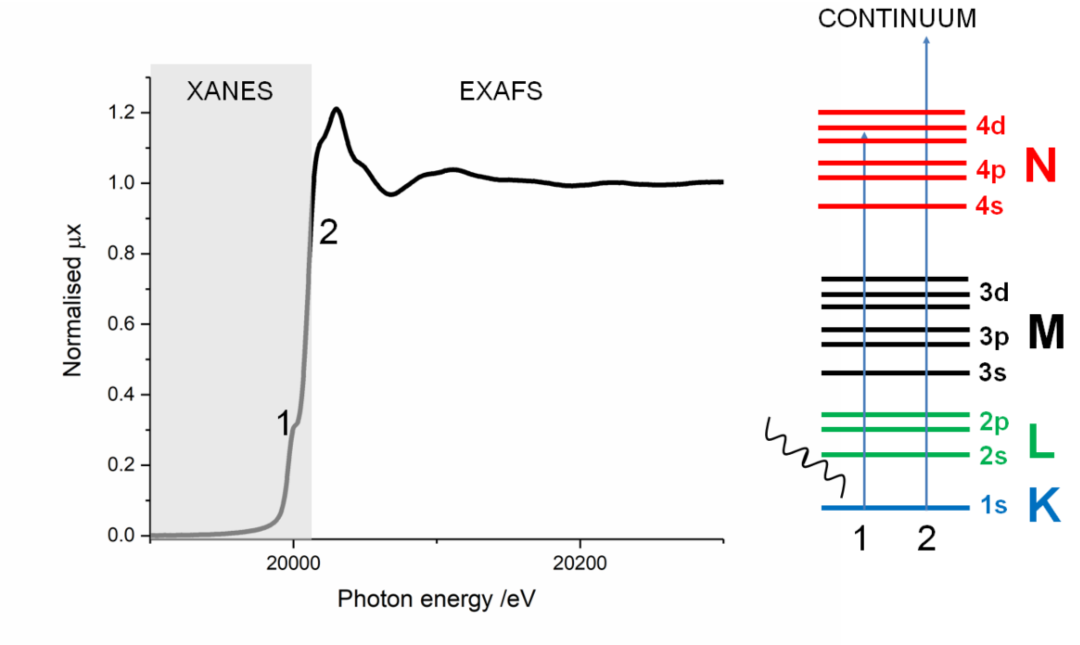

Figure 2-7: Molybdenum K-edge X-ray absorption spectrum for molybdenum-doped TiO_2. The rise and bump denoted 1 is the pre-edge feature, whereas 2 denotes the edge. The band diagram shows the physical transition from pre-edge to near-edge X-ray absorption spectrum.

nucleus is shielded less due to fewer electrons in the outer shells, hence more energy is required to remove inner electrons. Features 1 and 2 give electronic information and are referred to as X-ray absorption near-edge structure (XANES) measurements.

Local structural information for atoms can be obtained from the spectra at higher energies than the absorption edge, referred to as extended X-ray absorption fine structure (EXAFS). EXAFS are a result of the interaction of electrodes expelled into the continuum and neighbouring atoms.

Mo, Ti, and V K-edge XAS was carried out on beamline B18 (Rutherford Appleton Lab, Harwell, UK) at Diamond Light Source. A Si (111) monochromator was used for XAS in the energy ranges 19800 to 21000, 4900 to 5200, and 5265 to 6300 eV for Mo, Ti, and V K-edges, respectively. Pellets with a diameter of 13 mm were prepared to be used for XAS measurements. The total mass of the pellets was 150 mg. The required mass of samples depended on the atomic concentration of the studied elements in the samples and varied between 1 and 80 mg. The pellets were diluted with cellulose and pressed. Data was collected in transmission mode and interpreted with Athena software.

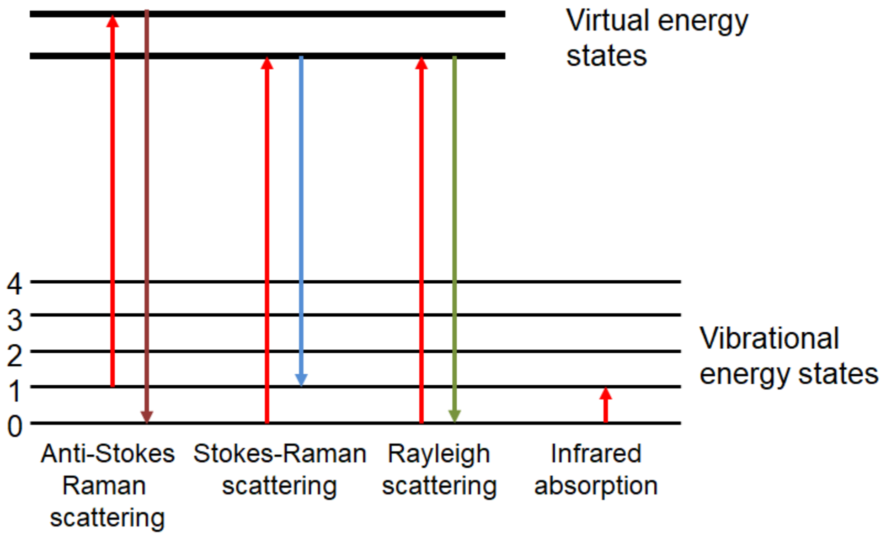

Figure 2-8: Diagram showing the different energy states involved in Raman spectroscopy.

2.2.4. Raman Spectroscopy

Non-destructive Raman spectroscopy allows for the differentiation of materials. A monochromatic light source is used to identify the characteristic scattering of light by a crystal lattice. The inelastic Raman-effect measured by the technique is a result of the collision between a vibrational crystal lattice and a photon in the monochromatic ray of light. Because the energy difference between the Raman-scattered photon and the photon emitted by the monochromatic source is equal to the difference between the energy levels of a molecular vibration, the shift in energy is characteristic for a material (see Figure 2-8). If the energy of the photon and the energy of the scattered wavelength are the same, the collision between photon and crystal lattice can be considered elastic (Rayleigh scattering).[114]

Raman spectroscopy used a HORIBA-JY T64000 (Horiba UK Ltd., Northampton, UK) with 1800 gr mm^{-1} grating. The excitation source was an Ar^{+} laser. The wavelength was 514.5 nm and the power 5 mW.

2.2.5. Transmission Electron Microscopy (TEM)

In transmission electron microscopy (TEM), the light source of an optical microscope is replaced with an electron beam. Because the resolution of an optical microscope is limited to ca. 0.5 µm by the wavelength of visible light, the analysis of smaller particles requires a radiation with a smaller wavelength. At one end of the TEM, an electron source emits electrons, which move through an ultra-high vacuum column towards the sample. Multiple electromagnetic lenses focus the electron beam. Samples must be prepared at a low concentration on a highly conductive substrate (often carbon-coated copper or gold grids). After the focused electron beam interacts with the sample, the electrons of the electron beam which are transmitted through the sample then interact with a detector to form an image. The image is then focused on a fluorescent screen or other such device.

High-resolution transmission electron microscopy (TEM) was performed using a Jeol JEM 2100 (JEOL UK Ltd., Welwyn Garden City, UK) with a LaB_6 filament to determine particle size, interlayer spacings, as well as particle morphology for all samples. A Gatan Orius digital camera was used for image capture of the samples that were pipetted on 300-mesh holey carbon-coated copper film grids (Agar Scientific, Stansted, UK).

2.2.6. Energy Dispersive X-ray Spectroscopy (EDX)

Energy dispersive X-ray spectroscopy (EDX) is an analytical technique used for elemental analysis. It heavily relies on the unique atomic structures of elements and the excitation of electrons via a high-energy beam of particles. Each atom will have electrons in discrete energy states around its nucleus. The incident high-energy radiation beam can excite a ground state electron, resulting in it being ejected from the K- or L-shell. To return to the lowest energy state, an electron from a higher energy shell will then fill the created electron hole (see Figure 2-9). The energy difference between the electron in the higher-energy shell and that in the lower-energy shell can then be released as X-rays.

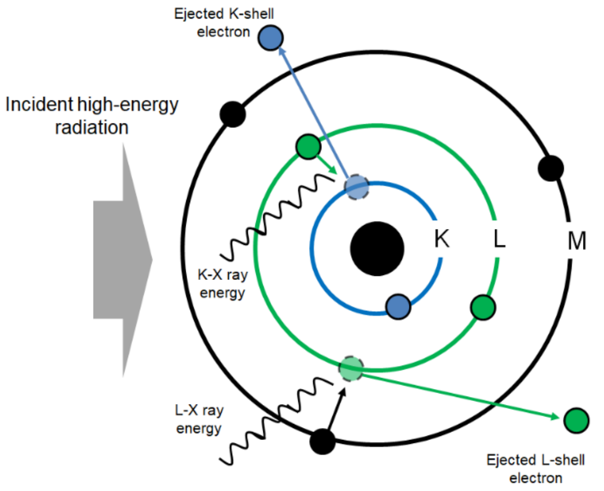

Figure 2-9: Diagram showing the ejection of electrons from inner shells by high-energy radiation and the energy emitted from electrons from outer shells dropping to lower shells, which is measured for Energy Dispersive X-ray spectroscopy (EDX).

The amount and energy of X-rays collected with an energy-dispersive spectrometer can be used to calculate the elemental composition of a sample.

Energy dispersive X-ray spectroscopy (EDX) was performed using the Jeol JEM 2100 for elemental analysis of the samples that was also used for TEM.

2.2.7. Scanning Electron Microscopy (SEM)

Scanning electron microscopy (SEM) is a microscopy technique used to measure the topography of particles or compounds. An electron source emits a beam of primary electrons, which is focused on a sample whilst travelling through a column under ultra-high vacuum containing a number of electromagnetic lenses. The electron beam interacts with the surface of the sample, where secondary electrons are generated from the collision of primary electrons and weakly bonded electrons in the outer shells of atoms on or near the surface of the sample. The generated secondary electrons are measured by using a secondary electron detector. The yield and angle of secondary electrons depends on the smoothness of the sample’s surface, with more secondary electrons being emitted on rough surfaces. Beyond secondary electron generation, the interaction of the primary electron beam with the sample also produces backscattered electrons and X-rays. These can also be detected and used to form digital images.

To study the surfaces of electrodes before and after cycling, field emission scanning electron microscopy (FE-SEM) images were recorded with a JEOL JSM-6700F microscope using an accelerating voltage of 5 kV.

2.2.8. BET Specific Surface Area Measurements

Brunauer-Emmett-Teller (BET) is a method to determine the specific surface area (SSA) or pore volume of a material via gas adsorption/desorption. In BET, adsorption isotherms are measured using the amount of gas (typically N_2) adsorbed at a range of pressures at constant temperature (usually 77K, using liquid nitrogen). It requires that gas molecules adsorb on a solid in layers, that the separate layers of adsorbent do not interact, and that each layer can be treated discretely.[218]

The BET equation is usually arranged as in Equation 2.5:[219]

$$\frac{P}{n_{ad}(P_S-P)} = \frac{1}{n_m C} + \frac{C-1}{n_m C}\frac{P}{P_s} \qquad (2.5)$$

n_{ad} is the amount of absorbed N_2 at a relative pressure P/P_S, whereas n_m is the monolayer capacity of the material, and C is a constant which depends on the adsorption enthalpy of the first layer of gas adsorbed, which can be calculated by measuring the amount of adsorbed gas at different relative pressures.[219]

The slope and intercept of the absorbed gas at different relative pressures give C and n_m, respectively. It is known that one molecule of N_2 with a cross sectional area of 0.162 nm^2 can be adsorbed per 0.162 nm^2 of surface area, hence the specific surface area can be calculated using Equation 2.6:

$$S_{BET} = \frac{v_m N s}{V m} \qquad (2.6)$$

S_{BET} is the specific surface area of the sample, v_m is the volume of the adsorbed gas, N is Avogadro's number, s the adsorption cross section of the adsorbing material, V the molar volume of the adsorbed gas, and m the mass of the material.

Brunauer-Emmett-Teller (BET) surface area measurements were carried out using nitrogen gas adsorption/desorption using a Micromeritics Tristar II (Micromeritics Co., Georgia, USA). The samples were degassed at 150 °C overnight using N_2.

2.2.9. Tap Density

The tap density, which is an important factor in achieving a high (volumetric) energy & power density,[220] was determined by measuring 2 g of the powder into a graduated cylinder. The cylinder was then tapped vertically on a bench 300 times by hand.

The tap density ρ_{TAP} (in g cm^{-3}) was then calculated using the volume after tapping V_{TAP} and the material mass m in Equation 2.7:

$$\rho_{TAP} = \frac{m}{V_{TAP}} \qquad (2.7)$$

2.3. Electrochemical Characterisation

Electrochemical characterisation was carried out using electrodes made from a mixture of active material, conductive agent, and binder, which were cast onto a current collector (see Figure 2-11). Copper foil (9 µm, PI-KEM, Staffordshire, UK) was used as the current collector for negative electrode materials used in LIBs and Li-HECs. This is because cheaper, lighter aluminium foil alloys with lithium below 0.6 V vs. Li/Li^+ and could, therefore, not be used for LIBs. Because aluminium does not alloy with sodium, however, aluminium foil was used as current collector for both NIB and Na-HEC negative electrodes.[32,140]

Testing was carried out in both half-cells and full-cells. For half cells, Li or Na metal acted as both reference and counter electrode (see Figure 2-10a). Because the redox potential of any active material to be assessed will be higher than that of Li or Na, respectively, the working electrode will always act as positive electrode. Therefore, even if the material is intended as a negative electrode in a full cell, it will be lithiated/sodiated upon discharge and delithiated/desodiated on charging.

As discussed in Section 1.2, when the setup for an electrochemical measurement causes large ohmic drops due to large currents or high resistivity, three-electrode setups with a reliable, nonpolarizable, and reproducible reference electrode and a counter electrode are preferable. Whilst three-electrode setups for LIB testing have been proposed using a micro-reference electrode of lithium and lithium counter electrodes, the potential of the reference has been shown to be influenced by passivation and aging.[221] Reference electrodes using $Li_4Ti_5O_{12}$ and $LiFePO_4$ have been proposed due to their relatively stable potential over time.[221,222] In this thesis, two-electrode setups were used for all LIB and NIB testing, where Li or Na metal acted as pseudo-reference. Although this is the convention for the testing of negative or positive electrodes in LIBs/NIBs, it must be considered when interpreting the results.

Full-cells were used to assess the performance of Li-HECs/Na-HECs. Activated carbon electrodes were employed as positive electrodes, whereas various active materials were used in the pseudocapacitive negative electrodes (see Figure 2-10b).

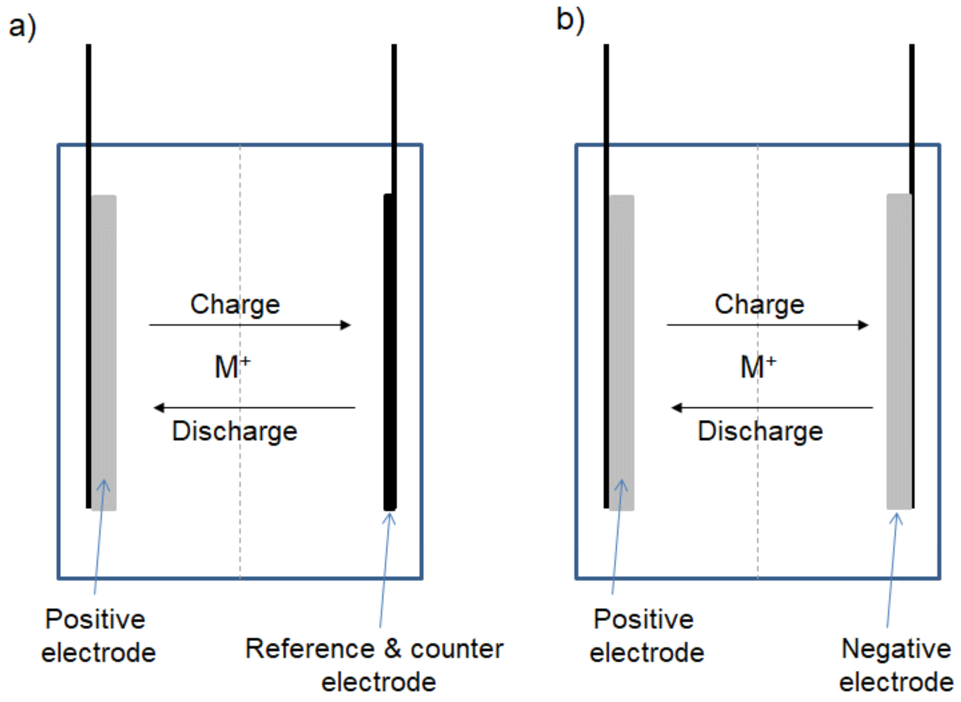

Figure 2-10: Diagrams showing a) an electrochemical half-cell and b) a full-cell.

2.3.1. Electrode Preparation

For the working electrodes (WE), an ink was prepared by mixing of the active material, a conductive agent (carbon black, Super P, Alfa Aesar, Heysham, UK), and a binder (Polyvinylidene fluoride [PVDF], PI-KEM, Staffordshire, UK). The weight ratio of active material to conductive agent to binder was 80:10:10 wt.% for all samples. A 10 wt.% solution of PVDF in N-Methyl-2-pyrrolidone (NMP, Sigma Aldrich, Dorset, UK) was prepared in advance. The NMP solution was mixed by hand with both the carbon and the active material. A viscous slurry was created by the addition of more NMP. The ink was prepared by ball milling at 800 rpm for 1 h. The ink was then cast on copper foil (9 µm, PI-KEM, Staffordshire, UK) for testing in LIBs & Li-HECs, or on aluminium foil (15 µm, PI-KEM, Staffordshire, UK) for testing in NIBs and Na-HECs. The electrodes were then dried on a hotplate until the solvent had evaporated. Residual solvent in the electrode sheets could dry further overnight. Before the electrodes were introduced into an Ar filled glovebox, they were dried in a vacuum oven at temperatures > 70 °C. The mass loading of active materials varied in the range 1.2 to 2.5 mg cm^{-2}, depending on the sample.

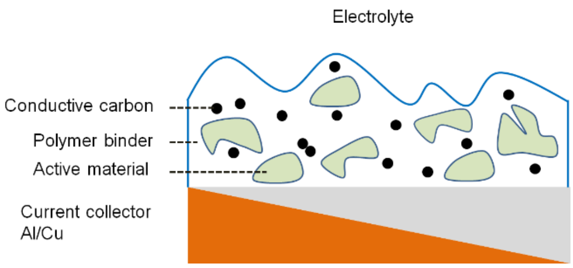

Figure 2-11: Diagram showing the structure of a composite electrode made up of a polymeric binder (usually PVDF), a conductive additive (usually carbon), and the active material cast onto a current collector (aluminium or copper).

The positive electrodes were prepared by mixing of an activated carbon (AC) active material (YP50F, Kuraray Chemical Co., Japan) with the same polymeric binder (PVDF, 8 wt.% solution in NMP) and conductive carbon (Super P) as for the negative electrodes in a Bühler high torque mixer (Bühler AG, Uzwil, Switzerland) for five hours, in a mass ratio of active material to binder to carbon of 87:8:5 wt.%. The slurry was coated on 15 μm aluminium foil using a Megtec reel-to-reel coater with a comma bar setup. The electrodes then passed through a three-phase oven for drying. Any residual solvent or water were removed by drying under vacuum at 120 °C for 12 hours. The mass loading of the positive electrodes was ca. 4.5 mg cm^{-2} and the electrodes were supplied by Warwick Manufacturing Group (WMG) at Warwick University.

2.3.2. Cell Assembly

Tests were carried out in CR2032 coin cells and Swagelok-type cells. Diagrams of both can be found in Figure 2-12. The constituent parts are similar and fulfil the same functions in each type of cell. For coin cells, bottom and top casings are in contact with one electrode each, providing mechanical stability and electrical conductivity, whereas for Swagelok-type cells, these are provided by stainless steel plungers. Working electrode, electrolyte-drenched separator, and lithium metal are the active constituents in both coin cells and Swagelok cells. A stainless-steel spacer and spring are used to provide compression in both. Whilst coin cells must be crimped to ensure an air-tight seal, the Swagelok-type cells are sealed by two ferrules per plunger. Electrical insulation between both electrodes is ensured by the polymer sealing ring for coin cells

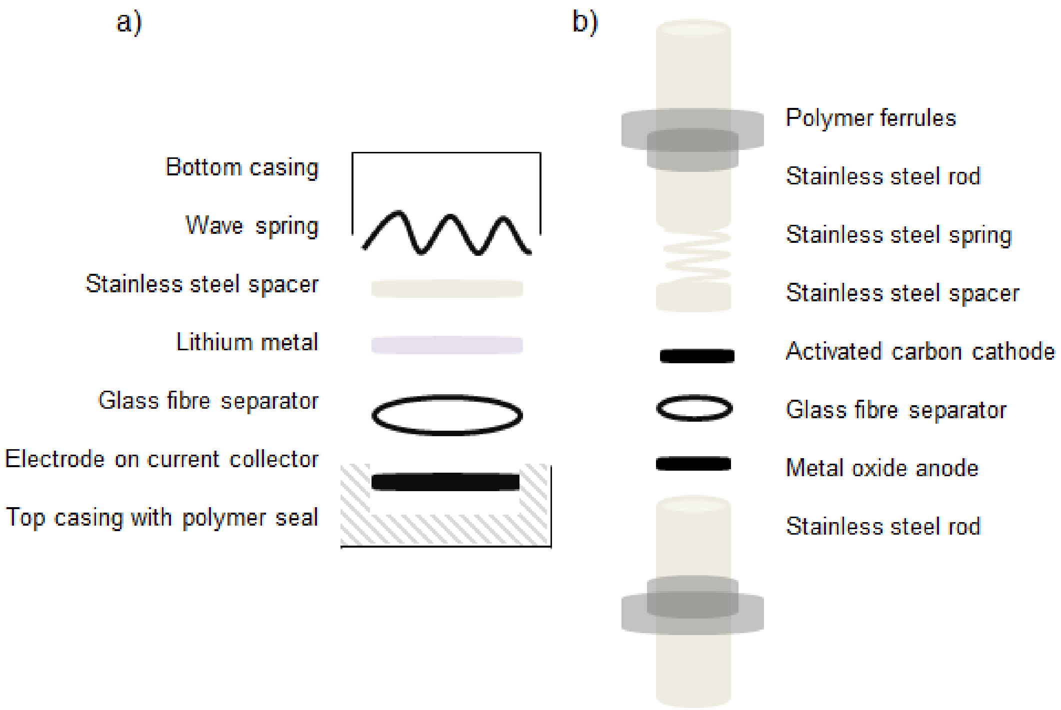

Figure 2-12: Diagram showing the components and their order for the assembly of a) a coin cell and b) a two-electrode Swagelok cell.

and the Swagelok perfluoroalkoxy alkane (PFA) union fitting itself for Swagelok cells (see Figure 2-13).

For testing of half-cells, 2032-type coin cells were assembled in an Ar-filled glovebox (MBraun UNIlab, Germany) with concentrations of O_2 and H_2O below 1 ppm. Lithium foil (PI-KEM) or sodium metal (Sigma Aldrich, Dorset, UK, Steinheim, Germany) discs were used as counter electrode and pressed by hand onto a stainless-steel spacer. Standard Li-ion salt containing organic electrolyte (1 M $LiPF_6$ in 1:1 by volume EC/DMC, BASF) or Na-ion electrolyte (1 M NaPF6 in 1:1 by volume EC/DMC, BASF) were used. The order of parts in the coin cell assembly was bottom casing, WE, separator (GF/D glass microfiber, WHATMAN, Buckinghamshire, UK), 150 µL of electrolyte, CE, spacer, spring, and the top casing of the coin cell. They were stacked up and a crimping device was used to crimp the cells to seal them.

For Li/Na-HEC testing, Swagelok-type cells were assembled in an Ar-filled glovebox. They were constructed in a similar fashion to that described above, only that instead of a metal counter electrode activated carbon cathodes were used.

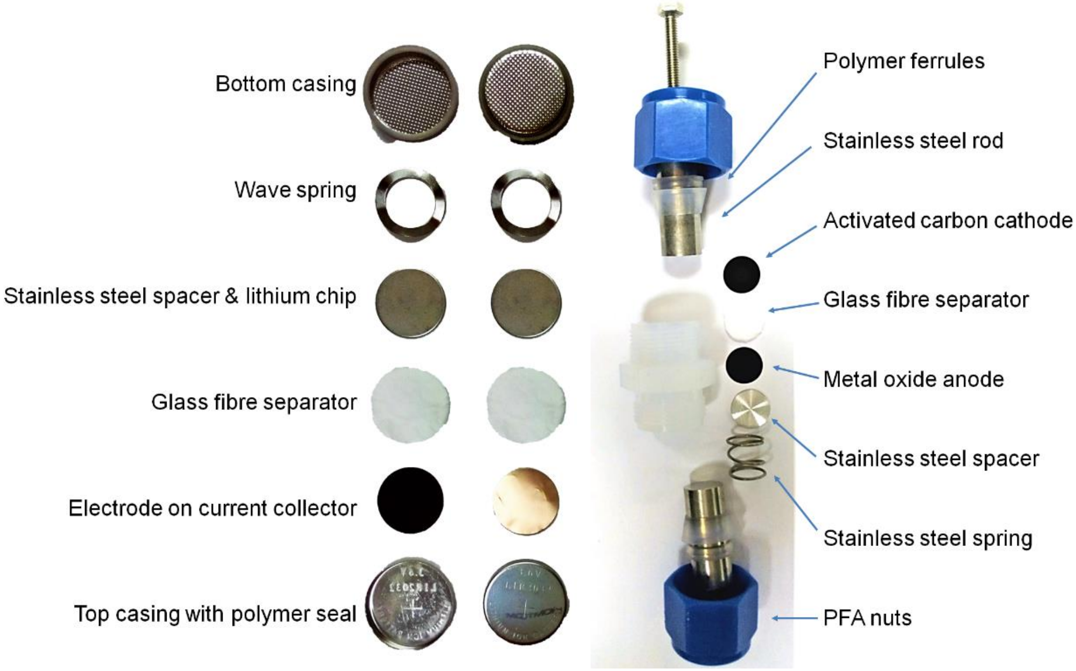

Figure 2-13: Photographs of the components of both coin cells and Swagelok-type cells.

The Swagelok cells consisted of ½” PFA Swagelok fitting (PFA-820-6, bored through) with the accompanying PFA ferrules and nuts, ½” stainless steel rod (SS316), a stainless-steel spring (Goodfellow), and a stainless-steel spacer (Goodfellow).

2.4. Conclusions

As discussed above, CHFS was used to synthesise a variety of nanosized transition metal oxides, nanocomposites, and mixed vanadium/molybdenum oxides. A variety of physical characterisation techniques such as XRD, XPS, XAS, TEM, SEM, and BET were used.

In the following Chapter 3, the synthesis and characterisation of Mo, V or Nb-doped anatase will be described and discussed.

3. Highly Pseudocapacitive Anatase Negative Electrodes via Doping

3.1. Aims

Various polymorphs of TiO_2, MoO_3, V_2O_5, and Nb_2O_5 have been reported to show excellent performance as negative electrodes in LIBs at high applied currents, especially when nanosized. The aim of this work was to try and further improve the high-power performance of TiO_2 (anatase) by doping with Mo(VI), V(V), or Nb(V). It was believed that the doping of such metals would lead to higher pseudocapacitive charge storage due to increased electronic conductivity and improved Li-ion diffusion. Furthermore, it was believed that these advantages would be present in NIBs as well as LIBs and lead to improved performance in Li-HECs and Na-HECs.

3.2. Introduction

Titania (TiO_2) is a promising material for use in negative electrodes in energy storage devices. It consists of inexpensive and abundant titanium (see Figure 1-15), is non-toxic, environmentally benign and shows minimal volume change upon lithiation (see Figure 1-18).[118] When lithium ions intercalate into titania, there is a change in the oxidation state of titanium as shown in Equation 3.1:[119]

$$\mathrm{Ti^{4+}O_2 + xLi^+ + xe^- \rightleftharpoons Li_x(Ti^{3+}_x Ti^{4+}_{1-x})O_2} \qquad (3.1)$$

The oxidation state change from Ti^{4+} to Ti^{3+} accommodates for the additional positive charge due to the intercalated lithium cation. The operating potential of all TiO_2 polymorphs is in the range 1.6 to 2.1 V vs. Li/Li^+. TiO_2 has a theoretical capacity of ca. 170 mAh g^{-1} (assuming the reversible intercalation of 0.5 moles of lithium ions per mole of TiO_2), which is about half of the theoretical capacity of graphite (370 mAh g^{-1}).[5]

When used as active material for negative electrodes in NIBs, TiO_2 has a significantly lower active potential vs. Na/Na^+ than it does vs. Li/Li^+. The active potential window is in the range 0.1 to 1.0 V vs. Na/Na^+,[15,59,178,223] depending on the polymorph as well as the size and crystallinity of the particles. The larger ionic radius of sodium cations compared to lithium cations (and the higher ionisation potential of the former) can lead to a larger polarization during charge/discharge.[224] As shown in Equation 3.2, upon sodium insertion and deinsertion during charge and discharge, respectively, the change in oxidation state for titanium is analogous to the reaction for TiO_2 in LIBs:

$$\mathrm{Ti^{4+}O_2 + xNa^+ + xe^- \rightleftharpoons Na_x(Ti^{3+}_xTi^{4+}_{1-x})O_2} \qquad (3.2)$$

Density functional theory (DFT) calculations have suggested that the anatase crystal structure of TiO_2 offers two diffusion paths for Na^+, along both the *a*- and *b*-axes, whereas rutile only offers one diffusion path for Na^+ along the *c*-axis. This suggested better Na^+ diffusion properties of anatase compared to rutile.[225]

Achieving high power density and high energy density simultaneously is considered the holy grail of energy storage. Because of the advantages of Li-HECs/Na-HECs, they are of significant interest to achieve these goals (as described in Section 1.3.2.3). Because of the high active potential of TiO_2 (anatase) vs. Li/Li^+, there is no formation of SEI, therefore, it is considered an ideal candidate as negative electrode in Li-HECs.

Nanosized TiO_2 has been shown to exhibit excellent cycling performance at high current rates because of significant pseudocapacitive contributions to charge storage. Polymorphs such as anatase,[52] TiO_2(B),[55] and bronze[56] have all been shown to exhibit highly pseudocapacitive charge storage in LIBs when nanosized. In NIBs, amorphous nanotubes,[58] anatase TiO_2/TiO_2(B)-graphene composites,[59] and anatase TiO_2 mesocages [60] have shown pseudocapacitive charge storage behaviour.

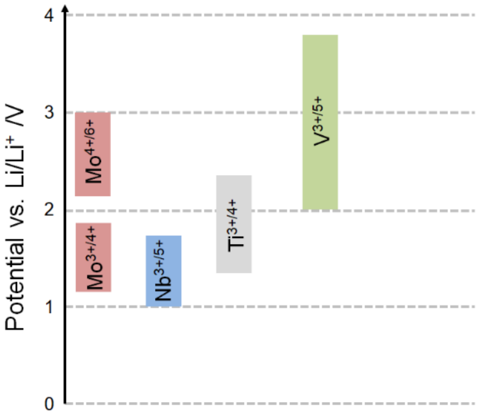

Figure 3-1: Active potential windows for the redox reactions of various transition metal ions versus Li/Li^+.

One disadvantage of TiO_2 as an active material is its low electronic conductivity, which is due to the wide band gap of anatase TiO_2 (ca. 3.2 eV).[226] The electronic conductivity can be increased by the introduction of dopants into the anatase structure, including Mo^{6+},[227] V^{5+},[228] and Nb^{5+}.[53] The dopants are expected to introduce conduction band electrons.[226] Furthermore, the introduction of cations of a higher oxidation state than Ti(IV) is expected to lead to Ti(IV) vacancies.[53,227] Because of its excellent electronic conductivity, Nb^{5+}-doped anatase (TiO_2) has previously been investigated as a transparent conductive oxide.[229]

Molybdenum, vanadium, and niobium were selected as dopants to improve the electrochemical performance of TiO_2 in both Li-ion and Na-ion systems. All are relatively abundant and inexpensive (see Figure 1-15) and have redox couples readily available for redox reactions with lithium ions at potentials vs. Li/Li^+ which are ideal for Li-HECs (see Figure 3-1). In this chapter, the direct and continuous synthesis of Mo^{6+}, V^{5+}, and Nb^{5+}-doped TiO_2 was described. The influence of the incorporation of these dopants into the crystal structure on the electrochemical properties of titania (anatase) was studied. The impact of doping on charge storage properties, alkali metal-ion diffusion, and conductivity were studied and discussed for LIBs, NIBs, Li-HECs, and Na-HECs.

3.3. Materials & Methods

3.3.1. Synthesis of Mo-, V-, or Nb-doped Anatase TiO_2

The synthesis of the materials was carried out as described in Section 2.1.1.

3.3.2. Physical Characterisation of Mo-, V-, or Nb-doped Anatase TiO_2

The physical characterisation of the materials was carried out according to the methods described in Section 2.2. The methods used included PXRD, XPS, XAS, TEM, BET, Raman spectroscopy, tap density, and EDX.

3.3.3. Electrochemical Characterisation of Mo-, V-, or Nb-doped Anatase TiO_2

Electrodes were prepared, and cells assembled, as described in Section 2.3. The electrochemical characterisation was carried out according to the methods described in Section 1.4.5.

3.3.3.1. Electrochemical Characterisation in LIB/NIB Half-cells

For LIBs, all testing was carried out in CR2032 half-cells, with electrodes cast on copper foil. All tests were carried out in the potential range 1.0 to 3.0 V vs. Li/Li^+. Cyclic voltammograms were recorded in the range of scan rates 0.05 to 100 mV s^{-1}. Galvanostatic measurements were carried out in the same potential window, in the range of specific currents 0.1 to 15.0 A g^{-1}.

For NIBs, all testing was carried out in CR2032 half-cells, with electrodes cast on aluminium foil. All tests were carried out in the potential range 0.1 to 3.0 V vs. Na/Na^+. Cyclic voltammograms were recorded at scan rates in the range 0.05 to 5.0 mV s^{-1}. Galvanostatic measurements were carried out in the same potential window, using specific currents in the range 0.1 to 10.0 A g^{-1}. All tests were carried out using an Arbin Instrument Model BT2000 battery tester (Caltest Instruments, Guildford, UK).

Electrochemical Impedance Spectroscopy (EIS) was carried out using CR2032 coin cells using a Gamry Interface 1000 instrument, in the frequency range 500 kHz to 50 mHz, with an AC current of 0.01 A rms.

3.3.3.2. Electrochemical Characterisation in Li/Na-HECs

All tests on Li/Na-HECs were carried out in Swagelok-type two-electrode cells. The design of the cells is shown in Section 2.3.2.

Li-HECs were tested potentiodynamically by CV at scan rates in the range 5 to 100 mV s^{-1}. Li-HECs were tested galvanostatically by cycling at current densities in the range 0.5 to 20 mA cm^{-2}. Na-HECs were tested potentiodynamically by CV at scan rates in the range 5 to 100 mV s^{-1}. Na-HECs were also tested galvanostatically by cycling at current densities in the range 0.5 to 20 mA cm^{-2}. The specific currents (based on the mass of active material in both anode and cathode) that were equivalent to the reported current densities were reported alongside the results. All tests were performed using a Gamry Interface 1000 instrument (Gamry Instruments, Pennsylvania, US).

3.4. Results and Discussion

3.4.1. Physical Characterisation of Mo-, V-, or Nb-doped Anatase TiO_2

After the continuous hydrothermal flow synthesis and subsequent freeze-drying, the nanoparticle slurries were collected with > 90 % yield. Any losses were due to unoptimized cleaning because of low sample quantities, for example during dialysis or after freeze-drying. The tap densities of the as-collected powders were 1.2, 1.3, 1.3, and 1.3 g cm^{-3} for undoped TiO_2, $Mo_{0.1}Ti_{0.9}O_2$, $V_{0.2}Ti_{0.8}O_2$, and $Nb_{0.25}Ti_{0.75}O_2$, respectively. These tap densities were significantly higher than those of comparable anode active materials such as nanosized $Li_4Ti_5O_{12}$, which has been shown to have a tap density of 0.8 g cm^{-3}.[230]

To gain insight into the structure of the samples, PXRD and Raman spectroscopy were carried out. PXRD patterns for all as-prepared powders were shown in Figure 3-2. The patterns were a good match with the peaks for ICSD

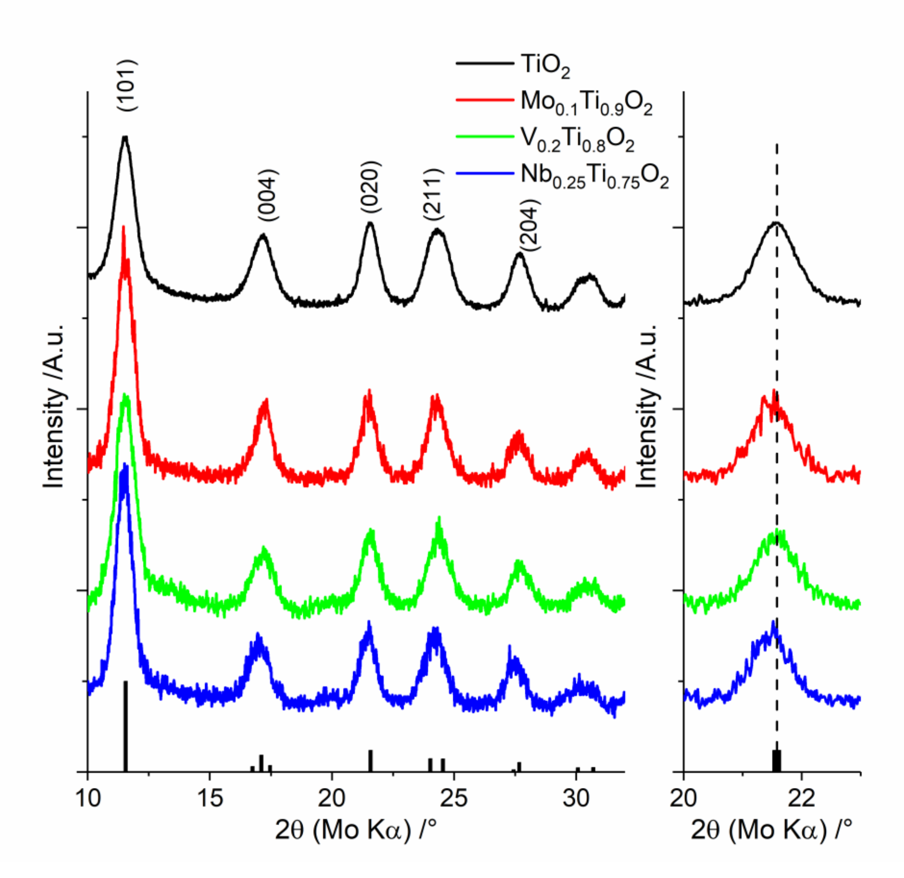

Figure 3-2: Powder X-ray diffraction patterns for the doped and undoped TiO_2 samples with bars representing peaks of ICSD reference pattern no. 09852 corresponding to anatase (TiO_2).

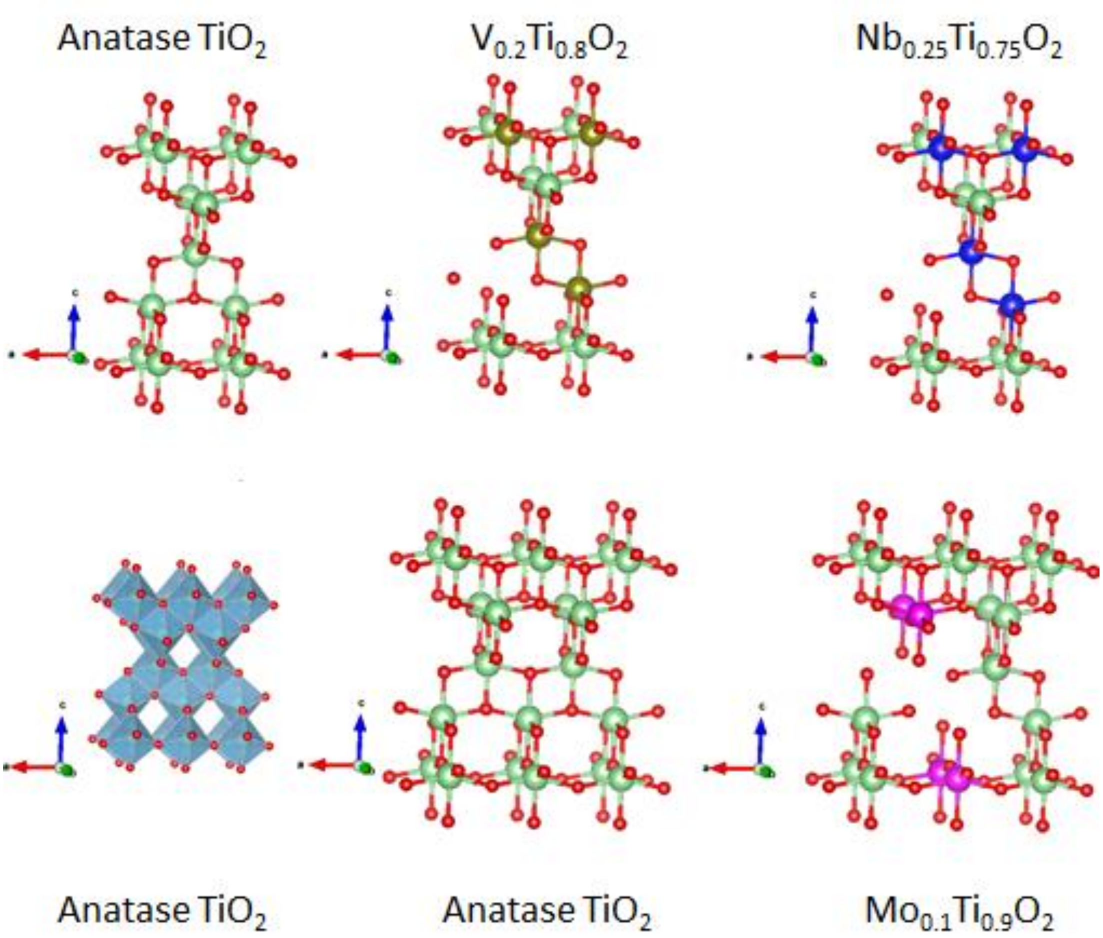

Figure 3-3: Structural models for anatase (TiO_2) and the proposed structures with dopant atoms (Mo(VI) -purple, V(V) – gold, Nb(V) – blue), including the suggested Ti(IV) vacancies.

reference number 09852 corresponding to anatase TiO_2. The peaks of the XRD patterns were generally broad as a result of the nanosizing of the samples. This was a result of the smoother transition between destructive and constructive interference according to Bragg’s law for smaller particles compared to larger particles, which is a result of fewer crystal layers diffracting for each plane. No impurity peaks for molybdenum, vanadium, or niobium oxides were observed. Hence, a body centred crystal structure (space group $I4_1/amd$) of anatase consisting of TiO_6 octahedra in planar double chains was expected. Upon doping, a small shift of peak positions to lower 2θ values was observed for the samples doped with Nb and Mo, which was most likely caused by lattice expansion due to homogenous doping. The expansion was a result of the larger ionic radius of the cations compared to Ti^{4+}.[231,232] This was confirmed by the calculation of lattice parameters, which showed an increase of the

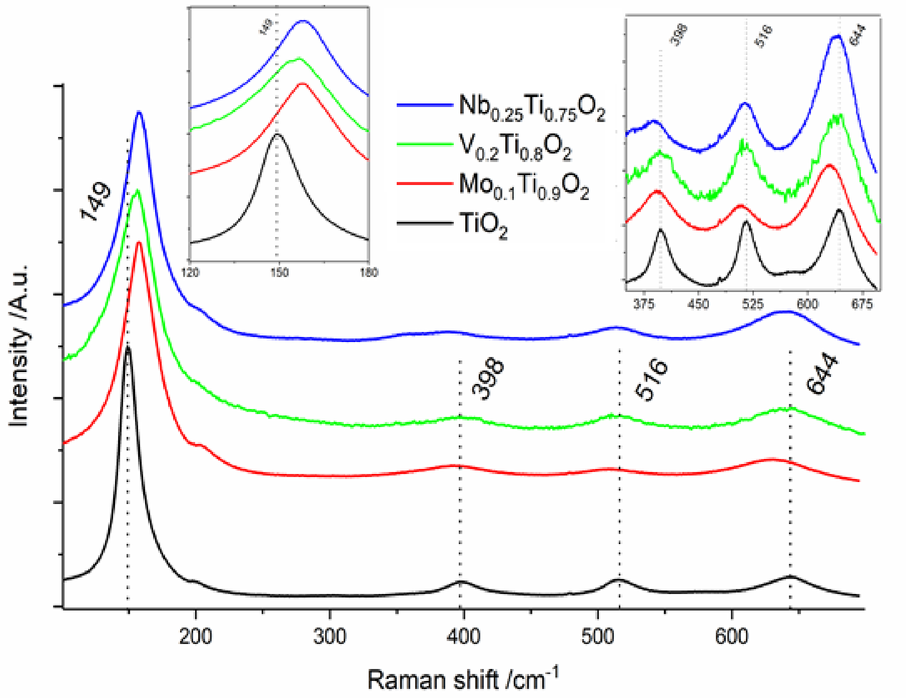

Figure 3-4: Raman spectra for the doped and undoped TiO_2 samples with insets showing enlarged regions to show the shifts observed for the doped samples.

unit cell volume from 135.77 Å^3 for TiO_2 to 137.54, 135.90 and 136.89 Å^3 for $Mo_{0.1}Ti_{0.9}O_2$, $V_{0.2}Ti_{0.8}O_2$ and $Nb_{0.25}Ti_{0.75}O_2$, respectively (see Table 3-1). The unit volume cell for $V_{0.2}Ti_{0.8}O_2$ was minimally larger than for TiO_2, which was surprising considering the ionic radius of V^{5+} is smaller than that of Ti^{4+}. The estimation of the crystallite size domain using the Scherrer equation (Equation 2.2.) for the five major peaks in each XRD pattern suggested crystallite domain sizes in the range 4 to 4.5 nm for TiO_2, $Mo_{0.1}Ti_{0.9}O_2$, and $Nb_{0.25}Ti_{0.75}O_2$. For $V_{0.2}Ti_{0.8}O_2$, the estimated domain size was just 3.8 nm. Mo^{6+}, V^{5+}, and Nb^{5+} were expected to replace Ti^{4+} in the anatase lattice. This led to the creation of one Ti^{4+} vacancy per two Mo^{6+}, four V^{5+}, or four Nb^{5+}. The suggested crystal structures along with models of the crystal structure of anatase are shown in Figure 3-3. This has previously been suggested for the doping of anatase with V^{5+} or Mo^{6+}.[123,233]

Table 3-1: Lattice parameters a and c, and the cell volume V for TiO_2, $Mo_{0.1}Ti_{0.9}O_2$, $V_{0.2}Ti_{0.8}O_2$, and $Nb_{0.25}Ti_{0.75}O_2$.

	a [Å]	c [Å]	V [Å^3]
TiO_2	3.7809	9.5143	135.77
$Mo_{0.1}Ti_{0.9}O_2$	3.8228	9.4116	137.54
$V_{0.2}Ti_{0.8}O_2$	3.7832	9.4998	135.90
$Nb_{0.25}Ti_{0.75}O_2$	3.7983	9.4881	136.89

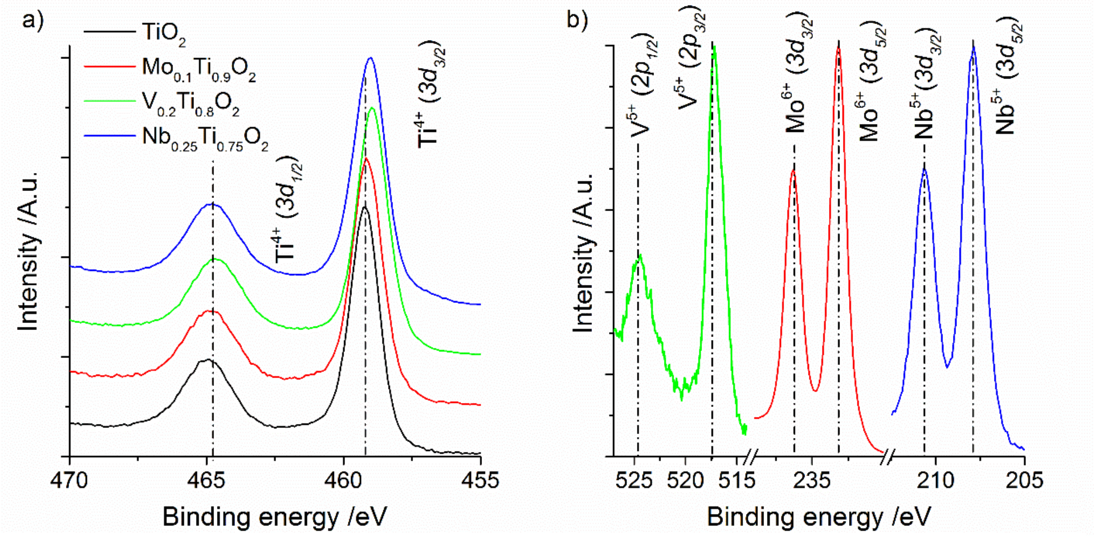

Figure 3-5: X-ray photoemission spectra of doped and undoped anatase samples for a) Ti *2p* and b) Mo *3d*, V *2p*, and Nb *3d* regional scans.

The Raman spectra of the materials are shown in Figure 3-4. For undoped TiO_2, peaks were observed at 149 (E_g), 198 (E_g) 398 (B_{1g}), 516 (B_{1g}+A_{1g}) and 644 cm^{-1} (E_g). These peaks were in good agreement with the six expected Raman-active modes of TiO_2 (anatase).[234] As was observed from the PXRD patterns, no peaks from possible impurities such as rutile TiO_2 or vanadium, molybdenum, or niobium oxides were observed. Upon doping titania with Mo^{6+}, V^{5+}, or Nb^{5+}, the main peak at 149 cm^{-1} was shifted to higher wavenumbers, which could be indicative of an expansion of the unit cell.[235,236] The shift was most pronounced for $Mo_{0.1}Ti_{0.9}O_2$ and $Nb_{0.25}Ti_{0.75}O_2$, which was in line with the expected volume expansion. However, even the peak for V-doped TiO_2 was shifted. The other peaks were shifted to slightly lower wave numbers, indicating an increased bond length due to the formation of Nb-O-Ti, V-O-

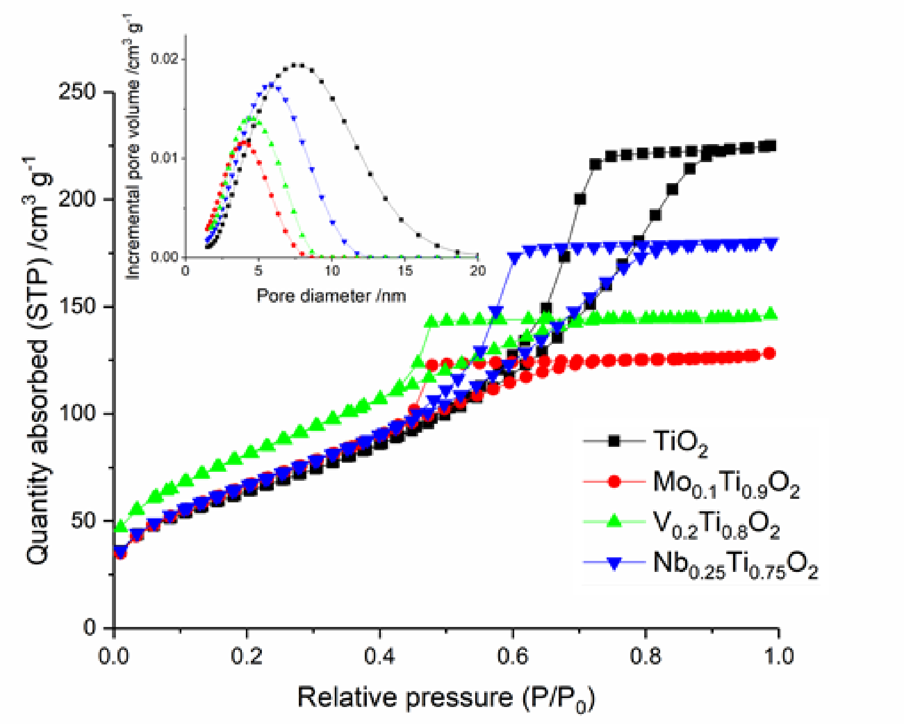

Figure 3-6: N_2 absorption/desorption isotherms for the various TiO_2 samples.

Ti, and Mo-O-Ti bonds.[237] A reported shift to lower wave numbers and an increasing intensity of the E_g peak at ca. 644 cm^{-1} has previously been associated with the formation of metal-oxygen bonds (here Nb-O, V-O, and Mo-O bonds), for example for Gd-doped TiO_2 and a Gd-O Eg mode.[237,238]

XPS was carried out to determine the valence state and semi-quantitative chemical composition of the surface of the materials. The Ti *2p* level binding energies for Ti $2p_{3/2}$ and Ti $2p_{1/2}$ were nearly identical for all samples at ca. 459.2 and 465.0 eV, respectively (see Figure 3-5). The calculated spin orbital splitting of ca. 5.8 eV for Ti *2p* was in good agreement with that expected for the core levels of Ti(IV). For the doped samples, only a minimal shift to higher binding energy levels was observed. The spin orbit splitting as well as the consistent symmetry of the peaks indicated that no reduced Ti species were present as a result of the doping.[234]

For Mo-doped anatase (see Figure 3-5b), the dopant peaks were located at binding energies of 236.0 and 232.8 eV for Mo $3d_{5/2}$ and Mo $3d_{3/2}$, respectively. This indicates a spin orbit splitting of 3.2 eV, which was in good agreement with the core levels expected for Mo(VI).[239] For Nb-doped titania (anatase), high resolution spectra showed peaks at binding energies of 207.9 and 210.7 eV for Nb $3d_{5/2}$ and

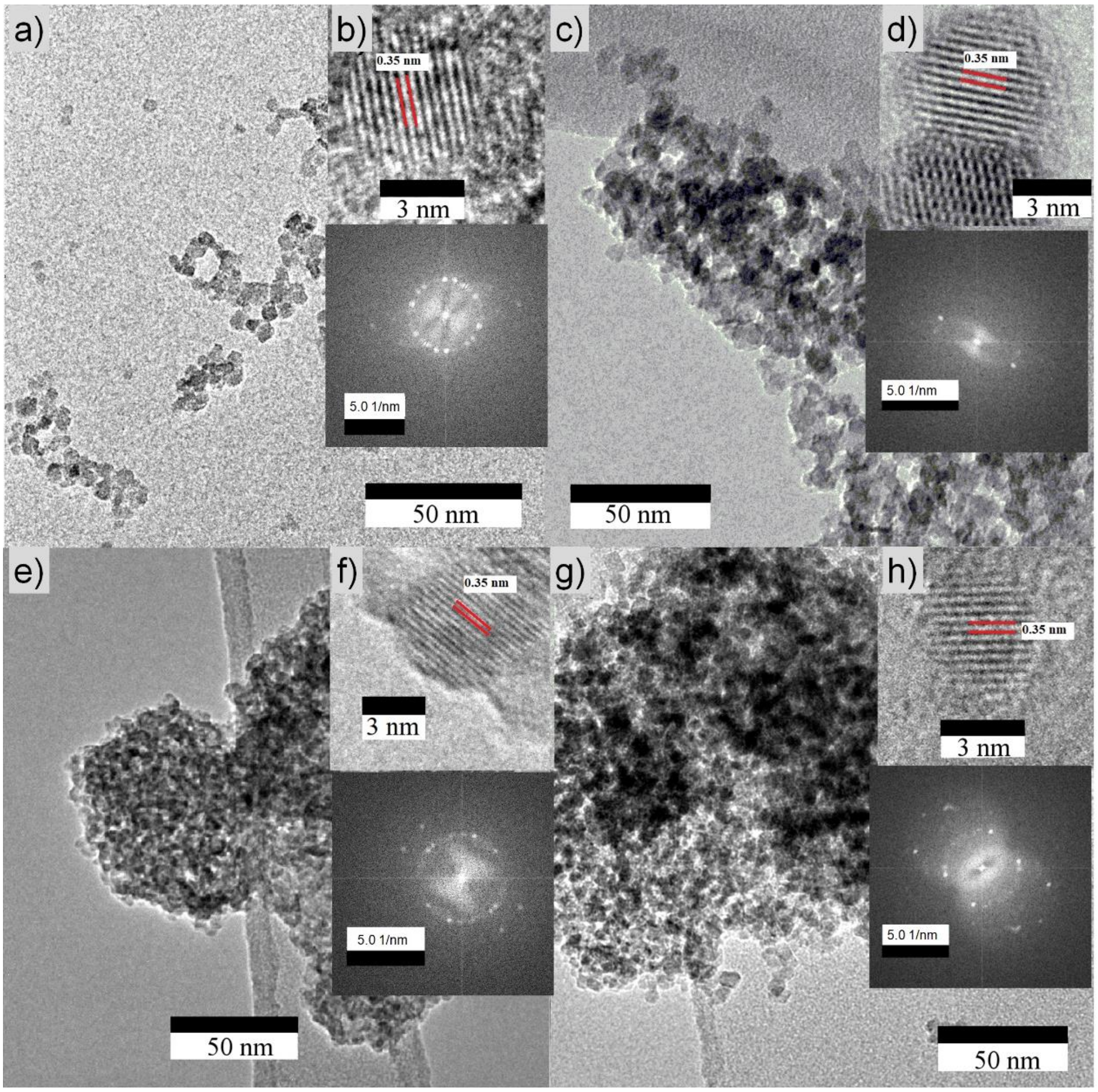

Figure 3-7: Transmission electron micrographs for a) and b) TiO_2, c) and d) $Mo_{0.1}Ti0.9O_2$, e) and f) $V_{0.2}Ti_{0.8}O_2$, and g) and h) $Nb_{0.25}Ti_{0.75}O_2$. Fourier transforms are also shown.

Nb $3d_{3/2}$, respectively. This indicated a spin orbit splitting of 2.8 eV, which could be assigned to Nb(V). For V-doped TiO_2 (anatase), high resolution spectra showed peaks at binding energies of 517.1 and 524.4 eV for V $2p_{3/2}$ and V $2p_{1/2}$, respectively. The position of these peaks, as well as the spin orbit splitting of 7.3 eV, were in line with V(V) species in V_2O_5 samples.[240]

Because no additional peaks were observed in the high-resolution XPS spectra for any dopant, a single valence state was assumed for Mo(VI), V(V), and Nb(V). Due to the implied charge imbalance induced by the pentavalent and hexavalent dopants, cationic vacancies (or additional oxygen in interstitial sites) could be expected. This has previously been reported for TiO_2 (anatase) with high-valence cation

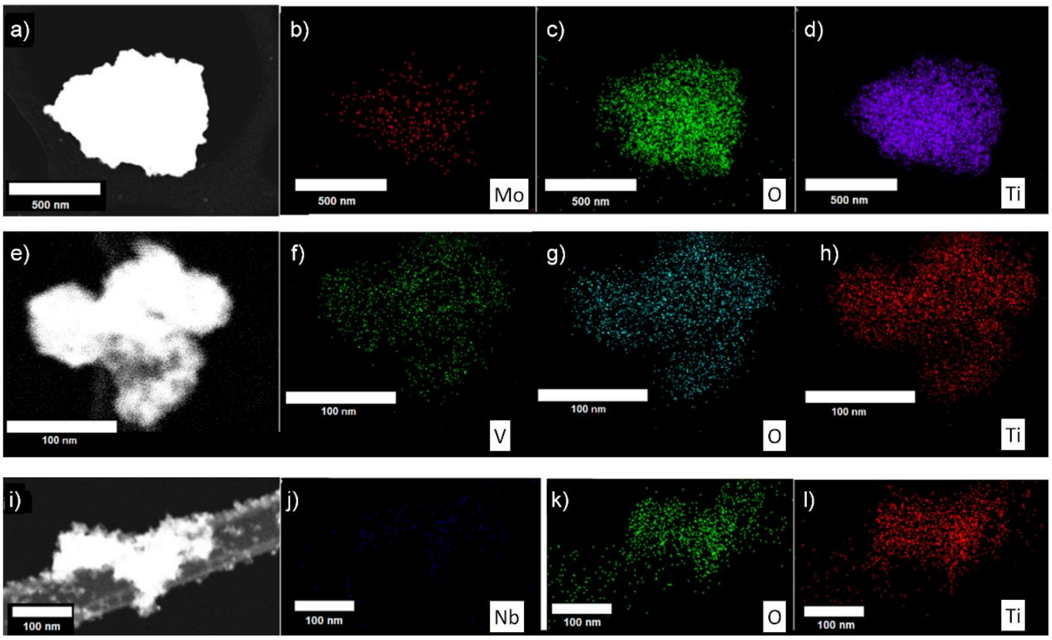

Figure 3-8: Dark-field micrographs for a) $Mo_{0.1}Ti_{0.9}O_2$, e) $V_{0.2}Ti_{0.8}O_2$, and i) $Nb_{0.25}Ti_{0.75}O_2$, together with corresponding EDX maps for Mo, O, and Ti Kα (b, c, and d, respectively); V, O, and Ti Kα (f, g, and h, respectively); Nb, O, and Ti Kα (j, k, and l, respectively).

dopants.[123,233] The semi-quantitative analysis of XPS peak areas showed concentration of 72 and 75 at.% oxygen for $Mo_{0.1}Ti_{0.9}O_2$ and $Nb_{0.25}Ti_{0.75}O_2$, respectively, which was more than the nominal 67 at.% expected, indicating there were cationic vacancies. However, this could have been a result of oxygen bound on the surface of the carbon tape used to affix the samples or hydration of some of the samples.

BET measurements showed very similar desorption and absorption isotherms for TiO_2, $Mo_{0.1}Ti_{0.9}O_2$, and $Nb_{0.25}Ti_{0.75}O_2$ (see Figure 3-6), which indicated similar measured specific surface areas of 233 (± 5), 237 (± 5), and 237 (± 5) m^2 g^{-1}, respectively. For $V_{0.2}Ti_{0.8}O_2$, the absorbed quantities of N_2 were significantly higher (see Figure 3-6), which indicated that the specific surface area was significantly higher at 297 (± 5) m^2 g^{-1}. Furthermore, the average pore width did differ significantly between samples and was 11.9, 4.9, 5.4, and 6.6 nm for TiO_2, $Mo_{0.1}Ti_{0.9}O_2$, $V_{0.2}Ti_{0.8}O_2$ and $Nb_{0.25}Ti_{0.75}O_2$, respectively (see inset Figure 3-6).

Transmission electron microscopy (TEM) revealed that all samples showed similar morphologies of spherical, uniform particles in larger agglomerates (see Figure

3-7a, c, e, and g). Particles sizes were narrowly distributed around ca. 5 nm for each sample. This was in line with the crystallite sizes calculated via the Scherrer equation from XRD patterns. The interlayer spacing for the (101) interplanar distance of anatase of 0.35 nm, which was also the major peak observed in the PXRD patterns above, was observable in each sample (see Figure 3-7b, d, f, and h).

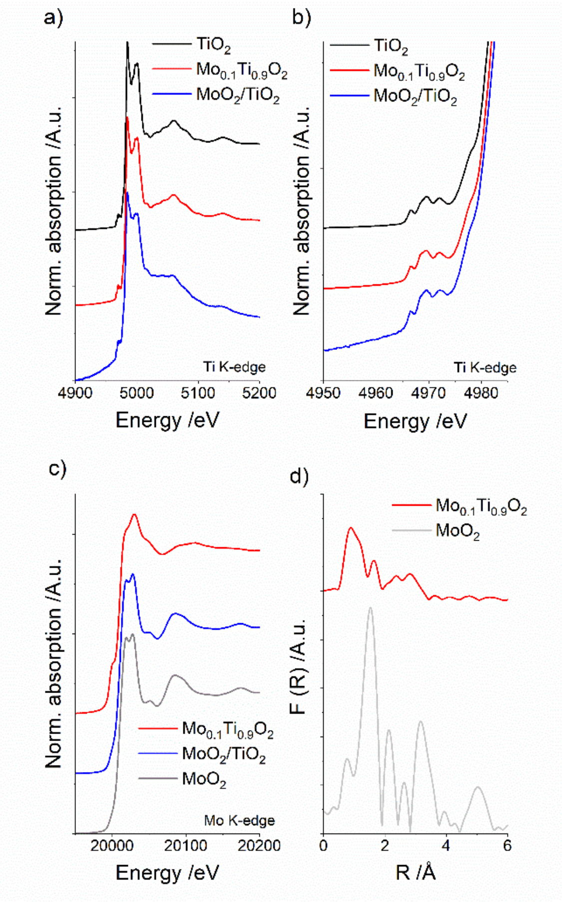

Figure 3-9: X-ray absorption spectra for the a and b) Ti K-edge and c) Mo K-edge. c) Experimental radial distribution plots for the Mo K-edge.

Energy-dispersive X-ray spectroscopy (EDX) mapping showed a homogenous distribution of dopant ions in each sample (see Figure 3-8). EDX was also used to determine the concentration of each metal dopant, which corresponded well with the nominal concentration from the synthesis. The atom percentages of dopants were determined to be ca. 24 at.% Nb(V), 18 at.% V(V) and 10 at.% Mo(VI) with relation to Ti(IV) in the doped TiO_2 (anatase) samples $Nb_{0.25}Ti_{0.75}O_2$, $V_{0.2}Ti_{0.8}O_2$, and $Mo_{0.1}Ti_{0.9}O_2$, respectively.

X-ray absorption spectroscopy (XAS) data for the Ti K-edge (see Figure 3-9a) of TiO_2 and $Mo_{0.1}Ti_{0.9}O_2$ showed no difference in edge position, which confirmed the results from XPS that Ti(IV) was the only oxidation state of titanium present in $Mo_{0.1}Ti_{0.9}O_2$. The noticeable pre-edge feature consisted of three separate peaks (see Figure 3-9b) associated with the 1s to 3d quadrupole transitions and dipole transitions from 1s to 4p states at higher energies.[241]

The Mo K-edge spectra for Mo-doped TiO_2 showed a pre-edge feature (see Figure 3-9c), which could be attributed to the 1s-4d transition, which has been associated with tetrahedral geometry but can also be present in (distorted) octahedral geometries, which is referred to as "tetrahedralization".[242–244] Furthermore, a post-edge feature that has previously been used to analyse the shift to lower energies for the transition from Mo(VI) to Mo(IV) confirmed the oxidation state of Mo(VI) in Mo-doped TiO_2.[245] The Fourier transform (FT) of the Mo K-edge EXAFS was plotted in Figure 3-9d. Molybdenum in $Mo_{0.1}Ti_{0.9}O_2$ was coordinated significantly different to molybdenum in the MoO_2 reference. The FT of the Mo-doped TiO_2 sample did not match that expected for MoO_3, which shows a major feature below 1 Å, indicating the different coordination environment.[246] Furthermore, expected Mo-Mo coordination features at ca. 3 Å were barely present, which possibly indicated that there was little Mo-Mo coordination.[247]

3.4.2. Electrochemical Characterisation of Mo-, V-, or Nb-doped Anatase TiO_2

3.4.2.1. Electrochemical Performance in LIB and NIB Half-cells

Cyclic voltammograms of Li-ion and Na-ion half-cells at different scan rates for the TiO_2 samples were examined to determine the intercalation and pseudocapacitive charge storage behaviour of the electrodes. For Li-ion half-cells, at a scan rate of 0.05 mV s^{-1}, clear anodic (Li^+ extraction) and cathodic (Li^+ intercalation) peaks could be observed for all samples at ca. 2.0 and 1.7 V vs. Li/Li^+, respectively. However, as the scan rate was increased, the undoped sample (see Figure 3-10a) showed only minor peak broadening and increase in specific currents at potentials other than that of the peaks, whereas all doped samples showed significant peak broadening and higher specific currents at potentials around the peaks (Figure 3-10b to d). These peaks typically indicate a miscibility gap and a two-phase transition as lithium ions are inserted into the lattice.[79] Broader peaks indicated that Li-ion intercalation sites with a broader energy distribution were involved in Faradaic reactions.[248] This is common for amorphous and nanocrystalline materials, as these intercalation sites tend to be surface-near or surface sites which are more accessible at fast scan rates because diffusion-limitations are less pronounced.[55]

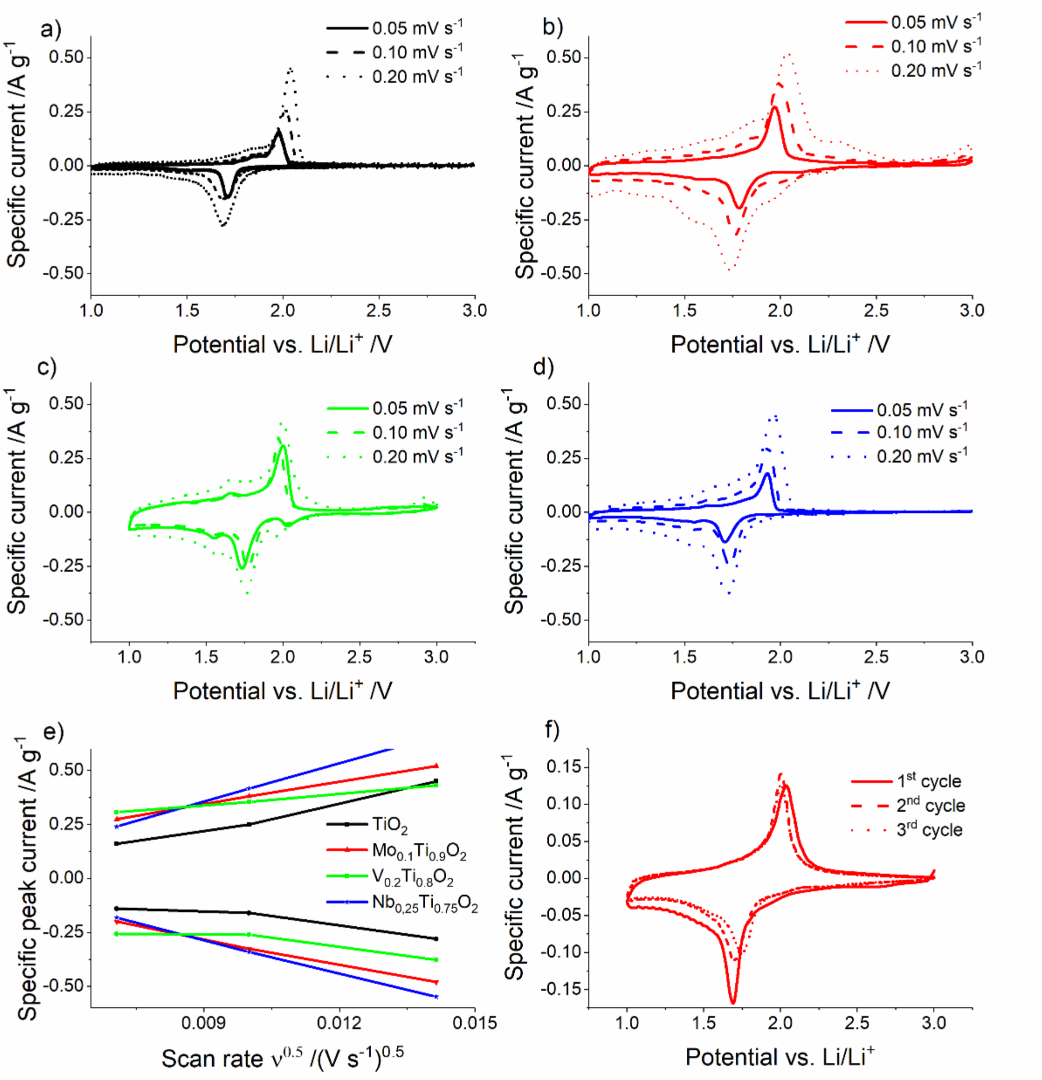

Figure 3-10: Cyclic voltammograms at different scan rates for LIB half-cells containing a) TiO_2, b) $Mo_{0.1}Ti_{0.9}O_2$, c) $V_{0.2}Ti_{0.8}O_2$, and d) $Nb_{0.25}Ti_{0.75}O_2$. e) The specific peak currents plotted over the square root of the scan rate. f) First three CVs at 0.05 mV s^{-1} for $Mo_{0.1}Ti_{0.9}O_2$.

Table 3-2: Apparent Li-ion diffusion coefficients for the different undoped and doped anatase samples.

	TiO_2	$Mo_{0.1}Ti_{0.9}O_2$	$V_{0.2}Ti_{0.8}O_2$	$Nb_{0.25}Ti_{0.75}O_2$
Anodic D_{Li} [cm^2 s^{-1}]	3.1×10^{-11}	6.2×10^{-11}	6.0×10^{-11}	7.5×10^{-11}
Cathodic D_{Li} [cm^2 s^{-1}]	1.5×10^{-11}	4.3×10^{-11}	4.0×10^{-11}	4.9×10^{-11}

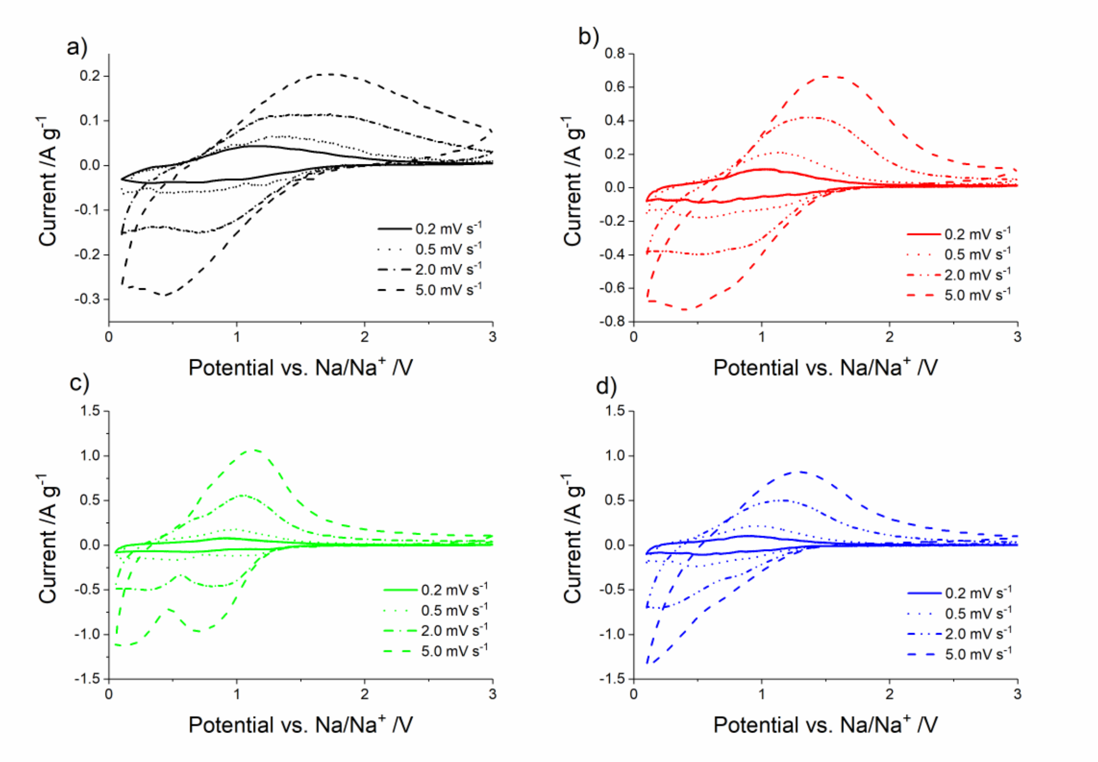

Figure 3-11: Cyclic voltammograms at different scan rates in NIB half-cells for a) TiO_2, b) $Mo_{0.1}Ti_{0.9}O_2$, c) $V_{0.2}Ti_{0.8}O_2$, and d) $Nb_{0.25}Ti_{0.75}O_2$.

The apparent lithium-ion diffusion coefficients calculated from the plots of anodic and cathodic specific peak currents versus square root of the scan rate (see Figure 3-10e) via the Randles-Sevcik method (see Equation 1.32) can be seen in Table 3-2. As would be expected from the results of the scan rate testing, the diffusion coefficients for the doped samples were significantly higher than for undoped TiO_2. Both anodic and cathodic diffusion coefficients were at least three-fold higher in the doped samples. This was in line with previous reports in the literature.[232,233,249]

As described in Section 1.5.1.1, the contributions to charge storage from both diffusion-limited and pseudocapacitive redox reactions can be separated using the specific charge at different scan rates. As can be seen in Table 3-3, the pseudocapacitive contributions to charge storage increased significantly for all doped samples compared to pure TiO_2, at any scan rate. This was especially significant at slower scan rates such as 0.1 mV s^{-1}, at which the pseudocapacitive contribution for pure TiO_2 was 53 %, whereas those for $Mo_{0.1}Ti_{0.9}O_2$, $V_{0.2}Ti_{0.8}O_2$, and $Nb_{0.25}Ti_{0.75}O_2$ were 69, 73, and 81 %, respectively.

Table 3-3: Proportions of charge storage from pseudocapacitive and diffusion-limited processes for the doped and undoped anatase (TiO_2) in LIB half-cells.

Scan rate		TiO_2	$Mo_{0.1}Ti_{0.9}O_2$	$V_{0.2}Ti_{0.8}O_2$	$Nb_{0.25}Ti_{0.75}O_2$
0.1 mV s^{-1}	Pseudocapacitive [%]	53	69	73	81
	Diffusion-limited [%]	47	31	27	19
1.0 mV s^{-1}	Pseudocapacitive [%]	78	88	87	93
	Diffusion-limited [%]	22	12	13	7
10.0 mV s^{-1}	Pseudocapacitive [%]	92	100	100	100
	Diffusion-limited [%]	8	0	0	0

Cyclic voltammograms of Na-ion half-cells for the TiO_2 and doped TiO_2 samples were recorded at various scan rates and examined to determine the intercalation and pseudocapacitive charge storage behaviour of the electrodes towards Na^+. Anodic (Na^+ extraction) and cathodic (Na^+ insertion) peaks appeared at 1.0 and 0.4, 0.9 and 0.5, 1.1 and 0.7, as well as 0.9 and 0.5 V vs. Na/Na^+ for TiO_2 (Figure 3-11a), $Mo_{0.1}Ti_{0.9}O_2$ (Figure 3-11b), $V_{0.2}Ti_{0.8}O_2$ (Figure 3-11c), and $Nb_{0.25}Ti_{0.75}O_2$ (Figure 3-11d), respectively, at a scan rate of 0.2 mV s^{-1}. Higher scan rates led to more pronounced peak separation, indicative of greater mass transport resistance[71] for all samples, but most significantly for the undoped TiO_2 (anatase). All cyclic voltammograms became more capacitor-like at high scan rates.[55] Importantly, in comparison to the CVs of the analogous Li-ion half-cells, all samples showed significantly broader, less defined peaks indicative of less pronounced two-phase transitions. Because of the larger ionic radius of Na^+ compared to Li^+, the higher ionization potential of the former can lead to a larger polarization during charge/discharge.[224] Generally, the two-phase transition of anatase upon sodiation in Equation 3.2 should be similar to that during lithiation (see Equation 2.21).

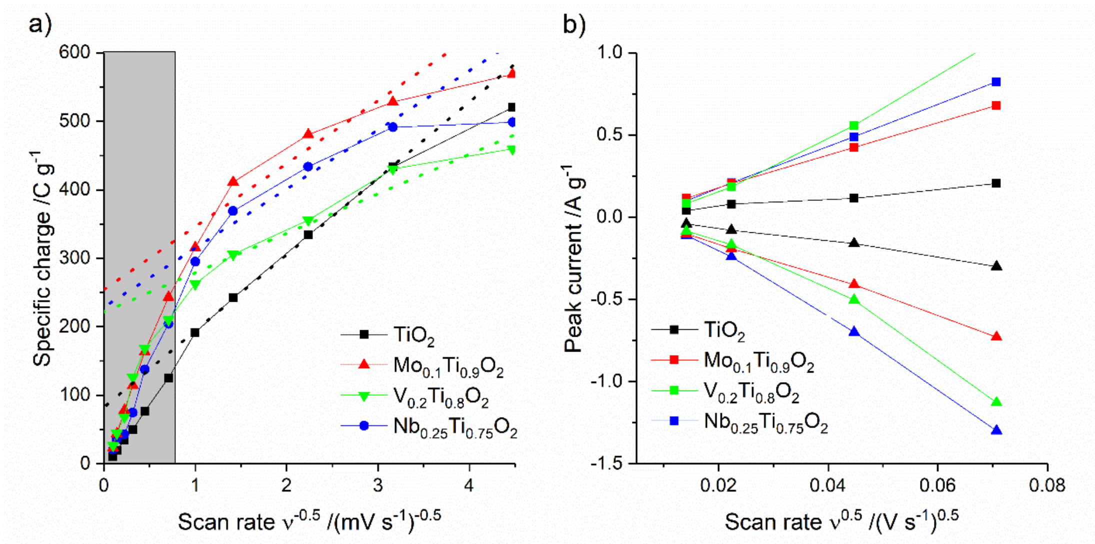

Figure 3-13: a) Specific charge versus reciprocal of the square root of the scan rate for all anatase samples as negative electrode materials in NIB half-cells. The intercept of the straight lines with the ordinate show the charge at a theoretical, infinitely fast scan rate. The values in the shaded area were discounted (high scan rate region). b) Specific peak currents of lithiation (negative) and delithiation (positive) plotted over the square root of the scan rate.

Clearly, pseudocapacitive charge storage contributions, rather than intercalation and two-phase transitions, played a significant role in Na-ion half-cells,

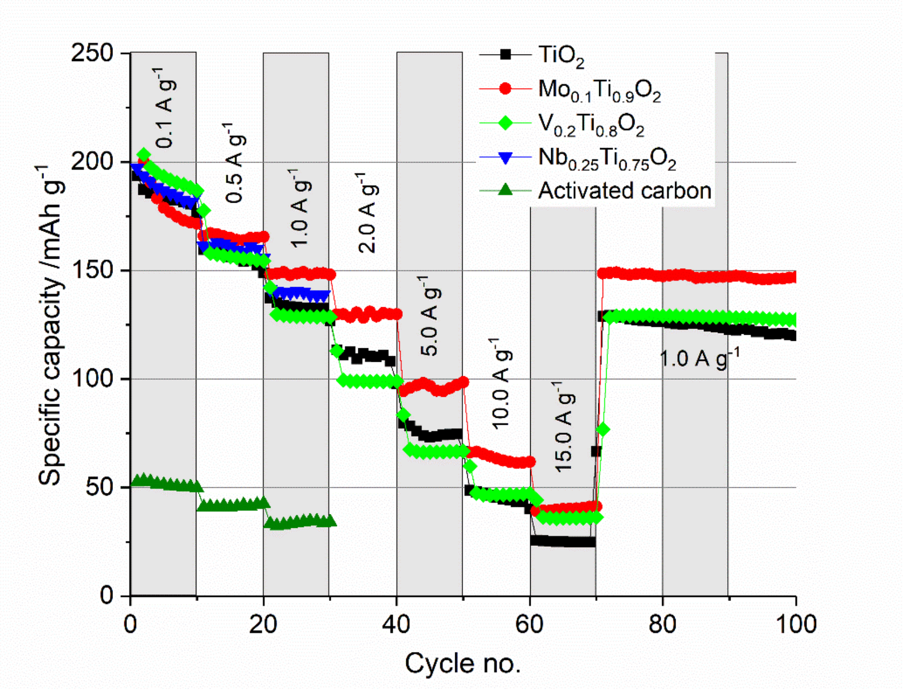

Figure 3-12: Specific capacities for TiO_2, $Mo_{0.1}Ti_{0.9}O_2$, $V_{0.2}Ti_{0.8}O_2$, and $Nb_{0.25}Ti_{0.75}O_2$ cycled in the potential window of 1.0 to 3.0 V vs. Li/Li^+ in LIB half-cells.

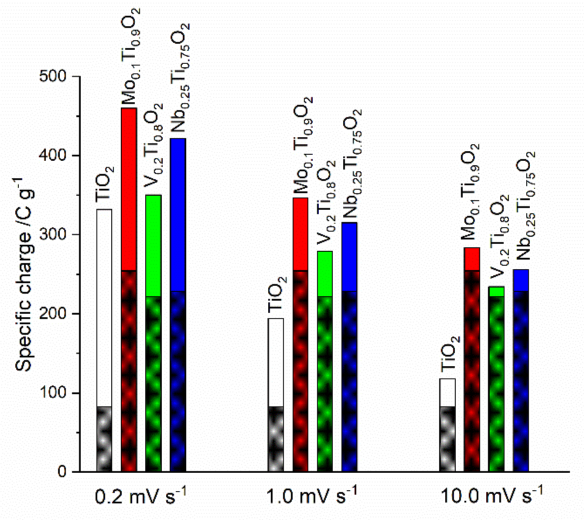

Figure 3-14: Pseudocapacitive (shaded area) and diffusion-limited contributions to charge storage at various scan rates for TiO_2, $Mo_{0.1}Ti_{0.9}O_2$, $V_{0.2}Ti_{0.8}O_2$, and $Nb_{0.25}Ti_{0.75}O_2$ in NIB half-cells.

even at relatively low scan rates. This indicated that the two-phase transition from tetragonal TiO_2 (anatase) towards orthorhombic $M_{0.5}TiO_2$ (where M = Li, Na) [128] was significantly favoured over a homogenous change in crystal structure during sodiation. It has previously been suggested that for TiO_2 (anatase) in Na-ion cells, a large proportion of charge will be stored via pseudocapacitance, and if a change in crystal lattice occurs it is a disproportionation into $Na_{0.25}TiO_2$, metallic Ti and Na_2O.[250]

The specific anodic peak currents for the undoped and doped samples were plotted versus the square root of the scan rate in Figure 3-13b. The Randles-Sevcik method (see Equation 1.32) was used to calculate apparent Na-ion diffusion coefficients for all samples in Na-ion half-cells, as described above for equivalent Li-ion cells. The results are shown in Table 3-4; as observed in Li-ion half-cells, the doped titania samples showed significantly higher apparent Na-ion diffusion coefficients than the undoped titania sample. However, whilst there was only a three-fold increase in diffusion coefficient for Li-ion, for Na-ion there was at least a ten-fold increase in diffusion coefficient for the doped samples compared to undoped TiO_2. The Na-ion diffusion coefficients were also generally significantly lower than for Li-ion, which could have been a result of the larger ionic radius of Na^+ compared to Li^+.

Table 3-4: Apparent Na-ion diffusion coefficients for the different undoped and doped anatase (TiO_2) samples.

	TiO_2	$Mo_{0.1}Ti_{0.9}O_2$	$V_{0.2}Ti_{0.8}O_2$	$Nb_{0.25}Ti_{0.75}O_2$
Anodic D_{Na} [cm^2 s^{-1}]	1.9×10^{-13}	2.0×10^{-12}	3.1×10^{-12}	2.3×10^{-12}
Cathodic D_{Na} [cm^2 s^{-1}]	2.8×10^{-13}	1.9×10^{-12}	3.0×10^{-12}	4.4×10^{-12}

Table 3-5: Proportions of charge storage from diffusion-limited and pseudocapacitive processes for the different undoped and doped anatase (TiO_2) samples at different scan rates in NIB half-cells.

Scan rate		TiO_2	$Mo_{0.1}Ti_{0.9}O_2$	$V_{0.2}Ti_{0.8}O_2$	$Nb_{0.25}Ti_{0.75}O_2$
0.2 mV s^{-1}	Pseudocapacitive [%]	25	55	63	54
	Diffusion-limited [%]	75	45	37	46
1.0 mV s^{-1}	Pseudocapacitive [%]	42	72	79	73
	Diffusion-limited [%]	58	28	21	27
10.0 mV s^{-1}	Pseudocapacitive [%]	70	90	92	89
	Diffusion-limited [%]	30	10	8	11

The proportions of diffusion-limited and pseudocapacitive charge storage contributions were separated using the Trasatti method (see Section 1.5.1.1).[64,73,80] The results yielded by this analysis are shown in Table 3-5. At a scan rate of 10.0 mV s^{-1}, the pseudocapacitive contributions to charge storage were 70, 90, 92, and 89 % for TiO_2, $Mo_{0.1}Ti_{0.9}O_2$, $V_{0.2}Ti_{0.8}O_2$, and $Nb_{0.25}Ti_{0.75}O_2$.

Because of the faster nature of pseudocapacitive charge storage compared to charge storage via diffusion-limited intercalation, these results indicated superior rate behaviour of the doped samples compared to undoped anatase.[59,73,80] The specific charge stored at each scan rate is shown, and diffusion-limited and pseudocapacitive charge separated, in Figure 3-14.

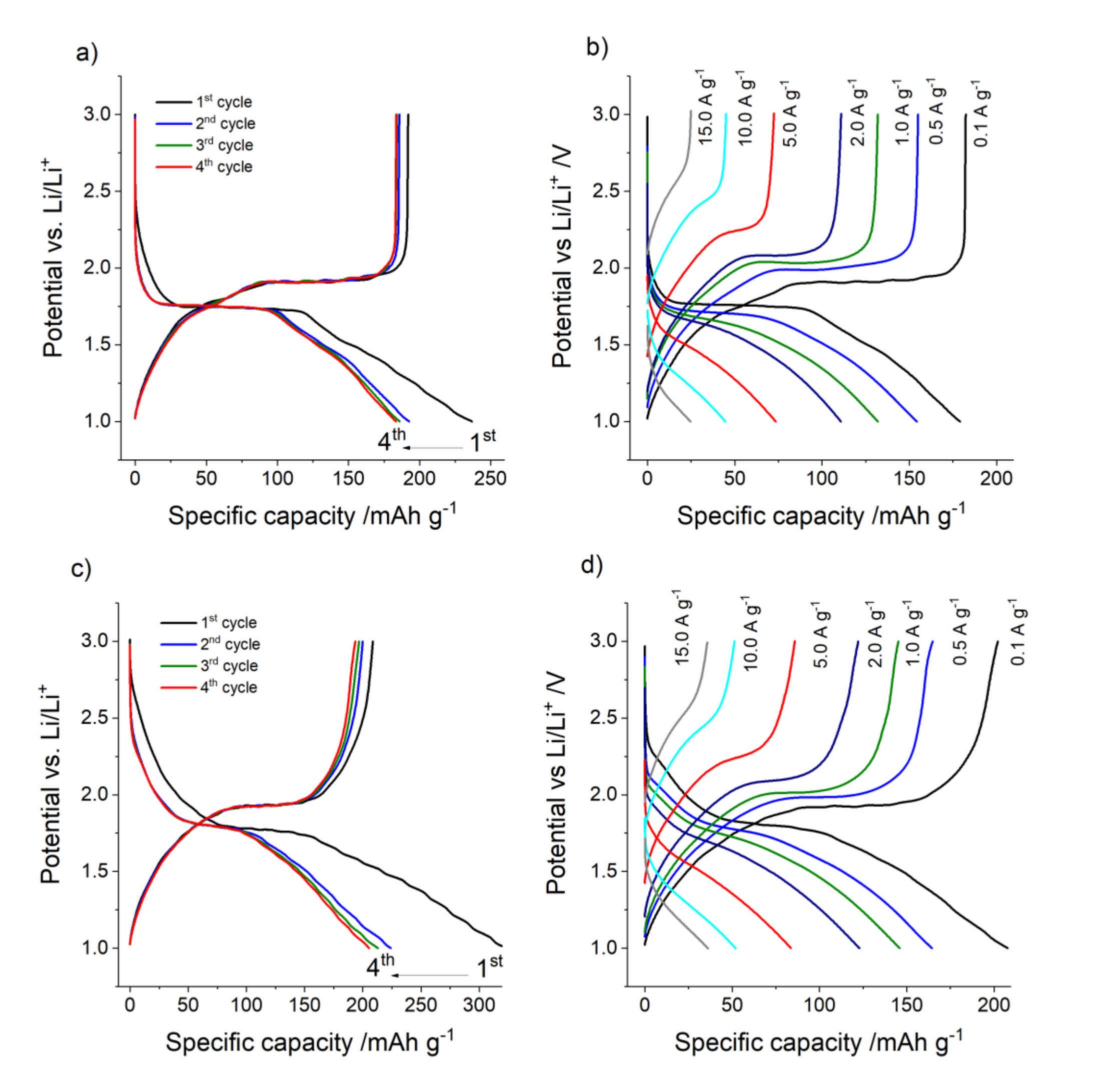

Figure 3-15: Galvanostatic charge/discharge curves in LIB half-cells for a) the first four cycles at 0.1 A g^{-1} for TiO_2, b) at different specific currents for TiO_2, c) the first 4 cycles at 0.1 A g^{-1} for $Mo_{0.1}Ti_{0.9}O_2$, and d) at different specific currents for $Mo_{0.1}Ti_{0.9}O_2$.

To analyse the improved rate performance of the doped samples compared to the undoped anatase in Li-ion half-cells, galvanostatic charge/discharge measurements were carried out at various specific currents and plotted in Figure 3-12. At a specific current of 0.5 A g^{-1}, the specific capacities were ca. 155, 170, 155 and 160 mAh g^{-1} for TiO_2, $Mo_{0.1}Ti_{0.9}O_2$, $V_{0.2}Ti_{0.8}O_2$, and $Nb_{0.25}Ti_{0.75}O_2$ electrodes, respectively. At higher specific currents, $Mo_{0.1}Ti_{0.9}O_2$ showed significantly higher specific discharge capacities than TiO_2 (100 and 65 mAh g^{-1} compared to 75 and 45 mAh g^{-1}, respectively, at 5 and 10 A g^{-1}, respectively). This meant that at a specific current of 5 A g^{-1} (equivalent to a C-rate of ca. 30 C), 100 mAh g^{-1} (ca. 60 % of theoretical specific capacity) could be stored in 72 s. At the highest specific current of

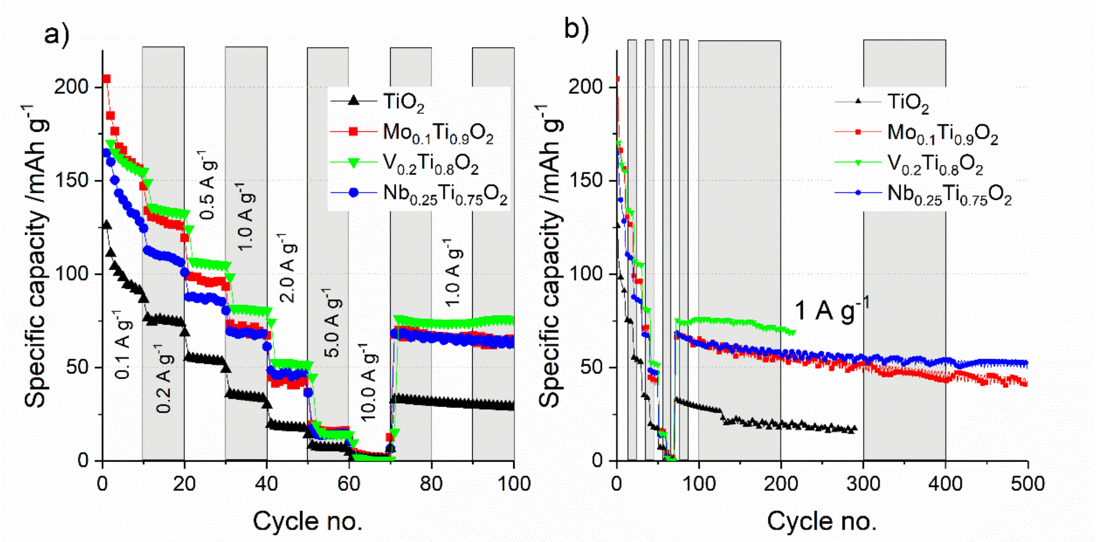

Figure 3-16: Galvanostatic charge/discharge capacities at varying specific currents for a) tens of and b) hundreds of cycles in NIB half-cells.

15 A g^{-1} (equivalent to a C-rate of ca. 90), the specific capacities for $Mo_{0.1}Ti_{0.9}O_2$ and TiO_2 were 42 and 25 mAh g^{-1}, respectively. This showed that doped TiO_2 (anatase) had significantly better high rate properties than undoped TiO_2, which was in line with the higher pseudocapacitive charge storage as indicated by scan rate testing.

The galvanostatic charge/discharge curves of TiO_2 and $Mo_{0.1}Ti_{0.9}O_2$ of the first four cycles (see Figure 3-15a and c) showed various significant differences: The first lithiation capacity for $Mo_{0.1}Ti_{0.9}O_2$ was significantly higher than for TiO_2 (325 compared to 240 mAh g^{-1}, respectively). The first discharge capacity was similar for both, indicating that the undoped TiO_2 showed better Coulombic efficiency in the first cycle. After the first cycle, the discharge capacity for both materials stabilized, at around 180 to 190 mAh g^{-1} for $Mo_{0.1}Ti_{0.9}O_2$ and around 175 mAh g^{-1} for TiO_2, respectively. The most interesting, however, was the different shapes of the curves: for TiO_2, there was an obvious and stable two-phase transition responsible for more than half of the exhibited capacity. This two-phase transition was seen from the plateaus of the curves at ca. 2.00 and 1.75 V vs. Li/Li$^+$ in the charge and discharge curves, respectively. Whilst there was a plateau in the curves for $Mo_{0.1}Ti_{0.9}O_2$, there was a slight slope to that plateau and it was significantly shorter than for undoped TiO_2. A higher proportion of the capacity came from sloped parts of the profile, indicating a higher contribution of pseudocapacitive processes to the charge storage in the doped

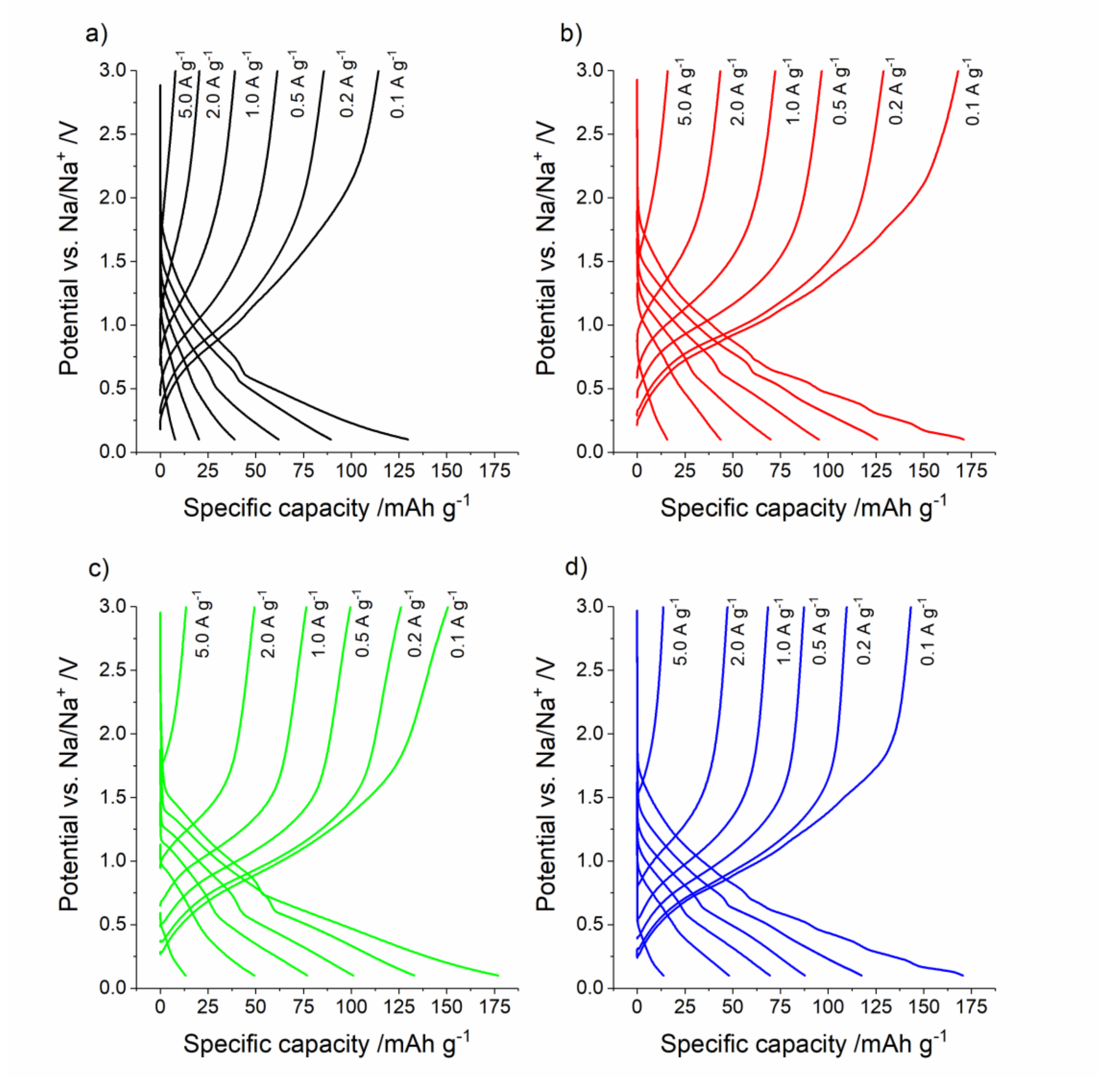

Figure 3-17: Galvanostatic charge/discharge curves in NIB half-cells at different specific currents for a) TiO_2, b) $Mo_{0.1}Ti_{0.9}O_2$, c) $V_{0.2}Ti_{0.8}O_2$, and d) $Nb_{0.25}Ti_{0.75}O_2$.

sample. These observations were in good agreement with the cyclic voltammograms in LIB half-cells shown in Figure 3-10. As the CV results indicated, charge storage in bulk intercalation sites (via a two-phase transition) steadily declined with increasing specific current, for both undoped TiO_2 and $Mo_{0.1}Ti_{0.9}O_2$ (see Figure 3-15b and d), respectively.

The specific discharge capacities at different specific currents for all doped and undoped TiO_2 samples cycled galvanostatically in Na-ion half-cells were plotted in Figure 3-16a and b. At a specific current of 0.1 A g^{-1}, the initial specific capacities were ca. 125, 205, 170, and 165 mAh g^{-1} for Na-ion half-cells using TiO_2, $Mo_{0.1}Ti_{0.9}O_2$, $V_{0.2}Ti_{0.8}O_2$, and $Nb_{0.25}Ti_{0.75}O_2$ as active materials, respectively. However, because of the formation of SEI and other processes resulting in irreversible capacity losses, after 10 cycles at a specific current of 0.1 A g^{-1}, the specific capacities had fallen to 85, 155, 150, and 125 mAh g^{-1}, respectively. At higher specific currents of 2 A g^{-1}, the doped samples showed good rate retention with specific capacities of ca. 50 mAh g^{-1}, whereas the specific capacity of undoped TiO_2 had fallen to 20 mAh g^{-1}. After cycling at higher specific currents and returning the specific current to 1.0 A g^{-1}, the specific capacities returned to ca. 75 and 30 mAh g^{-1} for the doped and undoped samples, respectively. These values were consistent with the values before cycling at very high rates of up to 10.0 A g^{-1}. After over 400 cycles at 1.0 A g^{-1}, the specific capacities had decreased to ca. 45 and 55 mAh g^{-1} for $Mo_{0.1}Ti_{0.9}O_2$ and $Nb_{0.25}Ti_{0.75}O_2$, respectively. For $V_{0.2}Ti_{0.8}O_2$, the specific capacity was more stable at ca. 70 mAh g^{-1} after 200 cycles.

The charge/discharge curves at different specific currents for all doped titania samples in Na-ion half-cells revealed no plateaus that would have been indicative of two-phase intercalation (see Figure 3-17). This was in good agreement with anatase nanoparticles previously reported in the literature.[14,16,58] Because of the small particle size, and hence high specific surface area, the previously described "solid-solution host" behaviour of the particle surface towards Li-ions can also be assumed to be effective towards Na-ions.

A further investigation via electrochemical impedance spectroscopy (EIS) of Na-ion half-cells, at open circuit voltage, revealed significantly higher change transfer resistance for the undoped samples compared to the doped samples (see Figure 3-18). The solution resistance R_e (the high-frequency intercept with the real impedance axis) was similar in all samples (6 to 7 Ω). This confirmed expectations, because it was a result of the resistance of the experimental setup (e.g. resistance caused by the electrolyte, the separator, coin cell casing, connections), which was consistent for all samples. In contrast, the charge transfer resistances were significantly lower for the doped samples (but especially for $V_{0.2}Ti_{0.8}O_2$ and $Nb_{0.25}Ti_{0.75}O_2$) than for undoped TiO_2. This has previously been observed for Nb-doped anatase.[251] For the doped samples, the maximum of the high-frequency semicircle was significantly lower for $Nb_{0.25}Ti_{0.75}O_2$ (at ca. 27 Ω) than for TiO_2 (at ca. 62 Ω), indicating lower impedance for the electrodes with doped anatase active materials. This agreed with previous findings for Nb-doped TiO_2 as active material in LIB half-cells.[53]

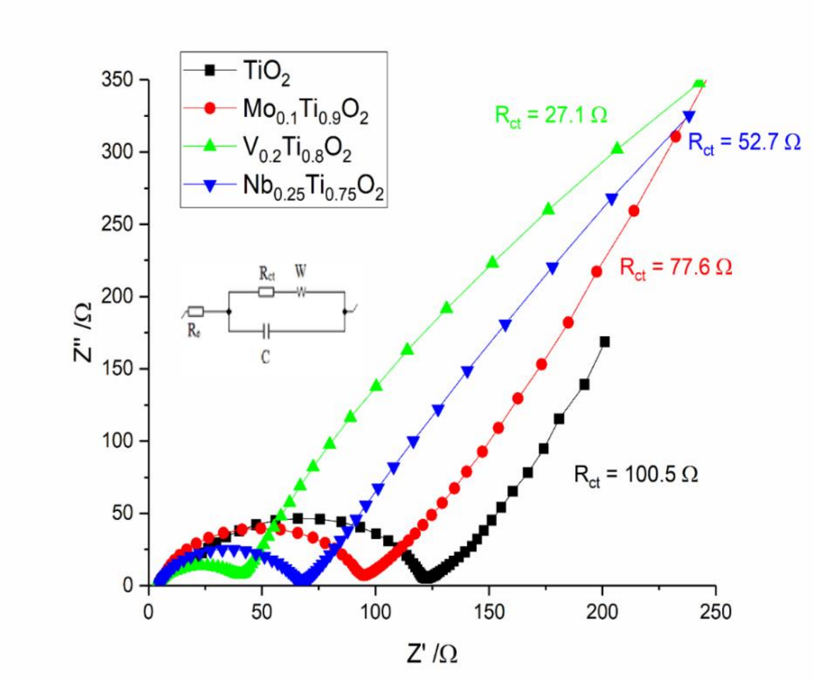

Figure 3-18: Nyquist plot of the electrochemical impedance spectroscopy of NIB half-cells using the different doped or undoped TiO_2 active materials.

The Warburg impedance coefficients ($\sigma_{warburg}$) were calculated from the magnitude of admittance (Y_0) obtained during fitting in Equation 3.3. Then, the diffusion coefficients in the solids were calculated using the Warburg impedance coefficients ($\sigma_{warburg}$) using Equation 3.4:[252]

$$\sigma_{\mathrm{warburg}} = \left(\frac{1}{\sqrt{2}\,Y_0}\right) \tag{3.3}$$

$$\mathrm{D} = 0.5\left(\frac{\mathrm{RT}}{\mathrm{AF}^2\sigma_{\mathrm{warburg}}\mathrm{C}}\right)^2 \tag{3.4}$$

D is the diffusion coefficient, *R* the gas constant, *T* the absolute temperature, *A* the interface area between the electrode and electrolyte (simplified as the geometric area of the electrodes), *F* is Faraday constant, and *C* is the concentration of cations in the electrolyte. The diffusion coefficients were 1.05, 2.88, 2.21, and 5.61×10^{-11} cm^2 s^{-1} for TiO_2, $Mo_{0.1}Ti_{0.9}O_2$, $V_{0.2}Ti_{0.8}O_2$, and $Nb_{0.25}Ti_{0.75}O_2$, respectively. These values were significantly higher than those calculated from the scan rate tests (see Table 3-4).

3.4.2.2. *Electrochemical Performance in Li-HECs and Na-HECs*

Because of the excellent electrochemical performance of the doped TiO_2 samples in both Li-ion and Na-ion half-cells versus metallic Li and Na, respectively, especially at high applied currents, they were considered promising materials for high-performance Li-ion and Na-ion hybrid electrochemical capacitors (Li/Na-HECs). Compared to half-cells, the metal counter/reference electrodes (lithium or sodium) were replaced by activated carbon positive electrodes. The mass ratio of active material in positive activated carbon electrodes and negative TiO_2 electrodes was calculated to allow equal charge to be stored in each electrode as described in Section 1.5.2.2. The mass ratio of active material in the positive and negative electrodes was ca. 2:7 and 1:4 for Li-HECs and Na-HECs, respectively.

Cyclic voltammograms of the Li-HECs showed profiles that resembled a mixture of the individual electrode profiles (see Figure 3-19). Whilst capacitive behaviour was suggested by a rectangular shape of the CVs, there were peaks that were indicative of intercalation-controlled charge storage. This has previously been reported in the literature.[253–256] The cathodic and anodic redox peaks were at ca. 2.3 and 2.1 V for the Li-HECs studied at 1.0 mV s^{-1}. Cyclic voltammograms of the different Li-HECs were used to calculate the specific capacitances via Equation 3.5 at different scan rates:

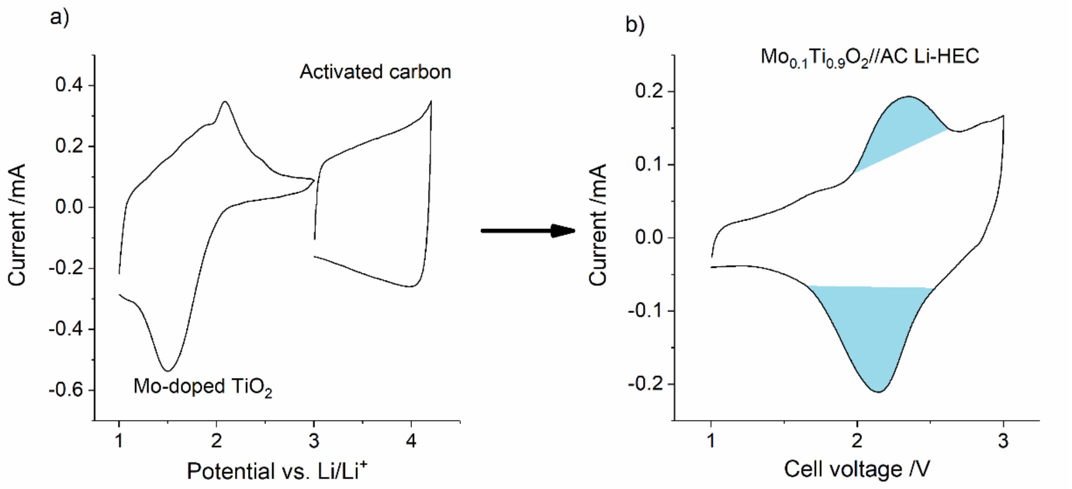

Figure 3-19: Cyclic voltammograms of a) $Mo_{0.1}Ti_{0.9}O_2$ and AC in separate LIB half-cells vs. Li metal at 0.5 mV s^{-1} and b) a $Mo_{0.1}Ti_{0.9}O_2$/AC Li-HEC at 1.0 mV s^{-1}.

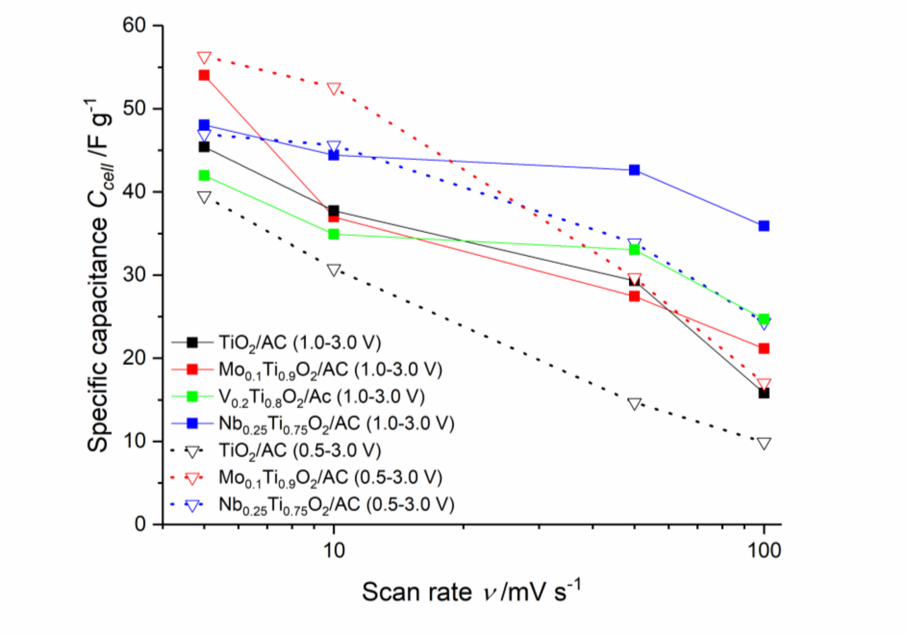

Figure 3-20: Specific capacitances of different Li-HECs at various scan rates, as determined from cyclic voltammograms.

$$C_{cell} = q/(\Delta V \times m) \tag{3.5}$$

q is the charge in C, *ΔV* is the voltage change in V, and *m* is the mass of active material in both the anode and cathode (in grams). Li-HECs were cycled in two different potential windows of 0.5 to 3.0 V and 1.0 to 3.0 V, respectively. At a scan rate of 5 mV s^{-1}, $Mo_{0.1}Ti_{0.9}O_2$/AC Li-HECs showed the highest capacitance of 54 F g^{-1} (corresponding to a specific capacity of 37 mAh g^{-1}) in the wide potential range and 56 F g^{-1} (corresponding to a specific capacity of 31 mAh g^{-1}) in the narrow potential range, respectively (see Figure 3-20). $V_{0.2}Ti_{0.8}O_2$/AC Li-HECs retained a capacitance of 25 F g^{-1} at a scan rate of 100 mV s^{-1}. $Nb_{0.25}Ti_{0.75}O_2$/AC Li-HECs retained the initial specific capacitance of 47 F g^{-1} (corresponding to a specific capacity of 33 mAh g^{-1}) in the wide potential range at a scan rate of 5 mV s^{-1} best and showed a specific capacitance of 37 F g^{-1} (corresponding to 26 mAh g^{-1}) at 100 mV s^{-1}. TiO_2/AC Li-HECs showed much lower specific capacitances than the other samples.

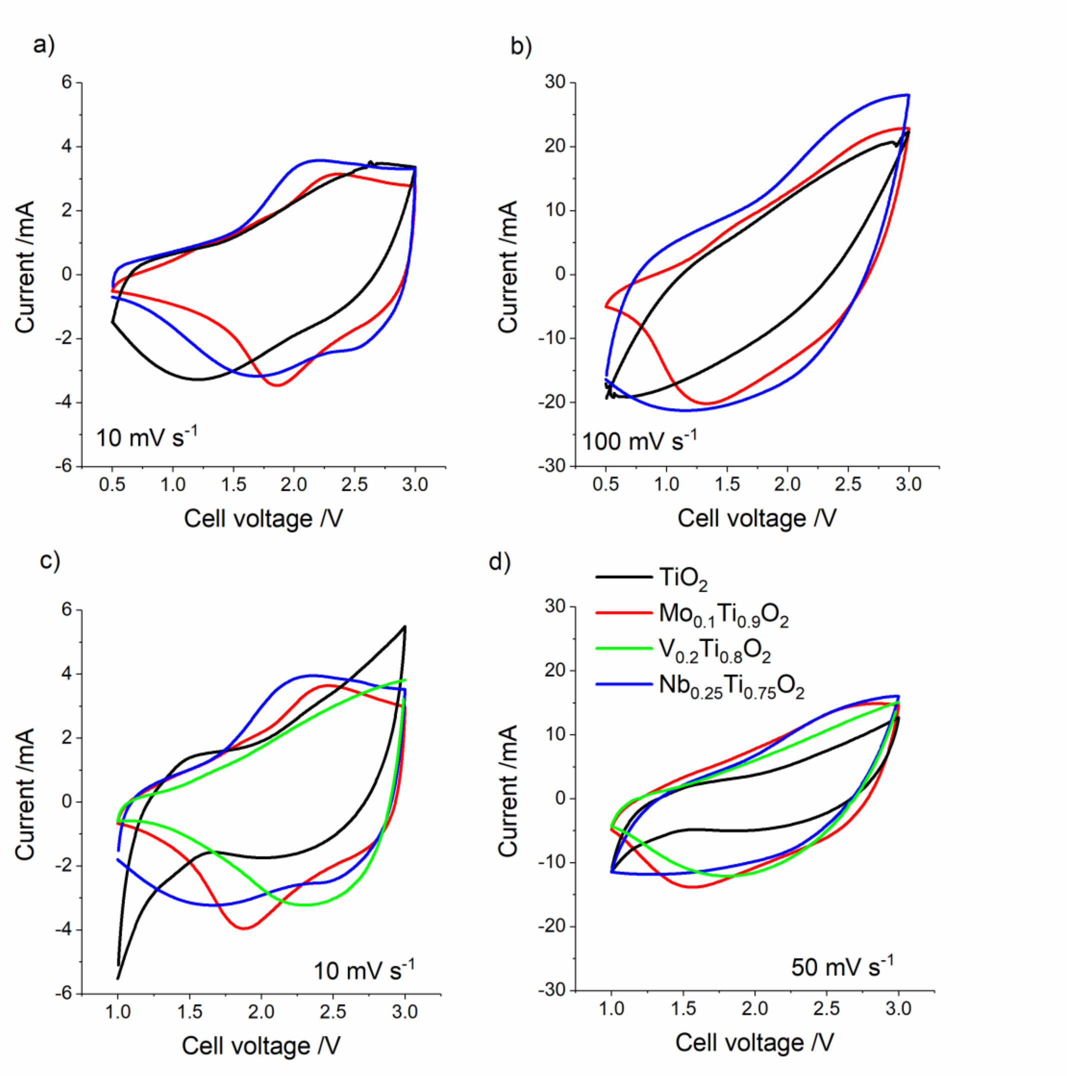

Figure 3-21: Cyclic voltammograms for TiO_2/AC, $Mo_{0.1}Ti_{0.9}O_2$/AC, $V_{0.2}Ti_{0.8}O_2$/AC, and $Nb_{0.25}Ti_{0.75}O_2$/AC Li-HECs in the potential ranges (a and b) 0.5 to 3.0 and (c and d) 1.0 to 3.0 V at scan rates of a) 10, b) 100, c) 10, and d) 50 mV s^{-1}.

This could be explained by lower pseudocapacitive contributions to charge storage, under a range of specific currents, including at high rates. This was indicated by the difference between cyclic voltammograms at lower scan rates (see Figure 3-21a and c) compared to those at higher scan rates (see Figure 3-21b and d). At higher scan rates, the plots show more rectangular shapes for the doped samples, whereas TiO_2/AC Li-HECs showed much flatter profiles. This indicated significantly less capacitive behaviour, as previously explained.

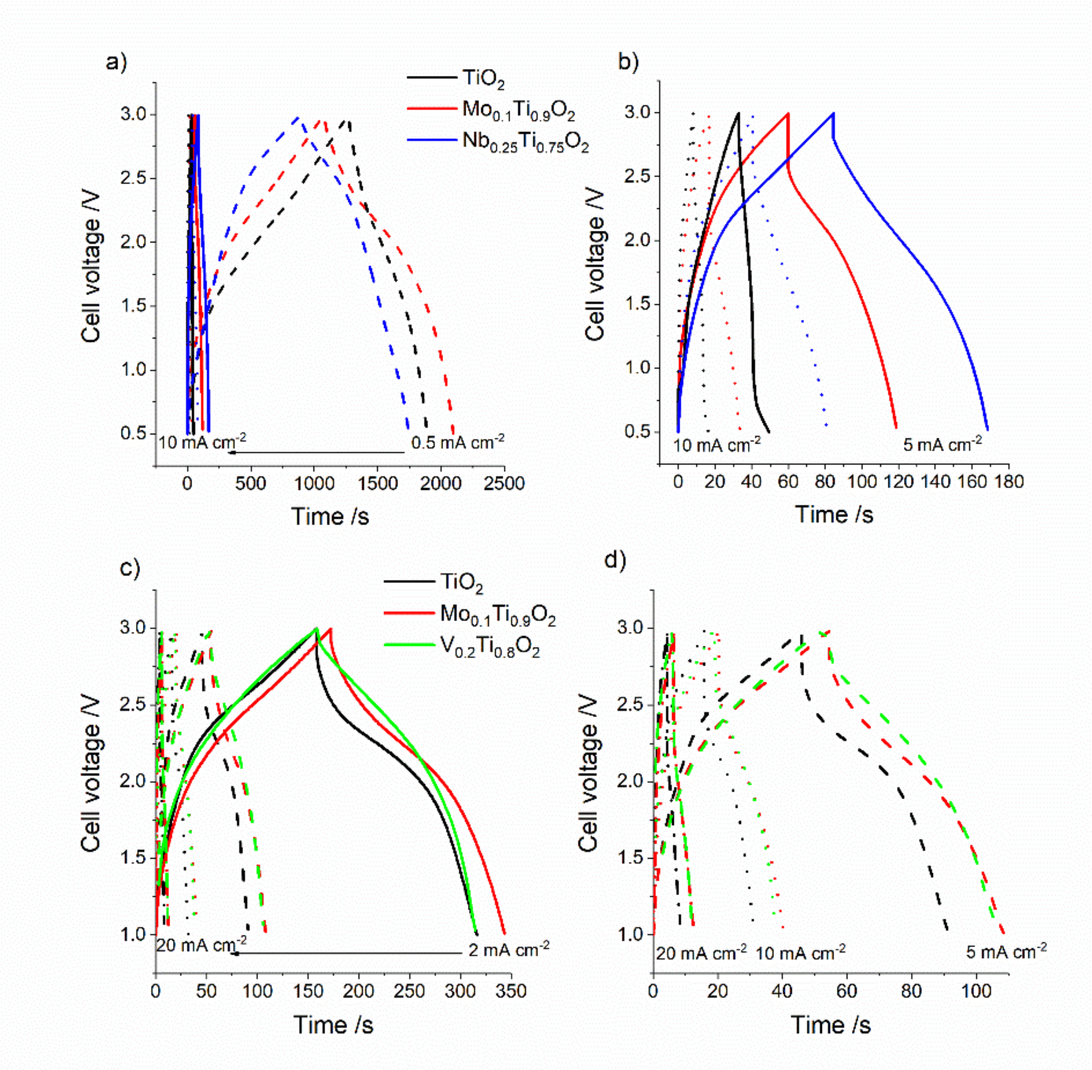

Figure 3-22: a) and b) Galvanostatic charge/discharge curves for the Li-HECs cycled in the potential window 0.5 to 3.0 V, at current densities of 0.5 (solid lines), 5 (dashes), and 10 mA cm^{-2} (dotted lines). c) and d) Galvanostatic charge/discharge curves of the Li-HECs cycled in the potential window 1.0 to 3.0 V, at current densities of 2 (solid lines), 5 (dashes), 10 (dotted lines), and 20 mA cm^{-2} (dash-dot).

Galvanostatic charge/discharge measurements were studied to further investigate the electrochemical performance of the Li-HECs. The specific capacitance as well as the power and energy densities of the cells were calculated according to the methods described in Sections 1.5.2 and 1.5.2.1. The cells were cycled in the potential windows 0.5 to 3.0 V and 1.0 to 3.0 V, at current densities in the range 0.5 to 50 mA cm^{-2}, equivalent to specific currents in the range 0.1 to 10 A g^{-1}, based on the mass of active materials in both cathode and anode. The charge and discharge plots from galvanostatic cycling deviated from the expected shape for purely capacitive charge storage (triangular) because a combination of intercalative, pseudocapacitive, and capacitive charge storage mechanisms were active. During charge, Li-ions both intercalated into the doped TiO_2 anatase active material in the negative electrodes and was stored via Faradaic reactions which appear capacitive, on or near the surface of the nanoparticles. On the other hand, hexafluorophosphate anions formed a Helmholtz double layer on the surface of the activated carbon positive electrode. Hence, the deviation from the capacitive charge/discharge profile indicated suboptimal mass balancing in anode and cathode.

As expected from their high specific capacitances at high scan rates, $Nb_{0.25}Ti_{0.75}O_2$/AC Li-HECs showed the best performance at high current densities (see Figure 3-22a and b). This was partly because the equivalent series resistance, which resulted in an IR drop of the potential, especially at higher applied currents, was significantly lower for the $Nb_{0.25}Ti_{0.75}O_2$/AC Li-HECs than the other Li-HECs. This was possibly due to the lower charge transfer impedance of $Nb_{0.25}Ti_{0.75}O_2$ compared to undoped TiO_2.[53]

In the wider potential window of 0.5 to 3.0 V, the specific capacitance of $Nb_{0.25}Ti_{0.75}O_2$/AC Li-HECs was 40, 38 and 34 F g^{-1} at current densities of 0.5, 5, and 10 mA cm^{-2} (equivalent to ca. 0.1, 1 and 2 A g^{-1}), respectively (see Figure 3-23). In contrast, $Mo_{0.1}Ti_{0.9}O_2$/AC Li-HECs showed a specific capacitance of 42 F g^{-1} (equivalent to a specific capacity of 30 mAh g^{-1}) at 0.5 mA cm^{-2}, which declined to 22 F g^{-1} (equivalent to a specific capacity of 10 mAh g^{-1}) at 10 mA cm^{-2}. TiO_2/AC Li-HECs, on the other hand, showed specific capacitances of only 38 and 9 F g^{-1} at 0.5 and 10 mA cm^{-2}, respectively.

In the narrower potential window (1.0 to 3.0 V), the Li-HECs containing doped samples performed significantly better especially at high rates (see Figure 3-23). The $Mo_{0.1}Ti_{0.9}O_2$/AC Li-HECs retained specific capacitances of 35, 31, 26, and 21 F g^{-1} at current densities of 2, 5, 10, and 20 mA cm^{-2} (equivalent to ca. 0.4, 1, 2, and 4 A g^{-1}), respectively. $V_{0.2}Ti_{0.8}O_2$/AC Li-HECs showed specific capacitances of 38, 37, 30, and 23 F g^{-1} at current densities of 2, 5, 10, and 20 mA cm^{-2}, respectively. For the $Nb_{0.25}Ti_{0.75}O_2$/AC Li-HECs, the calculated specific capacitances were 43, 38, 33, and 20 F g^{-1}, at current densities of 2, 5, 10, and 20 mA cm^{-2}, respectively. The

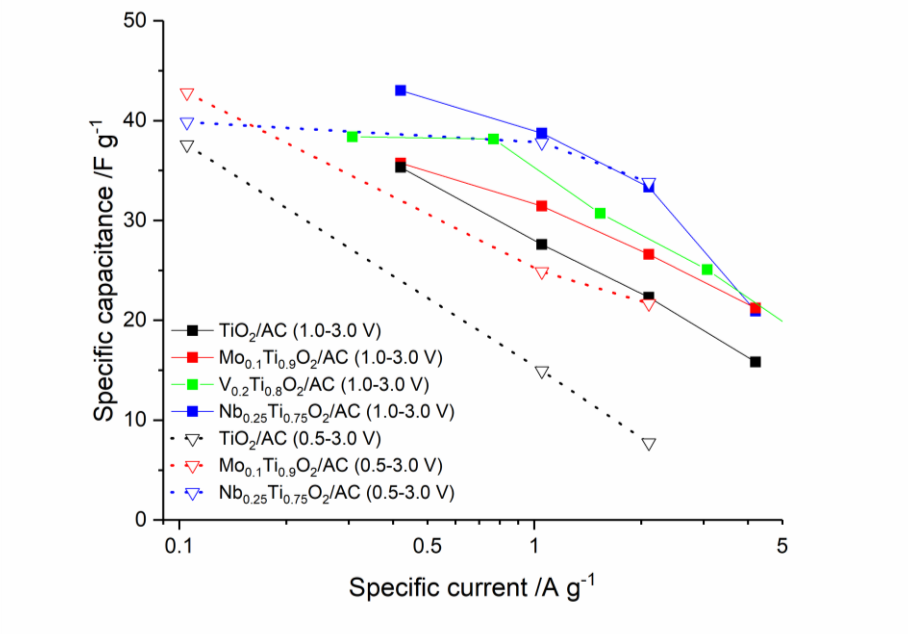

Figure 3-23: Specific capacitances of TiO_2/AC, $Mo_{0.1}Ti_{0.9}O_2$/AC, $V_{0.2}Ti_{0.8}O_2$/AC, and $Nb_{0.25}Ti_{0.75}O_2$/AC Li-HECs at different applied specific currents (based on the mass of active material in both anode and cathode) in the two potential windows 1.0 to 3.0 and 0.5 to 3.0 V, respectively.

TiO_2/AC Li-HECs showed better retention than in the wider potential window, but still the lowest capacitances of 34, 27, 22, and 16 F g^{-1} at the same current densities as above.

The galvanostatic testing of cycling stability and rate performance for a $Mo_{0.1}Ti_{0.9}O_2$/AC Li-HEC is shown in Figure 3-24. Whilst the specific capacity was relatively stable at the lowest current density of 2 mA cm^{-2} (falling from ca. 20 to 19 mAh g^{-1}), it was stable at the higher current densities and was still ca. 15 mAh g^{-1} after 600 cycles, when the current density was returned to 5 mA cm^{-2}. The Coulombic efficiency was only 99 % at low current densities, possibly due to the IR drop, whereas at higher current densities, it approached 100 %.

The gravimetric energy and power density for the Li-HECs were calculated using Equations 1.36 and 1.37 and plotted in a Ragone plot in Figure 3-25, alongside similar devices reported in the literature. The plotted values were for Li-HECs employing a variety of negative electrode materials such as TiO_2-reduced graphene oxide [253,257] and anatase TiO_2 [253], $Li_4Ti_5O_{12}$ [257,258], TiO_2-B [259], TiO_2(B)

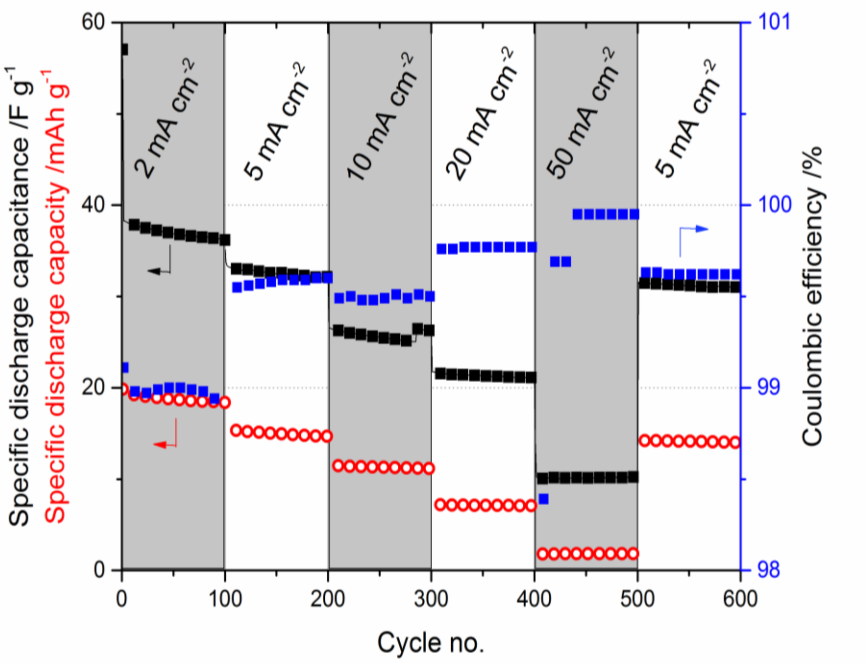

Figure 3-24: Galvanostatic cycling performance (capacity, capacitance, Coulombic efficiency) of a $Mo_{0.1}Ti_{0.9}O_2$/AC Li-HEC at current densities of 2, 5, 10, 20, and 50 mA cm^{-2} (equivalent to specific currents of ca. 0.4, 1, 2, 4, and 10 A g^{-1}) in the narrower potential window 1.0 to 3.0 V.

[260], $LiCrTiO_4$ [261], Ti_9O_{17} [262], and TiO_2 microspheres wrapped with graphene nanosheets (against a graphene nanosheet positive electrode).[263]

In the wider potential window of 0.5 to 3.0 V, $Mo_{0.1}Ti_{0.9}O_2$/AC Li-HECs delivered the highest energy density of 51 Wh kg^{-1} (at a power density of 180 W kg^{-1}). Because of the significantly better capacity retention in this potential window, $Nb_{0.25}Ti_{0.75}O_2$/AC Li-HECs showed better performance at higher power densities. At power densities of 1700 and 3200 W kg^{-1}, $Nb_{0.25}Ti_{0.75}O_2$/AC Li-HECs showed specific energy densities of 41 and 36 Wh kg^{-1}, respectively. This compared favourably against comparable devices in the literature (see references in Figure 3-25)

In the narrower potential window of 1.0 to 3.0 V, the average power at the same current density increased due to the higher average cell voltage. $Mo_{0.1}Ti_{0.9}O_2$/AC Li-HECs showed the highest energy densities of 29 and 12 Wh kg^{-1}, at power densities of 2000 and 6700 W kg^{-1}, respectively. At the highest power density of 14100 W kg^{-1}, the energy density was still 2.5 Wh kg^{-1}. $V_{0.2}Ti_{0.8}O_2$/AC Li-HECs showed energy

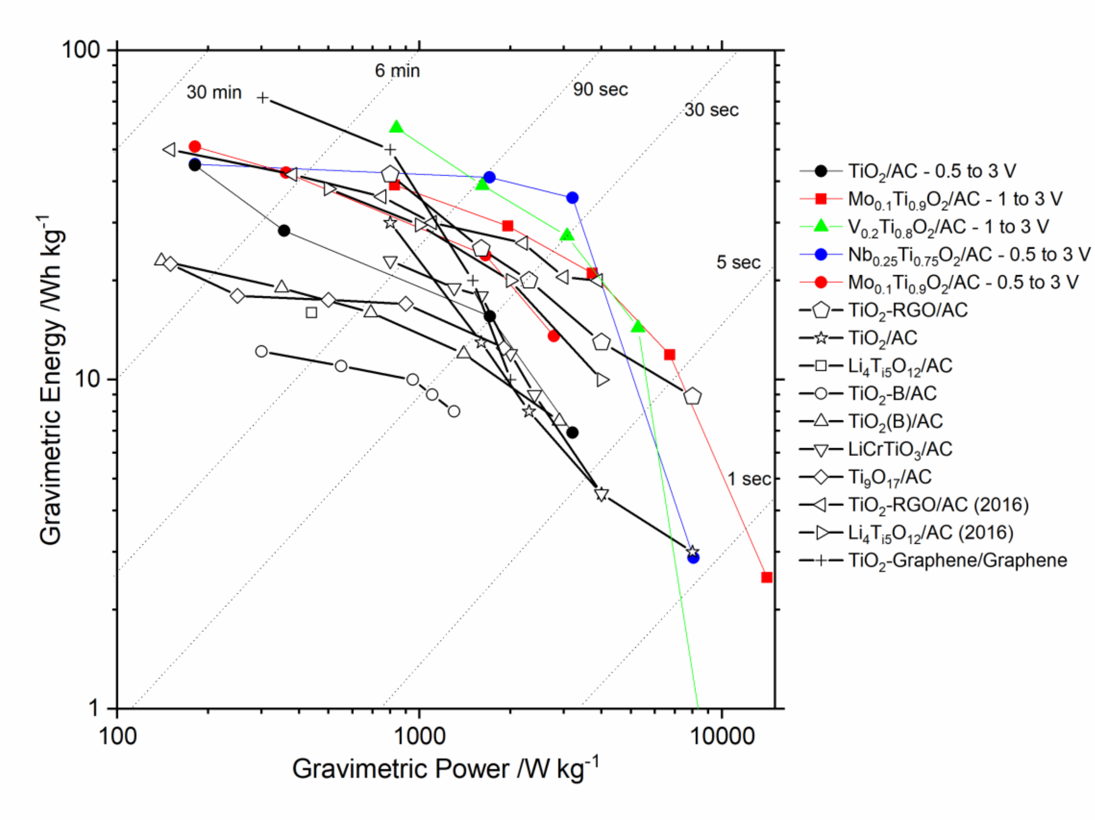

Figure 3-25: Ragone plot comparing the gravimetric power and energy densities for TiO_2/AC, $Mo_{0.1}Ti_{0.9}O_2$/AC, $V_{0.2}Ti_{0.8}O_2$/AC, and $Nb_{0.25}Ti_{0.75}O_2$/AC Li-HECs with similar devices reported in the literature. Literature examples used negative electrodes such as TiO_2-reduced graphene oxide and anatase TiO_2,[253] $Li_4Ti_5O_{12}$,[258] TiO_2-B,[259] TiO_2(B),[260] $LiCrTiO_4$,[261] Ti_9O_{17},[262] TiO_2-Reduced Graphene oxide (2016) and $Li_4Ti_5O_{12}$ (2016),[257] and TiO_2 microspheres wrapped with graphene nanosheets versus a graphene nanosheet positive electrode.[263]

densities of 55 and 14 Wh kg^{-1}, at power densities of 840 and 5280 W kg^{-1}, respectively.

Na-HECs of all anatase electrodes versus activated carbon positive electrodes were cycled in the potential windows 0.0 to 3.0 and 1.0 to 4.0 V, respectively. From galvanostatic cycling in Na-ion half cells, a specific capacity of ca. 100 mAh g^{-1} (at a specific current of 0.2 A g^{-1}) was assumed for the TiO_2 samples. For the AC electrodes, the specific capacitance was also determined from half-cell testing. The specific capacitance of ca. 60 F g^{-1} (at a specific current of 0.2 A g^{-1}) was calculated using the discharge time of 440 s in the potential window 4.0 to 2.5 V vs. Na/Na$^+$. Since the expected potential window of the AC cathode in the Na-HEC was ca. 1.5 V, this was used to calculate the mass ratio of active material in positive and negative electrode of ca. 1:4. At this mass ratio, the charge stored by each electrode was equal (see Figure 3-26).

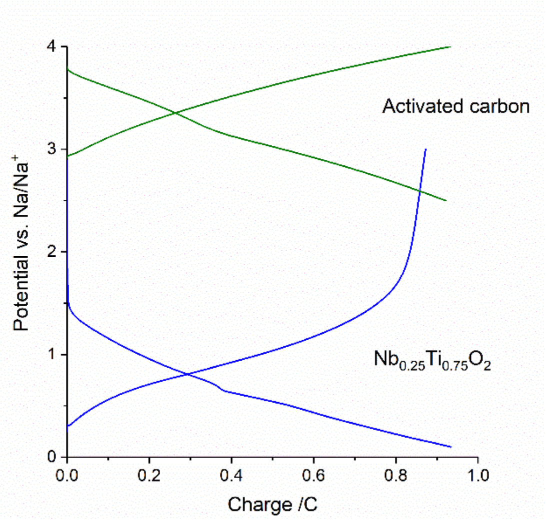

Figure 3-26: Charge stored by a $Nb_{0.25}Ti_{0.75}O_2$ electrode as well as an activated carbon (AC) electrode at a specific current of 0.2 A g^{-1}.

Galvanostatic charge/discharge cycling was carried out in the range of current densities 0.5 to 20 mA cm^{-2} (equivalent to specific currents in the range ca. 0.1 to 4.5 A g^{-1}, based on the mass of active material in both anode and cathode). Because of the lower sodiation and desodiation potentials vs. Na/Na$^+$ for TiO_2, compared to the lithiation and delithiation potentials vs. Li/Li$^+$, the Na-HECs could be cycled to potentials up to 4.0 V.[264] Cycling a Li-HEC to higher potentials could push the electrolyte above its stability window on the positive electrode/electrolyte interface. Cycling the Na-HECs to high potentials, however, could lead to sodium plating. On the other hand, cycling Na-HECs below 1.0 V was not expected to contribute significantly to charge storage, because the sodiation

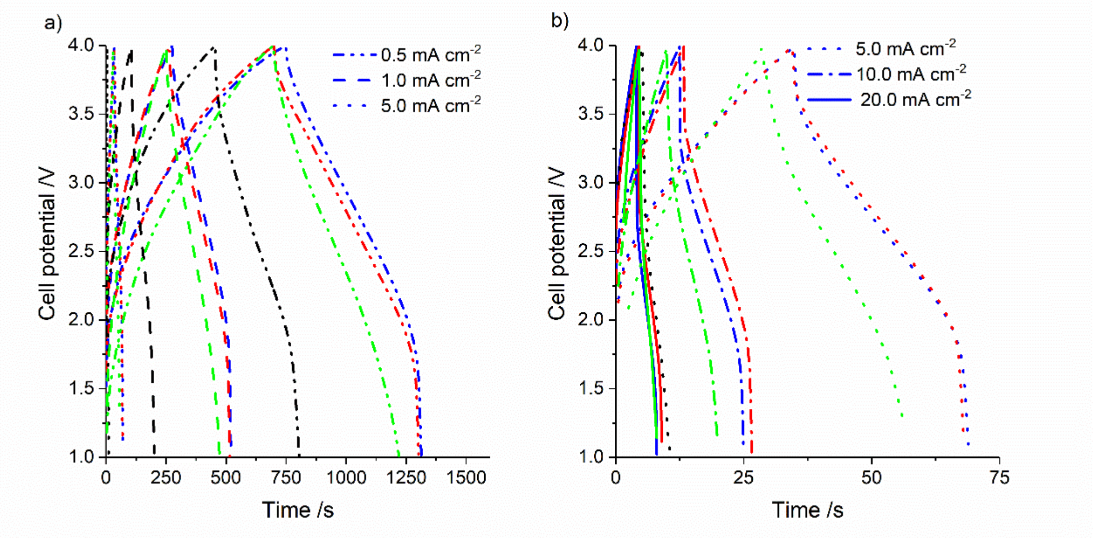

Figure 3-27: a) and b) Galvanostatic charge/discharge curves for TiO_2/AC, $Mo_{0.1}Ti_{0.9}O_2$/AC, $V_{0.2}Ti_{0.8}O_2$/AC, and $Nb_{0.25}Ti_{0.75}O_2$/AC Na-HECs in black, red, green, and blue, respectively, at various current densities.

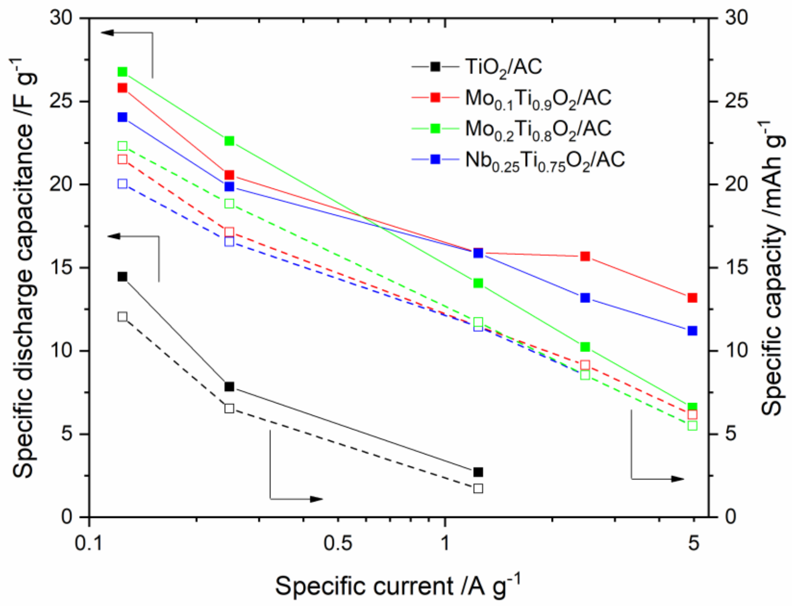

Figure 3-28: Specific capacitance (solid lines) and specific capacity (dashed lines) for TiO$_2$/AC, Mo$_{0.1}$Ti$_{0.9}$O$_2$/AC, V$_{0.2}$Ti$_{0.8}$O$_2$/AC, and Nb$_{0.25}$Ti$_{0.75}$O$_2$/AC Na-HECs at various applied specific currents.

activity of TiO$_2$ begins at ca. 1.5 V vs. Na/Na$^+$ (see above) and AC is active above ca. 2.5 V vs. Na/Na$^+$. This could explain the limited performance of Na-HECs cycled in this potential range which have previous been reported in literature.[265]

Galvanostatic charge/discharge measurements for all Na-HECs were carried out at current densities of 0.5, 1, 5, 10, and 20 mA cm^{-2} and plotted in Figure 3-27a and b. As for Li-HECs, the plots deviated from the triangular shape which would be expected for purely capacitive charge storage (such as EDLCs). This agreed with previous reports for similar Na-HECs.[265] The deviation can be attributed to fast Faradaic reaction of Na-ions with the active material in the negative electrode.[33,266] The combination of Faradaic and non-Faradaic charge storage mechanisms is apparent from this.[261,267] Like the expected reaction mechanism in Li-HECs, Faradaic reactions of Na$^+$ with TiO$_2$ and the adsorption of hexafluorophosphate anions onto the surface of the activated carbon are expected to occur during charging of the Na-HEC. During discharge, PF$_6^-$ desorbs back into the electrolyte and Na$^+$ is extracted from TiO$_2$.[80,81,268]

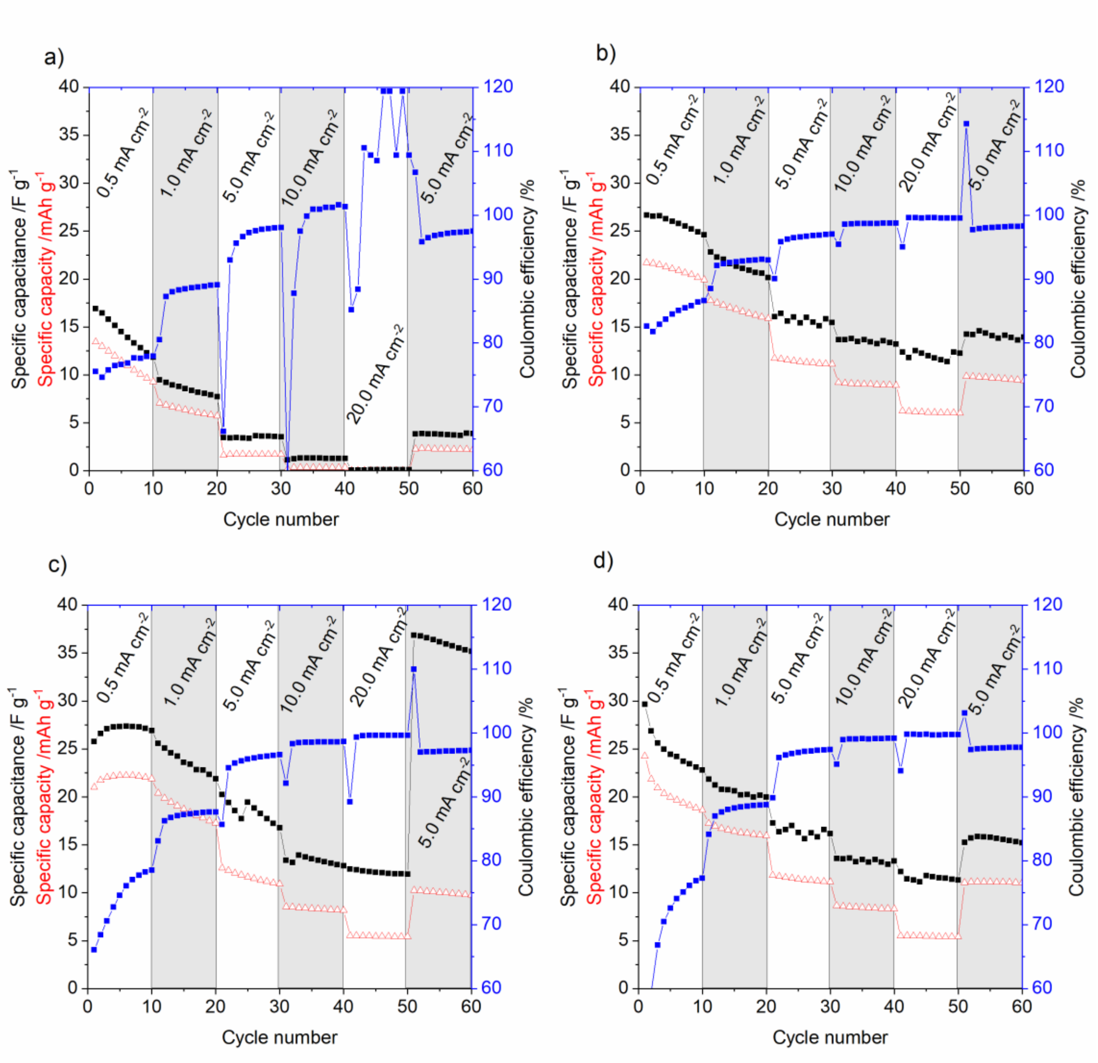

Figure 3-29: Galvanostatic charge/discharge performance of a) TiO_2/AC, b) $Mo_{0.1}Ti_{0.9}O_2$/AC, c) $V_{0.2}Ti_{0.8}O_2$/AC, and d) $Nb_{0.25}Ti_{0.75}O_2$/AC Na-HECs in the potential window 1 to 4 V.

The specific discharge capacitances and capacities at various specific current for the different Na-HECs were plotted in Figure 3-28. The $Nb_{0.25}Ti_{0.75}O_2$/AC Na-HEC showed specific capacitances of 24, 20, 16, 13, and 11 F g^{-1} (ca. 20, 17, 11, 9, and 6 mAh g^{-1}, respectively) at current densities of 0.5, 1, 5, 10, and 20 mA cm^{-2}, respectively. At the same current densities, the specific capacitance for the $Mo_{0.1}Ti_{0.9}O_2$/AC Na-HEC was 26, 21, 16, 15, and 13 F g^{-1} (22, 17, 11, 9, and 6 mAh g^{-1}), respectively. In contrast, the $V_{0.2}Ti_{0.8}O_2$/AC Na-HEC showed the highest specific capacitances and capacities at the lower specific current densities. At the same current densities as the other samples, the $V_{0.2}Ti_{0.8}O_2$/AC Na-HEC showed specific capacitances of 27, 23, 15, 10, and 7 F g^{-1} (23, 19, 11, 8, and 5 mAh g^{-1}), respectively. The TiO_2/AC Na-HEC showed relatively poor performance overall. Specific discharge

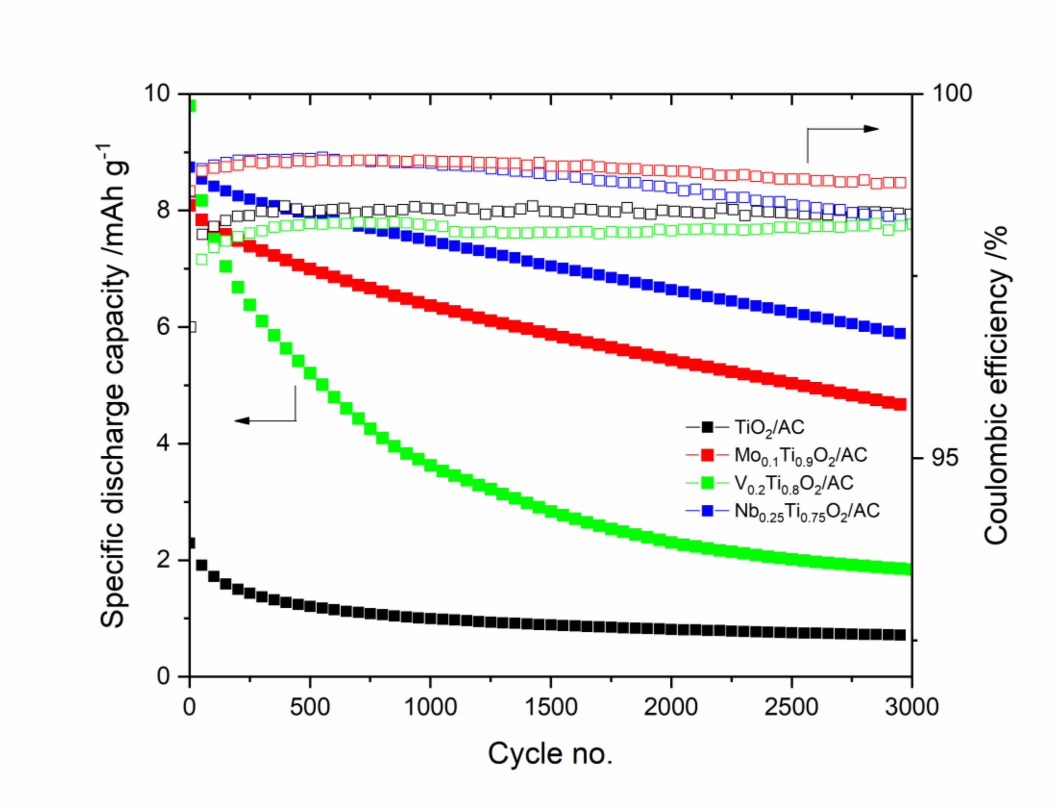

Figure 3-30: Long term cycling performance of the various Na-HECs at a current density of 5 mA cm^{-2}.

capacitances of only 14, 8, and 3 F g^{-1} (12, 7, and 2 mAh g^{-1}) were obtained at current densities of 0.5, 1, and 5 mA cm^{-2}, respectively, which were consistent with the poor charge storage properties observed from Na-ion half-cell measurements.

The cycling performance of all Na-HECs was plotted in Figure 3-29. All Na-HECs suffered from relatively low Coulombic efficiencies in initial cycles at low current densities (possibly due to irreversible processes associated with SEI formation). At higher current densities, Coulombic efficiencies approached 100 % for all samples. TiO_2/AC Na-HECs showed no remaining capacitance at a current density of 20 mA cm^{-2} (see Figure 3-29a), whereas all Na-HECs with doped TiO_2 negative electrode still showed significant capacitance at 20 mA cm^{-2} of above 10 F g^{-1} (see Figure 3-29b, c, and d, respectively).

The capacity retention for both $Mo_{0.1}Ti_{0.9}O_2$/AC and $Nb_{0.25}Ti_{0.75}O_2$/AC Na-HECs was ca. 75 % after 3000 cycles at a specific current density of 5 mA cm^{-2}, with high Coulombic efficiencies over 98 % (see Figure 3-30). The capacity retention

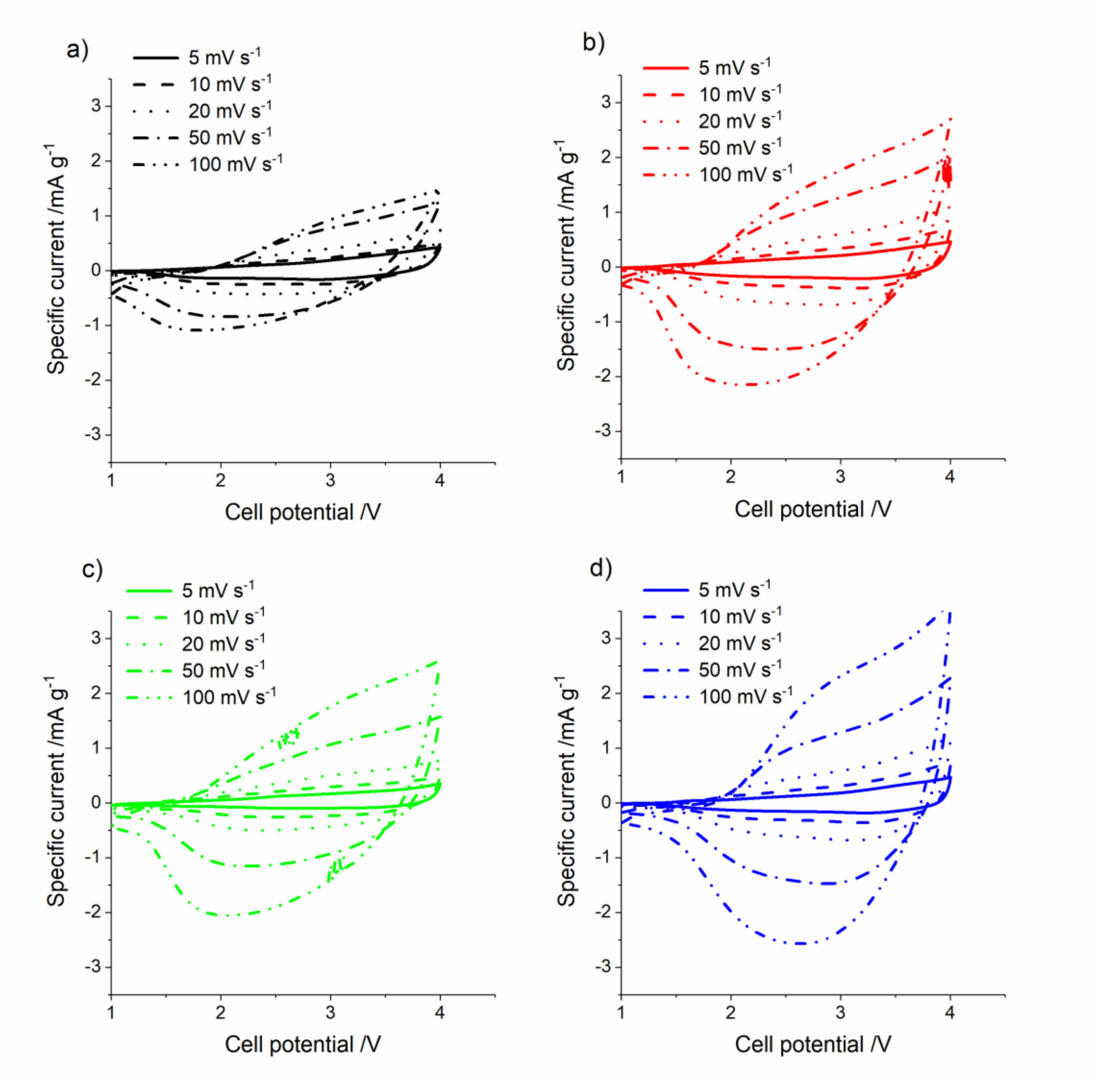

Figure 3-31: Cyclic voltammograms for a) TiO_2/AC, b) $Mo_{0.1}Ti_{0.9}O_2$/AC, c) $V_{0.2}Ti_{0.8}O_2$/AC, and d) $Nb_{0.25}Ti_{0.75}O_2$/AC Na-HECs at various scan rates.

was comparable to Na-HECs previously reported in the literature such as Na-titanate/AC,[33] N-doped TiO_2/AC,[264] or $NiCo_2O_4$/AC. [265] In comparison, both the TiO_2/AC and $V_{0.2}Ti_{0.8}O_2$/AC Na-HECs made herein showed significantly poorer capacity retention.

Cyclic voltammograms, especially for Na-HECs with doped TiO_2 electrodes, resembled the rectangular plots expected for capacitive charge storage (see Figure 3-31b, c, and d, for $Mo_{0.1}Ti_{0.9}O_2$/AC, $V_{0.2}Ti_{0.8}O_2$/AC, and $Nb_{0.25}Ti_{0.75}O_2$/AC Na-HECs, respectively). At high scan rates, peaks deviating from the expected rectangular cyclic voltammograms became more distinctive, as previously reported for similar devices.[253–256] This could indicate that the mass balance between anode and cathode was imperfect at higher scan rates. As for Li-HECs, cyclic voltammograms of Na-HECs were used to calculate their specific capacitance at different scan rates using Equation 3.5.

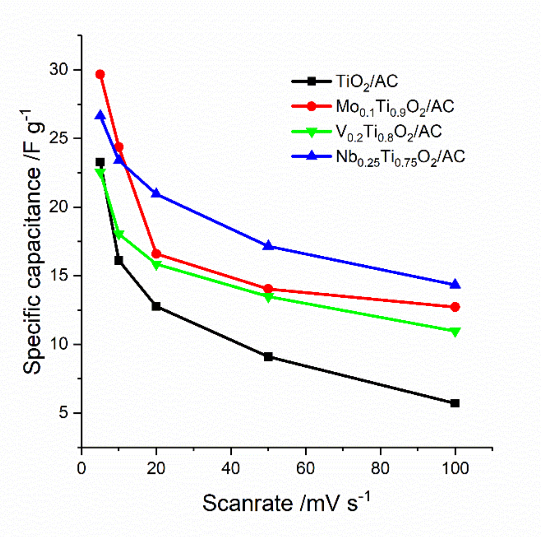

Figure 3-32: Specific capacitances calculated for the different Na-HECs at different scan rates cycled in the potential window 1 to 4 V.

The calculated specific capacitances were in good agreement with those from galvanostatic measurements. $Mo_{0.1}Ti_{0.9}O_2$/AC Na-HECs showed the highest specific capacitance of 30 F g^{-1} at 5 mV s^{-1}, compared to 23, 27 and 23 F g^{-1} for $Nb_{0.25}Ti_{0.75}O_2$/AC, $V_{0.2}Ti_{0.8}O_2$/AC, and TiO_2/AC Na-HECs, respectively. The Na-HECs using doped titania negative electrodes also showed much better capacitance retention at 100 mV s^{-1}, with capacitances of 13, 12, and 14 F g^{-1}, compared to 6 F g^{-1}, for $Mo_{0.1}Ti_{0.9}O_2$/AC, $V_{0.2}Ti_{0.8}O_2$/AC, $Nb_{0.25}Ti_{0.75}O_2$/AC, and TiO_2/AC Na-HECs, respectively (see Figure 3-32).

Gravimetric energy and power densities were calculated using Equations 1.36 and 1.37. They were plotted in a Ragone plot alongside similar devices reported in the literature (see Figure 3-33). The energy and power densities for devices reported in the literature such as $NiCoO_2$/AC,[265] AC/Na-titanate,[33] AC/AC,[33] $Na_4Mn_9O_{18}$/AC,[266] V_2O_5/CNT-AC,[80] Nb_2O_5@C/AC,[269] Na-TNT/graphite,[270] Na-TNT/AC,[270] and $Na_2Ti_2O_4(OH)_2$/Porous carbon[271] Na-HECs, plotted alongside the $Mo_{0.1}Ti_{0.9}O_2$/AC, $V_{0.2}Ti_{0.8}O_2$/AC, and $Nb_{0.25}Ti_{0.75}O_2$/AC Na-HECs, demonstrated the excellent performance of the Na-HECs presented herein compared to similar devices.

The $Mo_{0.1}Ti_{0.9}O_2$/AC Na-HEC delivered the highest observed energy density of 60 Wh kg^{-1} at a power density of 350 W kg^{-1}. It also retained energy density the best, exhibiting 31 and 13 Wh kg^{-1} at power densities of 3360 and 10650 W kg^{-1}, respectively. The $V_{0.2}Ti_{0.8}O_2$/AC Na-HEC showed energy densities of 56 and 20

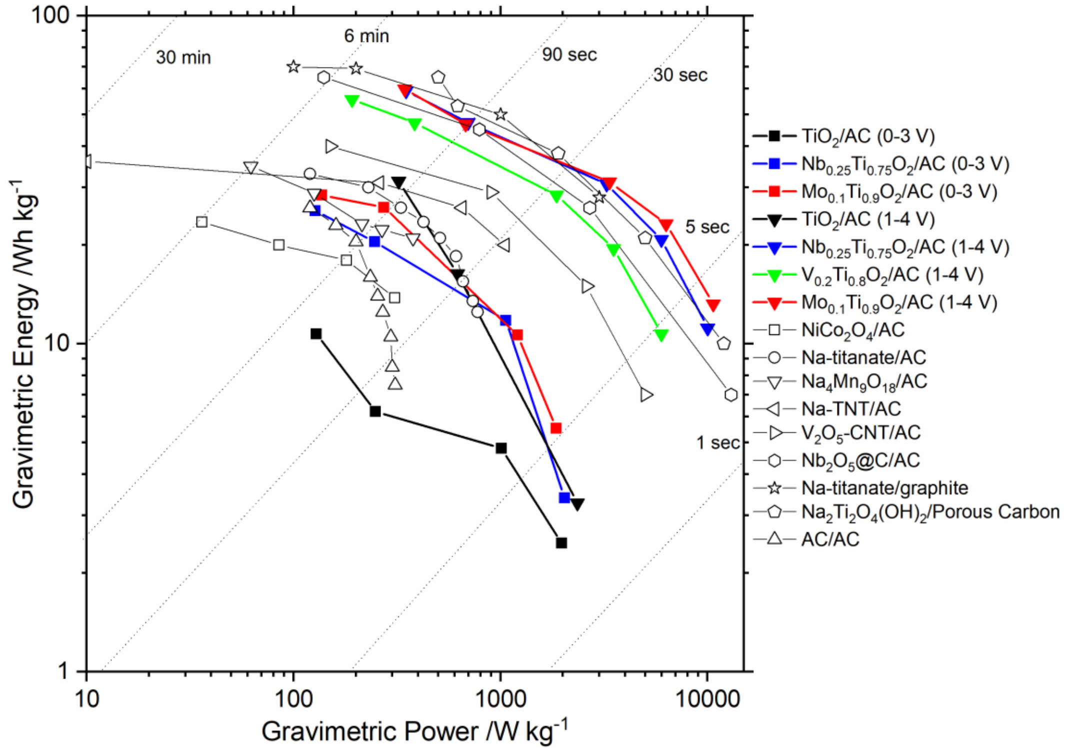

Figure 3-33: Ragone plot comparing the gravimetric power and energy of the TiO_2/AC, $Mo_{0.1}Ti_{0.9}O_2$/AC, $V_{0.2}Ti_{0.8}O_2$/AC, and $Nb_{0.25}Ti_{0.75}O_2$/AC Na-HECs with similar devices from the literature such as $NiCoO_2$/AC,[265] AC/Na-titanate,[33] AC/AC,[33] $Na_4Mn_9O_{18}$/AC,[266] V_2O_5/CNT-AC,[80] Nb_2O_5@C/AC,[269] Na-TNT/graphite,[270] Na-TNT/AC,[270] and $Na_2Ti_2O_4(OH)_2$/Porous carbon[271] Na-ion (hybrid) capacitors.

Wh kg^{-1} at power densities of 190 and 3515 W kg^{-1}, respectively. The $Nb_{0.25}Ti_{0.75}O_2$/AC Na-HEC performed equally well as the $Mo_{0.1}Ti_{0.9}O_2$/AC Na-HEC, showing an energy density of 21 Wh kg^{-1} at a power density of 6000 W kg^{-1}. The TiO_2/AC Na-HEC showed significantly poorer performance, with energy densities of 31 and 3 Wh kg^{-1} at moderate power densities of 322 and 2350 W kg^{-1}, respectively.

3.4.2.3. Electrochemical Performance of HECs after Pre-lithiation/sodiation

As discussed in Section 1.3.2.3, the charge storage mechanism of an activated carbon positive electrode in Li/Na-HECs is the non-Faradaic formation of a Helmholtz double layer, which is comprised of hexafluorophosphate anions on the positive electrode's surface (see Figure 3-34a). PF_6^- adsorption occurs upon charging and desorption upon discharging. Both processes occur above the zero-charge potential (E_0).

If there is an additional source of cations (Li^+/Na^+) in the system, the active potential window of the activated carbon positive electrode can be extended to below E_0 (see Figure 3-34b). In this case, upon charging, Li^+/Na^+ is first desorbed from the activated carbon positive electrode (below E_0), after which PF_6^- is adsorbed onto the activated carbon positive electrode (above E_0). On discharging, hexafluorophosphate anions are desorbed first, after which Li^+ is adsorbed onto the positive electrode.[272,273]

Usually, an electrochemical pre-lithiation/sodiation of the negative electrode is used to provide the additional cation source. Because this step is time-consuming and costly, there has been some research directed at eliminating the necessity for pre-lithiation, via the addition of a sacrificial lithium source material. For example,

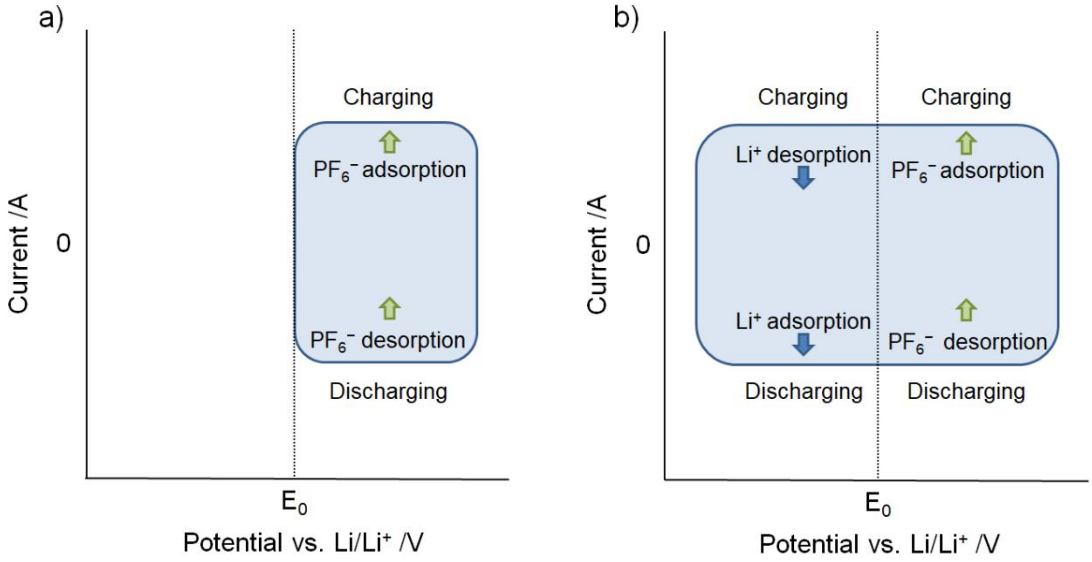

Figure 3-34: Diagram showing a cyclic voltammogram for the activated carbon positive electrode in a Li-HEC showing the charge storage mechanism a) without and b) with an additional Li^+ source.

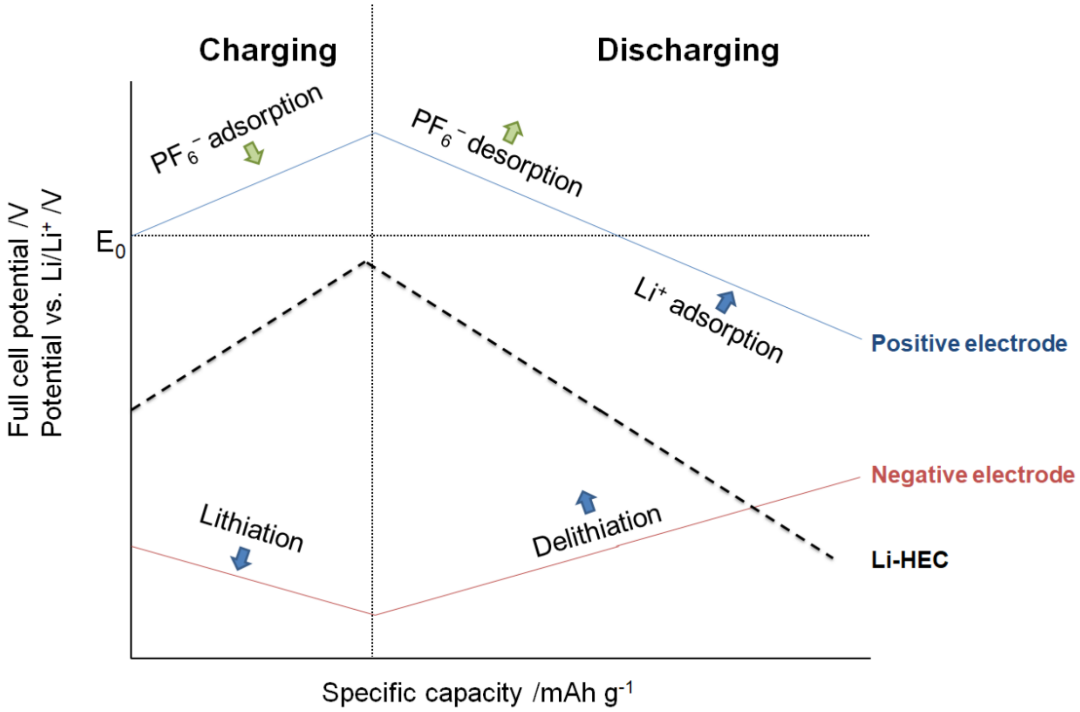

Figure 3-35: First galvanostatic charge and discharge curves for a Li-HEC and the individual positive and negative electrodes.

Li_2CuO_2 was added to the activated carbon positive electrode in a $Li_4Ti_5O_{12}$/AC Li-HEC. Upon cycling, Li_2CuO_2 released lithium ions and converted into electrochemically (mostly) inactive but highly electronically conductive CuO.[272]

Upon the first charge, the pre-lithiated negative electrode in a Li-HEC will be further lithiated, whereas the activated carbon positive electrode adsorbs hexafluorophosphate anions (see Figure 3-35). Upon the first discharge, hexafluorophosphate anion desorption and lithium ion adsorption both occur on the activated carbon positive electrode. Delithiation occurs on the negative electrode. Both the lithium ions from pre-lithiation and those from the lithiation during the first charge are delithiated from the negative electrode. During continued cycling, on the positive electrode, Li-ion desorption and hexafluorophosphate adsorption take place upon charging; hexafluorophosphate desorption and Li-ion adsorption occur during discharge.

For a $Mo_{0.1}Ti_{0.9}O_2$/AC Li-HEC, with a pre-lithiated $Mo_{0.1}Ti_{0.9}O_2$ negative electrode lithiated to ca. 50 % capacity, the shape of the cyclic voltammogram changed significantly, compared to a non-pre-lithiated Li-HEC (see Figure 3-36). At a scan rate

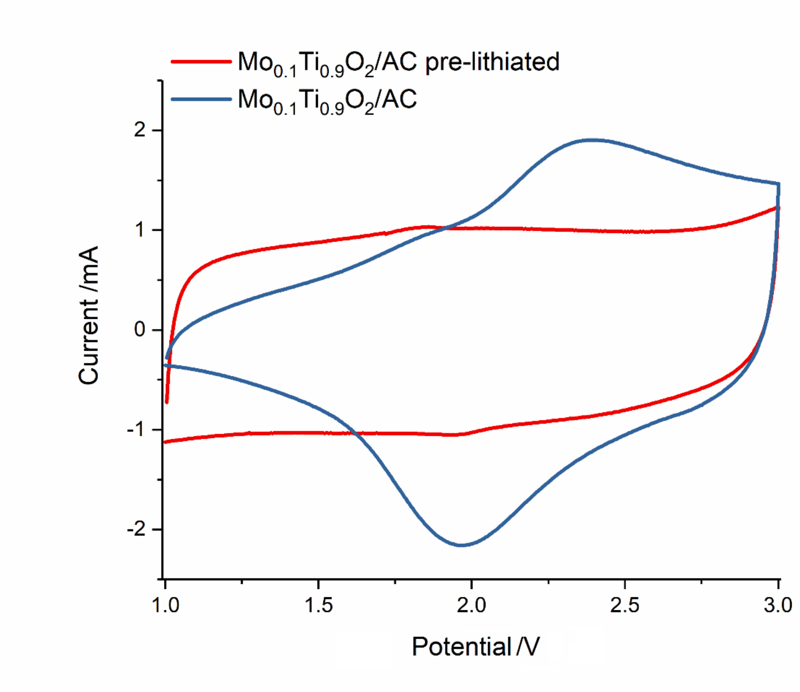

Figure 3-36: Cyclic voltammograms of pre-lithiated and non-pre-lithiated $Mo_{0.1}Ti_{0.9}O_2$/AC Li-HECs.

of 5 mV s^{-1}, the $Mo_{0.1}Ti_{0.9}O_2$/AC Li-HEC without pre-lithiation showed significant redox peaks, indicative of suboptimal capacitive behaviour. This was because the charge storage mostly occurred above 2 V, because only PF_6^- adsorption and desorption occurred upon cycling. For the pre-lithiated $Mo_{0.1}Ti_{0.9}O_2$/AC Li-HEC, the cyclic voltammogram showed exclusively capacitive behaviour, because both PF_6^- and Li^+ adsorption and desorption occurred on the positive electrode.

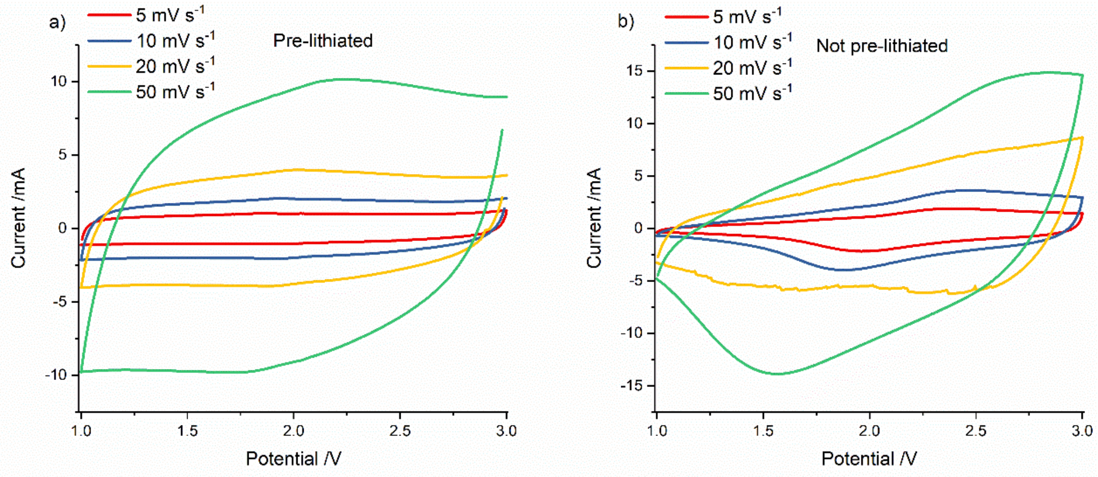

Figure 3-37: Cyclic voltammograms at various scan rates for a) a pre-lithiated and b) a non-pre-lithiated $Mo_{0.1}Ti_{0.9}O_2$/AC Li-HEC.

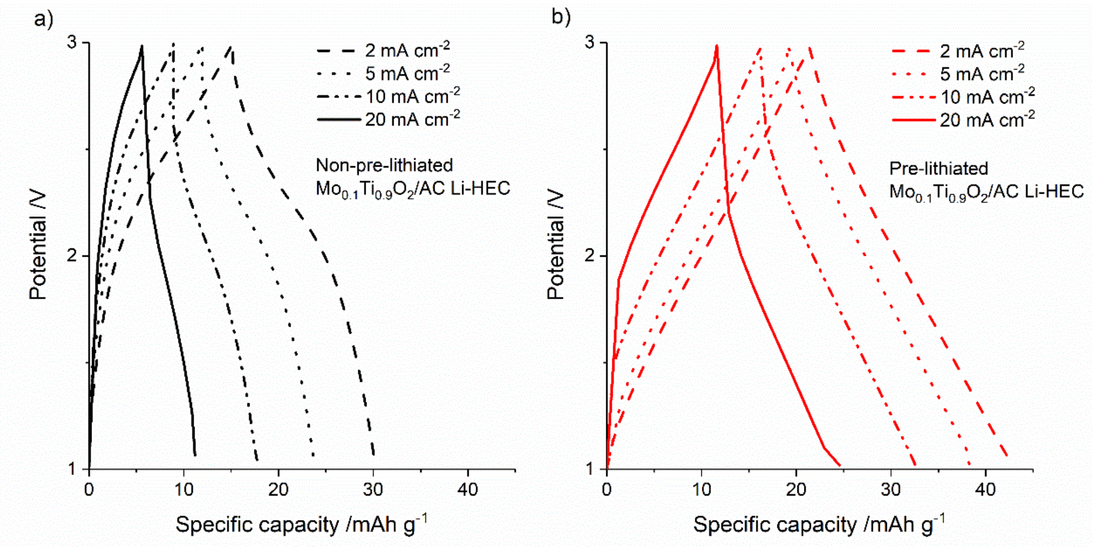

Figure 3-38: Galvanostatic charge/discharge curves for a) a non-pre-lithiated and b) a pre-lithiated $Mo_{0.1}Ti_{0.9}O_2$/AC Li-HEC.

The same was true for the cyclic voltammograms of the Li-HECs at higher scan rates (see Figure 3-37). The shape of the voltammogram at 50 mV s^{-1} for the non-pre-lithiated $Mo_{0.1}Ti_{0.9}O_2$/AC Li-HEC was distorted, with significantly separated peaks upon charge/discharge. The cyclic voltammogram for the pre-lithiated $Mo_{0.1}Ti_{0.9}O_2$/AC Li-HEC still showed nearly ideal capacitive charge storage, indicated by a rectangular plot.

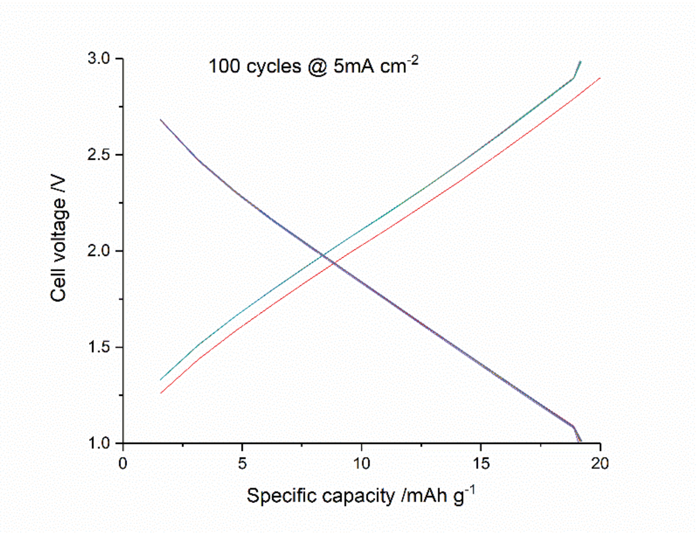

Figure 3-39: $Mo_{0.1}Ti_{0.9}O_2$/AC Li-HEC cycled for one hundred galvanostatic charge/discharge cycles at a current density of 5 mA cm^{-2}, equivalent to ca. 1.2 A g^{-1}.

The near-perfect capacitive charge storage behaviour of the pre-lithiated $Mo_{0.1}Ti_{0.9}O_2$/AC Li-HEC was also observed from the triangular galvanostatic charge/discharge plots. Whereas a non-pre-lithiated $Mo_{0.1}Ti_{0.9}O_2$/AC Li-HEC mostly released charge in the range 3.0 to 2.0 V upon discharge (see Figure 3-38a) at all current densities (2, 5, 10, and 20 mA cm^{-2}), for the

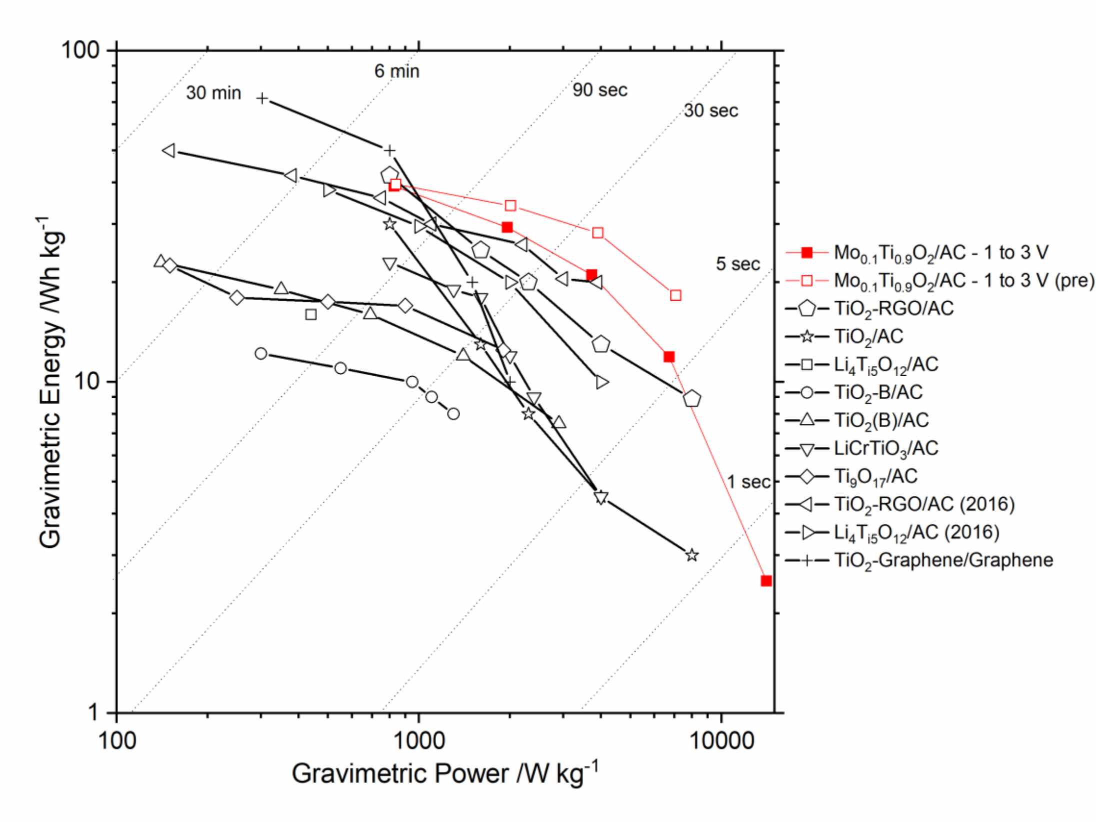

Figure 3-40: Ragone plot showing the non-pre-lithiated and pre-lithiated $Mo_{0.1}Ti_{0.9}O_2$/AC Li-HECs compared to a range of devices previously reported in the literature.

pre-lithiated $Mo_{0.1}Ti_{0.9}O_2$/AC Li-HEC, the discharge occurred throughout the entire potential window 3.0 to 1.0 V (see Figure 3-38b). This was in line with the observations discussed above. One hundred charge/discharge curves for the pre-lithiated Li-HEC were all nearly identical (except for the first charge cycle), showing significantly improved stability compared to a non-pre-lithiated $Mo_{0.1}Ti_{0.9}O_2$/AC Li-HEC (see Figure 3-39).

The gravimetric energy and power densities for both the pre-lithiated and non-pre-lithiated Li-HECs were calculated (using Equations 1.36 and 1.37) and plotted in a Ragone plot with the same Li-HEC devices reported in the literature as in Section 3.4.2.2 (see Figure 3-40). The performance was improved by pre-lithiation, especially at higher power densities. At 3.9 and 7.1 kW kg^{-1}, the pre-lithiated $Mo_{0.1}Ti_{0.9}O_2$/AC Li-HEC showed energy densities of 28 and 18 Wh kg^{-1}, respectively, whereas the non-pre-lithiated $Mo_{0.1}Ti_{0.9}O_2$/AC Li-HEC showed energy densities of 21 and 11 Wh kg^{-1} at comparable power densities (3.6 and 6.5 W kg^{-1}, respectively).

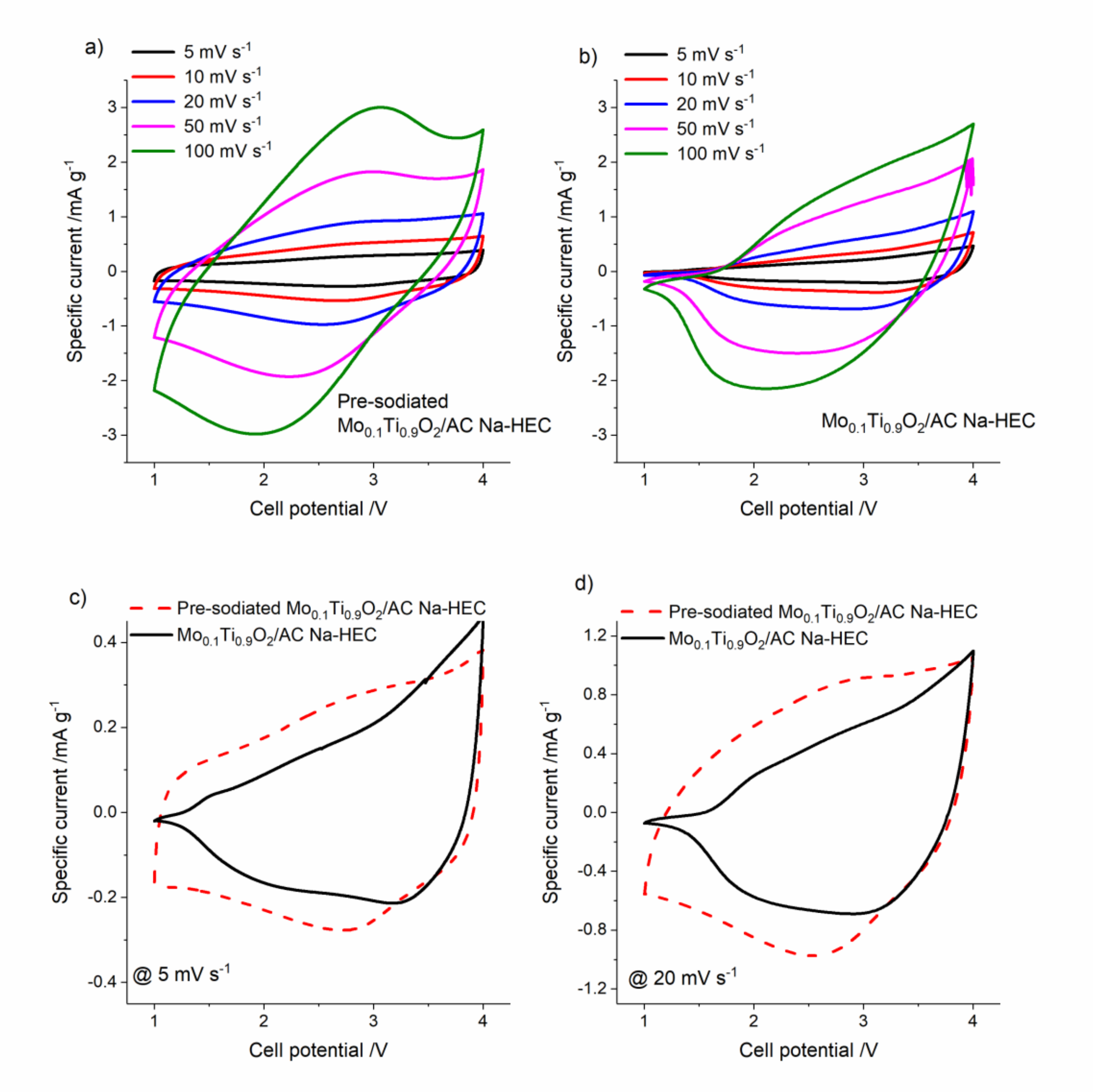

Figure 3-41: Cyclic voltammograms at various scan rates for a) a pre-sodiated and b) a non-pre-sodiated $Mo_{0.1}Ti_{0.9}O_2$/AC Na-HEC. Comparison of a pre-sodiated and a non-pre-sodiated $Mo_{0.1}Ti_{0.9}O_2$/AC Na-HEC at scan rates of c) 5 and d) 20 mV s^{-1}.

Whilst pre-lithiation in TiO_2/AC Li-HECs widens the active potential window of the positive electrode, there is no active cation loss due to SEI formation or irreversible side reaction to compensate for. For LIBs and NIBs with anodes that require the formation of SEI, conversion/alloying anodes, and Na-HECs with significant first cycle losses, pre-lithiation/sodiation can compensate for active cation losses. Various techniques have been used for pre-lithiation/sodiation, including electrochemical addition, chemical addition, via additives, and via direct contact with the metal.[274]

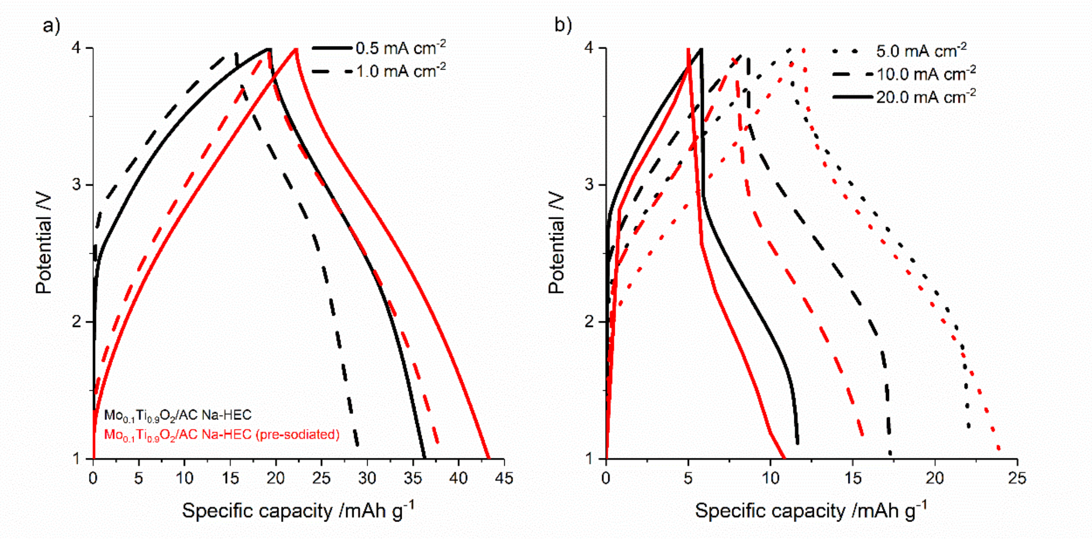

Figure 3-42: Galvanostatic charge/discharge cycling densities for a pre-sodiated and a non-pre-sodiated $Mo_{0.1}Ti_{0.9}O_2$/AC Na-HEC at current densities of a) 0.5 and 1.0 mA cm^{-2} and b) 5.0, 10.0, and 20 mA cm^{-2}.

A $Mo_{0.1}Ti_{0.9}O_2$/AC Na-HEC was constructed using a $Mo_{0.1}Ti_{0.9}O_2$ negative electrode which had been cycled for a full cycle in a half-cell in the potential range 3.0 to 0.1 V vs. Na/Na$^+$. After the first cycle, the electrode was sodiated to ca. 50 % capacity. This led to a significant change in the shape of the voltammograms compared to the non-pre-sodiated $Mo_{0.1}Ti_{0.9}O_2$/AC Na-HEC. For all scan rates (5, 10, 20, 50, and 100 mV s^{-1}), the voltammograms for the pre-sodiated $Mo_{0.1}Ti_{0.9}O_2$/AC Na-HEC broadened significantly (see Figure 3-41a) compared to a non-pre-sodiated $Mo_{0.1}Ti_{0.9}O_2$/AC Na-HEC (see Figure 3-41b). At a scan rate of 5 mV s^{-1}, the cyclic voltammogram of the pre-sodiated $Mo_{0.1}Ti_{0.9}O_2$/AC Na-HEC was nearly rectangular, indicating capacitive charge storage (see Figure 3-41c). Compared to the non-pre-sodiated $Mo_{0.1}Ti_{0.9}O_2$/AC Na-HEC, charge and discharge occurred below ca. 2.5 V. This was a result of Na$^+$ adsorption onto the activated carbon positive electrode during discharge, and Na$^+$ desorption upon charging. Above ca. 2.5 V, PF_6^- adsorption occurred during charging, and desorption during discharging, in both the pre-sodiated and non-pre-sodiated $Mo_{0.1}Ti_{0.9}O_2$/AC Na-HEC. This was analogous to the mechanisms previously discussed for pre-lithiated and non-pre-lithiated Li-HECs. At a scan rate of 20 mV s^{-1}, the shape of the cyclic voltammograms of the pre-sodiated $Mo_{0.1}Ti_{0.9}O_2$/AC Na-HEC deviated slightly from the rectangular shape expected for

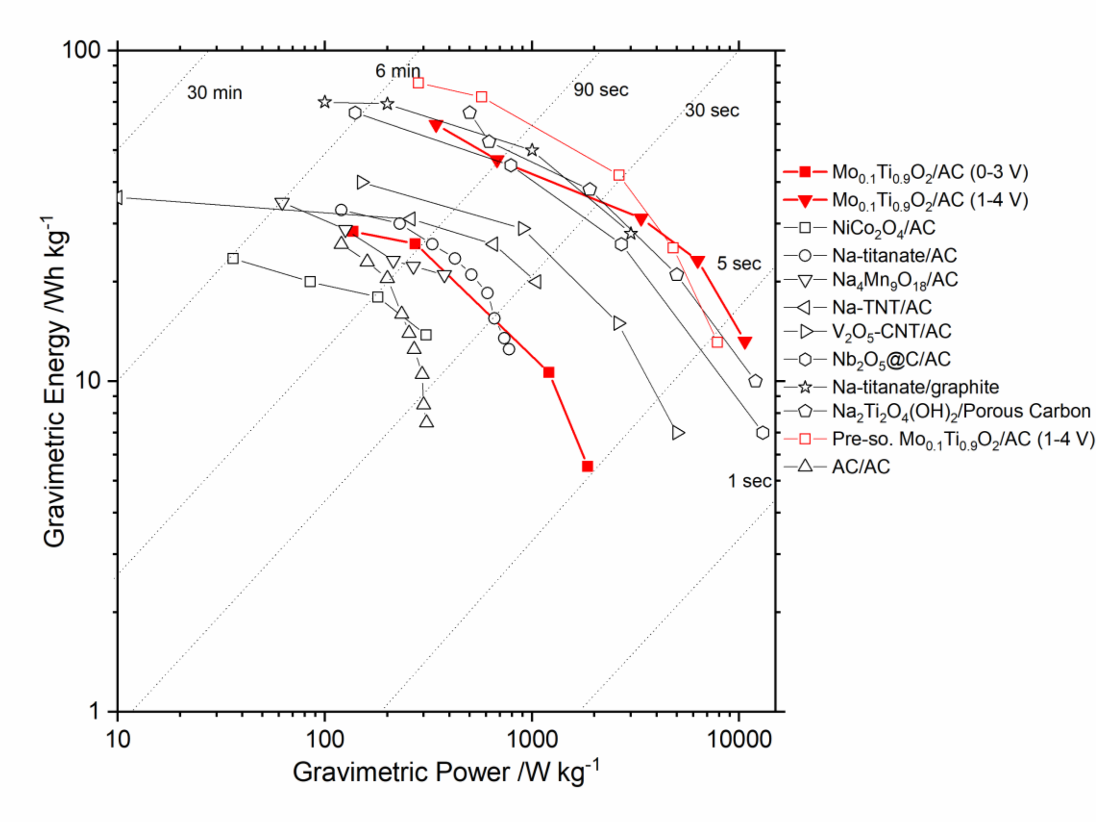

Figure 3-43: Ragone plot showing a non-pre-sodiated and a pre-sodiated $Mo_{0.1}Ti_{0.9}O_2$/AC Na-HECs compared to a range of devices previously reported in the literature.

capacitive behaviour but was still significantly more rectangular than the CV for the non-pre-sodiated Na-HEC.

The charge and discharge below 2.5 V for the pre-sodiated $Mo_{0.1}Ti_{0.9}O_2$/AC Na-HEC could also be observed from the galvanostatic charge/discharge profiles. Especially at the lower current densities (0.5 and 1.0 mA cm^{-2}), this resulted in higher specific capacities and more triangular galvanostatic charge/discharge profile (see Figure 3-42a). Whilst the profile at higher current densities (10.0 and 20.0 mA cm^{-2}) was still more triangular for the pre-sodiated Na-HEC (see Figure 3-42b), the overall capacity was slightly lower than for the non-pre-sodiated $Mo_{0.1}Ti_{0.9}O_2$/AC Na-HEC. This was partly due to the larger Ohmic (IR) drop of the pre-sodiated Na-HEC.

Both gravimetric energy and power densities were calculated for the pre-sodiated $Mo_{0.1}Ti_{0.9}O_2$/AC Na-HEC (using Equations 1.36 and 1.37) and compared to the non-pre-sodiated $Mo_{0.1}Ti_{0.9}O_2$/AC Na-HEC in a Ragone plot, along with the same Na-HEC devices reported in the literature as in Section 3.4.2.2 (see Figure 3-43). At intermediate power densities, the specific energy densities for the pre-sodiated $Mo_{0.1}Ti_{0.9}O_2$/AC Na-HEC were significantly higher than for the non-pre-sodiated $Mo_{0.1}Ti_{0.9}O_2$/AC Na-HEC. The pre-sodiated $Mo_{0.1}Ti_{0.9}O_2$/AC Na-HEC showed energy densities of 80, 73, and 42 Wh kg^{-1}, at power densities of 280, 570, and 2630 W kg^{-1}, respectively. At comparable power densities (340, 680, and 3360 W kg^{-1}), the non-pre-sodiated $Mo_{0.1}Ti_{0.9}O_2$/AC Na-HEC showed specific energy densities of 60, 47, and 31 Wh kg^{-1}.

3.5. Conclusions

The results showed that doping can have tremendously beneficial effects on the electrochemical properties of TiO_2 as active material for negative electrodes in Li-ion and Na-ion based systems. Whilst the nanosizing of all studied materials played a role in the good high-power performance of the samples, the materials doped with Nb(V) and Mo(VI) had a similar specific surface area as undoped TiO_2, whereas the sample doped with V(V) had a higher surface area. The doped samples all showed lower charge transfer resistance and a higher proportion of charge stored via pseudocapacitive processes. Specific surface area was not the decisive factor for the preferred charge storage mechanism. A “solid-solution host” type behaviour was observed for the surfaces of the materials in both Li-ion and Na-ion half-cells and was significantly more pronounced for the doped samples. It can be assumed that doping with transition metal ions of higher valence than the Ti(IV) ion improved “solid-solution host” behaviour. This could partly be associated with the creation of Ti(IV) vacancies. Because of the excellent performance of the doped samples in both Li-ion and Na-ion half-cells, it was expected that hybrid electrochemical capacitors made using electrodes of these samples as negative and activated carbon positive electrodes would show good performance at high power densities.

The energy densities at high power densities of the Na-HECs showed promise due to the high contributions of fast, pseudocapacitive charge storage and the large potential window. Pre-lithiation/sodiation was shown to significantly improve energy and power densities of the Li/Na-HECs, by increasing the active potential window of the positive electrodes. However, neither the optimum dopant amount, nor potential mixed doping with two or even three dopants was explored so far and will be the subject of a compositional study in Chapter 4.

The research presented herein opens a host of questions for potential further research. Computational analysis of heterometallic dopants in anatase TiO_2 has shown that Ti(IV) vacancies can host the intercalation of multi-valent ions such as Mg(II) and Al(III). Experimental exploration of these metal-ion chemistries would be rewarding. Furthermore, improvements of the performance of Li/Na-HECs could be achieved either by using cathodes with higher specific capacitance or by improving the conductivity of anodes to improve performance at very high power. Additionally, developing novel pre-lithiation methods, for example by introducing a sacrificial Li-ion source to the anode or cathode mixture, to dispense with the pre-lithiation step would be important for potential commercialisation. Finally, binder-free and additive-free electrode manufacturing, which has recently been explored for titanium carbide (MXene) in Na-HECs,[275] offers interesting opportunities for improved manufacturing.

4. High-throughput Combinatorial Study of High Power Mo-, V-, and Nb-(co-)doped Anatase TiO_2 Anodes

4.1. Aims

Doping anatase TiO_2 with Mo(VI), V(V), or Nb(V) can improve its high-power performance as anode active material in LIBs, as shown in Chapter 3 above. CHFS offers a unique method to quickly synthesise a wide range of doped samples with similar physical properties. A range of 35 (co-)doped anatase samples were synthesised within ca. 5 hours in CHFS and then analysed via XRD, BET, XPS, and Raman spectroscopy. Potential synergetic (and antagonistic) effects of different dopant combinations were investigated by studying the electrochemical performance of the powders as active materials for negative electrodes in LIB half-cells.

4.2. Introduction

As has been discussed in Chapter 3, anatase TiO_2 is a promising material for anodes in LIBs and NIBs, because it is a stable active material that performs well at high power and because titanium is abundant and inexpensive. Heterometallic doping with higher valence state cations can improve electronic conductivity and electrochemical charge storage performance.

The potential synergistic effects of co-doping anatase TiO_2 have been explored for various applications. C/N co-doping and Fe/Co co-doping have been explored for photocatalytic applications,[276,277] whilst N/La co-doping of TiO_2 was explored in dye-sensitized solar cells.[278] Fe/S co-doped anatase nanotubes have been explored as lithium-ion battery anodes, showing markedly improved cycling stabilities and rate performance compared to undoped anatase nanotubes due to increased electronic conductivity and lithium ion diffusion coefficients.[279]

Because of the speed and versatility of CHFS, it can be used to produce a library of doped materials with consistent properties.[280–282] Thus, to further probe the best dopants for TiO_2 in LIBs, in this chapter, CHFS was used to synthesise a range of 35 samples, with combined doping concentrations of Mo(VI), V(V), and Nb(V) up to 15 at.%. The samples were prepared within a single day and trends in properties were investigated using single dopants as well as samples with two or all three dopants.

4.3. Materials & Methods

4.3.1. Synthesis of Mo-, V-, and Nb-(co)doped Anatase TiO_2

The synthesis of the materials was carried out as described in Section 2.1.2.

4.3.2. Physical Characterisation of Mo-, V-, and Nb-(co)doped Anatase TiO_2

The physical characterisation of the materials was carried out according to the methods described in Section 2.2. Because of the large number of samples, quick screening was required, hence, only PXRD, XPS, BET, and Raman spectroscopy were employed.

4.3.3. Electrochemical Characterisation of Mo-, V-, and Nb-(co)doped Anatase TiO_2

The electrodes were prepared, and Li-ion half-cells assembled, as described in Section 2.3. The electrochemical characterisation was carried out according to the methods described in Section 1.4.5.

4.3.3.1. Electrochemical Characterisation in Li-ion Half-cells

All electrochemical testing was carried out in CR2032 Li-ion half-cells, with electrodes cast on copper foil. All tests were carried out in the potential range 1.0 to 3.0 V vs. Li/Li^+. Galvanostatic measurements were carried out in the range of specific currents 0.1 to 15.0 A g^{-1}.

4.4. Results and Discussion

4.4.1. Physical Characterisation of Mo-, V-, and Nb-(co)doped Anatase TiO_2

PXRD was carried out for all samples. All patterns were in good agreement with the peaks for ICSD reference pattern no. 09852 (space group I*41/a*, see Appendix, Figure A1) for anatase TiO_2. None of the patterns revealed peaks of any possible impurity phases such as molybdenum, vanadium, or niobium oxides. Shifts in peak positions upon doping could be observed for the doped and co-doped samples (see

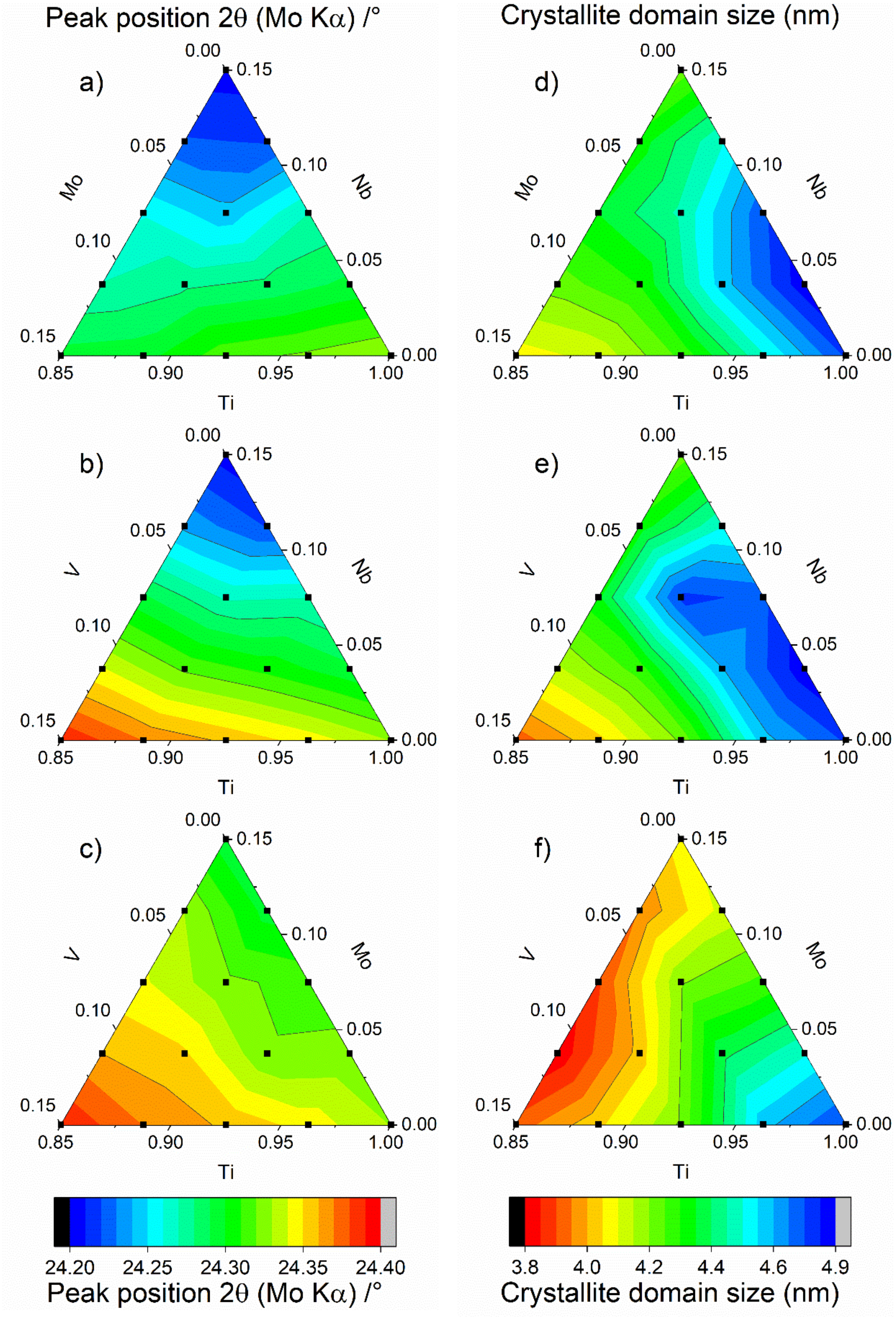

Figure 4-1: Ternary plots of the (211) peak positions for a) Mo/Nb, b) Nb/V, and c) Mo/V (co-)doped TiO_2 samples. Ternary plots of the crystallite domain size (calculated using the Scherrer equation) for d) Mo/Nb, e) Nb/V, and f) Mo/V (co-)doped TiO_2 samples.

Figure 4-1a to c), which could potentially be explained by changes in lattice parameters due to the doping of TiO_2 with Mo(VI), Nb(V), and V(V). For the (211) peak, shifts to lower 2θ values occurred when doped with Mo(VI) or Nb(V). The shifts for the samples doped with Nb(V) were more pronounced than for the samples doped with Mo(VI). The shifts to lower values of 2θ were expected to be due to lattice expansion, which was a result of the larger ionic radii of the dopant cations compared to the Ti(IV) they replace in the crystal lattice, as described in Chapter 3.[231,232] For samples doped with V(V), the (211) peak shifted to higher 2θ values, which was associated with lattice contraction due to the smaller ionic radius of V(V) compared to the Ti(IV) ions it replaced in the lattice (see Figure 4-1b and c). Similar observations were made for the (101) and (020) peaks (see Appendix). The crystallite domain sizes were estimated using the Scherrer equation (see Equation 2.2). The highest domain sizes were calculated for undoped TiO_2 and samples with low concentrations of Nb(V) doping (see Figure 4-1d to f). The largest observed crystallite sizes were ca. 4.9 nm, whereas the smallest crystallite sizes of ca. 3.8 nm were observed for

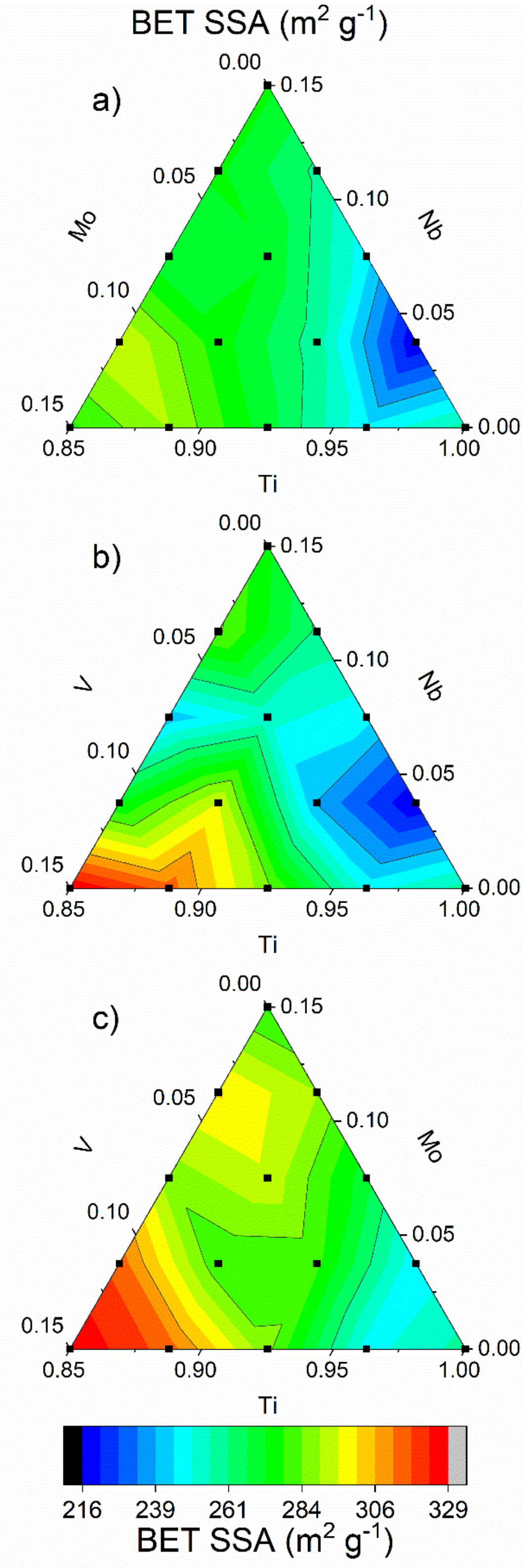

Figure 4-2: Ternary plots of the BET specific surface areas for a) Mo/Nb, b) Nb/V, and c) Mo/V (co-)doped TiO_2 samples.

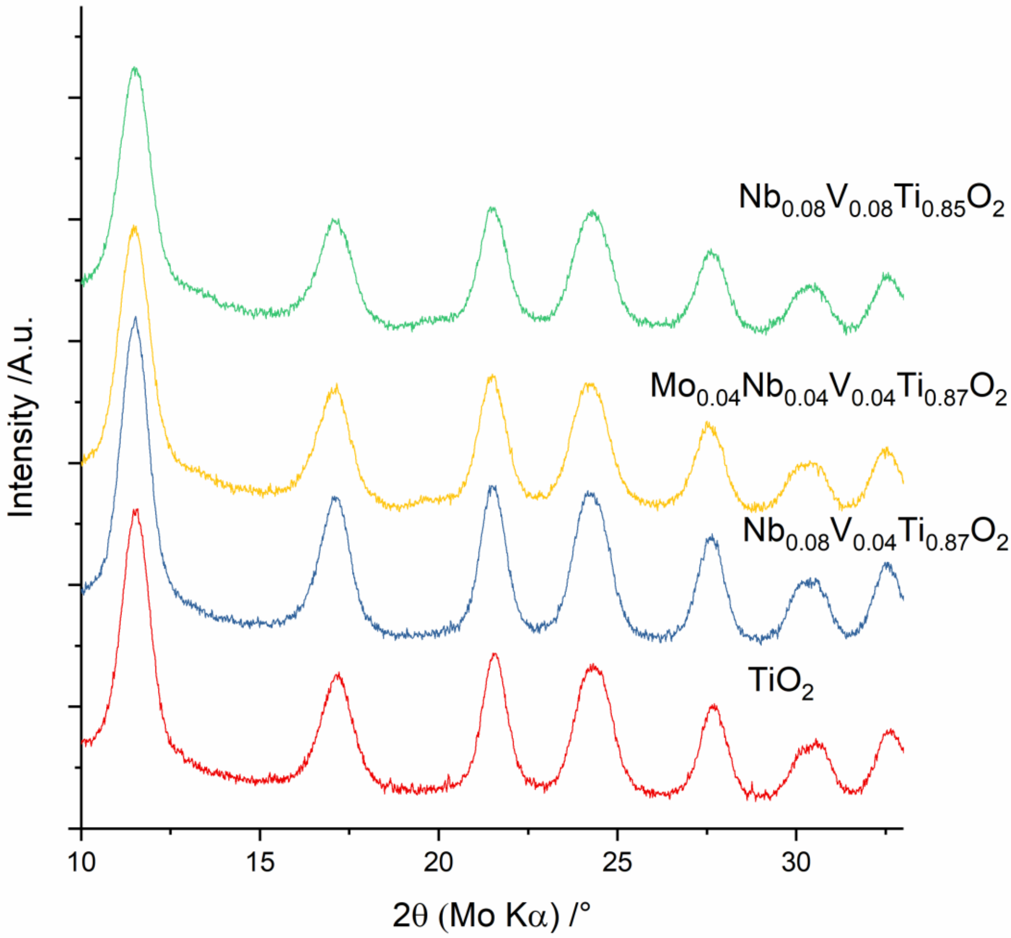

Figure 4-3: X-ray diffraction patterns for selected samples TiO_2, $Nb_{0.08}V_{0.04}Ti_{0.87}O_2$, $Mo_{0.04}Nb_{0.04}V_{0.04}Ti_{0.87}O_2$, and $Nb_{0.08}V_{0.08}Ti_{0.85}O_2$.

samples containing high dopant concentrations of V(V) (Figure 4-1e and f). X-ray diffraction patterns for selected samples were plotted in Figure 4-3.

BET SSA measurements revealed consistent values for the Mo/Nb co-doped samples. The only sample with a SSA not in the range 250 to 290 m^2 g^{-1} was $Nb_{0.04}Ti_{0.96}O_2$, which showed a SSA of 216 m^2 g^{-1} (see Figure 4-2). Variations for the samples containing vanadium were significantly larger. $V_{0.15}Ti_{0.85}O_2$ revealed a surface area of 329 m^2 g^{-1}, whilst both $V_{0.11}Ti_{0.89}O_2$ and $Mo_{0.04}V_{0.11}Ti_{0.85}O_2$ showed surface areas in the range 305 to 315 m^2 g^{-1}. More generally, co-doping did not seem to significantly change the surface areas of the materials, whereas an increased dopant concentration in general led to an increase in surface area. These findings were consistent with the crystallite domain sizes determined via the Scherrer equation, which showed similar trends.

The shift of the major peak (E_g vibrational state at a Raman shift of 149 cm^{-2}) in the Raman spectra for the doped and undoped anatase (TiO_2) samples was analysed and is shown in Figure 4-4.[234] Whilst the shift of this peak has previously been associated with changing particle sizes of nano-titania, no such correlation could be found when contrasting the results for SSAs and Raman peak shifts in Figure 4-2 and Figure 4-4, respectively. Doping with both individual dopants and co-doping with multiple dopants resulted in a shift to higher wave numbers. However, it appeared that the peak shift due to molybdenum doping was significantly more pronounced than for either niobium or vanadium doping. Co-doping increased the peak shift to higher wave numbers significantly, with the largest shifts occurring for $Mo_{0.08}Nb_{0.08}Ti_{0.85}O_2$ and $Mo_{0.08}V_{0.08}Ti_{0.85}O_2$. Since this peak shift has previously been associated with an expansion of the unit cell

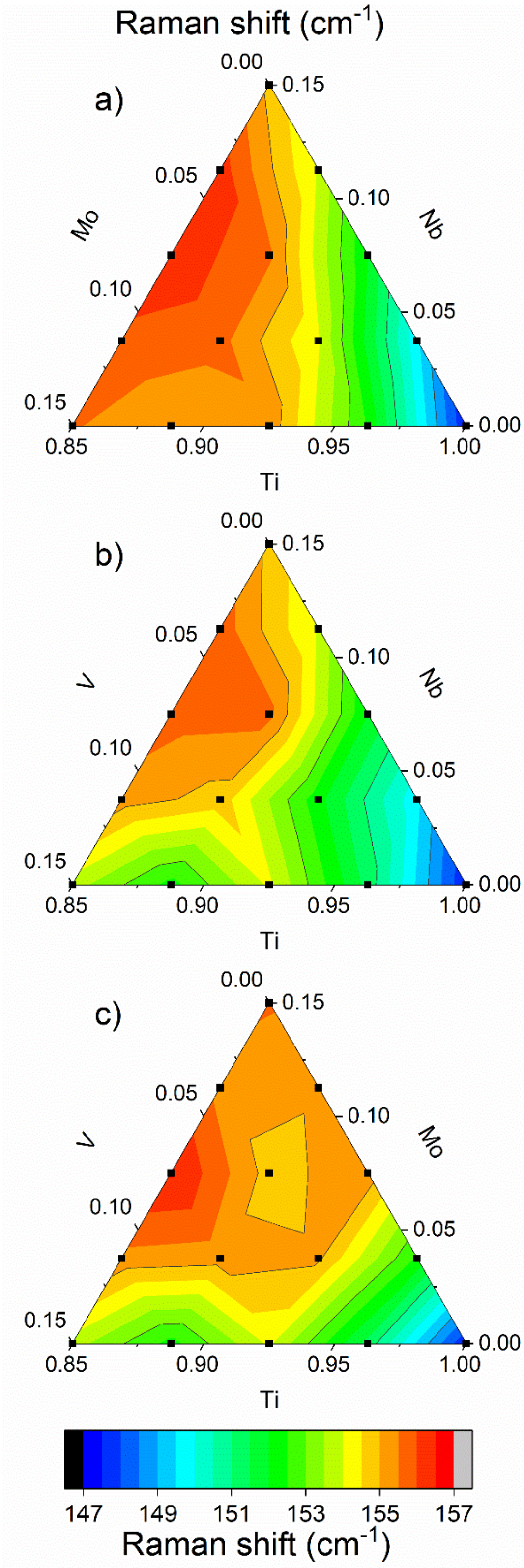

Figure 4-4: Ternary plots of the Raman shift for the major E_g peak for a) Mo/Nb, b) Nb/V, and c) Mo/V (co-)doped TiO_2 samples.

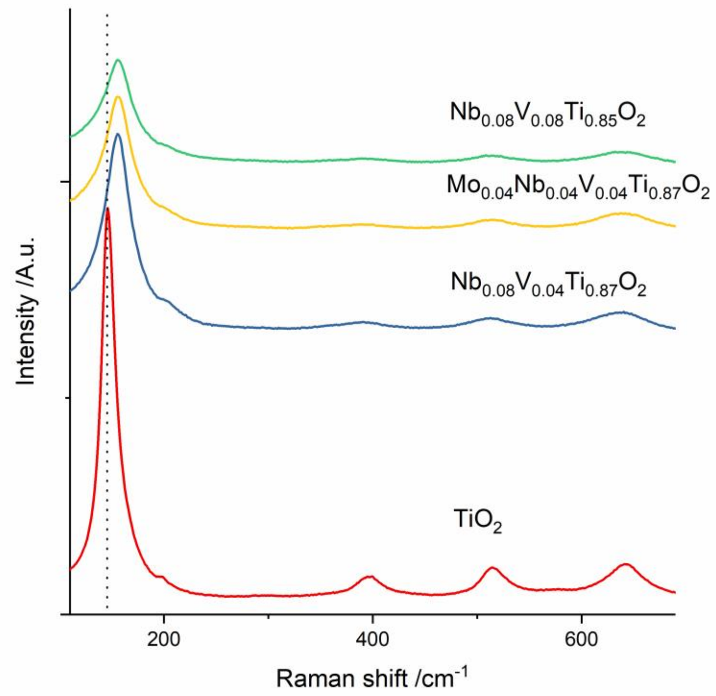

Figure 4-5: Raman spectra for selected samples TiO_2, $Nb_{0.08}V_{0.04}Ti_{0.87}O_2$, $Mo_{0.04}Nb_{0.04}V_{0.04}Ti_{0.87}O_2$, and $Nb_{0.08}V_{0.08}Ti_{0.85}O_2$.

volume,[235,236] this trend might indicate that the variety of dopants in co-doped samples increased the change in unit cell. Furthermore, no impurity peaks were detected in the Raman spectra for any of the samples. Raman spectra for selected samples can be seen in Figure 4-5, which besides the obvious peak shifts also demonstrates the lower intensities for the Raman spectra of the doped samples.

XPS was conducted for all samples. The XPS spectra confirmed the oxidation states of Ti(IV), Mo(VI), V(V), and Nb(V). There were no obvious trends noticeable from XPS, because the oxidation states and atomic quantities were in line with expectations: Ti(IV), Mo(VI), V(V), and Nb(V) were the only oxidation states of metals present.

4.4.2. Electrochemical Characterisation of Mo-, V-, and Nb-(co-)doped Anatase TiO_2

Galvanostatic charge/discharge cycling was conducted at varying specific currents in the potential range 3.0 to 1.0 V vs. Li/Li$^+$. Ternary plots of the specific capacities for

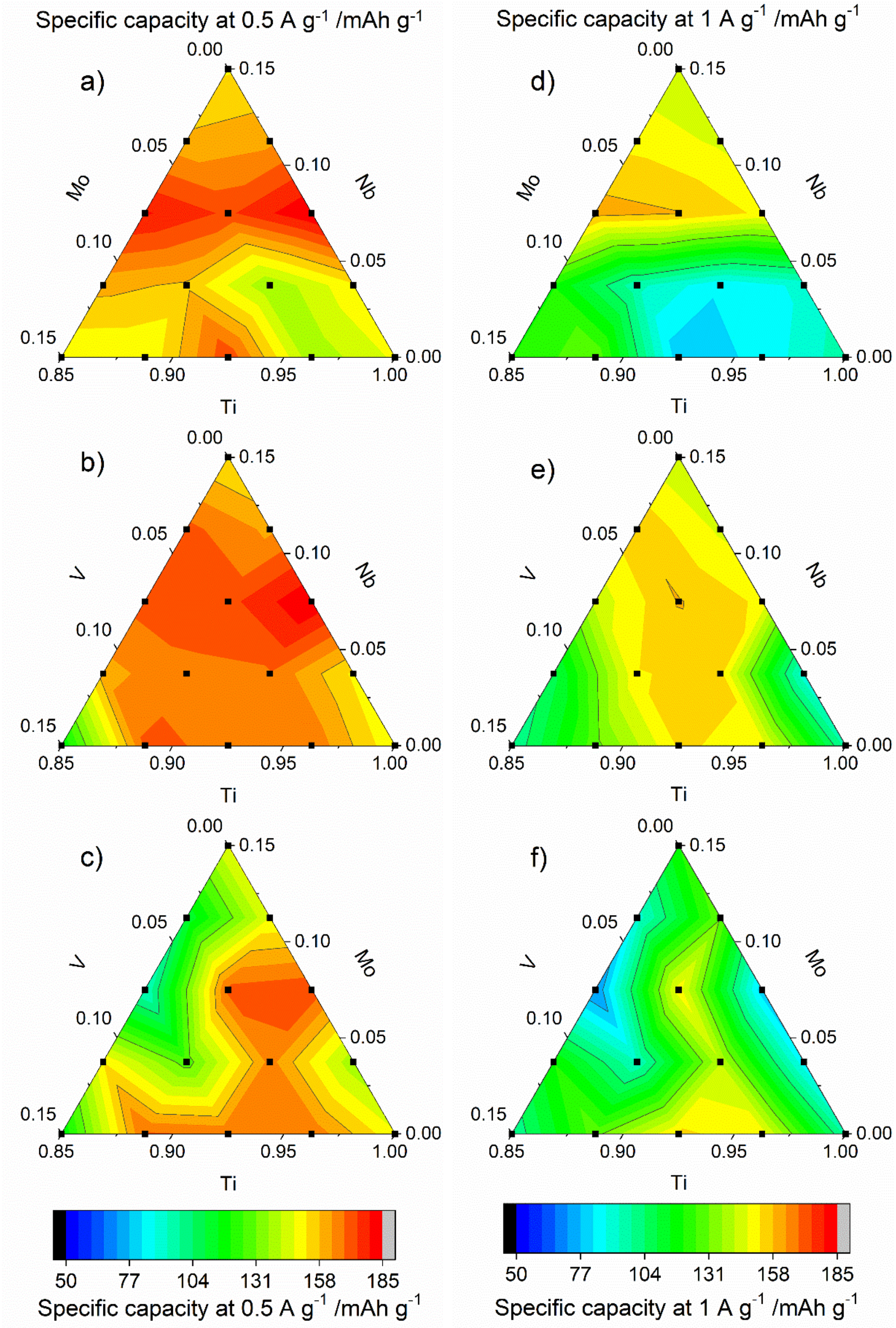

Figure 4-6: Ternary plots of the specific capacities at a specific current of 0.5 A g^{-1} for a) Mo/Nb, b) Nb/V, and c) Mo/V (co-)doped TiO_2 samples. Ternary plots of the specific capacities at a specific current of 1.0 A g^{-1} for d) Mo/Nb, e) Nb/V, and f) Mo/V (co-)doped TiO_2 samples.

all samples at specific currents of 0.5, 1.0, and 2.0 A g^{-1} were plotted in Figure 4-6a to c, Figure 4-6d to f, and Figure 4-7a to c, respectively.

At a specific current of 0.5 A g^{-1}, the specific capacity was in the range 90 to 185 mAh g^{-1}. Pure nanosized TiO_2 (anatase) showed a specific capacity of 148 mAh g^{-1}, close to the arithmetic mean of the maximum and minimum values. A molybdenum/vanadium co-doped sample showed the lowest specific capacity of 90 mAh g^{-1} ($Mo_{0.08}V_{0.08}Ti_{0.85}O_2$). Generally, co-doping with molybdenum and vanadium significantly reduced the performance of the samples. This could have been a result of antagonistic effects caused by the molybdenum and vanadium doping, since doping with just one of the two ions could improve the specific capacity. The best results were achieved for doping just with niobium, however, co-doping of niobium with either vanadium or molybdenum with a medium concentration of niobium also led to marked improvements at this specific current, compared to pure TiO_2. The highest value of ca. 185 mAh g^{-1} was achieved for $Nb_{0.08}Ti_{0.92}O_2$, but $Mo_{0.04}Nb_{0.08}Ti_{0.89}O_2$ and $Mo_{0.08}Nb_{0.08}Ti_{0.85}O_2$ showed similarly high specific capacities of ca. 180 mAh g^{-1}. For vanadium/niobium doping, $V_{0.04}Nb_{0.04}Ti_{0.92}O_2$, $V_{0.04}Nb_{0.08}Ti_{0.89}O_2$, and $V_{0.08}Nb_{0.08}Ti_{0.85}O_2$ showed specific capacities of ca. 175 mAh g^{-1}. Doping with high concentrations of vanadium or molybdenum seemed to be detrimental to specific capacities.

Table 4-1: Specific capacities at different specific currents and after 500 cycles at a specific current of 5 A g^{-1} for TiO_2 and the four samples with three co-dopants.

Sample	**Specific current [A g^{-1}]**			
	0.5	1	2	5 (after 500 cycles)
TiO_2	148	97	70	80
$Mo_8Nb_4V_4Ti_{85}$	156	110	74	89
$Nb_8Mo_4V_4Ti_{85}$	165	149	121	119
$Mo_4V_4Nb_4Ti_{89}$	147	120	88	107
$V_8Mo_4Nb_4Ti_{85}$	132	102	78	91

Interestingly, these trends remained true for specific currents of 1.0 and 2.0 A g^{-1}: Co-doping with molybdenum and vanadium led to poor performance, with

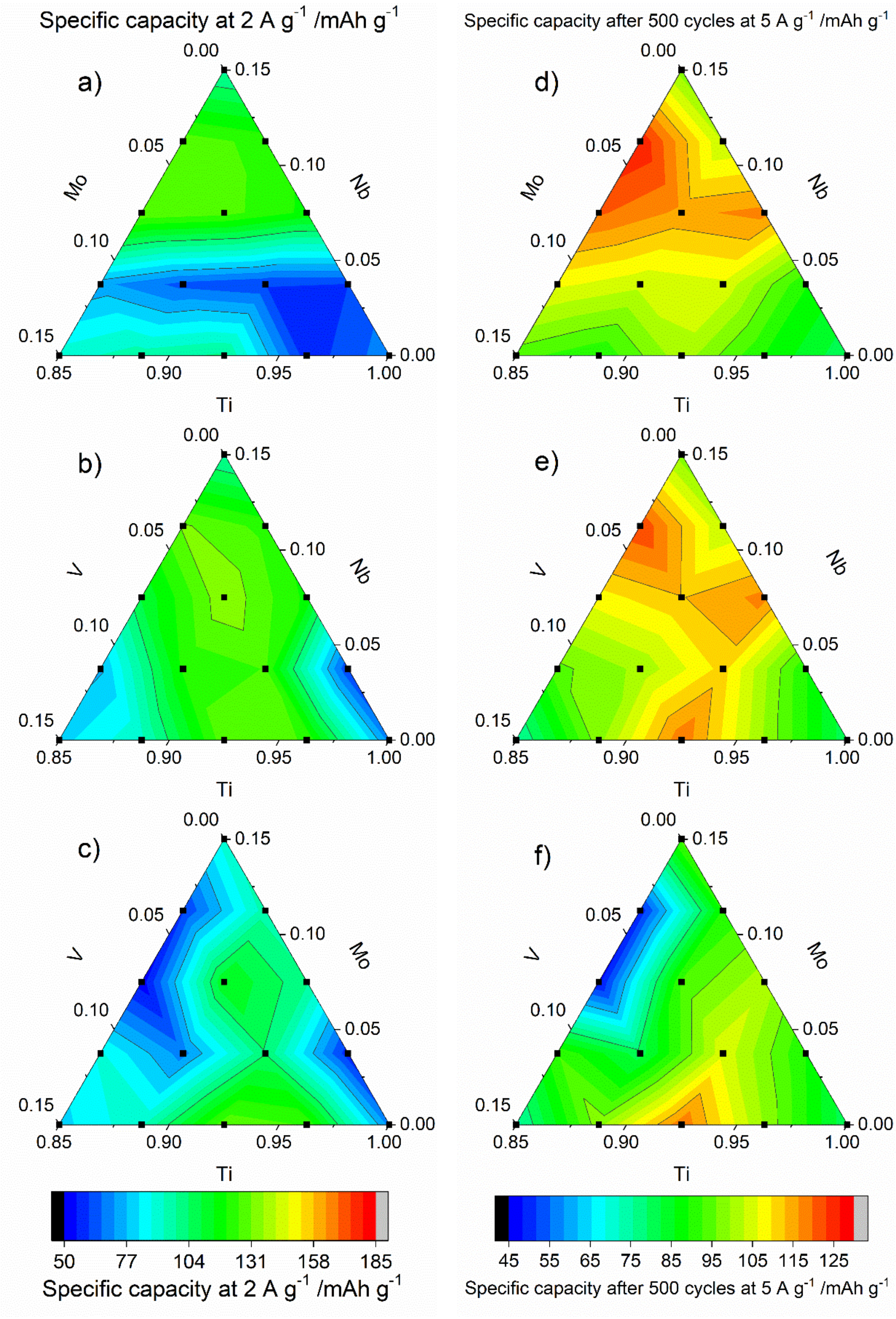

Figure 4-7: Ternary plots of the specific capacities at a specific current of 2.0 A g^{-1} for a) Mo/Nb, b) Nb/V, and c) Mo/V (co-)doped TiO_2 samples. Ternary plots of the specific capacities after 500 cycles at a specific current of 5.0 A g^{-1} for a) Mo/Nb, b) Nb/V, and c) Mo/V (co-)doped TiO_2 samples.

$Mo_{0.08}V_{0.08}Ti_{0.85}O_2$ showing the poorest performance with specific capacities of 69 and 50 mAh g^{-1} at specific currents of 1.0 and 2.0 A g^{-1}, respectively. Pure nanosized TiO_2 showed specific capacities of 97 and 79 mAh g^{-1} at the same specific currents. The co-doped samples with 7.5 at.% niobium dopant showed the highest specific capacities at both 1.0 and 2.0 A g^{-1}. Whilst $Nb_{0.08}Ti_{0.92}O_2$ showed specific capacities of 151 and 118 mAh g^{-1} at 1.0 and 2.0 A g^{-1}, respectively, molybdenum/niobium co-doping resulted in specific capacities of 160 and 159 mAh g^{-1} and 130 and 128 mAh g^{-1} at 1.0 and 2.0 A g^{-1}, respectively, for $Mo_{0.04}Nb_{0.08}Ti_{0.89}O_2$ and $Mo_{0.08}Nb_{0.08}Ti_{0.85}O_2$, respectively. Furthermore, vanadium/niobium co-doping led to a synergetic effect, increasing the specific capacities to 155 and 158 mAh g^{-1} and 135 and 132 mAh g^{-1} for $V_{0.04}Nb_{0.04}Ti_{0.92}O_2$ and $V_{0.04}Nb_{0.08}Ti_{0.89}O_2$, respectively, at specific currents of 1.0 and 2.0 A g^{-1}, respectively.

The cycling stability of all materials was tested by cycling in the potential window 1.0 to 3.0 V vs. Li/Li^+ at a specific current of 5.0 A g^{-1} for 500 cycles. Ternary plots of the specific capacities after 500 cycles for all samples were plotted (see Figure 4-7d to f). Whilst all samples showed some capacity fade over the 500 cycles, it was mostly limited to below 20 % of the initial specific capacities (see Figure 4-8). As discussed above, co-doping with molybdenum and vanadium led to very poor performance; after 500 cycles, $Mo_{0.08}V_{0.08}Ti_{0.85}O_2$ showed a specific capacity of just 47 mAh g^{-1}, whereas undoped TiO_2 showed a capacity of 80 mAh g^{-1}. In contrast, co-doping with either niobium/vanadium or niobium/molybdenum was shown to have a positive effect on cycling stability. For molybdenum and niobium co-doping, the specific capacities after 500 cycles were as high as 126 and 121 mAh g^{-1} for $Mo_{0.04}Nb_{0.11}Ti_{0.85}O_2$ and $Mo_{0.08}Nb_{0.08}Ti_{0.85}O_2$, respectively. Additionally, for the co-doping with vanadium and niobium, the specific capacities after 500 cycles were as high as 123 and 113 mAh g^{-1} for $V_{0.04}Nb_{0.11}Ti_{0.85}O_2$ and $V_{0.04}Nb_{0.08}Ti_{0.89}O_2$, respectively.

Finally, co-doping with all three dopants was explored and the specific capacities are shown in Table 4-1. The samples co-doped with the higher concentrations of molybdenum or vanadium ($Mo_{0.08}Nb_{0.04}V_{0.04}Ti_{0.85}O_2$ and

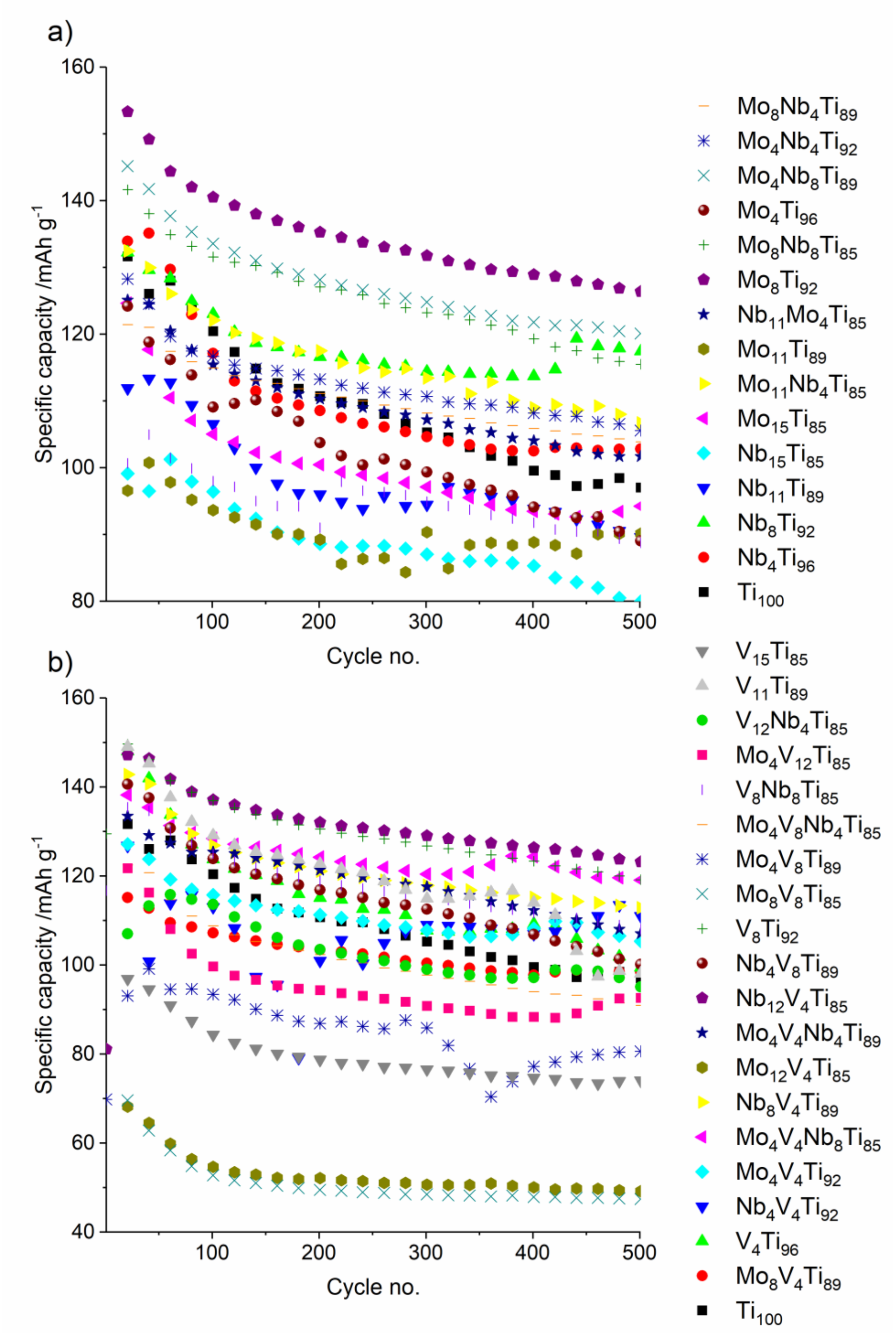

Figure 4-8: Evolution of specific capacities with cycle number for LIB half-cells cycled in the potential range 1.0 to 3.0 V vs. Li/Li^+ at a specific capacity of 5.0 A g^{-1} for a) Mo/Nb, b) Mo/V, and Nb/V (co-)doped anatase TiO_2 samples.

$V_{0.08}Mo_{0.04}Nb_{0.04}Ti_{0.85}O_2$, respectively) did not significantly increase performance under these test conditions. This seemed to confirm a potential antagonistic effect of co-doping with molybdenum and vanadium. Whilst co-doping with equal concentrations of molybdenum, vanadium, and niobium ($Mo_{0.04}V_{0.04}Nb_{0.04}Ti_{0.89}O_2$) increased the specific capacity at higher specific currents slightly (from 70 to 88 mAh g^{-1} at 5.0 A g^{-1} compared to TiO_2), improvements for the sample containing a higher concentration of niobium were significantly larger. This mirrored the behaviour for the co-doped samples discussed above, where the samples with slightly higher concentrations of niobium (8 or 11 at.%), co-doped with vanadium or molybdenum, led to the biggest improvements. The specific capacities for $Nb_{0.08}Mo_{0.04}V_{0.04}Ti_{0.85}O_2$ were 165, 149, 121, and 119 mAh g^{-1} (compared to 148, 97, 70, and 80 mAh g^{-1} for pure TiO_2) at specific currents of 0.5, 1.0, 2.0, and 5.0 A g^{-1}.

4.5. Conclusions

The results showed that co-doping can have beneficial effects on the performance of anatase TiO_2 as active material for negative electrodes in Li-ion batteries. However, it is important to consider the potential synergistic or antagonistic effects of various dopants.

Whilst the BET SSA increased significantly with increasing vanadium concentration, neither molybdenum nor niobium dopant seemed to have a comparable effect. Raman peak shifts, on the other hand, resulted from any doping. Whilst the observed shifts of peak positions were smallest for the samples with just one dopant, co-doping significantly increased the peak shifts. Especially samples with ca. 8 at.% of both dopants showed the largest peak shifts.

With regards to the electrochemical performance, molybdenum and vanadium co-doping led to antagonistic effects, which led to poor performance at high current rates and cycle life. Co-doping that included higher concentrations of niobium with either molybdenum or vanadium, however, was shown to have a synergetic effect that improved the specific capacities significantly. For example, whilst pure TiO_2 (anatase) showed a capacity of 80 mAh g^{-1} after 500 cycles at a specific current of 5.0 A g^{-1}, $Mo_{0.04}Nb_{0.11}Ti_{0.85}O_2$, $Mo_{0.08}Nb_{0.08}Ti_{0.85}$, $V_{0.04}Nb_{0.11}Ti_{0.85}O_2$, and $V_{0.04}Nb_{0.08}Ti_{0.89}O_2$ showed specific capacities of 126, 121, 123, and 113 mAh g^{-1}, respectively.

Furthermore, co-doping with all three dopants showed that adding additional dopants could further improve performance of co-doped samples. As for the co-doped samples with just two dopants, for the sample containing a relatively higher concentration of niobium ($Nb_{0.08}Mo_{0.04}V_{0.04}Ti_{0.85}O_2$), a significantly improved performance at different specific currents was observed, to 165, 149, 121, and 119 mAh g^{-1} (from 148, 97, 70, and 80 mAh g^{-1} for pure TiO_2) at specific currents of 0.5, 1.0, 2.0, and 5.0 A g^{-1}.

In future, the exploration of the effects of co-doping on the electrochemical properties of anatase TiO_2 in Na-ion or multi-valent ion chemistries would be interesting. Whilst Mo, V, and Nb were selected as dopants due to their promise, other potential dopants with promise such as W(V), Ta(V), and Zr(V) should be explored. Additionally, cationic dopants such as N, which have been shown to improve electronic conductivity in anatase TiO_2, could be explored. Furthermore, metal dopants that themselves undergo conversion reactions such as Sn and Fe should be explored as potential high energy dopants.

Whilst the doping of anatase TiO_2 with elements that can undergo conversion or alloying reactions with lithium might be promising, so is the co-precipitation of conversion materials with anatase directly. This concept will be explored in Chapter 5.

5. Improvement of Conversion Materials by Co-precipitation with TiO_2

5.1. Aims

Conversion and alloying active materials show much higher specific capacities than insertion materials. Insertion materials, however, have excellent cycle life and low voltage hysteresis. The conversion materials MoO_2 and $NiCo_2O_4$ were co-precipitated with the insertion material TiO_2 to achieve better high current capabilities with improved cycle life. As discussed above, the co-precipitation of conversion materials with anatase might be promising in improving the cycling stability and specific capacities of anode active materials.

5.2. Introduction

As discussed in Section 1.4.3, the commercial application of conversion materials has been hindered by poor cyclability, which is a result of large volume changes during lithiation and delithiation, large voltage hysteresis upon cycling, and poor rate performance.

Various methods to improve cyclability, voltage hysteresis, and rate performance have been explored. These include the incorporation of a more stable inorganic phase, carbon coating, or nanosizing. The more stable phase should not undergo significant volume or structural changes upon cycling.[154,283] Additionally, the material should possess good chemical stability, such as TiO_2. TiO_2 has previously been used as stabilising phase for Li-ion anode materials, for example in MoS_2/TiO_2 composites.[284–286] A scalable method for the synthesis of nanoceramics such as CHFS, which allows for the incorporation of another stabilising phase in process, is highly desirable.[57,287,288]

5.2.1. TiO_2-stabilised MoO_2

Monoclinic molybdenum (IV) oxide (MoO_2) can be used as active material for LIB anodes, both as an intercalation anode[57,180,289] and a conversion material.[148,287,288,290–293] The intercalation reaction in the potential range 1.0 to 3.0 V vs. Li/Li^+ follows Equation 5.1:[180,293]

$$\mathrm{MoO_2}_{\mathrm{(mono)}} \rightleftharpoons \mathrm{Li_xMoO_2}_{(0.45<x<0.78,\mathrm{ortho})} \rightleftharpoons \mathrm{Li_{0.98}MoO_2}_{\mathrm{(mono)}} \qquad (5.1)$$

MoO_2 was first described as Li-ion intercalation material in 1989 and has a theoretical specific capacity of 209 mAh g^{-1}.[294] When lithiated, the crystal structure of monoclinic MoO_2 transforms into orthorhombic Li_xMoO_2 and upon further lithiation (above $x > 0.78$), transforms into monoclinic Li_xMoO_2. When cycled as a conversion material (at potentials below 1.0 V vs. Li/Li^+) its theoretical capacity is 838 mAh g^{-1}, four times its theoretical capacity when cycled as an intercalation material.[95] This is because the conversion reaction of lithiated Li_xMoO_2 follows Equation 5.2, which involves three electrons:[95,152,295]

$$\mathrm{Li_{0.98}MoO_2}_{\mathrm{(monoclinic)}} + 3.02\ \mathrm{Li^+} + 3.02\ \mathrm{e^-} \rightleftharpoons 2\mathrm{Li_2O} + \mathrm{Mo} \qquad (5.2)$$

The lithiated monoclinic $Li_{0.98}MoO_2$ converts to metallic molybdenum and lithium superoxide. However, in bulk MoO_2, kinetic constraints limit the back reaction to just one of the four electrons per Mo atom. MoO_2 has been considered a promising alternative as anode material in LIBs because of its significantly higher density 6.5 kg m^{-3} compared to graphite (2.3 kg m^{-3}), which could lead to better volumetric energy densities of commercial negative electrodes.[290]

5.2.2. Co-based Materials

5.2.2.1. TiO_2-stabilised $NiCo_2O_4$ and Co_2TiO_4

A variety of cobalt-based, mixed cobalt-titanium oxides and mixed nickel-cobalt oxides have been used in LIBs, including Co_3O_4,[296–302] Co_2TiO_4,[303] and $NiCo_2O_4$.[304–307] Substitution of some of the cobalt ions in Co_3O_4 can reduce the cost, improve the electrical conductivity, and improve the cycle life of the $M_xCo_{3-x}O_4$ materials.[304]

The lithiation and delithiation process for $NiCo_2O_4$ has been ascribed to the conversion reactions seen in Equations 5.3 to 5.6:[304]

$$\mathrm{NiCo_2O_4} + 8\ \mathrm{Li^+} + 8\ \mathrm{e^-} \rightarrow 4\mathrm{Li_2O} + \mathrm{Ni} + 2\mathrm{Co} \qquad (5.3)$$

$$\mathrm{Ni} + \mathrm{Li_2O} \rightleftharpoons \mathrm{NiO} + 2\ \mathrm{Li^+} + 2\ \mathrm{e^-} \qquad (5.4)$$

$$\mathrm{Co} + \mathrm{Li_2O} \rightleftharpoons \mathrm{CoO} + 2\ \mathrm{Li^+} + 2\ \mathrm{e^-} \tag{5.5}$$

$$\mathrm{CoO} + \frac{1}{3}\mathrm{Li_2O} \rightleftharpoons \frac{1}{3}\mathrm{Co_3O_4} + \frac{2}{3}\ \mathrm{Li^+} + \frac{2}{3}\ \mathrm{e^-} \tag{5.6}$$

Co_3O_4 has a cubic spinel structure and a theoretical capacity of 890 mAh g^{-1}, which is more than double the capacity of graphite. Co_3O_4/TiO_2 composites have previously been prepared to increase cyclability and high rate performance.[308,309] A hollow Co_3O_4/TiO_2 polyhedron sample synthesised via cation-exchange showed a capacity of ca. 400 mAh g^{-1} at a specific current of 2 A g^{-1}.[308] Recently, core shell CoO-$CoTiO_3$ nanotubes have shown an excellent capacity of 237 mAh g^{-1} at 4 A g^{-1}. The additional stability given to the CoO particles by the $CoTiO_3$ outer shell was believed to have accommodated for volume expansion and shrinking during cycling, enabling both better high rate and long term cycling properties.[130] Co_2TiO_4 has an inverse spinel structure, in which Co^{2+} occupies both tetrahedral and octahedral sites with the structure $[Co^{2+}]_{tetra}[Co^{2+}Ti^{4+}]_{octa}O_4$.[303,310–313] The material has only recently been considered as an active material for Li-ion negative electrodes. It showed a specific capacity of 137 mAh g^{-1} after 50 cycles at a specific current of 50 mA g^{-1} (205 mAh g^{-1} for a carbon-coated sample) and 48 mAh g^{-1} at 500 mA g^{-1} (64 mAh g^{-1} for carbon-coated).[303]

Substituting some of the cobalt in Co_3O_4 with cheaper and more eco-friendly metals has been suggested due to the cost and toxicity of cobalt.[304] Substitution with nickel has been shown to significantly increase the electronic conductivity of Co_3O_4.[305] Although the theoretical capacity of $NiCo_2O_4$ is 884 mAh g^{-1},[314] $NiCo_2O_4$ microspheres have been shown to exhibit a stable capacity of up to 1200 mAh g^{-1} after 30 cycles at 0.1 A g^{-1} and up to 400 mAh g^{-1} at a specific current of 1.6 A g^{-1}.[304] Furthermore, $NiCo_2O_4$ nanorods have been shown to exhibit fairly stable cycling performance of up to 650 mAh g^{-1} at 0.1 A g^{-1} after 150 cycles.[307] $NiCo_2O_4$ has a spinel structure akin to that of Co_3O_4, with nickel substituting cobalt in half of the octahedral sites and cobalt present in both octahedral and tetrahedral sites, giving a structure of $[Co]_{tetra}[CoNi]_{octa}O_4$.[304]

5.3. Materials and Methods

5.3.1. TiO_2-stabilised MoO_2

5.3.1.1. Synthesis of TiO_2/MoO_2 composites

The synthesis of the materials was carried out as described in Section 2.1.3.1. The rate of synthesis for all materials was > 85 g h^{-1}.

5.3.1.2. Physical characterisation of TiO_2/MoO_2 composites

The physical characterisation of the materials was carried out according to the methods described in Section 2.2. The methods included PXRD, XPS, XAS, TEM, BET, tap density, and EDX.

5.3.1.3. Electrochemical characterisation of TiO_2/MoO_2 composites

The electrochemical characterisation was carried out according to the methods described in Section 2.3. Additionally, to analyse if the positive effect of TiO_2 on the electrochemical properties of MoO_2 was a result of the direct synthesis of the composite, mixed TiO_2 and MoO_2 electrodes were fabricated. To achieve a similar ratio of TiO_2 to MoO_2 as in the sample denominated TiO_2/MoO_2-3, electrodes with a ratio of 64:16:10:10 wt.% of MoO_2:TiO_2:PVDF:Carbon black were prepared according to the methods in Section 2.3.

CVs of half-cells were performed in the potential range 0.1 to 3.0 V vs. Li/Li^+, at scan rates in the range 0.1 to 100 mV s^{-1}. Galvanostatic tests were carried out in the same potential range, at specific currents in the range 0.1 to 10.0 A g^{-1}.

Li-HECs were tested in the range of current densities 2.0 to 20.0 mA cm^{-2} (based on the geometric surface area of the electrodes, equivalent to ca. 0.3 to 3.0 A g^{-1}), in the potential window 1.0 to 3.0 V. CVs in the same potential window were performed at scan rates in the range 5 to 100 mV s^{-1}.

5.3.2. Co-based Materials

5.3.2.1. Synthesis of Co-based Materials

The synthesis of the materials was carried out as described in Section 2.1.3.2. The rate of synthesis for all samples was ca. 60 g h^{-1}.

5.3.2.2. *$Ni_xCo_{3-x}O_4$, Co_2TiO_4*

The physical characterisation of the materials was carried out according to the methods described in Section 2.2. The methods used for $Ni_xCo_{3-x}O_4$ and Co_2TiO_4 included PXRD, XPS, TEM, and BET.

The electrochemical characterisation was carried out according to the methods described in Section 2.3. CVs of half-cells were performed in the potential range 0.05 to 3.0 V vs. Li/Li^+, at scan rates in the range 0.1 to 5 mV s^{-1}. Galvanostatic tests were carried out in the same potential range, at specific currents in the range 0.1 to 10.0 A g^{-1}. EIS was performed with an AC current of 0.01 A rms, in the frequency range 100 kHz to 50 mHz.

5.3.2.3. *TiO_2-stabilised $NiCo_2O_4$*

The physical characterisation of the materials was carried out according to the methods described in Section 2.2. The methods used for the $NiCo_2O_4/TiO_2$ composites included PXRD, XPS, TEM, and BET.

The electrochemical characterisation was carried out according to the methods described in Section 2.3. CVs of half-cells were performed in the potential range 0.05 to 3.0 V vs. Li/Li^+, at scan rates in the range 0.1 to 5 mV s^{-1}. Galvanostatic tests were carried out in the same potential range, at specific currents in the range 0.1 to 10.0 A g^{-1}.

5.4. Results and Discussion

5.4.1. TiO_2-stabilised MoO_2

5.4.1.1. *Physical Characterisation of TiO_2/MoO_2 Composites*

PXRD patterns for the nanoparticulate MoO_2 and the five TiO_2/MoO_2 composites of different compositions revealed good matches with the peaks of the standard reference pattern for tugarinovite (monoclinic) MoO_2 (ICSD no. 23722, space group P2i/c). As can be seen in Figure 5-1, for all samples, the major peaks corresponded to the (011), (-211), and (-311) peaks for monoclinic MoO_2 (at 2θ = 11.9, 16.7, and 23.9 °, respectively). The XRD patterns for the composite samples all showed a shoulder associated with the (101) peak of TiO_2 (anatase) at 2θ = 11.6 °, to the left of the major

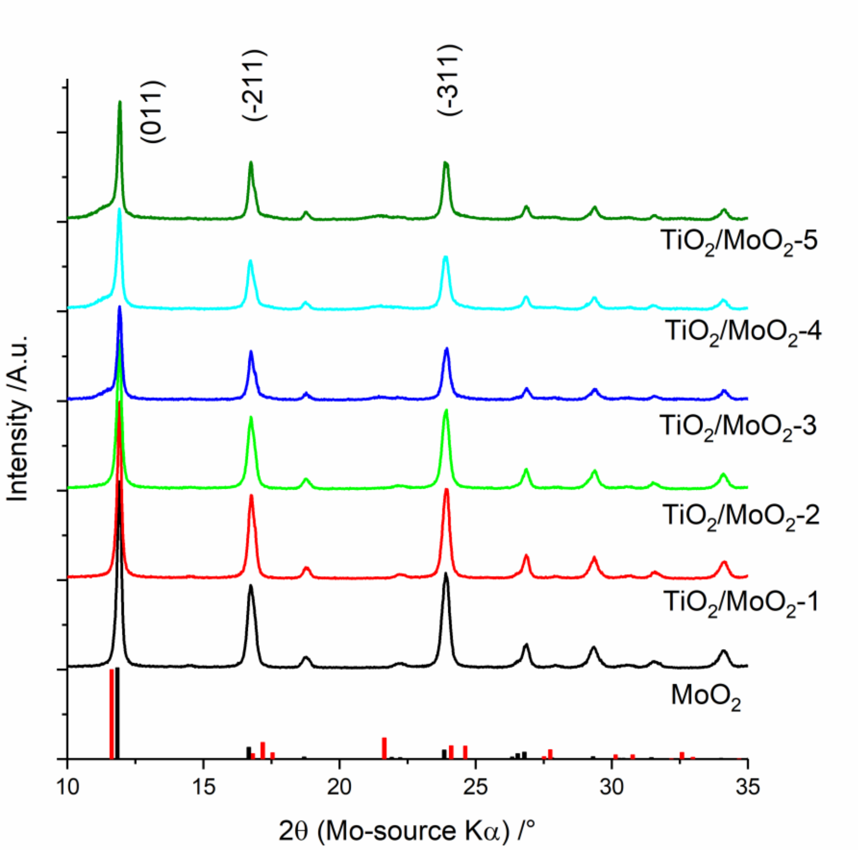

Figure 5-1: XRD patterns for MoO_2 and the TiO_2/MoO_2 composites, which are in good agreement with the peaks for the reference pattern for monoclinic MoO_2 (ICDS no. 23722, black bars). The composite TiO_2/MoO_2 samples, especially those with higher TiO_2 concentrations, additionally showed signs of shoulders in the peak positions for anatase TiO_2 (ICDS no. 09852, red bars).

(011) peak for MoO_2 at $2\theta = 11.9$ °. Additionally, a small peak appeared at $2\theta = 21.6$ ° for the composite samples with a high concentration of TiO_2, which was associated with the (200) peak of anatase TiO_2 (ICSD no. 09852, space group I41/a).

Deconvolution of the peaks for monoclinic MoO_2 and anatase TiO_2 showed separate phases for all composite samples (TiO_2/MoO_2-1 to TiO_2/MoO_2-5). Therefore, it was expected that there was no doping of Ti into MoO_2 or Mo into TiO_2. Using the areas of the peaks, the concentration of MoO_2 in the composites were 93, 85, 74, 70, and 62 wt.% for TiO_2/MoO_2-1 to TiO_2/MoO_2-5, respectively. This indicated that the actual concentration of TiO_2 was lower than expected from the nominal concentration during the synthesis. Molecular models of anatase TiO_2 and monoclinic MoO_2 can be seen in Figure 5-2.

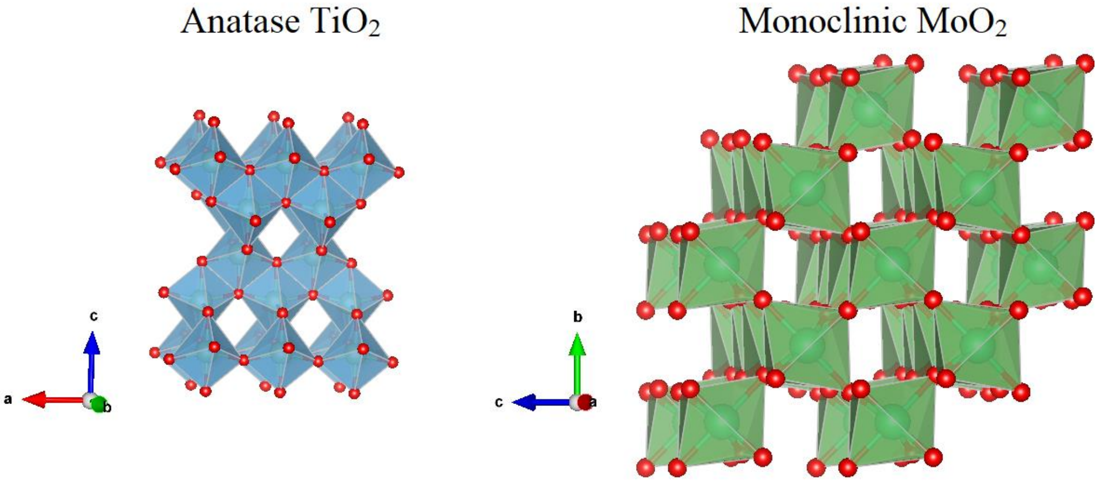
Anatase TiO_2

Monoclinic MoO_2

Figure 5-2: Molecular models of anatase TiO_2 and monoclinic MoO_2.

The concentrations and valence states of both titanium and molybdenum for the pure MoO_2 and the composite samples were determined via XPS. For the Mo *3d* spectra, three distinct peaks were observed for all composite samples, associated with the Mo $3d_{5/2}$ and Mo $3d_{3/2}$ binding energies (see Figure 5-3a). This indicated that there was more than a single valence state of molybdenum ions present on the surfaces of the materials. The three peaks were at ca. 229.6, 232.8, and 236.1 eV, respectively, but respective intensities varied with the concentration of Ti in the samples. The peaks at higher binding energies were more prevalent at low (or no) titanium concentration, whereas the peaks at lower binding energies became more prevalent at higher titanium concentrations. This was indicative of higher concentrations of Mo(IV) for the samples with higher titanium concentrations. The oxidation states other than Mo(IV) in MoO_2, both in the pure samples and the composites, were a result of surface oxidation to higher molybdenum oxidation states, such as Mo(V) or Mo(VI), as has previously been reported elsewhere.[46,47] It seemed that this surface oxidation was reduced for the composite samples with higher titanium concentrations, as indicated by the higher intensities of lower binding energy peaks.

The Ti *2p* spectra for all TiO_2/MoO_2 composites (TiO_2/MoO_2-1 to TiO_2/MoO_2-5) showed peaks at ca. 459.1 and 465.0 eV, which could be assigned to Ti $2p_{3/2}$ and Ti $2p_{1/2}$, respectively (see Figure 5-3b). The spin-orbit splitting energy was 5.9 eV, which was in keeping with the core levels of Ti(IV), both in the literature and those reported for pure TiO_2 in Section 3.4.1. Only minimal shifts in binding energies

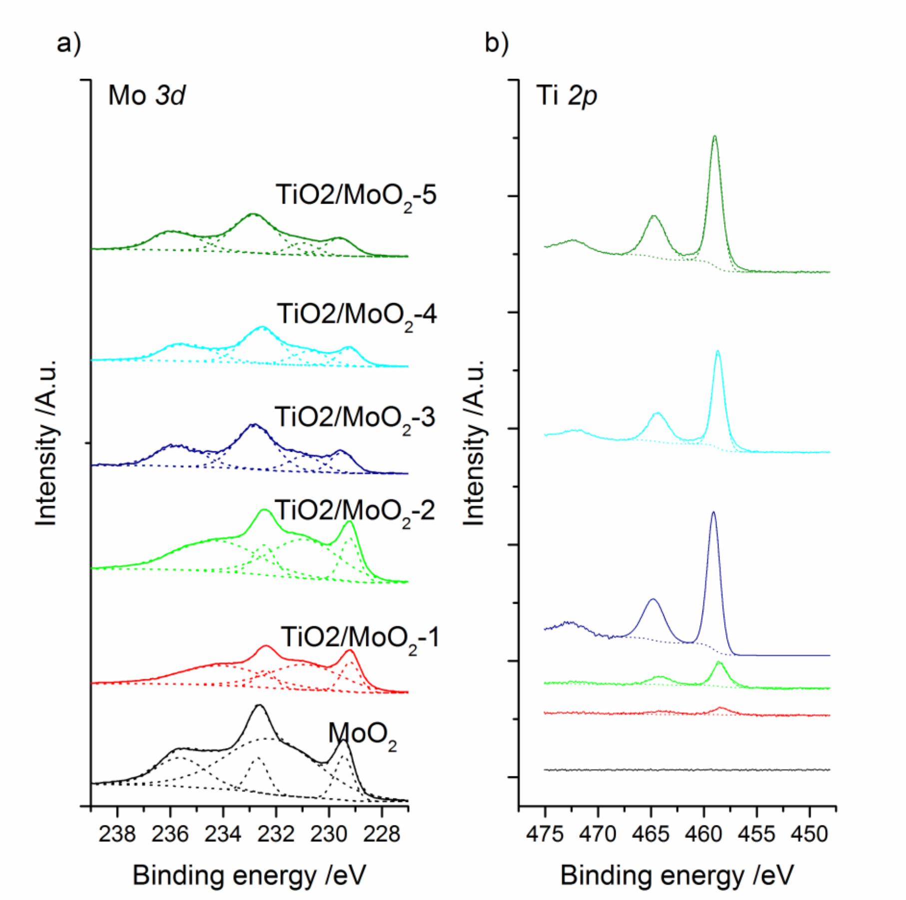

Figure 5-3: X-ray photoemission spectra of MoO_2 and the TiO_2/MoO_2 composites for a) Mo *3d* and b) Ti *2p*.

were observed for any of the composite samples. This indicated that no change in oxidation state occurred for the titanium species with the variation of molybdenum concentration in the composite samples.[234]

The concentrations of titanium and molybdenum in the samples were determined from the peak areas of the XPS spectra and compared to the nominal concentrations during the synthesis (see Figure 5-4). Whilst the experimentally determined concentration of Ti was lower than the nominal concentration during the synthesis at low concentrations (4 and 6 at.% compared to nominal concentrations of 5 and 10 %, respectively), it was higher for high concentrations (40, 49, and 56 at.% compared to nominal concentrations of 20, 33, and 50 at.%, respectively). This indicated an enrichment of TiO_2 on the surface of the composite.

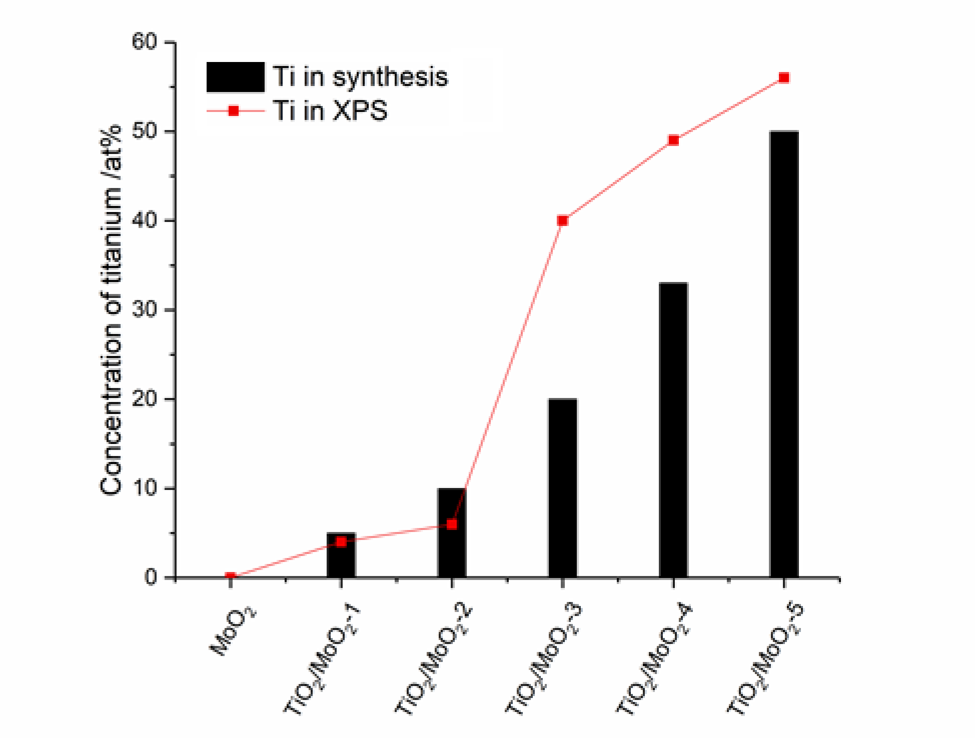

Figure 5-4: Comparison of the nominal titanium concentration during the synthesis and the experimental concentration determined via XPS peak area analysis.

The BET SSA values for the pure MoO_2 was ca. 21 m^2 g^{-1} and increased with increasing TiO_2 concentration in the composites (see Figure 5-5). Low molar ratios of TiO_2, such as in TiO_2/MoO_2-1, did not lead to an increase in SSA. However, the composite with a molar concentration of TiO_2 of 50 % showed a specific surface area of 150 m^2 g^{-1}, which was higher than would be expected for a simple mixture of TiO_2 and MoO_2.

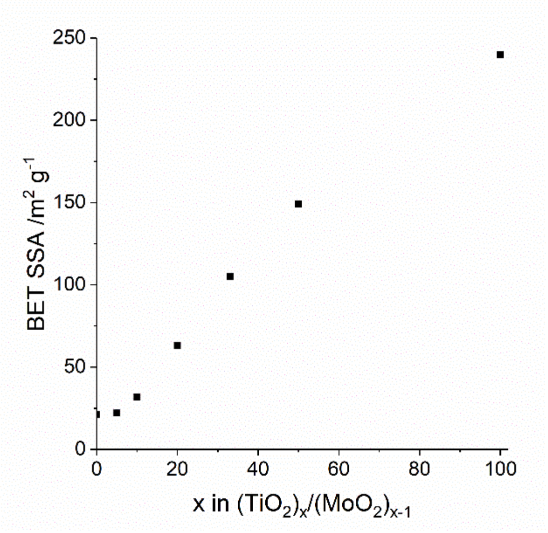

Figure 5-5: Relationship between the molar ratio of TiO_2 to MoO_2 in the TiO_2/MoO_2 composites and the BET surface areas.

Energy-dispersive X-ray spectroscopy (EDX) mapping showed homogenous distributions of Ti and Mo for each sample (see Figure 5-6). The mapping showed excellent, intimate mixing of the two nanomaterials of TiO_2

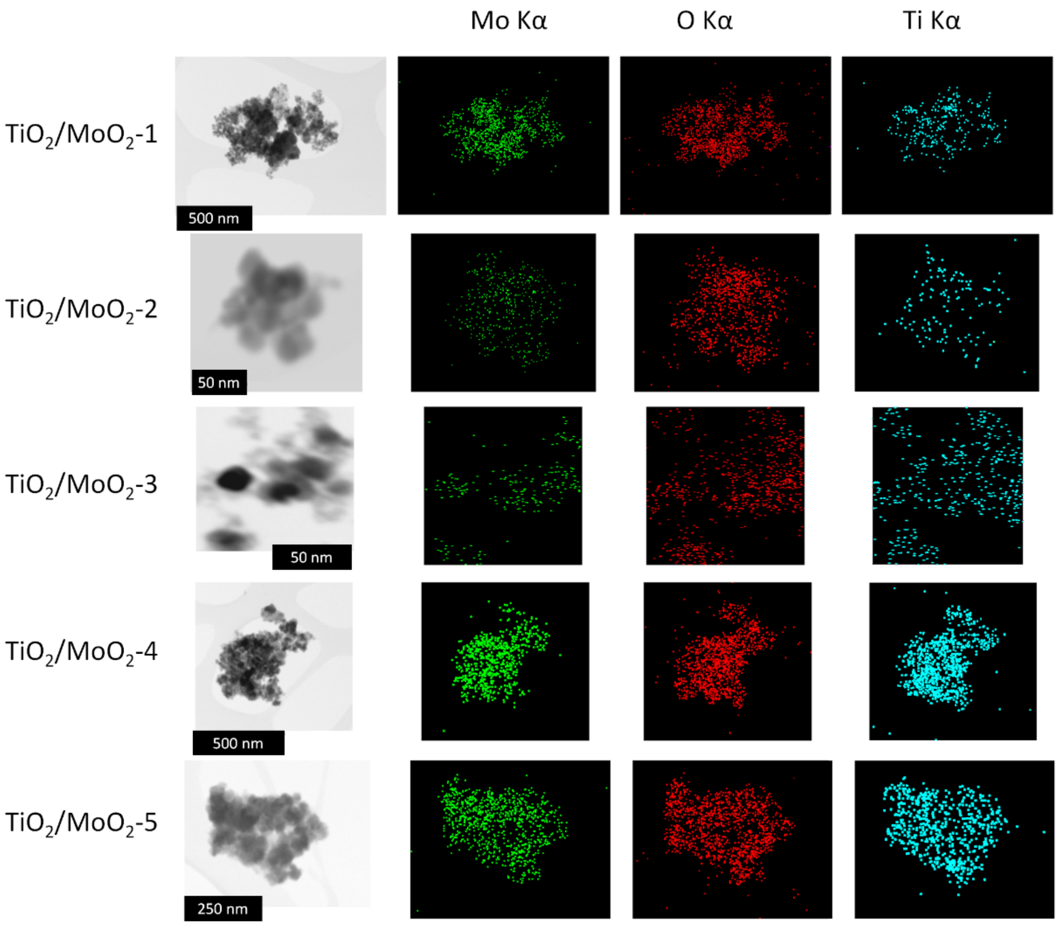

Figure 5-6: Bright-field micrographs for the TiO_2/MoO_2 composite samples with EDX maps for Mo Kα, O Kα, and Ti Kα.

and MoO_2, as would be expected when considering their synthesis via co-precipitation.

Transmission electron micrographs revealed mostly spherical particles in a range of sizes and agglomerates for MoO_2 (see Figure 5-7a), with an average particle size of 18.9 ± 6.2 nm (150 particles counted, see Appendix). As the MoO_2 was co-precipitated with TiO_2 in the synthesis, the average particle size and size distribution seemed to decrease, for example for TiO_2/MoO_2-1 (see Figure 5-7c), TiO_2/MoO_2-3 (see Figure 5-7e), and TiO_2/MoO_2-4 (see Figure 5-7g). The average particle size for TiO_2/MoO_2-3 was 9.1 ± 5.9 nm (150 particles counted, see Appendix). Furthermore, TEM images clearly showed lattice fringes for MoO_2 (see Figure 5-7b), TiO_2/MoO_2-1 (see Figure 5-7d), TiO_2/MoO_2-3 (see Figure 5-7f), and TiO_2/MoO_2-4 (see Figure 5-7h). Interlayer spacings of 0.34 and 0.24 nm could be observed for all

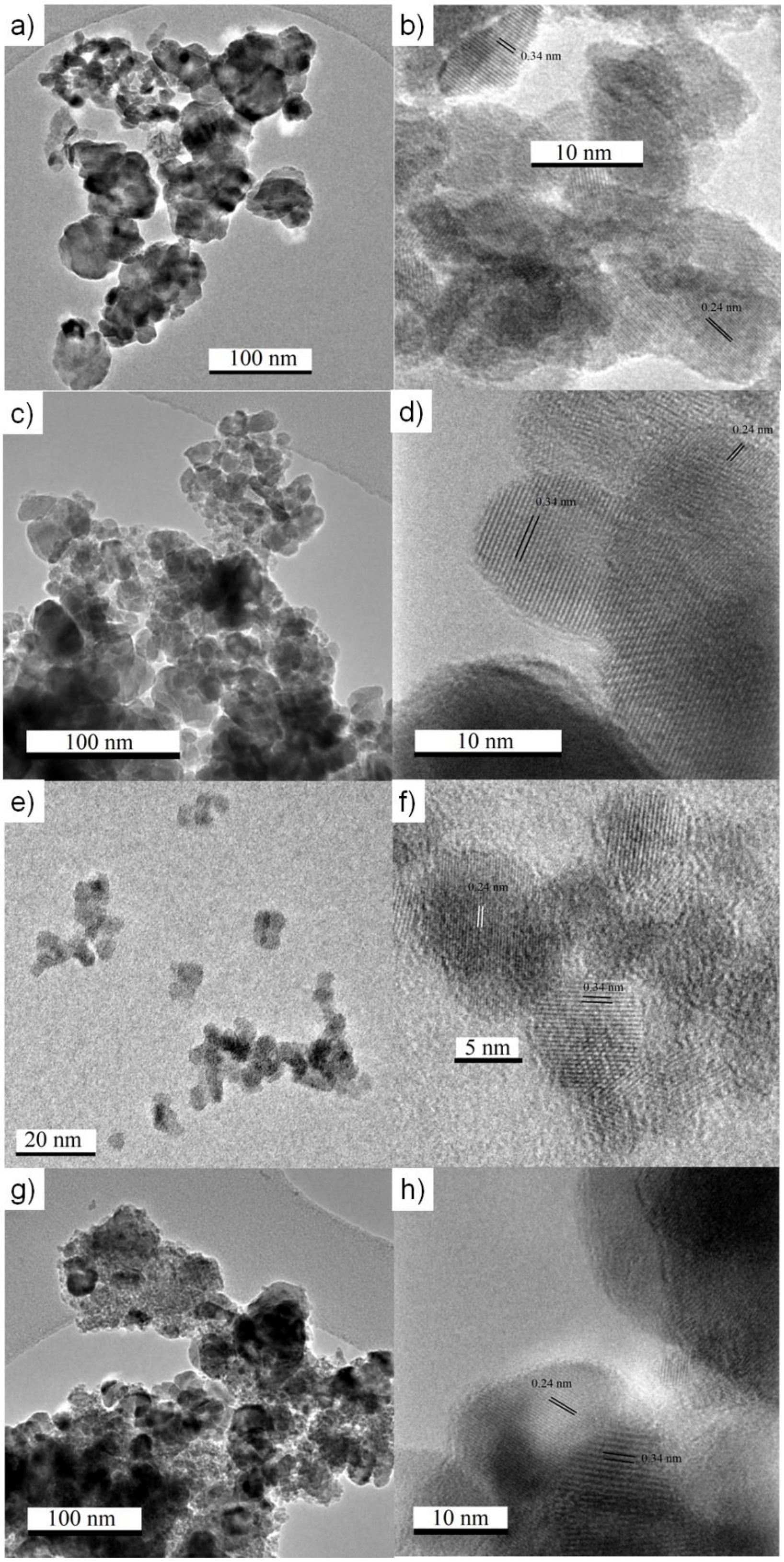

Figure 5-7: Transmission electron micrographs showing a general overview of particles and lattice fringes for (a and b) MoO_2, (c and d) TiO_2/MoO_2-1, (e and f) TiO_2/MoO_2-3, and (g and h) TiO_2/MoO_2-4.

samples, which likely correspond to the (011) and (-211) planes, respectively, of monoclinic MoO_2.

5.4.1.2. *Electrochemical Characterisation of TiO_2/MoO_2 Composites*

Cyclic voltammograms for MoO_2 and the composite materials revealed significant differences. The pure MoO_2 showed two anodic peaks at 1.5 and 1.8 V vs. Li/Li^+ at a scan rate of 0.1 mV s^{-1}, which were associated with the phase transformation from monoclinic to orthorhombic and orthorhombic to monoclinic as delithiation occurred (see Figure 5-8a and Equation 5.1).[180] Whilst the CVs for the composite samples with ca. 5 and 10 mol% TiO_2 (TiO_2/MoO_2-1 and TiO_2/MoO_2-2) only revealed small

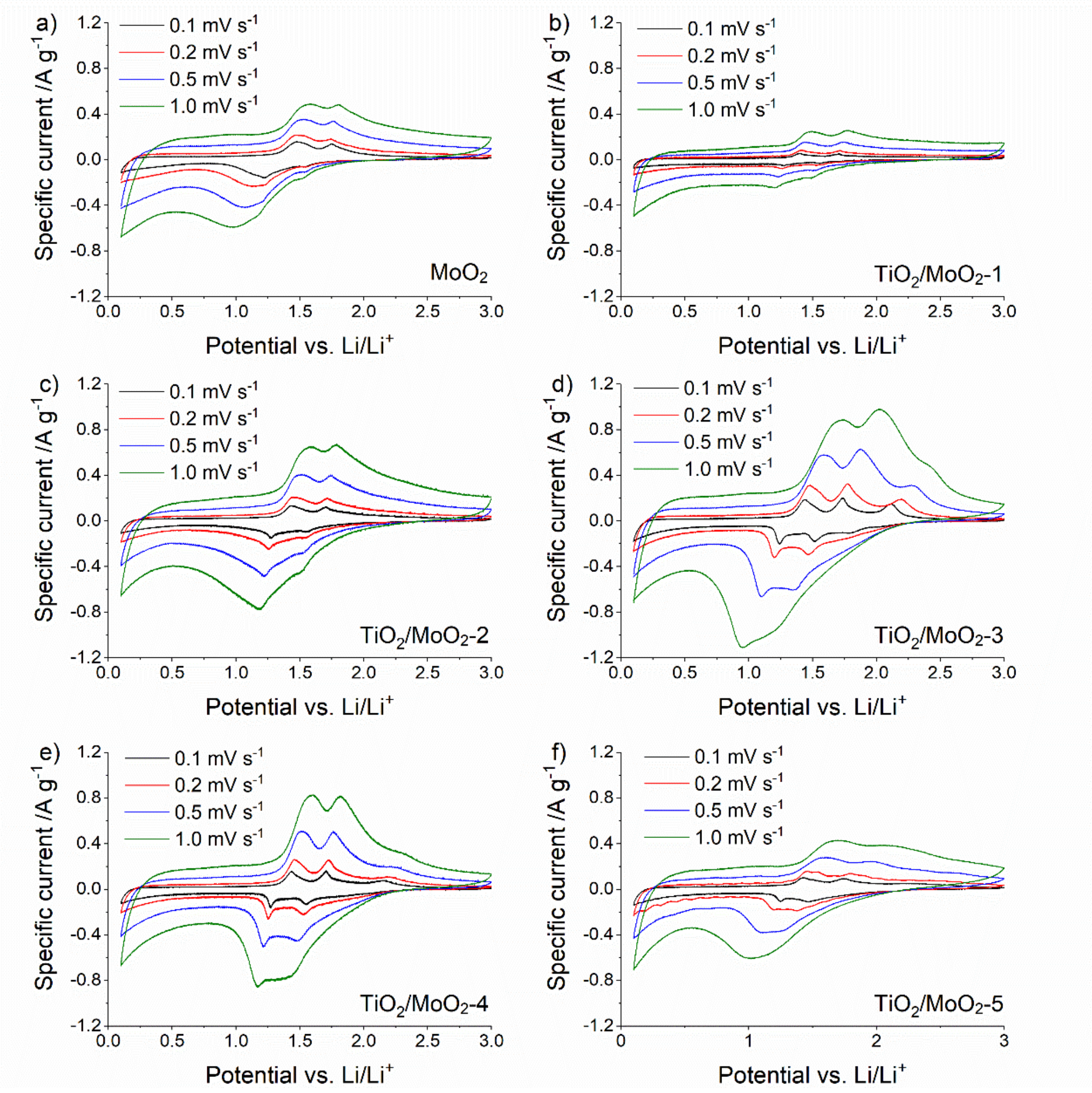

Figure 5-8: Cyclic voltammograms at scan rates of 0.1, 0.2, 0.5, and 1.0 mV s^{-1} for a) MoO_2, b) TiO_2/MoO_2-1, c) TiO_2/MoO_2-2, d) TiO_2/MoO_2-3, e) TiO_2/MoO_2-4, and f) TiO_2/MoO_2-5.

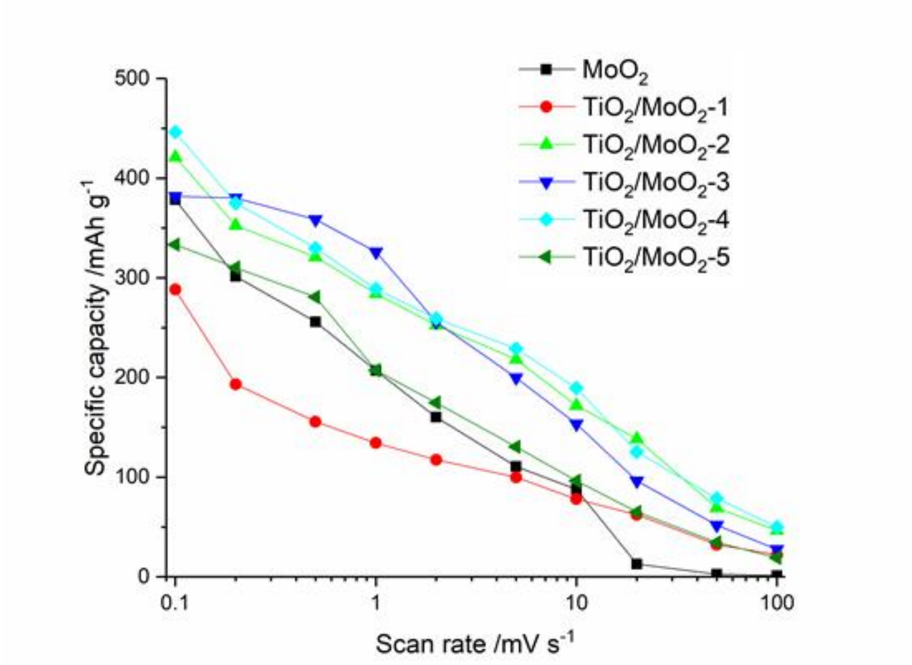

Figure 5-9: Specific capacities for MoO_2 and the TiO_2/MoO_2 composites at scan rates in the range 0.1 to 100 mV s^{-1}.

differences compared to MoO_2 (see Figure 5-8b and c), the shapes of the CVs for the composite materials with a higher mol% of TiO_2 were significantly different. Especially for the samples with 20 and 33 mol% (TiO_2/MoO_2-3 and TiO_2/MoO_2-4), additional anodic (lithium extraction) and cathodic (lithium insertion) peaks appeared at potentials of 2.1 V and 1.8 V vs. Li/Li^+, respectively (see Figure 5-8d and e). These could be ascribed to the reversible redox reaction related to the Ti^{3+}/Ti^{4+} transition in TiO_2 (see Section 3.1).[53,54] For the sample with an even higher molar concentration of TiO_2 (TiO_2/MoO_2-5, see Figure 5-8f), the additional peaks were also present, but broader than for the other composite samples.

As the scan rates were increased, overpotentials increased (indicated by increasing peak separation between cathodic and anodic sweeps) as was expected. Additionally, the peaks broadened, as would be expected for pseudocapacitive and intercalation active materials. At a scan rate of 1 mV s^{-1}, the additional lithiation and delithiation peaks due to TiO_2 were barely noticeable, and especially for TiO_2/MoO_2-5, the CVs were significantly broadened at higher potentials. However, the two anodic lithium extraction peaks were still distinguishable for all samples.

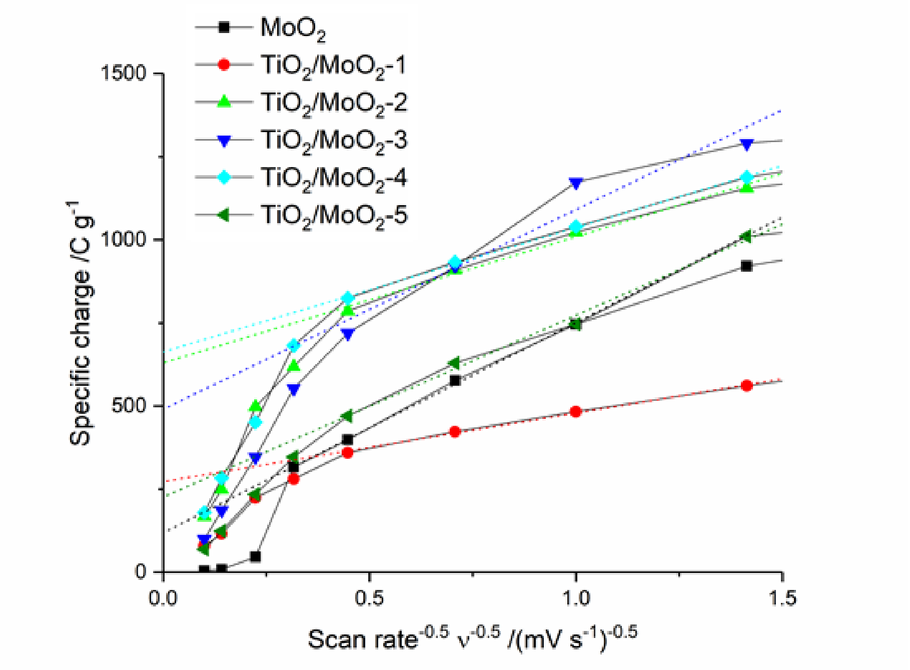

Figure 5-10: Specific charge for MoO_2 and the TiO_2/MoO_2 composites at scan rates in the range 0.1 to 100 mV s^{-1}.

Especially for the composite samples TiO_2/MoO_2-2, TiO_2/MoO_2-3, and TiO_2/MoO_2-4, an increase in scan rate led to significantly higher specific currents than for pure MoO_2, indicating superior rate performance. This was confirmed by the higher capacities the composite samples showed at higher scan rates (see Figure 5-9). For example, at a scan rate of 2 mV s^{-1}, the specific capacities were 160, 253, 256, and 259 mAh g^{-1} for MoO_2, TiO_2/MoO_2-2, TiO_2/MoO_2-3, and TiO_2/MoO_2-4, respectively.

To determine the pseudocapacitive contribution to the overall charge storage, the specific charge was plotted over the reciprocal square root of the scan rate, as explained in Section 1.5.1.1.[68,73,80] The pseudocapacitive charge storage at a theoretical, infinitely fast scan rate was determined from the intercept of the straight line, which was determined from the specific charge at intermediary scan rates. The pseudocapacitive charges at a theoretical, infinitely fast scan rate were 118, 273, 630, 490, 663, and 225 C g^{-1} for MoO_2, TiO_2/MoO_2-1, TiO_2/MoO_2-2, TiO_2/MoO_2-3, TiO_2/MoO_2-4, and TiO_2/MoO_2-5, respectively. This indicated that pseudocapacitive charge storage was significantly higher for the composite samples. The pseudocapacitive charges at unlimited scan rate for the composite samples TiO_2/MoO_2-2, TiO_2/MoO_2-3, and TiO_2/MoO_2-4 were higher than those reported for

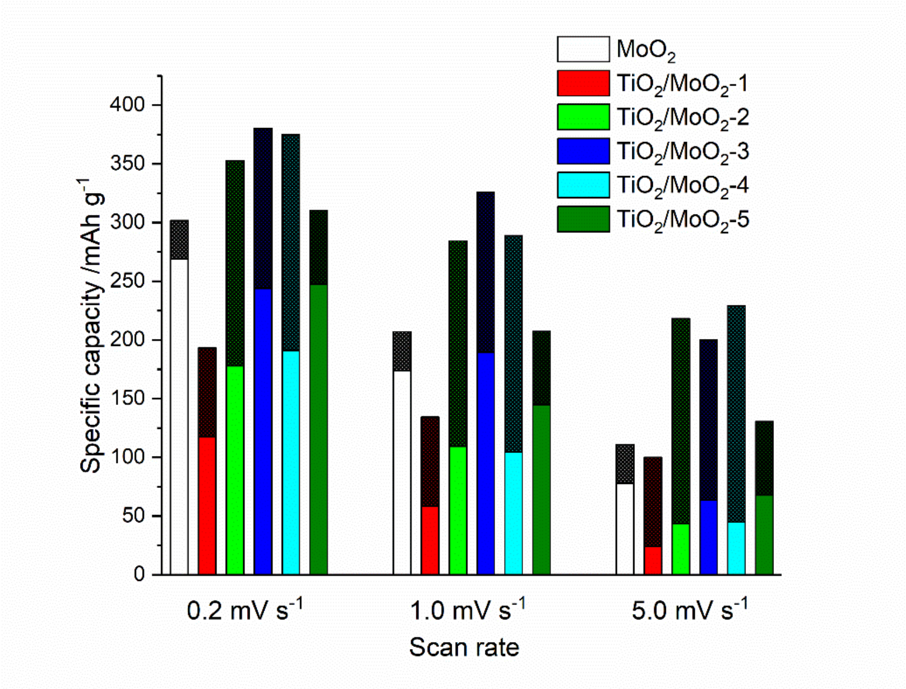

Figure 5-11: Contributions to charge storage from diffusion-limited and pseudocapacitive processes (shaded area) for the various samples at 0.2, 1.0, and 5.0 mV s^{-1}.

nanosized MoO_2 reported in the literature (literature value 300 C g^{-1}).[57] The pseudocapacitive and diffusion-limited contributions to charge storage were analysed in Table 5-1 and Figure 5-11. At a scan rate of 10 mV s^{-1}, pseudocapacitive contributions were near 80 % for all samples except the pure MoO_2 (only 30 %) and the composite sample containing 50 mol% TiO_2 (only 48 %). The improved pseudocapacitive charge storage and its larger contribution to the total charge storage in (some of) the composite samples was attributed to the small size of MoO_2 particles due to the TiO_2 seeds, the higher surface area, and the close interaction of TiO_2/MoO_2 in the composites, which could have facilitated rapid (near-)surface charge transfer processes.[99] The TiO_2 seeds may also have had a structural stabilising effect on the MoO_2.

Galvanostatic rate testing showed similar specific capacities of ca. 350 mAh g^{-1} after 10 cycles at 0.1 A g^{-1} for MoO_2, TiO_2/MoO_2-3, and TiO_2/MoO_2-4 (see Figure 5-12). The lowest specific capacities of ca. 185 mAh g^{-1} were observed for TiO_2/MoO_2-1, which was consistent with the results from potentiodynamic measurements. Coulombic efficiencies were poor in the first cycle for all samples, but rapidly improved once SEI formation concluded, and was consistently above 99 %,

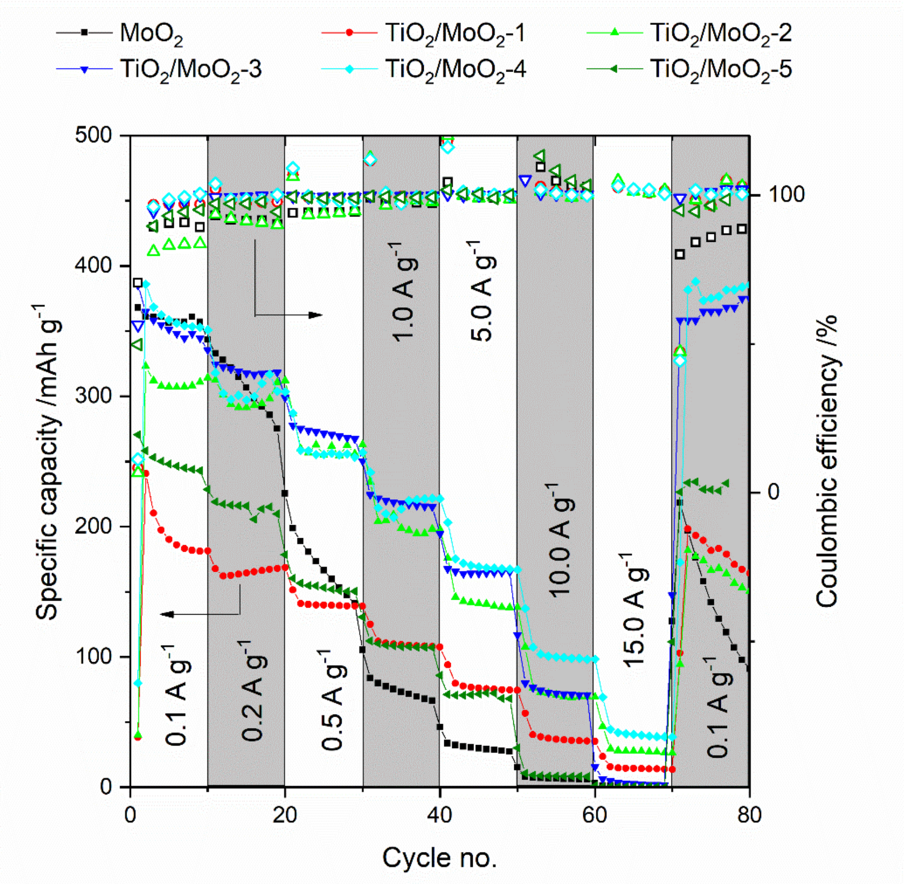

Figure 5-12: Galvanostatic charge/discharge cycling for MoO_2 and the TiO_2/MoO_2 composites, showing both Coulombic efficiency and specific capacities.

especially at higher rates. The specific capacity of the pure MoO_2 sample dropped significantly with cycle number and increasing applied current. When the specific current was increased to 0.2 and 0.5 A g^{-1}, the specific capacity declined significantly with each consecutive cycle. This could have been a result of instabilities of the electrode because of conversion reactions of the active material. At a specific current of 1.0 A g^{-1}, the specific capacity for MoO_2 had dropped to below 100 mAh g^{-1}, showing the poorest performance of all samples. At this current rate, TiO_2/MoO_2-2, TiO_2/MoO_2-3, and TiO_2/MoO_2-4 showed the highest specific capacities of ca. 200, 210, and 220 mAh g^{-1}, respectively. At a specific current of 5 A g^{-1}, the specific capacities for TiO_2/MoO_2-2, TiO_2/MoO_2-3, and TiO_2/MoO_2-4 were still 145, 160, and 160 mAh g^{-1}. To put this into context, this meant that 160 mAh g^{-1} could be charged or discharged in less than two minutes each.

After the specific current was returned to 0.1 A g^{-1} (after cycling at different specific currents of up to 15 A g^{-1} for 70 cycles), the specific capacities for both TiO_2/MoO_2-3 and TiO_2/MoO_2-4 returned to over 350 mAh g^{-1}, indicating excellent cycling stability. The capacities for the other samples also increased upon the decrease of the specific current, but not as significantly, or as stably, as for TiO_2/MoO_2-3 and TiO_2/MoO_2-4. The improved cycling stability and capacity at high applied currents for the composite TiO_2/MoO_2-3 and TiO_2/MoO_2-4 electrodes were attributed to a diluting and stabilising effect that the TiO_2 nanoparticles had on the normally unstable conversion reaction of MoO_2 (cycled below 1.0 V vs. Li/Li^+), because anatase undergoes minimal volume changes upon lithiation and delithiation (see Section 3.2). For comparison, pure TiO_2 synthesised via CHFS cycled in the same potential window of 0.1 to 3.0 V vs. Li/Li^+ showed specific capacities of ca. 225 and 120 mAh g^{-1}, at specific currents of 0.1 and 1.0 A g^{-1}, respectively.[204]

Table 5-1: Proportions of charge storage via pseudocapacitive processes for the different TiO_2/MoO_2 composites and pure MoO_2.

		Pseudocapacitive contributions to charge storage [%]				
Scan rate	MoO_2	TMO-1	TMO-2	TMO-3	TMO-4	TMO-5
0.2 mV s^{-1}	11	40	50	38	49	20
1.0 mV s^{-1}	16	56	62	53	64	30
10.0 mV s^{-1}	30	76	80	78	80	48

To further investigate the stability of the various composite materials, all materials were cycled at a relatively high specific current of 2.5 A g^{-1} (see Figure 5-13). As would have been expected, the electrodes made from pure MoO_2 showed a rapid decline in capacity, from over 250 mAh g^{-1} to below 100 mAh g^{-1} after 100 cycles and no retention of significant capacity after 250 cycles. Both the composites with the highest and lowest concentration of TiO_2 (TiO_2/MoO_2-5 and TiO_2/MoO_2-1, respectively) showed rapidly declining capacities as well as relatively low initial capacities, which indicated that a small and a large amount of TiO_2 were disadvantageous to the performance of MoO_2 in these electrodes. The samples with

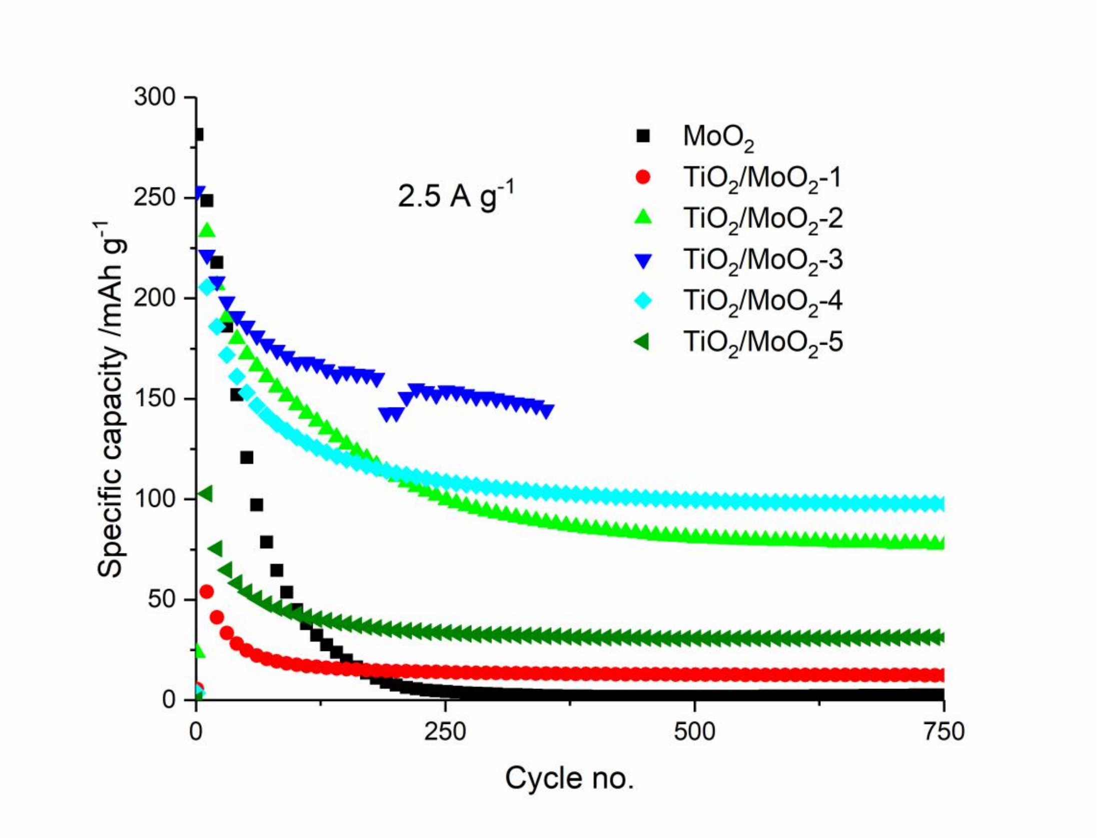

Figure 5-13: Galvanostatic cycling stability test at a specific current of 2.5 A g^{-1}.

intermediate TiO_2 concentrations, however, showed much better capacity retention. TiO_2/MoO_2-2, TiO_2/MoO_2-3, and TiO_2/MoO_2-4 showed specific capacities of over 100 mAh g^{-1} after 250 cycles. The TiO_2/MoO_2-3 composite retained a capacity of ca. 150 mAh g^{-1} after 350 cycles.

To ensure that the improved electrochemical properties in LIBs of selected composite samples was a result of the co-precipitation with TiO_2, electrodes were prepared by mixing 80 mol% of MoO_2 with 20 mol% of TiO_2, both synthesised via CHFS, as described in Sections 2.1.1 and 2.1.3. This ratio was equivalent to that in TiO_2/MoO_2-3. As can be seen from Figure 5-14a, the initial specific capacity for TiO_2/MoO_2-3 was 250 mAh g^{-1} and the coulombic efficiency was ca. 92 %, at a specific current of 2.5 A g^{-1}. After 350 cycles, the specific capacity was still 150 mAh g^{-1} and coulombic efficiencies were above 99.5 %. On the other hand, the manually mixed composite electrodes showed an initial specific capacity of 430 mAh g^{-1}, with a coulombic efficiency of 93 % (see Figure 5-14b). However, the specific capacity rapidly declined, so that after 50 cycles at a specific current of

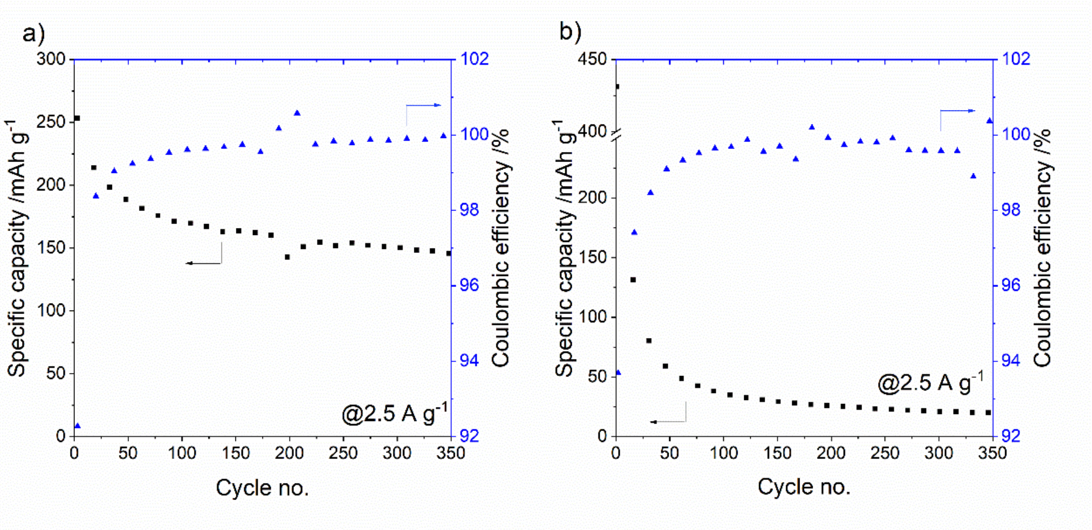

Figure 5-14: Comparison of long term galvanostatic cycling of electrodes made from a) TiO_2/MoO_2-3 and b) 20 mol% TiO_2 mixed with 80 mol% MoO_2.

2.5 A g^{-1}, the specific capacity was only ca. 50 mAh g^{-1}, and after 350 cycles, the specific capacity had fallen to 20 mAh g^{-1}. This was expected to be the remaining specific capacity provided by the TiO_2 component. Hence, it was suggested that the improved electrochemical performance of the composite samples was a result of the co-precipitation of MoO_2 with TiO_2, which acted as an “anchor” or low volume change additive that enabled greater cycling stability.

A comparison of the galvanostatic charge/discharge curves for MoO_2, TiO_2/MoO_2-1, and TiO_2/MoO_2-3 showed significant differences (see Figure 5-15). As expected from the CVs and the expected lithiation mechanism for MoO_2, the delithiation curve of the pure MoO_2 showed two plateaus at ca. 1.30 and 1.55 V vs. Li/Li^+, respectively, at a specific current of 0.1 A g^{-1}. However, TiO_2/MoO_2-3 showed an additional delithiation plateau at ca. 2.1 V vs. Li/Li^+, which was in line with results from CVs and attributed to the delithiation of TiO_2. In contrast, for TiO_2/MoO_2-1 (with just 5 mol% TiO_2), the intercalation reactions for MoO_2 seemed inhibited and no plateaus were observed at 0.1 A g^{-1}. This could have been a result of the additional grain boundaries due to the TiO_2, which, because of the low concentration, did not add any of the benefits shown at higher TiO_2 concentrations.

The difference in rate performance was most obvious for the galvanostatic charge/discharge plots of MoO_2 and TiO_2/MoO_2-3 at 1.0 A g^{-1}; whilst the curve for

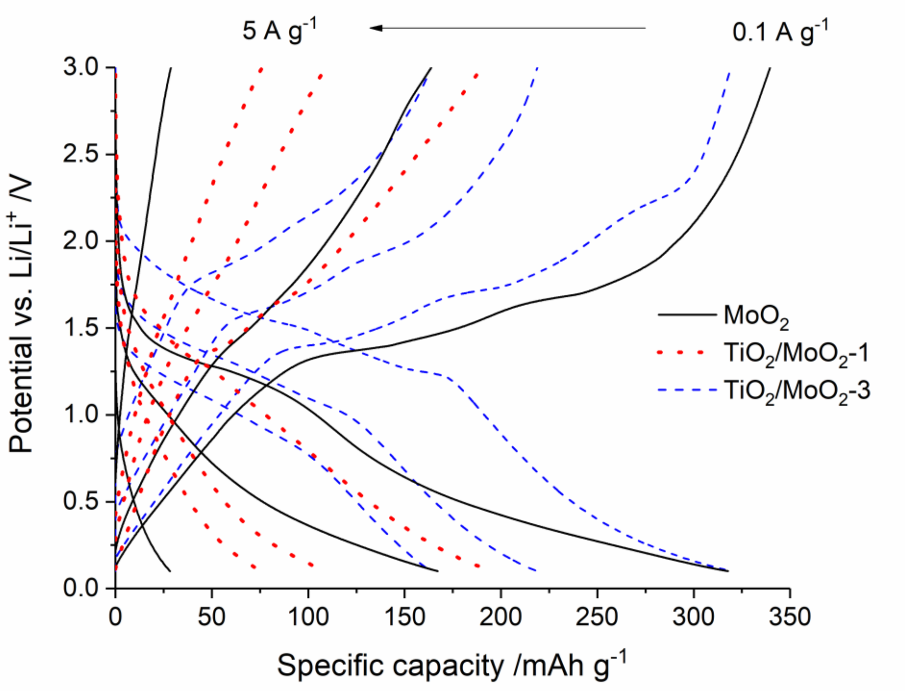

Figure 5-15: Galvanostatic charge/discharge curves for MoO_2, TiO_2/MoO_2-1, and TiO_2/MoO_2-3 at specific currents of 0.1, 1.0, and 5.0 A g^{-1}.

MoO_2 showed no plateaus, the curve for TiO_2/MoO_2-3 still showed three distinct plateaus. Interestingly, the additional delithiation capacity of TiO_2/MoO_2-3 compared to MoO_2 mostly occurred above 1.6 V vs. Li/Li$^+$. The average overpotentials for the charge stored were significantly lower for the composite sample than the pure MoO_2. This could indicate that conversion reactions, which are essential for the charge storage in pure MoO_2 at low potentials vs. Li/Li$^+$, were inhibited in the samples containing higher concentrations of TiO_2, and pseudocapacitive charge storage was promoted.

Post-mortem analysis of electrodes cycled for 40 cycles at a specific current of 0.2 A g^{-1} was carried out using scanning electron microscopy (SEM). Whilst an MoO_2 electrode showed significant connected cracks (see Figure 5-16b and d), a TiO_2/MoO_2-3 electrode showed significantly smaller and less connected cracking (see Figure 5-16a and c). Thus, the differences in volume changes during lithiation and delithiation for conversion reactions may be responsible for electrode cracking[149] (or even the cracking of larger agglomerates of active materials themselves).[148] Cracking of the electrode and agglomerates can result in poor capacity retention. It was expected that due to its chemical and structural stability, co-precipitation of MoO_2 with anatase improved the stability of the electrodes, as has previously been reported

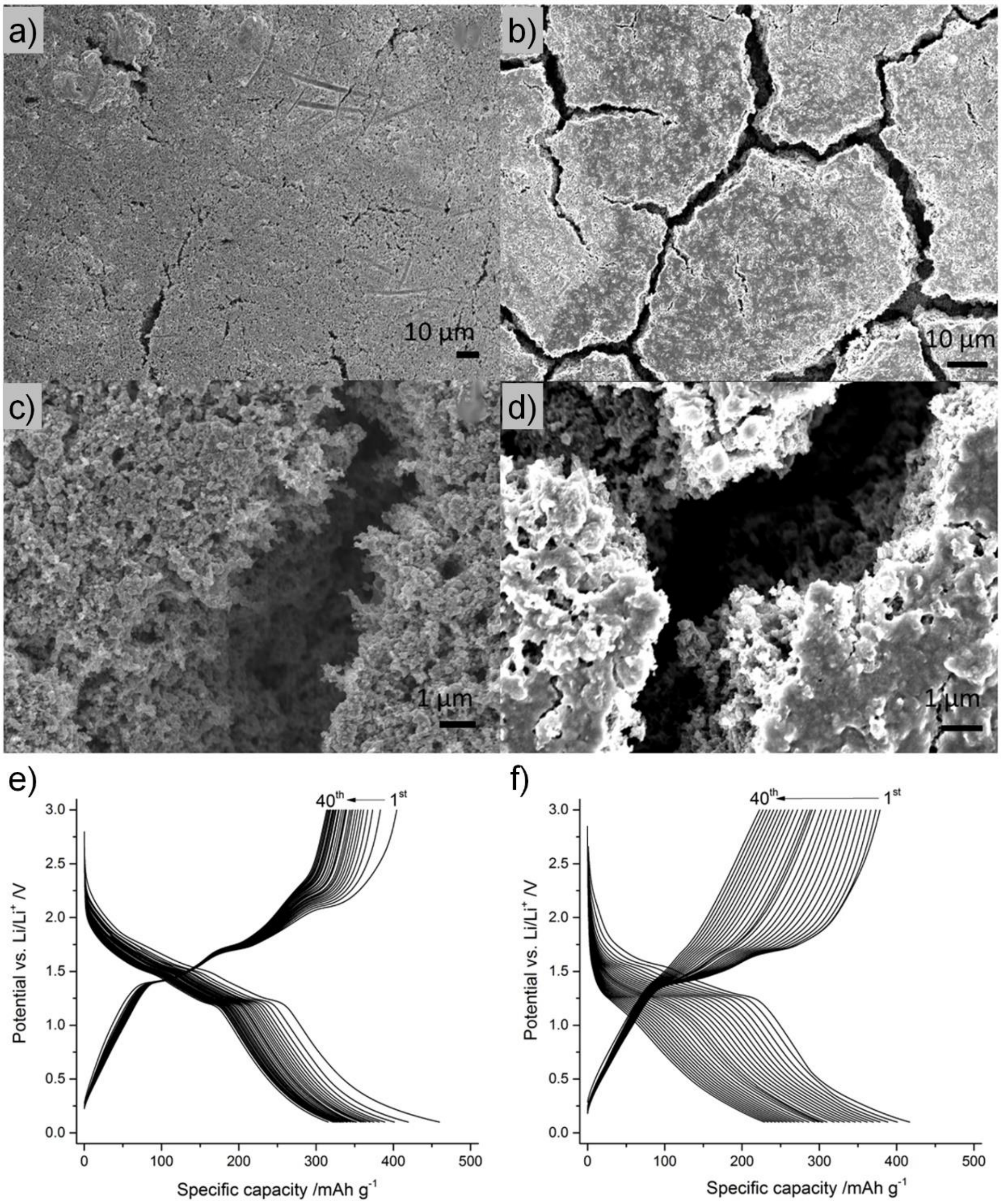

Figure 5-16: Scanning electron micrographs of electrodes made using (a and c) TiO_2/MoO_2-3 and (b and d) MoO_2 active material, after cycling for 40 cycles. Galvanostatic charge/discharge cycling for e) TiO_2/MoO_2 and f) MoO_2 for 40 cycles at 0.2 A g^{-1}.

for other composites such as $TiO_2@Fe_2O_3$ arrays,[153] $Fe_3O_4@TiO_2$ clusters,[154] and MoS_2/TiO_2 composites.[286] However, it is important to consider that the cracking could also have been a result of the manual handling of the electrodes during the deconstruction of the cell, the drying of the solvent in the electrolyte, or loading the electrodes to be measured by XPS. Therefore, the cracking cannot be guaranteed to be a result of the mechanism(s) discussed above.

Cracking has sometimes been associated with the use of high applied currents, due to the inhomogeneous distribution of Li^+ in the electrode which can be a result of diffusion limitations.[150] This could explain the rapid deterioration in specific capacities for the pure MoO_2 at higher current rates. In contrast, due to its structural stability, TiO_2 in the composite could have mitigated pulverization and capacity fade.[154] This could be observed from the significantly better reversibility of the lithiation and delithiation of the composite sample, compared to the pure MoO_2 containing electrodes, as observed in Figure 5-16e compared to Figure 5-16f. For 40 cycles, there was only a minimal change in the plateaus, indicative of the removal of Li^+ from the crystal structure during discharge for the composite sample (TiO_2/MoO_2-3). For half-cells containing pure MoO_2, these plateaus nearly disappeared under the same conditions. This was suggested to be due to the additional structural stability afforded by the presence of nano-TiO_2; the TiO_2 phase acted as a buffer for the volume changes[283] and as a support for the back-reaction of Li_2O during the delithiation, as shown in Equation 5.2.

Li-HECs were prepared using sample TiO_2/MoO_2-3 (20 mol% TiO_2) as the active material in the negative electrode and AC positive electrodes. As previously described, the materials were balanced to give an optimised performance.

To avoid significant degradation in early cycles due to the irreversible loss of lithium ions (because of irreversible side reactions and the creation of a SEI), the Li-HECs were cycled in a narrow potential window of 1.0 to 3.0 V. This avoided unacceptably high degradation, but also severely limited the usefulness of the material described in this chapter. The TiO_2/MoO_2 composite electrodes would have limited capacity if they were cycled in the potential window of only ca. 2.5 to 1.0 V vs. Li/Li^+ (rather than 3.0 to 0.1 V vs. Li/Li^+ as described above). As could be observed in both the CVs (see Figure 5-8a and d) and the charge/discharge profiles (see Figure 5-15), both a significant amount of charge storage occurred in the range 1.0 to 0.1 V vs. Li/Li^+ and the initial conversion and SEI formation consumed significant amounts of Li-ions. Because of this, pre-lithiation was used to improve the performance of

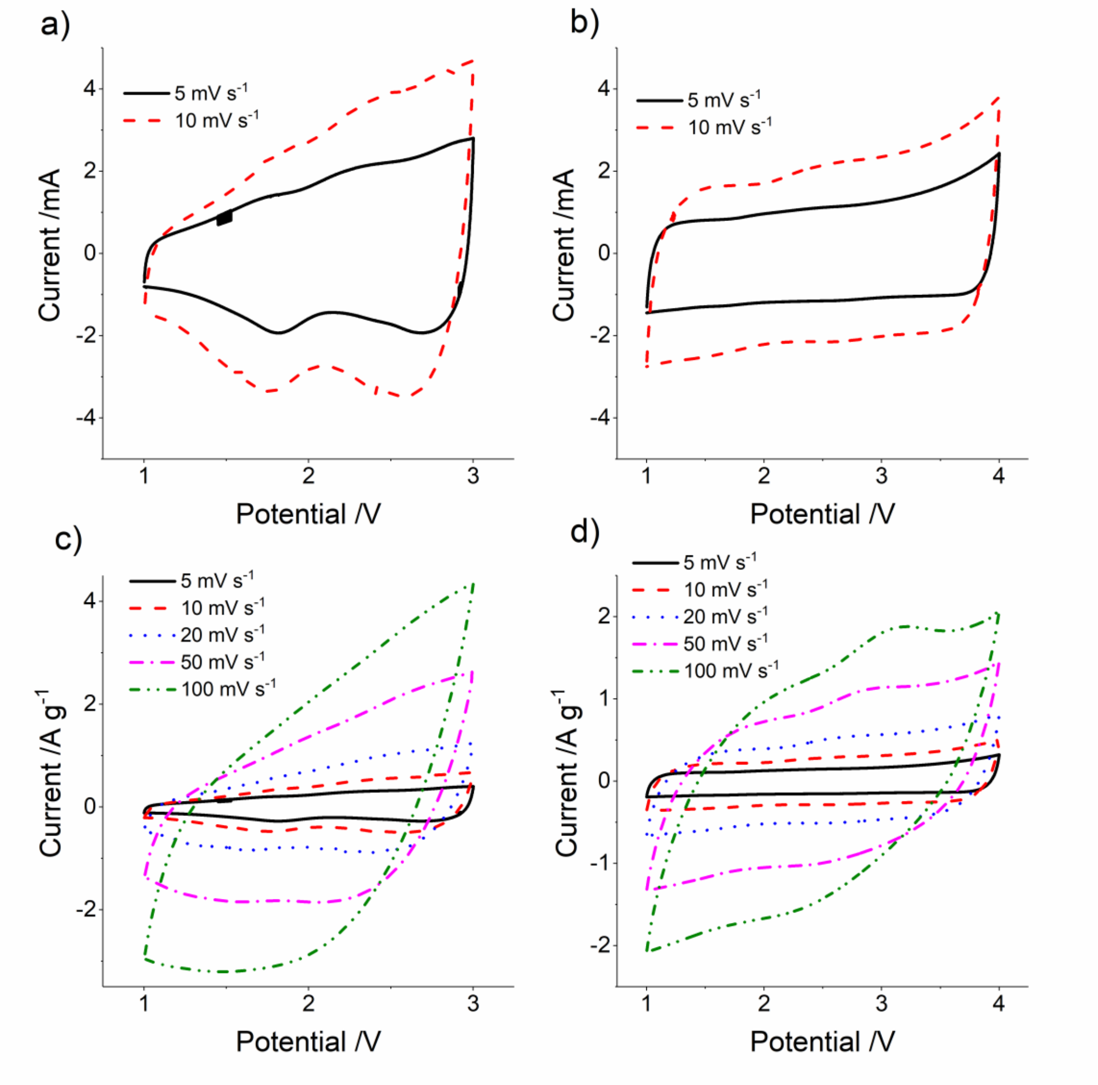

Figure 5-17: Cyclic voltammograms at scan rates of 5 and 10 mV s^{-1} for a) a non-pre-lithiated and b) a pre-lithiated TiO_2/MoO_2//AC Li-HEC. CVs at scan rates in the range 5 to 100 mV s^{-1}, for c) a non-pre-lithiated and d) a pre-lithiated TiO_2/MoO_2//AC Li-HEC.

TiO_2/MoO_2//AC Li-HECs, as discussed in Section 3.4.2.3. The pre-lithiated Li-HEC was cycled in the potential window 1.0 to 4.0 V.

The TiO_2/MoO_2//AC Li-HEC showed good capacitive behaviour during potentiodynamic cycling in the potential window 1.0 to 3.0 V at moderate scan rates of 5 and 10 mV s^{-1}, as indicated by a square shape of the CVs (see Figure 5-17a). However, there were appreciable peaks, which was indicative of imperfect balancing between active mass loadings. At higher scan rates of 50 and 100 mV s^{-1}, the CVs became distorted from square to trapezoid (see Figure 5-17c). However, for a pre-lithiated TiO_2/MoO_2//AC Li-HEC, the CVs were perfectly rectangular, indicating

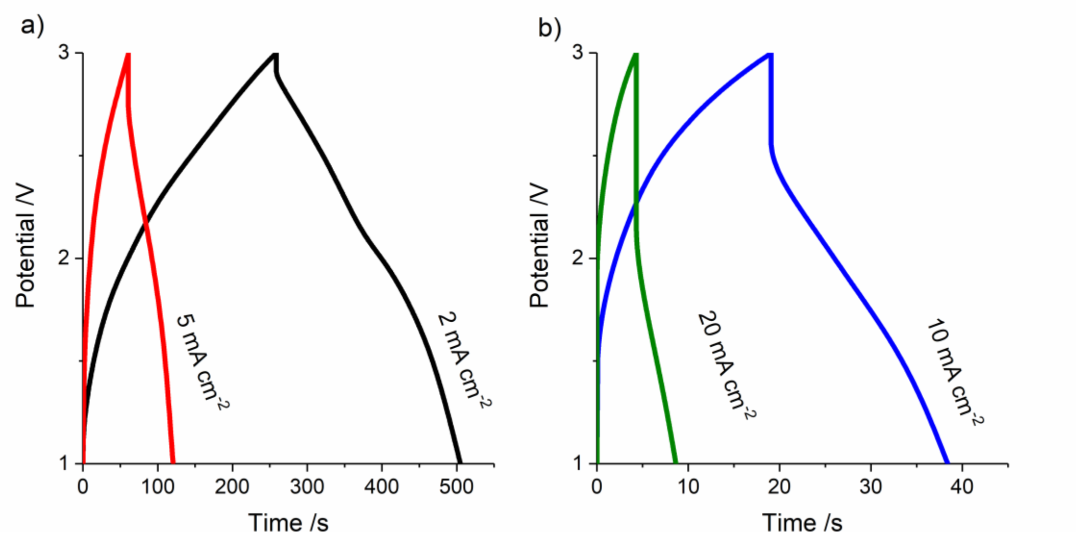

Figure 5-18: Galvanostatic charge/discharge curves of a non-pre-lithiated TiO_2/MoO_2//AC Li-HEC at current densities of a) 2 and 5 mA cm^{-2} and b) 10 and 20 mA cm^{-2}.

excellent capacitive behaviour (see Figure 5-17b). Even at the higher scan rates of 50 and 100 mV s^{-1}, the CVs were still rectangular, with only minor distortions (see Figure 5-17d).

The specific capacitances of a TiO_2/MoO_2//AC Li-HEC were significantly higher than for the pre-lithiated TiO_2/MoO_2//AC Li-HEC. A TiO_2/MoO_2//AC Li-HEC showed specific capacitances of 42, 32, and 18 F g^{-1} at scan rates of 5, 20, and 100 mV s^{-1}, respectively. The pre-lithiated TiO_2/MoO_2//AC Li-HEC showed specific

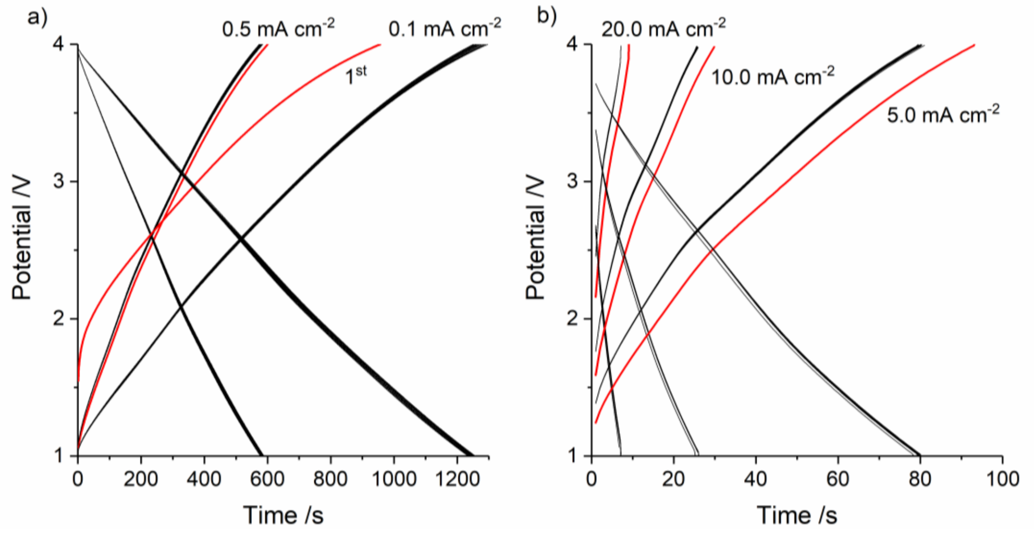

Figure 5-19: Galvanostatic charge/discharge curves for the first (red) and further 9 cycles of a pre-lithiated TiO_2/MoO_2//AC Li-HEC at current densities of a) 0.1 and 0.5 mA cm^{-2} and b) 5, 10, and 20 mA cm^{-2}.

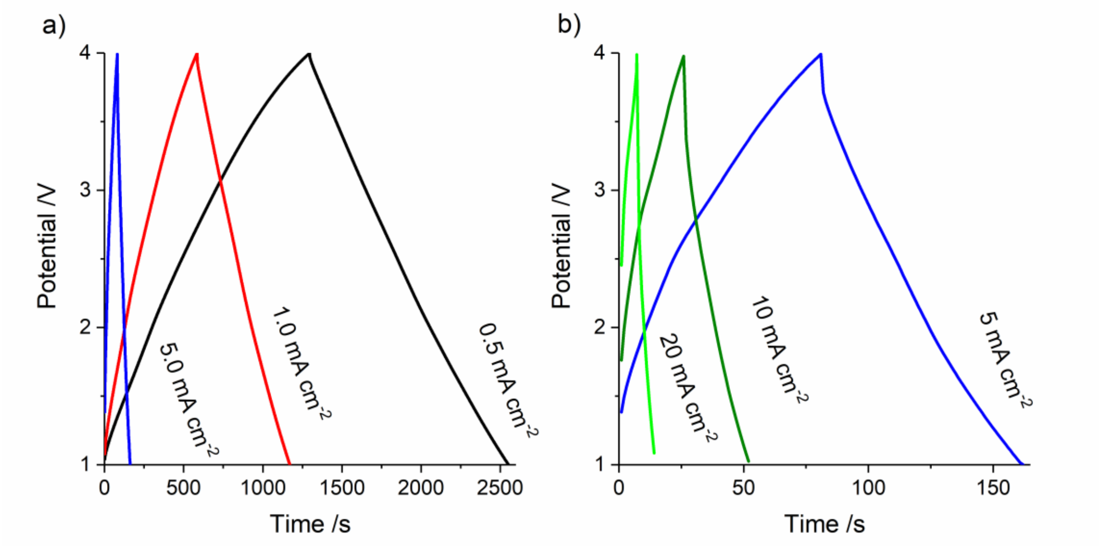

Figure 5-20: Galvanostatic charge/discharge curves of a pre-lithiated TiO_2/MoO_2//AC Li-HEC at current densities of a) 0.5, 1.0, and 5.0 mA cm^{-2} and b) 5, 10, and 20 mA cm^{-2}.

capacitances of 30, 23, and 11 F g^{-1} at scan rates of 5, 20, and 100 mV s^{-1}, respectively. When considering the larger potential window and the higher average potential of the pre-lithiated Li-HEC, the energy density for the pre-lithiated device was higher than for the non-pre-lithiated Li-HEC.

As the CVs, the charge/discharge curves for the TiO_2/MoO_2//AC Li-HEC showed capacitive behaviour, with curves only slightly diverging from the expected triangular shape expected for purely capacitive behaviour (see Figure 5-18a). At higher current densities of 10 and 20 mA cm^{-2}, the IR drop significantly increased, making the charge/discharge curves less triangular (see Figure 5-18b).

In contrast, for the pre-lithiated TiO_2/MoO_2//AC Li-HEC, the shape of the charge/discharge curves (in the wider potential window of 1.0 to 4.0 V) was perfectly triangular, corroborating the excellent capacitive behaviour as indicated by the CVs for the same HEC (see Figure 5-20a). For the pre-lithiated Li-HEC, even at the much higher current densities of 10 and 20 mA cm^{-2}, the IR drop remained much smaller than for the non-pre-lithiated Li-HEC and the triangular shape remained, indicating highly capacitive behaviour.

The pre-lithiation of a TiO_2/MoO_2//AC Li-HEC did not only lead to better capacitive behaviour, it also significantly increased cycling stability. Upon the first

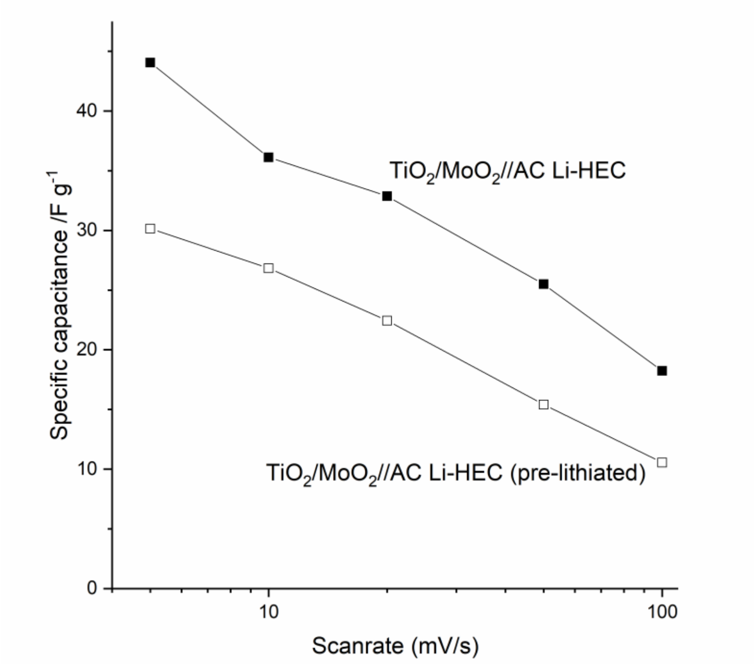

Figure 5-21: Specific capacitances at various scan rates for a non-pre-lithiated and a pre-lithiated TiO_2/MoO_2//AC Li-HEC.

charge cycle, the specific charge capacity was lower than the first discharge cycle. This was a result of the additional lithium from the pre-lithiation being released from the anode during discharge as explained in Section 3.4.2.3 (see Figure 5-19a). Furthermore, the higher OCV for the pre-lithiated HEC resulted in a higher initial potential for the first charge. For each subsequent cycle at higher current rates, the first charge was slightly longer than subsequent charges and discharges (see Figure 5-19a and b). This showed that when changing the current density, more lithium ions could be stored in the first cycle than removed, and in subsequent cycles, only the lithium ions that could be removed during the previous discharge could be replaced in the next charge. Generally, the differences between different cycles at the same current density were minimal, indicating good cycling stability.

The improved performance achieved via pre-lithiation, especially with regards to cycling stability and higher Coulombic efficiency, could be observed from cycling plots of specific capacitance and capacity of the different devices. Although the specific capacitances of the non-pre-lithiated TiO_2/MoO_2//AC Li-HEC were higher than those for the pre-lithiated TiO_2/MoO_2//AC Li-HEC (see Figure 5-21), this was a

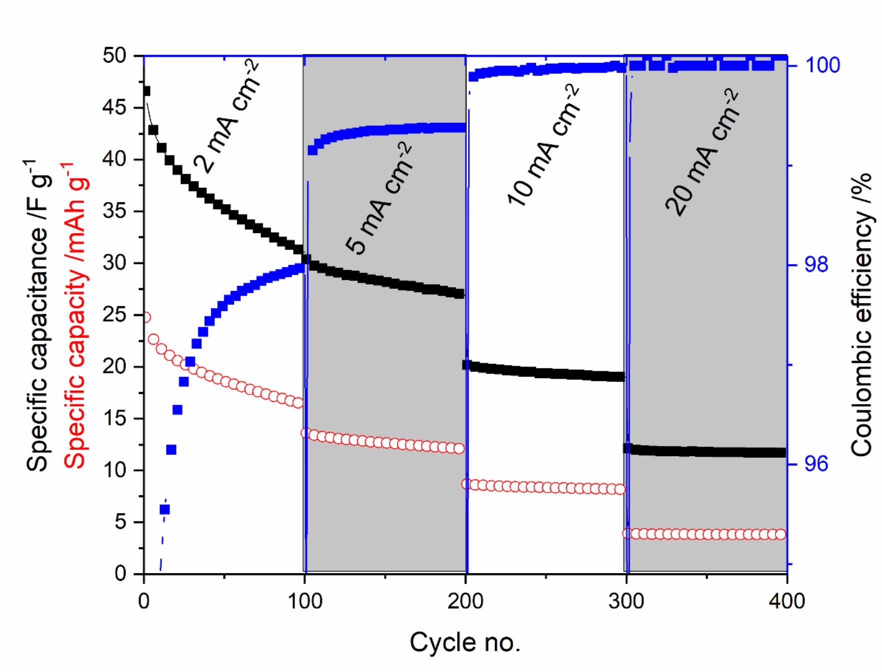

Figure 5-22: Specific capacitances, specific capacities, and Coulombic efficiencies from the galvanostatic cycling of a non-pre-lithiated TiO_2/MoO_2//AC Li-HEC at varying current densities of 2, 5, 10, and 20 mA cm^{-2}.

result of the smaller potential window the non-pre-lithiated Li-HEC was cycled in. Therefore, a comparison of the specific capacity and energy densities is more relevant.

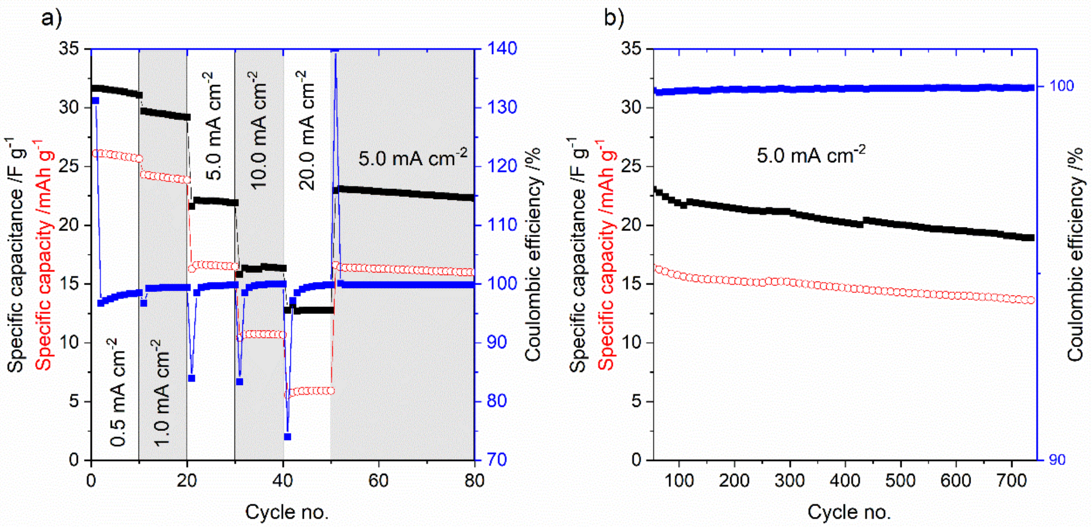

Figure 5-23: a) Specific capacitances, specific capacities, and Coulombic efficiencies from galvanostatic cycling of a pre-lithiated TiO_2/MoO_2//AC Li-HEC at varying current densities of 0.5, 1.0, 5.0, 10.0, and 20.0 mA cm^{-2}. b) Specific capacitances, specific capacities, and Coulombic efficiencies of the long-term galvanostatic cycling of a pre-lithiated TiO_2/MoO_2//AC Li-HEC at a current density of 5.0 mA cm^{-2}.

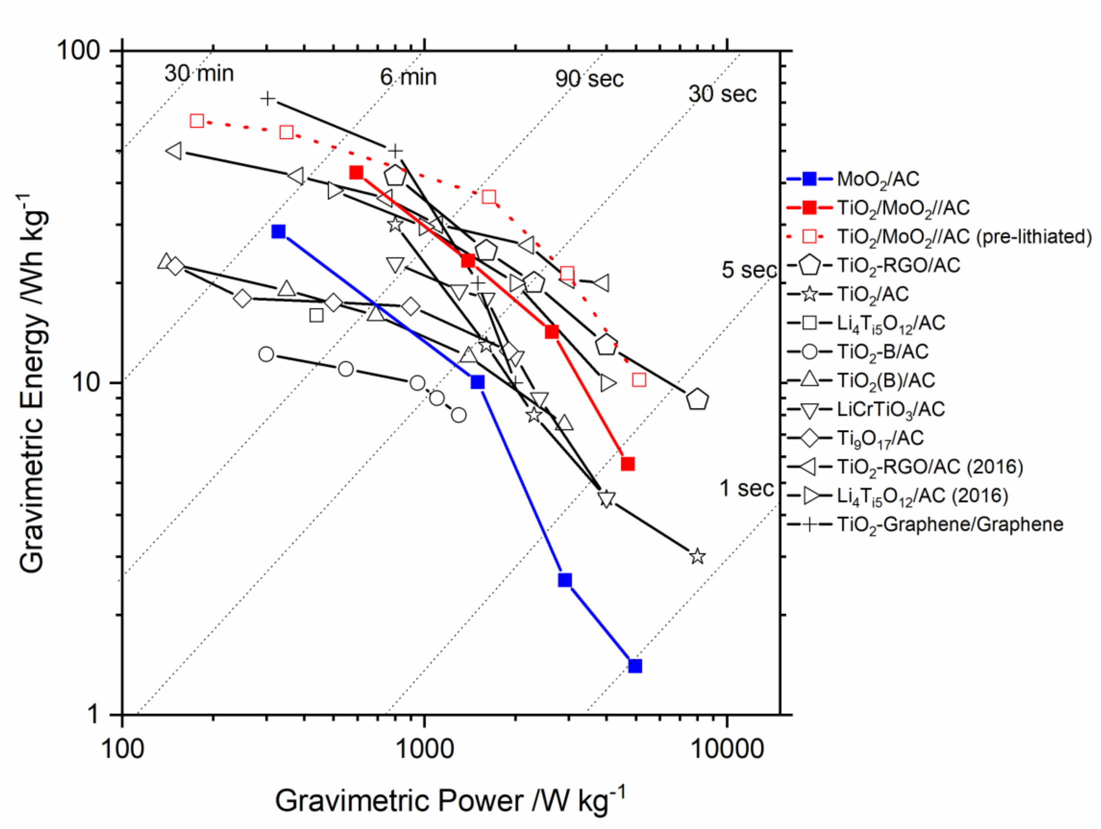

Figure 5-24: Ragone plot comparing the performance of the non-pre-lithiated and pre-lithiated TiO_2/MoO_2//AC Li-HECs and a MoO_2/AC Li-HEC with similar devices from the literature using anodes made of materials such as TiO_2-Reduced Graphene oxide and anatase TiO_2 [253], $Li_4Ti_5O_{12}$ [258], TiO_2-B [259], TiO_2(B) [260], $LiCrTiO_4$ [261], Ti_9O_{17} [262], TiO_2-Reduced Graphene oxide (2016) and $Li_4Ti_5O_{12}$ (2016) [257], and TiO_2 microspheres wrapped with graphene nanosheets versus a graphene nanosheet positive electrode [263].

A non-pre-lithiated TiO_2/MoO_2//AC Li-HEC showed a decrease in specific capacity from 25 to 16 mAh g^{-1} after 100 cycles at a current density of 2 mA cm^{-2} (see Figure 5-22). During these cycles, the Coulombic efficiency remained below 98 %. At higher current densities of 5 and 20 mA cm^{-2}, the specific capacities remained relatively stable (ca. 12.5 and 5 mAh g^{-1}, respectively). For a pre-lithiated TiO_2/MoO_2//AC Li-HEC, the initial Coulombic efficiency was above 130 % due to the additional Li-ions from the pre-lithiation being released upon the first discharge (see Figure 5-23a). In subsequent cycles at 0.5 mA cm^{-2}, the Coulombic efficiencies were over 98 %. The specific capacity was stable at ca. 26 mAh g^{-1} for 10 cycles at 0.5 mA cm^{-2} and even at higher current densities of 5 and 20 mA cm^{-2}, capacities were significantly higher than for the non-pre-lithiated Li-HEC (ca. 16 and 6 mAh g^{-1}, respectively). Furthermore, the pre-lithiated Li-HEC showed good cycling stability, with a fall in specific capacity from ca. 17 to ca. 14 mAh g^{-1} over 750 cycles at a current density of 5 mA cm^{-2} (see Figure 5-23b). Additionally, none of these considerations of Coulombic efficiency, cycling stability, or specific capacity, account for the improved energy and power densities achieved by the significantly higher average potential during discharge achieved by cycling the pre-lithiated TiO_2/MoO_2//AC Li-HEC up to 4 V.

As discussed for TiO_2/AC Li-HECs in Section 3.4.2.2, gravimetric energy and power densities were calculated using Equations 1.36 and 1.37. The energy and power densities were calculated for non-pre-lithiated and pre-lithiated TiO_2/MoO_2//AC Li-HEC and compared with the same devices from the literature as for TiO_2/AC Li-HECs, in a Ragone plot (see Figure 5-24). Additionally, a MoO_2/AC Li-HEC was prepared for comparison.

The pre-lithiated TiO_2/MoO_2//AC Li-HEC showed specific energy densities of 57, 36, and 10 Wh kg^{-1} at specific power densities of ca. 350, 1630, and 5130 W kg^{-1}. This was superior to the non-pre-lithiated TiO_2/MoO_2//AC Li-HEC, which showed energy densities of 43, 23, and 6 Wh kg^{-1} at power densities of ca. 600, 1400, and 4700 W kg^{-1}, respectively. As would have been expected from the above results, a MoO_2/AC Li-HEC showed the poorest performance, with energy densities of 29, 10, and 2 Wh kg^{-1} at power densities of ca. 330, 1500, and 4975 W kg^{-1}, respectively.

It was shown that the co-precipitation of MoO_2 with TiO_2 in CHFS could improve the cycling stability and rate performance of MoO_2 as active material in LIB and Li-HEC negative electrodes. Therefore, TiO_2/$NiCo_2O_4$ composites and Co_2TiO_4 were synthesised and tested as negative materials for LIBs to further study the influence of the inclusion of more stable TiO_2 on the electrochemical performance of conversion active materials. The synthesis and physical and electrochemical characterisation are described in Section 5.4.2.

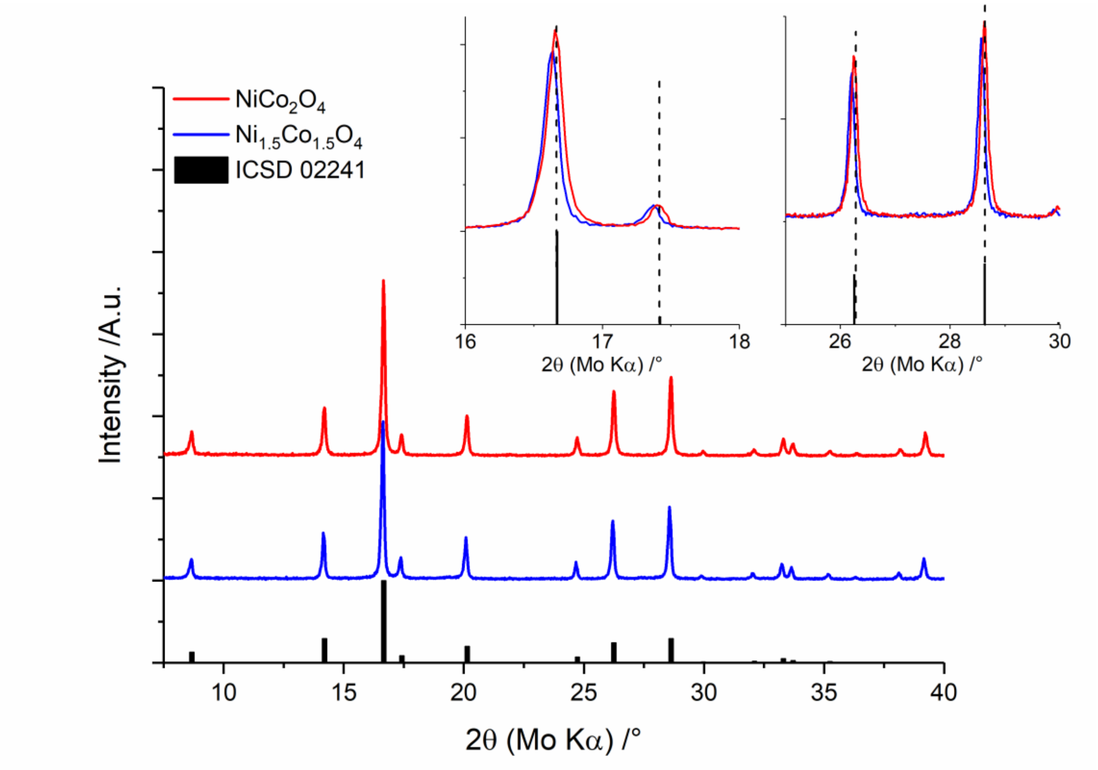

Figure 5-25: XRD patterns for $NiCo_2O_4$ (red) and $Ni_{1.5}Co_{1.5}O_4$ (blue) alongside the reference pattern for cubic spinel $NiCo_2O_4$ (black bars, ICSD no. 02241).

5.4.2. Co-based Materials

5.4.2.1. *$NiCo_2O_4$ and Co_2TiO_4*

XRD patterns for both $Ni_{1.5}Co_{1.5}O_4$ and $NiCo_2O_4$ matched the reference pattern for cubic spinel $NiCo_2O_4$ (ICSD reference no. 02241, space group Fd-3m). The main

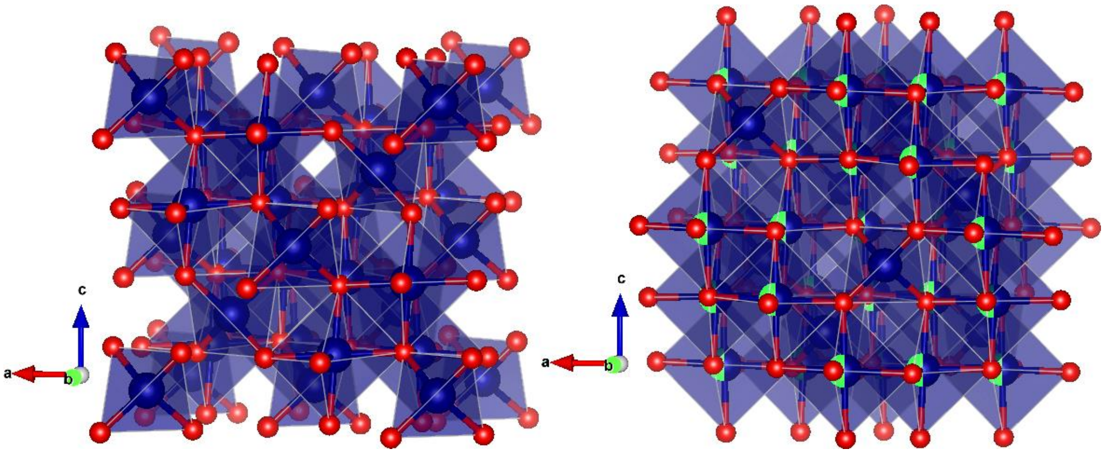

Figure 5-26: Polyhedral representations of spinel Co_3O_4 (left) and $NiCo_2O_4$ (right), with oxygen (red), cobalt (blue), and nickel (green) atoms.

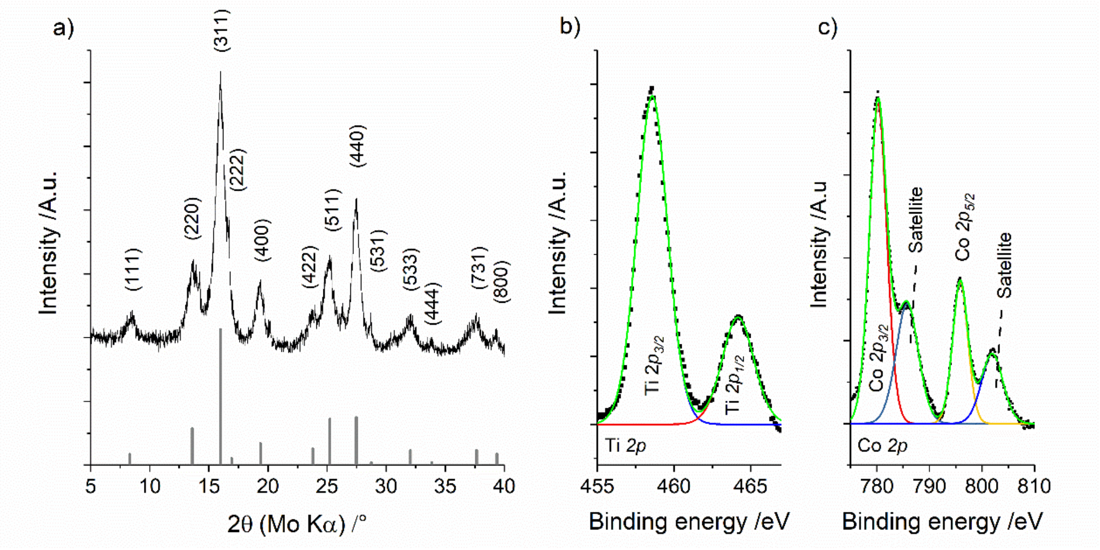

Figure 5-27: a) XRD pattern of Co_2TiO_4 alongside the reference pattern for cubic spinel Co_2TiO_4 (black bars, ICSD 69506). X-ray photoelectron spectra for Co_2TiO_4 at the binding energy levels of a) Ti *2p* and b) Co *2p*.

peaks at 2θ = 16.7, 26.3, and 28.6 ° were associated with the (311), (511), and (440) planes of the cubic spinel crystal structure (see Figure 5-25). No impurity phases of either NiO or CoO were detected. It has been shown in the literature that at synthesis temperatures above 500 °C, $NiCo_2O_4$ can decompose and form NiO or CoO.[306] It was expected that in the mixed metal spinel, the Ni replaces Co in the octahedral sites (see Figure 5-26). For $NiCo_2O_4$, this meant that half the cobalt ions in octahedral sites were replaced with nickel ions, whereas for $Ni_{1.5}Co_{1.5}O_4$, three quarters of cobalt ions in octahedral sites were expected to be replaced by nickel. Furthermore, there were

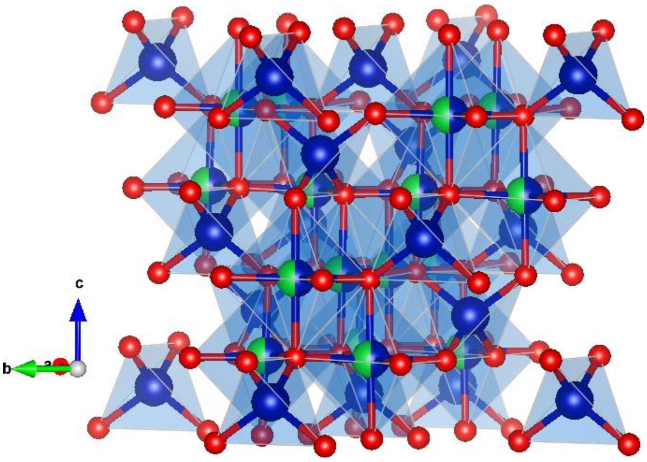

Figure 5-28: Polyhedral representation of spinel Co_2TiO_4 with oxygen (red), cobalt (blue), and titanium (green) atoms.

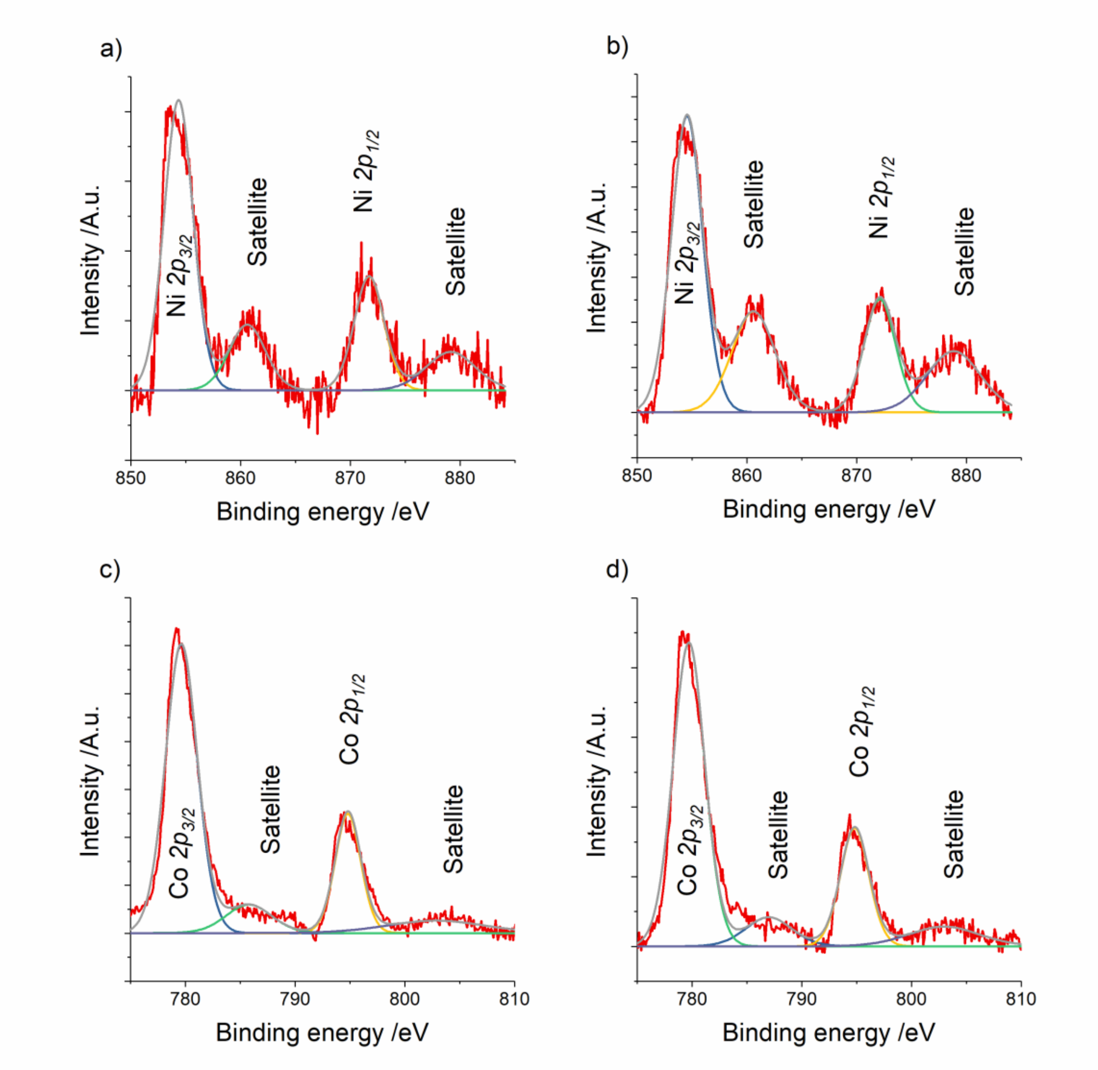

Figure 5-29: XPS spectra for $NiCo_2O_4$ at the binding energy levels of a) Ni *2p* and c) Co *2p*. XPS spectra for $Ni_{1.5}Co_{1.5}O_4$ at the binding energies of b) Ni *2p* and d) Co *2p*.

obvious peak shifts to lower 2θ values for all peaks of $Ni_{1.5}Co_{1.5}O_4$ compared to $NiCo_2O_4$. Whilst $NiCo_2O_4$ was a near-perfect match for the reference pattern (ICSD reference no. 02241), all peaks for $Ni_{1.5}Co_{1.5}O_4$ were shifted because of the additional substitution with nickel in the spinel, which could increase the unit cell volume due to the larger ionic radius of Ni compared to Co (see Figure 5-25, insets).

XRD patterns for Co_2TiO_4 were an excellent match for the reference pattern of cubic spinel Co_2TiO_4 (ICSD reference pattern 69506, space group Fd-3m). The main peaks at 2θ = 16.0, 25.2, and 27.5 ° were associated with the (311), (511), and (440) planes of the spinel crystal structure, respectively (see Figure 5-27a). No impurity phases for CoO or TiO_2 were detected. As can be seen from the peak positions and crystal structures, Co_2TiO_4 was confirmed as a Ti-substituted phase of Co_3O_4, just like $NiCo_2O_4$ is a Ni-substituted phase. However, as can be seen from a comparison of Figure 5-25 and Figure 5-27, there was significant broadening of the peaks in the XRD pattern for Co_2TiO_4 compared to those for $Ni_xCo_{3-x}O_4$. This indicated that the crystallite domain size for Co_2TiO_4 was significantly smaller than for $NiCo_2O_4$. Analysis of the domain sizes using the Scherrer equation for the five major peaks of Co_2TiO_4, $NiCo_2O_4$, and $Ni_{1.5}Co_{1.5}O_4$ gave estimates of ca. 5, 26, and 27 nm, respectively. For Co_3O_4 and $NiCo_2O_4$, both nickel and cobalt were expected to occur in both Co/Ni(III) and Co/Ni(II) oxidation states. In contrast, in Co_2TiO_4, Ti(IV) was

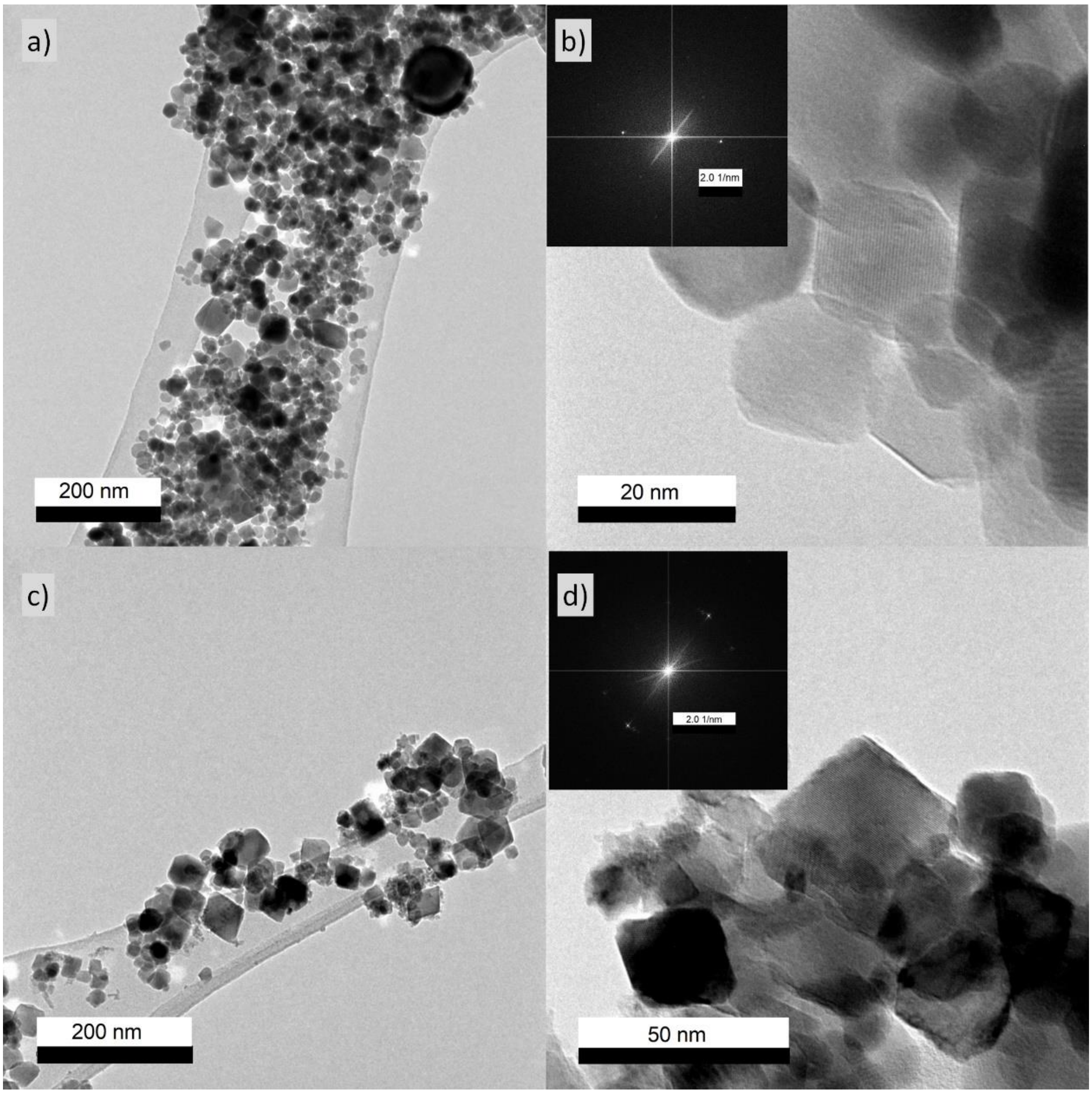

Figure 5-30: Transmission electron micrographs and reduced Fourier transforms for a + b) $NiCo_2O_4$ and c + d) $Ni_{1.5}Co_{1.5}O_4$.

expected to replace Co in half of the octahedral sites, resulting in Co(II) in all other octahedral sites as well as in the tetrahedral sites (see polyhedral model in Figure 5-28).

The differences in domain size between $Ni_xCo_{3-x}O_4$ and Co_2TiO_4 were supported by BET SSA data. The SSAs were ca. 30.0, 32.2, and 185.1 m^2 g^{-1} for $NiCo_2O_4$, $Ni_{1.5}Co_{1.5}O_4$, and Co_2TiO_4, respectively.

X-ray photoelectron spectroscopy was used to determine oxidation states and to semi-quantitively analyse elemental composition. Figure 5-27b shows the Ti *2p* binding energy spectrum, which showed peaks centred at ca. 459.1 and 464.7 eV for Ti $2p_{3/2}$ and Ti $2p_{1/2}$, respectively. This gave a spin orbit splitting of 5.6 eV. These values were in good agreement with the core levels of Ti(IV), indicating a single Ti oxidation state present.[54,315,316] The analysis of Co *2p* binding energies (see Figure 5-27c) revealed peaks at binding energies of ca. 780.3 and 796.2 eV for Co $2p_{3/2}$ and Co $2p_{1/2}$, respectively, which were in good agreement with the core levels of Co(II).[316,317] This gave an expectedly large spin orbital splitting of 15.9 eV. More importantly, strong satellite peaks were observed at 786.3 and 802.4 eV, with no indication of satellites at ~ 790 and 805 eV. Those satellites at higher binding energies would have been indicative of the presence of Co(III).[316,317] The satellites which appear in the XPS spectra of oxides of elements such as Co, Ni, Fe, and Mn are typically associated with energy loss of the generated photoelectron during the process

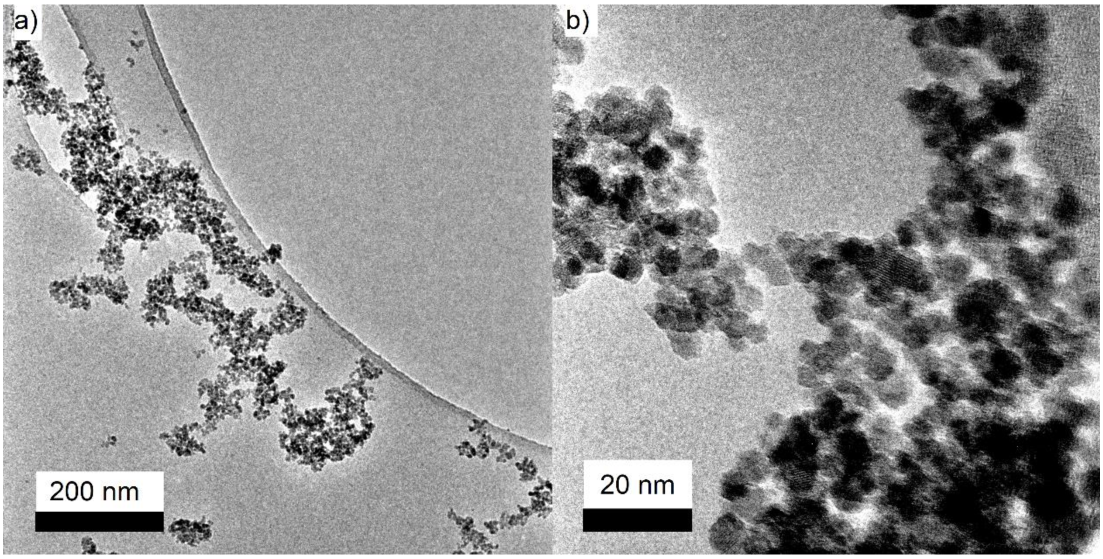

Figure 5-31: Transmission electron micrographs of Co_2TiO_4, showing a) an overview of particles and agglomerates and b) an enlarged section of particles with lattice fringes.

of leaving the atom. These shake-up satellites (giving rise to a feature at higher BEs) occur when the photoelectron interacts with an electron in the valence band of the atom and excites it (shake-up) and therefore the measured kinetic energy of the photoelectron is lower, giving rise to a peak at higher BEs (see Equation 2.3).[318,319] The elemental composition of the nanoparticles was determined semi-quantitively from the XPS spectra. The results indicated 28, 14 and 57 at.% of cobalt, titanium and oxygen, respectively. This was in good agreement with the expected 2:1:4 ratio for Co_2TiO_4.

XPS spectra for the Ni *2p* binding energies for both $NiCo_2O_4$ and $Ni_{1.5}Co_{1.5}O_4$ revealed evidence of mixed Ni(II) and Ni(III) oxidation states (see Figure 5-29a and

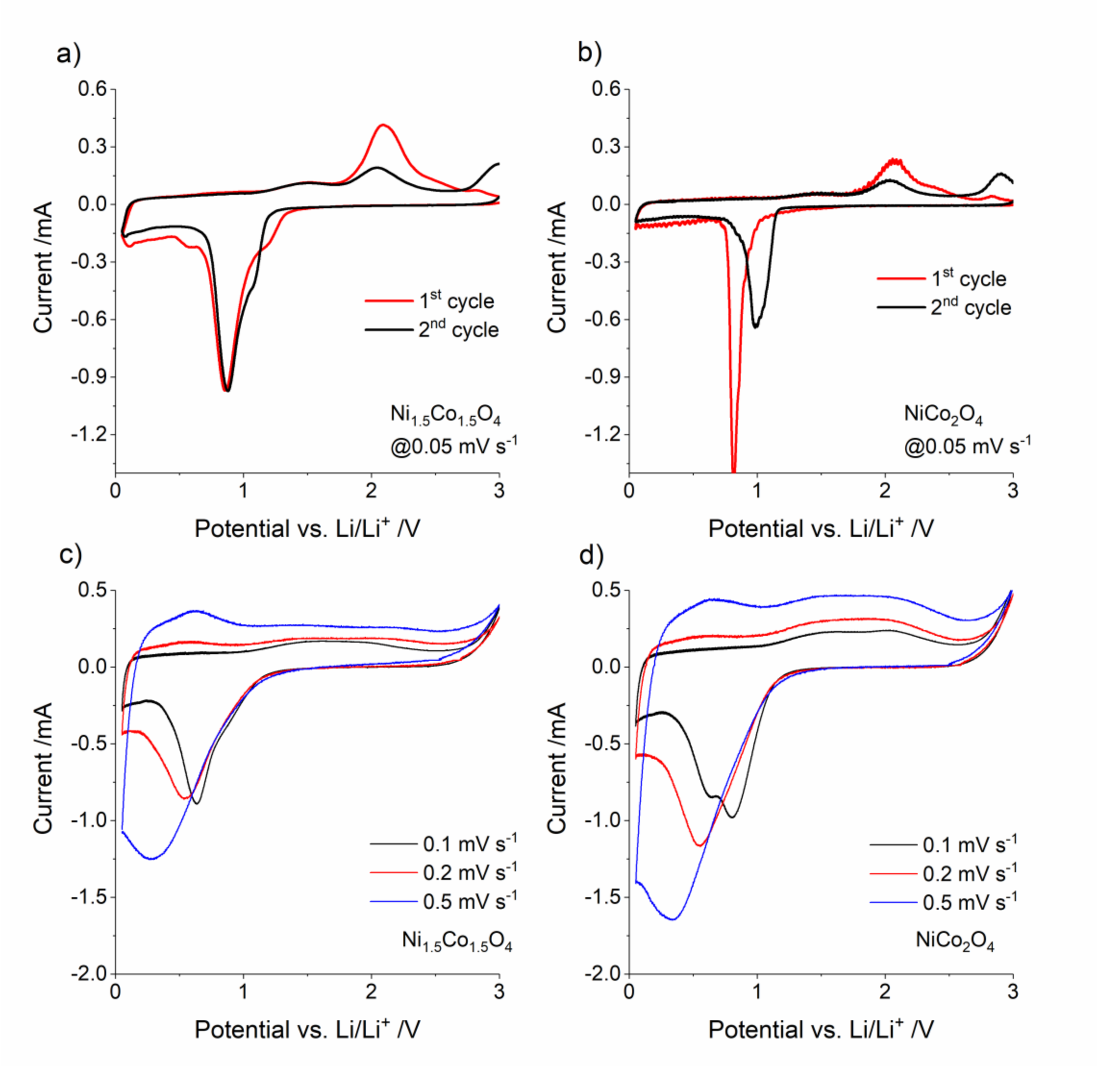

Figure 5-32: CVs of the first two cycles at a scan rate of 0.05 mV s^{-1} for a) $Ni_{1.5}Co_{1.5}O_4$ and b) $NiCo_2O_4$. CVs at scan rates of 0.1, 0.2, and 0.5 mV s^{-1} for c) $Ni_{1.5}Co_{1.5}O_4$ and d) $NiCo_2O_4$.

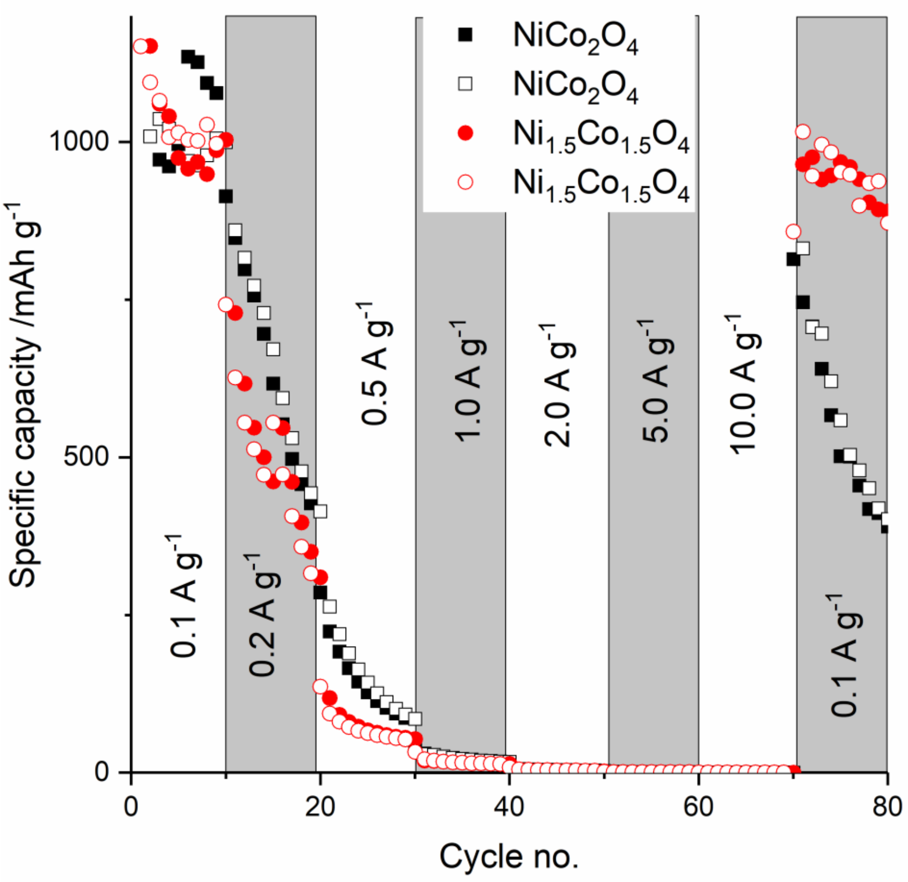

Figure 5-33: Galvanostatic charge/discharge cycling for $Ni_{1.5}Co_{1.5}O_4$ (circles) and $NiCo_2O_4$ (squares), showing both specific lithiation and delithiation capacities (filled and hollow symbols, respectively).

b, respectively). The satellites for Ni *2p3/2* and Ni *2p1/2* were slightly more pronounced for $Ni_{1.5}Co_{1.5}O_4$, which could have been a result of the higher concentration of nickel in these samples. For the Co *2p* binding energy levels, satellite peaks for both $NiCo_2O_4$ and $Ni_{1.5}Co_{1.5}O_4$ (see Figure 5-29c and d, respectively) were significantly suppressed compared to those seen for the Co *2p* binding energy levels in Co_2TiO_4 (see Figure 5-27c). This indicated that Co(II) and Co(III) oxidation states occurred in both $Ni_xCo_{3-x}O_4$ samples, whilst in Co_2TiO_4, only Co(II) was present. An exclusive Co(II) oxidation state in an oxide gives rise to significant satellites, whereas mixed Co(II)/Co(III) oxidation state gives rise to significantly repressed satellite peaks. Semi-quantitative analysis of the peak areas from XPS yielded atomic concentrations on the particle surfaces of 54 % Co and 46 % Ni for $Ni_{1.5}Co_{1.5}O_4$ and 72 % Co and 28 % Ni for $NiCo_2O_4$, relatively close to the expected values.

Transition electron micrographs (TEMs) revealed nanoparticles of varied size and morphology for both samples. Whilst the average particle size for $NiCo_2O_4$ was less varied, the nanoparticles were mostly cubic (see Figure 5-30a and b). For $Ni_{1.5}Co_{1.5}O_4$, particles also appeared cubic and the particle size was slightly more varied. However, the average particle size was similar for both (see Appendix). It was 23.2 (± 10.6) nm for $NiCo_2O_4$ and 27.7 (± 11.6) nm for $Ni_{1.5}Co_{1.5}O_4$). TEMs revealed significantly smaller cubic particles of Co_2TiO_4 compared to the $Ni_xCo_{3-x}O_4$ samples (see Figure 5-31a and b). The smaller particles were agglomerated. The average particle size was ca. 4.5 (±0.3) nm.

CVs revealed similar shapes for both $Ni_{1.5}Co_{1.5}O_4$ and $NiCo_2O_4$; in the cathodic sweep of the first cycle, a major peak associated with the decomposition of $Ni_xCo_{3-x}O_4$ and the reduction to metallic Ni and Co appeared at ca. 0.8 V vs. Li/Li^+ (see Figure 5-32a and b). On the subsequent anodic sweep, two peaks appeared, a smaller one at ca. 1.5 V vs. Li/Li^+, associated with the oxidation of metallic Ni to Ni(II) and a bigger one at ca. 2.1 V vs. Li/Li^+, associated with the oxidation of metallic Co to Co(II/III). This was in agreement with previously reported CVs for $NiCo_2O_4$.[306] In the second cycle, the anodic peak at 1.5 V vs. Li/Li^+ was retained, whereas the peak at 2.1 V vs. Li/Li^+ was significantly suppressed, indicating limited reversibility. In contrast to CVs previously reported in the literature, in the second cycle at 0.05 mV s^{-1}, a peak/rise in current appeared at potentials close to the upper potential limit of 3.0 V vs. Li/Li^+. This could have been the result of the formation of CoO or Co_3O_4.[304] One significant difference between the CVs of the two materials was the position of the peak during lithiation in the second cycle: while the peak shifted to a higher potential vs. Li/Li^+ for $NiCo_2O_4$, it remained constant for $Ni_{1.5}Co_{1.5}O_4$. Increasing scan rates led to a broadening of peaks and peak shifts to lower potentials for lithiation and higher potential for delithiation (see Figure 5-32c and d).

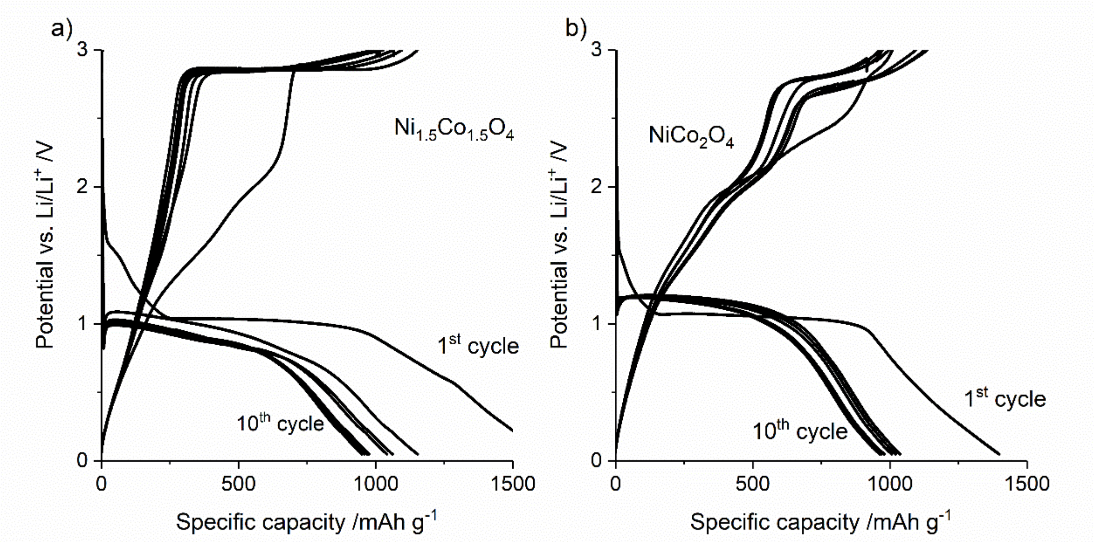

Figure 5-34: Galvanostatic charge/discharge profiles for a) $Ni_{1.5}Co_{1.5}O_4$ and b) $NiCo_2O_4$ for ten cycles at a specific current of 0.1 A g^{-1}.

Interestingly, at a scan rate of 0.1 mV s^{-1}, there seemed to be peak splitting in the lithiation peak of $NiCo_2O_4$, possibly as a result of the different contributions of the reduction of Ni and Co.

Galvanostatic charge/discharge measurements for $Ni_{1.5}Co_{1.5}O_4$ and $NiCo_2O_4$ revealed similar specific capacities of 980 and 965 mAh g^{-1} after 5 cycles at a specific current of 0.1 A g^{-1}. When the applied specific current was increased to 0.2 A g^{-1}, the specific capacity fell rapidly from 750 to ca. 260 mAh g^{-1} for $Ni_{1.5}Co_{1.5}O_4$ within ten cycles (and from 820 to 410 mAh g^{-1} for $NiCo_2O_4$). Very little capacity was retained for either sample at a specific current of 0.5 A g^{-1} or higher. When the specific current was returned to 0.1 A g^{-1}, $Ni_{1.5}Co_{1.5}O_4$ showed significantly better capacity retention than $NiCo_2O_4$; after ten further cycles at 0.1 A g^{-1}, $Ni_{1.5}Co_{1.5}O_4$ retained a specific capacity of 870 mAh g^{-1}, whereas the specific capacity of $NiCo_2O_4$ had fallen to ca. 380 mAh g^{-1}. The galvanostatic charge/discharge profiles revealed interesting electrochemical differences between both samples: After the first charge and

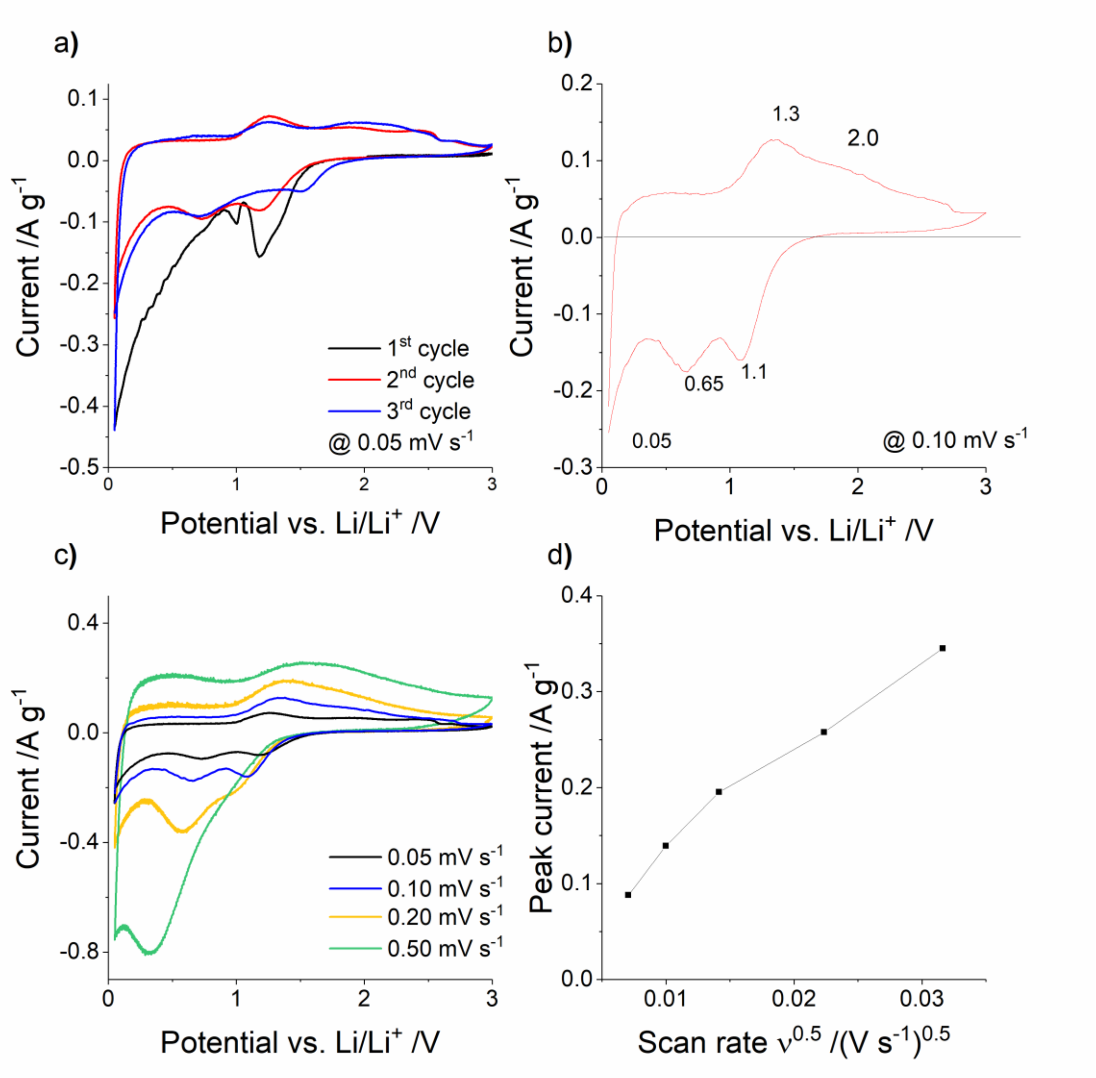

Figure 5-35: CVs of Co_2TiO_4 a) for the first three cycles at a scan rate of 0.05 mV s^{-1}, b) at a scan rate of 0.10 mV s^{-1}, and c) at scan rates of 0.05, 0.10, 0.20, and 0.50 mV s^{-1}. d) Peak currents of the anodic sweeps for Co_2TiO_4 over the square root of the scan rate.

discharge, nearly all delithiation capacity for $Ni_{1.5}Co_{1.5}O_4$ occurred at ca. 2.8 V vs. Li/Li$^+$ (see Figure 5-34a), indicating that the additional nickel retarded reoxidation of both Ni and Co, whereas for $NiCo_2O_4$, two different oxidation processes contributed to the capacity (see Figure 5-34b). Even though overpotentials were high for both samples (as would be expected for conversion materials), the increase in overpotential due to the additional Ni was significant.

For Co_2TiO_4, the first cycle showed significant irreversible processes. During the first cathodic sweep, there was a major peak around 1.2 V vs. Li/Li$^+$, a smaller peak at ca. 0.9 V vs. Li/Li$^+$ and a large rise in current towards the lower end of the

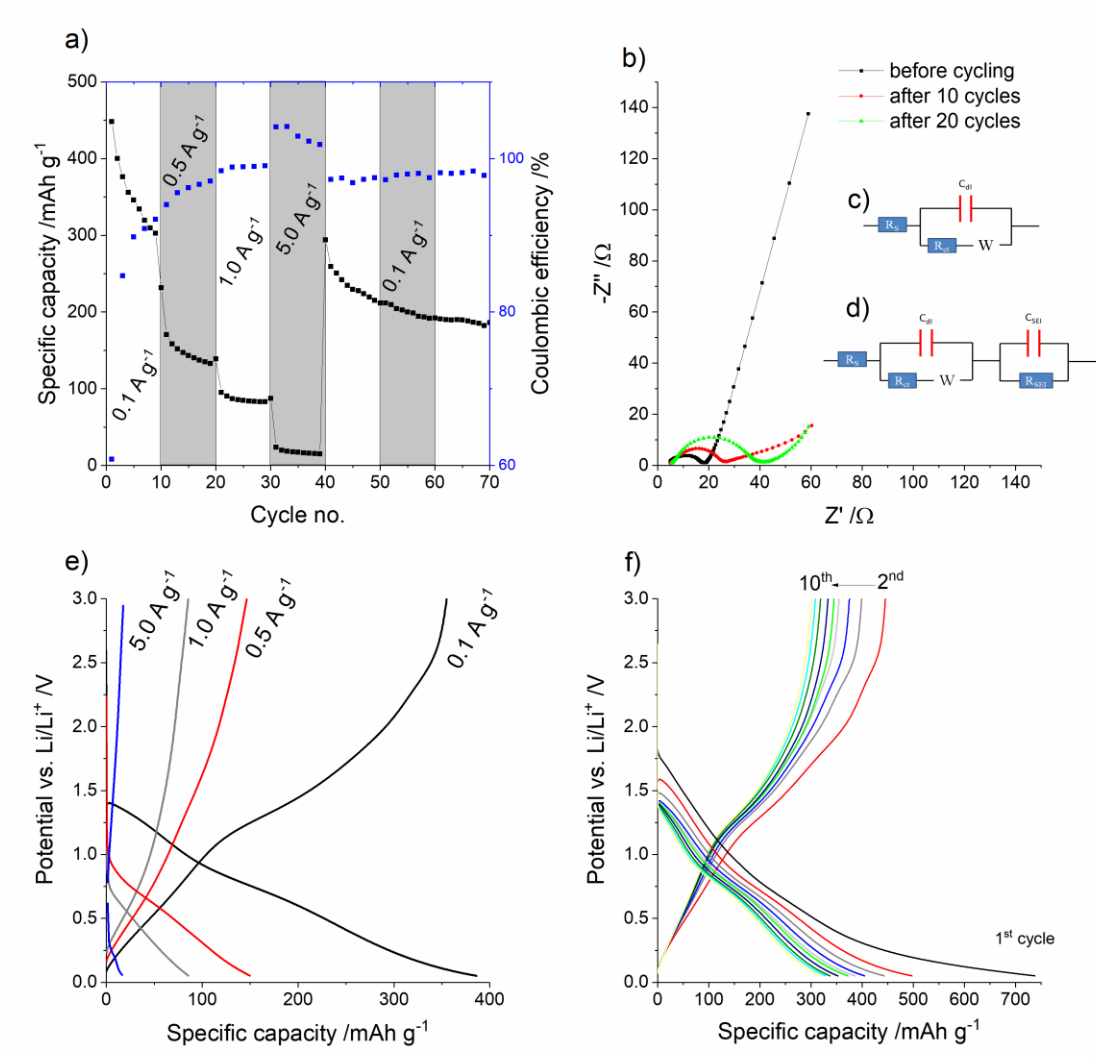

Figure 5-36: a) Galvanostatic charge/discharge cycling for Co_2TiO_4, showing specific capacities and Coulombic efficiencies. b) Nyquist plots for Co_2TiO_4 before and after cycling. Galvanostatic charge/discharge plots c) at different specific currents of 0.1, 0.5, 1.0, and 5.0 A g^{-1} and b) for the first 10 cycles at 0.1 A g^{-1}.

potential window at 0.05 V vs. Li/Li^+ (see Figure 5-35a). Previous reports have associated the peak at 1.2 V vs. Li/Li^+ with the insertion of small amounts of lithium into the Co_2TiO_4,[303] as has previously been reported for the cubic spinel $ZnFe_2O_4$.[320] The peak observed in the first cycle herein, however, was significantly larger than has previously been reported, which could be due to increased Li^+ insertion made possible by nanosizing. The peaks at lower potentials could be associated with the reduction and conversion reaction of Co_2TiO_4 into Co, TiO_2, and Li_2O as well as SEI formation. After the initial lithiation, the peaks observed for both cathodic and anodic sweeps stabilized. At a scan rate of 0.1 mV s^{-1}, CVs revealed major peaks upon

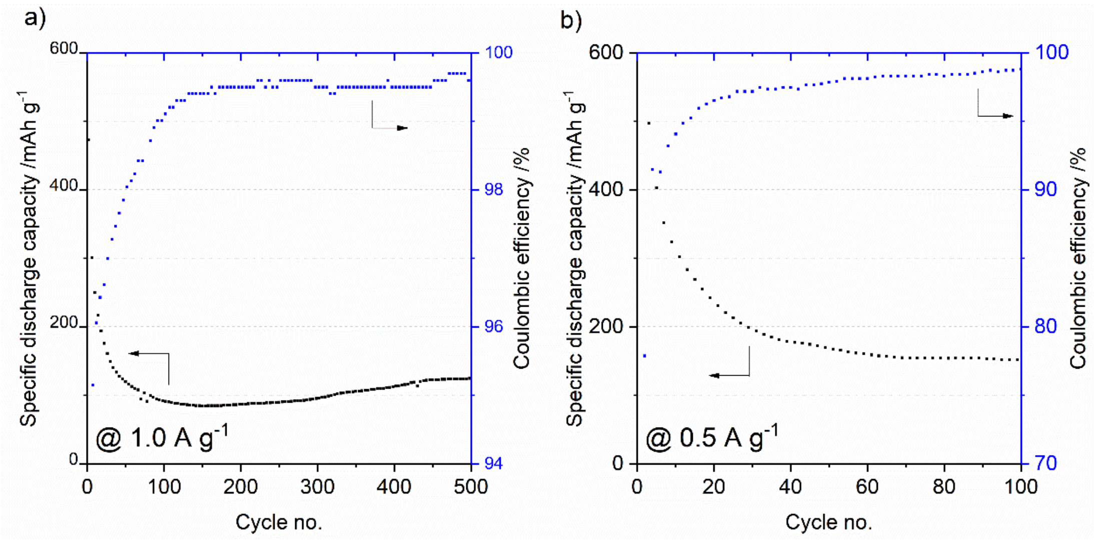

Figure 5-37: Galvanostatic charge/discharge cycling for Co_2TiO_4, showing specific capacities and Coulombic efficiencies at specific currents of a) 1.0 and b) 0.5 A g^{-1}.

lithiation at 1.1, 0.85, and 0.05 V vs. Li/Li^+, whilst delithiation peaks appeared at 1.3 and 2.0 V vs. Li/Li^+. This indicated that in this case, there was very little lithium insertion into TiO_2, which was expected from previous reports in the literature.[303] The reduction and oxidation could be associated with the peaks at 1.1 and 2.0 V vs. Li/Li^+. Upon an increase in scan rate, peaks broadened and merged together, so that for the CVs at a scan rate of 0.5 mV s^{-1}, only one lithiation peak appeared at 0.2 V vs. Li/Li^+, with delithiation occurring over the entire anodic sweep as indicated by positive currents over the entire cathodic sweep (see Figure 5-35c).

Galvanostatic charge/discharge cycling revealed good cycling stability for a conversion material: the initial specific discharge capacity at a specific current of 0.1 A g^{-1} was 450 mAh g^{-1}, which fell to ca. 300 mAh g^{-1} after ten cycles (see Figure 5-36a). The specific capacities at specific currents of 0.5, 1.0, and 5.0 A g^{-1} were 145, 95, and 15 mAh g^{-1}, respectively. EIS measurements before and after cycling revealed significant increases in charge transfer resistance after 10 and 20 cycles, which would be expected for Co_2TiO_4, which undergoes conversion reactions during lithiation and delithiation (see Figure 5-36b). The galvanostatic charge/discharge profiles at 0.1 A g^{-1} revealed a single sloping region for the lithiation and two sloping regions with different gradients for the delithiation (Figure 5-36c). At higher specific currents, the voltage profiles showed a single sloped region for both lithiation and delithiation, with increasing overpotentials. The first ten cycles at 0.1 A g^{-1} revealed a large initial

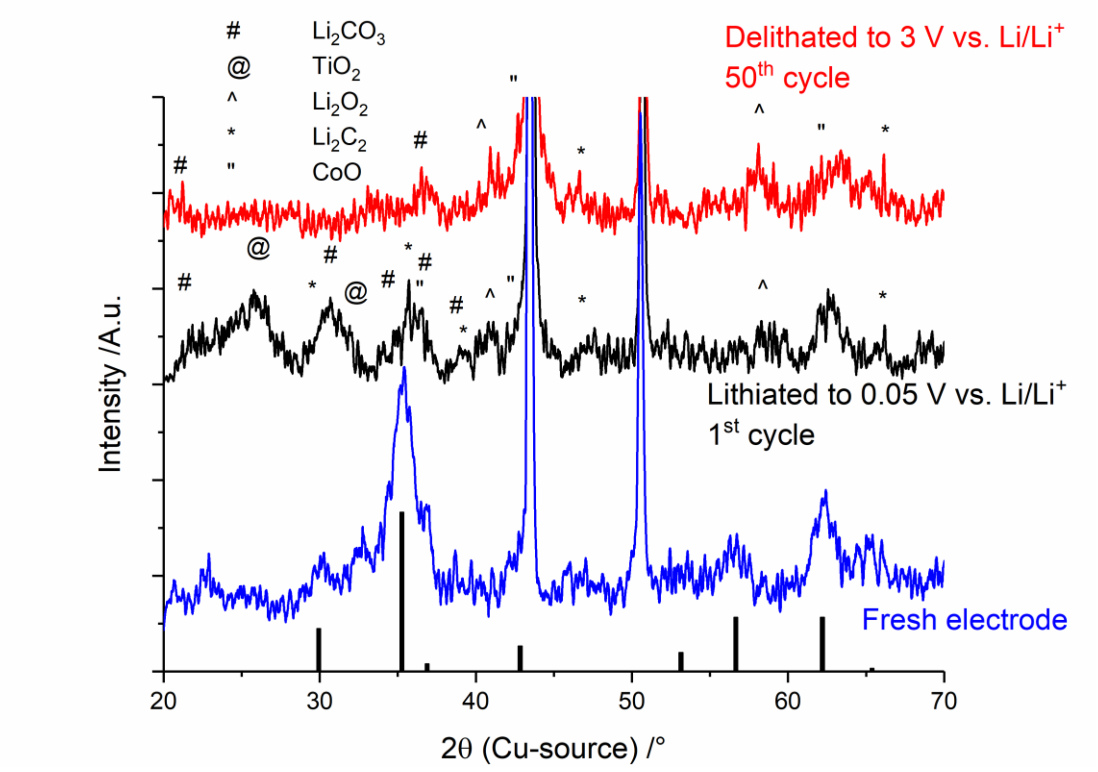

Figure 5-38: XRD patterns of fresh, lithiated, and cycled Co_2TiO_4 electrodes, alongside a reference pattern for Co_2TiO_4 (black bars, ICSD no. 69506).

lithiation capacity of 740 mAh g^{-1}, with a much smaller first delithiation capacity of ca. 450 mAh g^{-1} (Figure 5-36d). The high irreversible capacity in the first cycle was a result of the reduction of electrolyte during the formation of SEI. Upon cycling, there was continued capacity fading of about 33 % over ten cycles.

Cycling stability tests for the Co_2TiO_4 electrodes were conducted. At a specific current of 1.0 A g^{-1}, the initial delithiation capacity was ca. 475 mAh g^{-1}, but it fell rapidly to ca. 100 mAh g^{-1} after 100 cycles. After this, possibly due to gradual activation, the specific capacity rose slightly to ca. 120 mAh g^{-1} after 500 cycles (see Figure 5-37a). When cycled at a specific current of 0.5 A g^{-1}, the initial specific delithiation capacity was similar (ca. 490 mAh g^{-1}) but fell to only ca. 150 mAh g^{-1} after 100 cycles, indicating moderate stability for a conversion material (see Figure 5-37b).

To elucidate the reaction mechanism of Co_2TiO_4, ex-situ XRD was conducted for pristine electrodes, fully lithiated electrodes after the first cycle, and fully delithiated electrodes after 50 cycles (see Figure 5-38). The lithiated electrode showed evidence of Li_2CO_3, (Li)TiO_2, and Li_2O, whereas the delithiated electrode showed evidence of CoO. This was in good agreement with the expected reaction mechanism as previously proposed in the literature according to Equations 5.7 to 5.9:[303]

$$\mathrm{Co_2TiO_4} + 4\,\mathrm{Li^+} + 4\,\mathrm{e^-} \rightleftharpoons 2\mathrm{Li_2O} + \mathrm{TiO_2} + 2\mathrm{Co} \tag{5.7}$$

$$\mathrm{TiO_2} + \mathrm{xLi^+} + xe^- \rightleftharpoons \mathrm{Li_xTiO_2} \tag{5.8}$$

$$\mathrm{Li_xTiO_2} + 2\mathrm{Co} + 2\mathrm{Li_2O} \rightleftharpoons 2\mathrm{CoO} + \mathrm{TiO_2} + (4+\mathrm{x})\ \mathrm{Li^+} + (4+\mathrm{x})\mathrm{e^-} \tag{5.9}$$

As expected, there was no evidence for the presence of the Co_2TiO_4 phase in the delithiated sample after 50 cycles.

5.4.2.2. $TiO_2/NiCo_2O_4$

PXRD patterns for the different $TiO_2/NiCo_2O_4$ composites revealed good matches with the peaks of the reference pattern for cubic spinel $NiCo_2O_4$ (ICSD reference no. 02241, space group Fd-3m). As described for the pure $NiCo_2O_4$ in Section 5.4.2.1, the main peaks at 2θ = 16.7, 26.3, and 28.6 ° could be ascribed to the (311), (511), and (440) planes, respectively, of the cubic spinel phase (see Figure 5-39). As expected, peaks for TiO_2 (anatase) appeared with increasing TiO_2 concentration. The (101) and (200) peaks for TiO_2 (anatase) were visible at 2θ = 11.6 ° and at 2θ = 21.6 °, respectively. The peaks were a good match for the peaks of ICDS reference pattern no. 09852 (anatase TiO_2). These were the most obvious evidence of (nanoparticulate) TiO_2 in the samples (see Figure 5-39 inset). The peaks grew with an increasing concentration of TiO_2 in the composite samples from $NiCo_2O_4$ (no TiO_2) to $NiCo_2O_4$-4 (33 mol% TiO_2).

XPS was used to determine the oxidation states of the metal ions in the $TiO_2/NiCo_2O_4$ composites. The Ni *2p* binding energies for the $TiO_2/NiCo_2O_4$ composites were plotted in Figure 5-40a. As described for $NiCo_2O_4$ in Section 5.4.2.1, the peaks and their satellites revealed evidence of both Ni(II) and Ni(III) oxidation states for all composite samples. The Ti *2p* spectra, shown in Figure 5-40b, revealed peaks centred at ca. 459.1 and 464.7 eV for Ti $2p_{3/2}$ and Ti $2p_{1/2}$, respectively. This indicated a peak splitting of 5.6 eV, which was in good agreement with the core levels of Ti(IV), as would be expected for TiO_2 (anatase). The O *1s* peak was centred at ca. 530.6 eV, which is consistent with the peak position expected for metal-oxygen

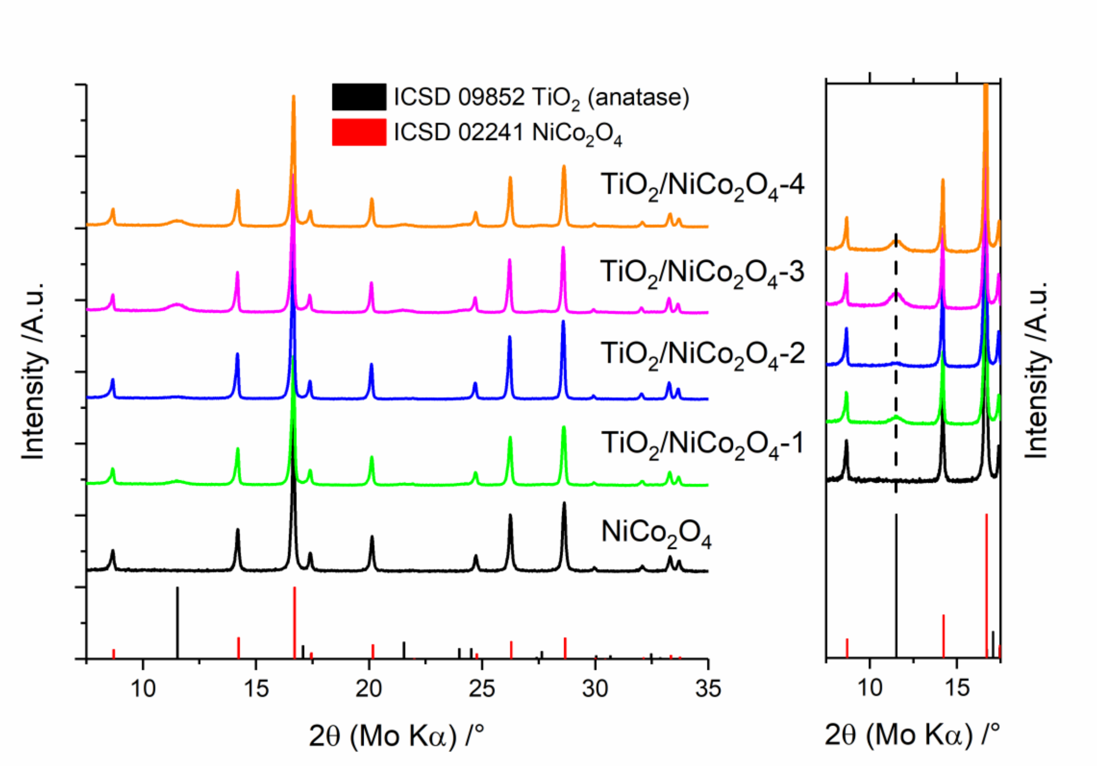

Figure 5-39: XRD patterns for $TiO_2/NiCo_2O_4$-1, $TiO_2/NiCo_2O_4$-2, $TiO_2/NiCo_2O_4$-3, and $TiO_2/NiCo_2O_4$-4 alongside the reference patterns for cubic spinel $NiCo_2O_4$ (red bars, ICSD no. 02241) and anatase TiO_2 (black bars, ICSD no. 09852). Inset) Enlarged region of the XRD patterns around the major peak for anatase TiO_2 at 2θ = 11.6 °.

bonds for Co-O, Ni-O, and Ti-O.[321,322] The Co *2p* binding energies were plotted in Figure 5-40d and revealed peaks at binding energies of ca. 780.3 and 796.2 eV for Co $2p_{3/2}$ and Co $2p_{1/2}$, respectively, which was in good agreement with the core levels of Co(II), as well as with the results for pure $NiCo_2O_4$.

Transmission electron microscopy revealed some changes in morphologies with increasing concentration of TiO_2. The micrographs for the sample with the lowest concentration of TiO_2 ($TiO_2/NiCo_2O_4$-1) showed particles similar to those of $NiCo_2O_4$, with many large cubic particles ($NiCo_2O_4$) and few clusters of smaller particles (presumably TiO_2). With increasing concentrations of TiO_2, the amount of TiO_2 nanoparticles visibly increased and seemed to form a network connecting the larger $NiCo_2O_4$ cubes together for $TiO_2/NiCo_2O_4$-4 (see Figure 5-41).

BET measurements revealed surface areas that increased with the TiO_2 content in the composites; they were 30.0, 35.8, 58.0, 71.6, and 89.5 $m^2\ g^{-1}$ for $NiCo_2O_4$,

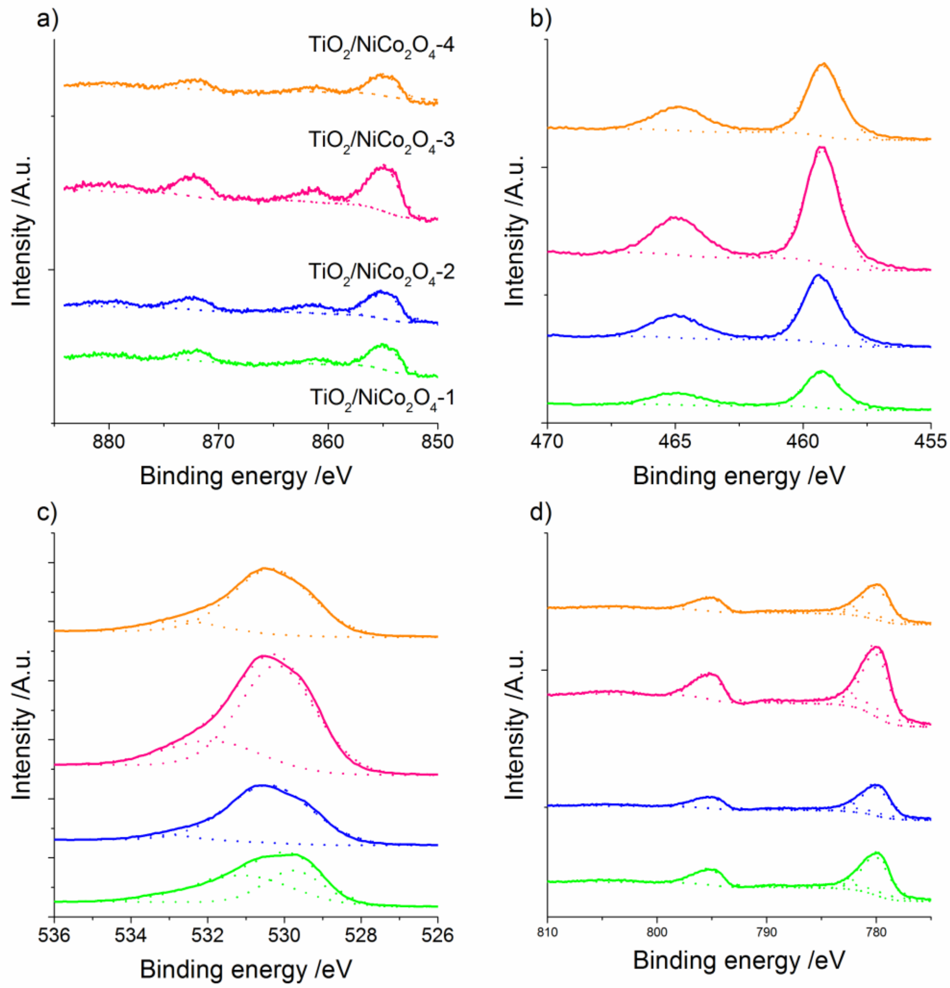

Figure 5-40: XPS spectra for the different composite $TiO_2/NiCo_2O_4$ samples at the binding energy levels of a) Ni *2p*, b) Ti *2p*, c) O *1s*, and d) Co *2p*.

$TiO_2/NiCo_2O_4$-1, $TiO_2/NiCo_2O_4$-2, $TiO_2/NiCo_2O_4$-3, and $TiO_2/NiCo_2O_4$-4, respectively.

Cyclic voltammograms for the composite samples revealed interesting trends for the influence of the co-precipitation of $NiCo_2O_4$ with TiO_2 (see Figure 5-42). At a scan rate of 0.05 mV s^{-1}, an increasing concentration of TiO_2 coincided with a shift of the peak during the cathodic sweep from ca. 0.6 V vs. Li/Li^+ for $TiO_2/NiCo_2O_4$-1 and $TiO_2/NiCo_2O_4$-2 to ca. 1.0 V vs. Li/Li^+ for $TiO_2/NiCo_2O_4$-4 (see Figure 5-42a). Furthermore, while the size of the peak at ca. 1.4 V vs. Li/Li^+ on the anodic sweep only decreased minimally with increased TiO_2 concentration, the size of the additional

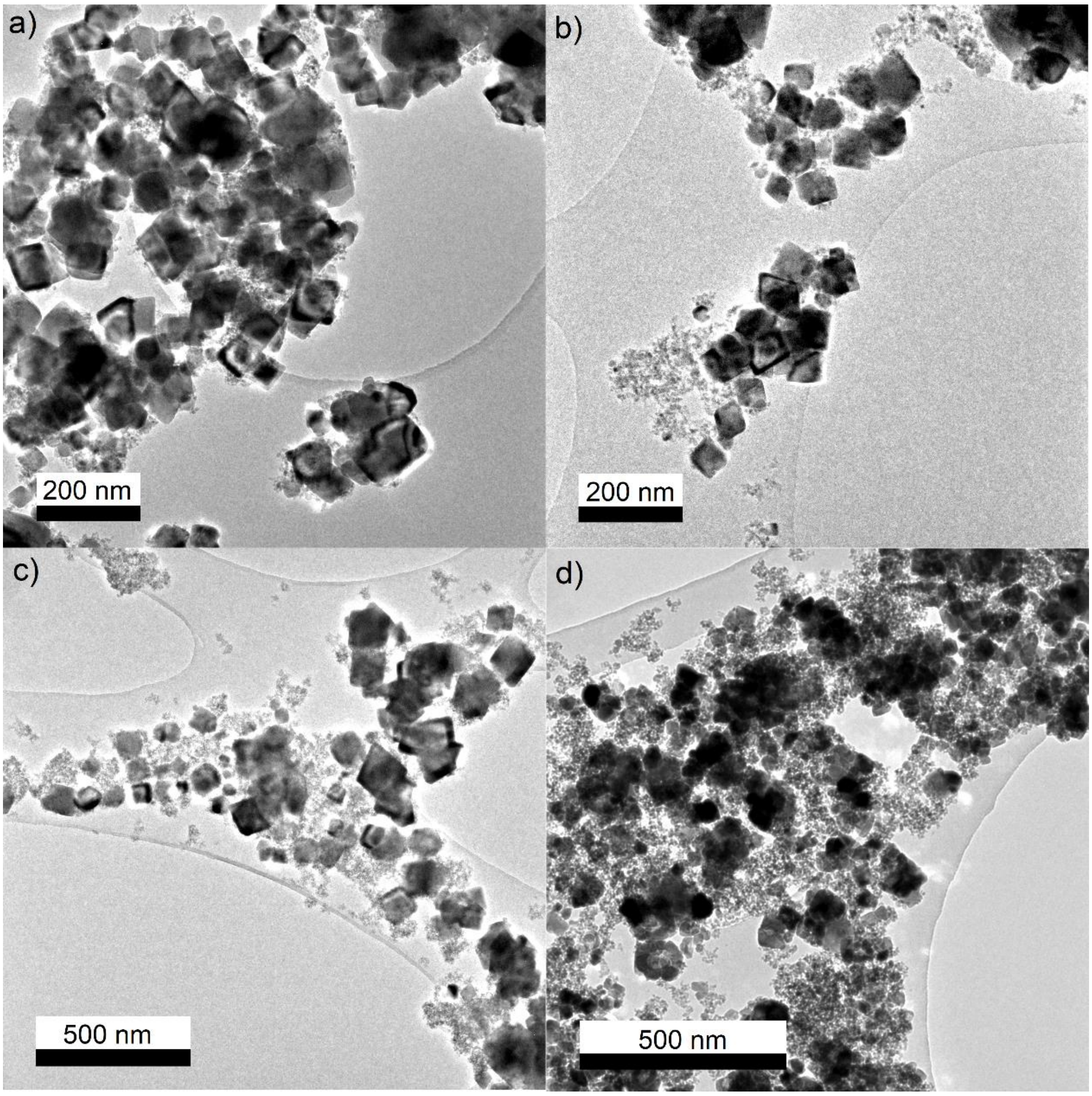

Figure 5-41: Transmission electron micrographs for a) $TiO_2/NiCo_2O_4$-1, b) $TiO_2/NiCo_2O_4$-2, c) $TiO_2/NiCo_2O_4$-3, and d) $TiO_2/NiCo_2O_4$-4.

peak at ca. 2.1 V vs. Li/Li^+ (which could be ascribed to the delithiation of $(Li_x)TiO_2$) increased with increasing TiO_2 content. The peak also appeared to become sharper with increasing TiO_2 content. The peak shifts overall indicated lower overpotentials, which would indicate much better energy efficiencies for the composite samples with higher TiO_2 concentrations, potentially due to a catalytic effect of TiO_2.

When the scan rate was increased to 0.1 and 0.2 mV s^{-1} (see Figure 5-42b and c, respectively), trends regarding peak shifts, overpotentials, and peak intensities due to the influence of TiO_2 held true; the peak in the cathodic sweep shifted significantly more for $TiO_2/NiCo_2O_4$-1 and $TiO_2/NiCo_2O_4$-2 than it did for $TiO_2/NiCo_2O_4$-3 and

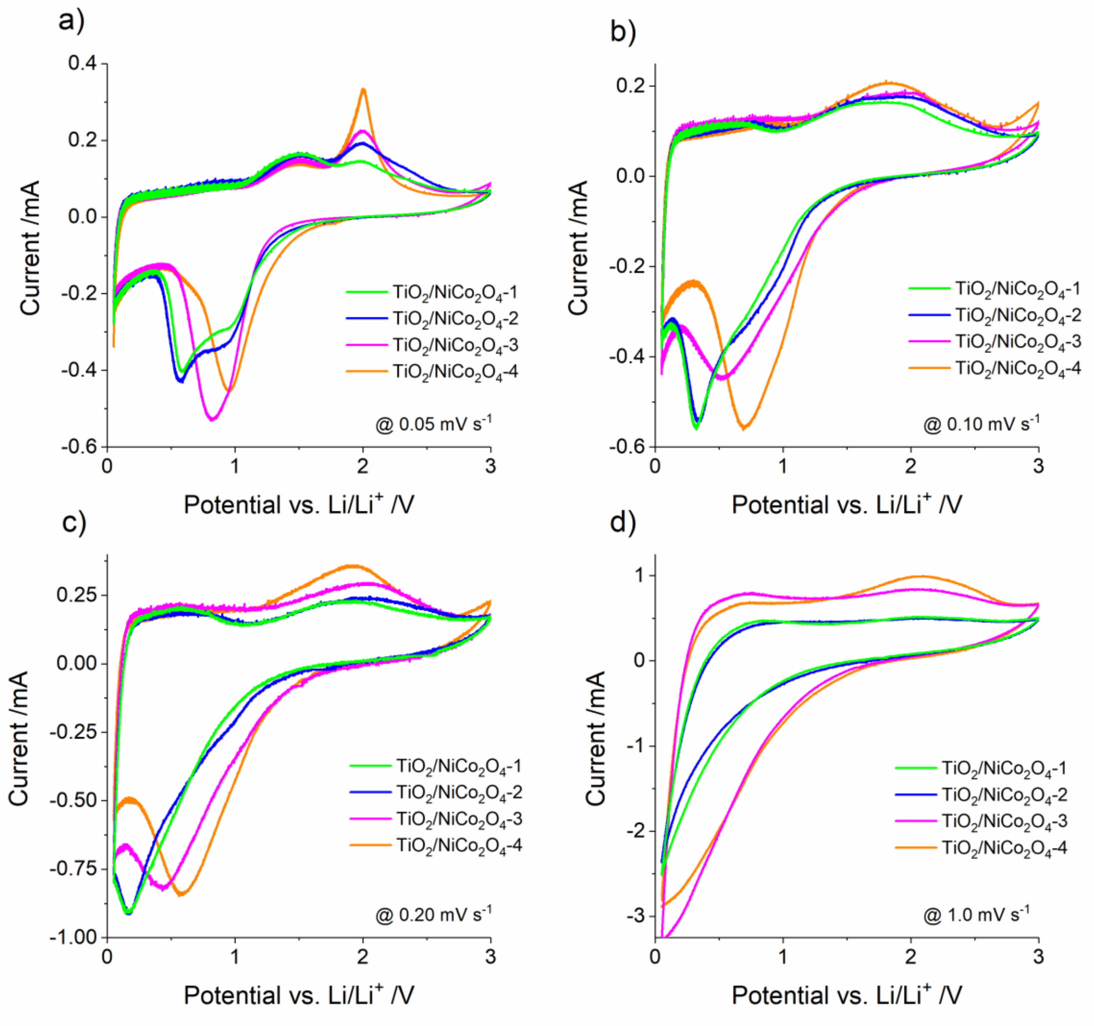

Figure 5-42: CVs for $TiO_2/NiCo_2O_4$-1, $TiO_2/NiCo_2O_4$-2, $TiO_2/NiCo_2O_4$-3, and $TiO_2/NiCo_2O_4$-4 at scan rates of a) 0.05, b) 0.10, c) 0.20, and d) 1.0 mV s^{-1}.

$TiO_2/NiCo_2O_4$-4. Peak broadening was observed for all samples, as would be expected from an increase in scan rate. Finally, when the scan rate was further increased to 1.0 mV s^{-1}, the peak broadening for $TiO_2/NiCo_2O_4$-3 and $TiO_2/NiCo_2O_4$-4 indicated much better charge storage at high rates than for $TiO_2/NiCo_2O_4$-1 and $TiO_2/NiCo_2O_4$-2 (see Figure 5-42d).

Galvanostatic charge/discharge cycling confirmed the conclusions drawn from CVs. Whilst all composite samples showed significant capacity fading in the first few cycles at 0.1 A g^{-1}, the benefits of co-precipitation with TiO_2 became apparent at higher applied specific currents; at a specific current of 0.5 A g^{-1}, all composite samples showed stable and higher specific capacities than pure $NiCo_2O_4$. The specific capacity

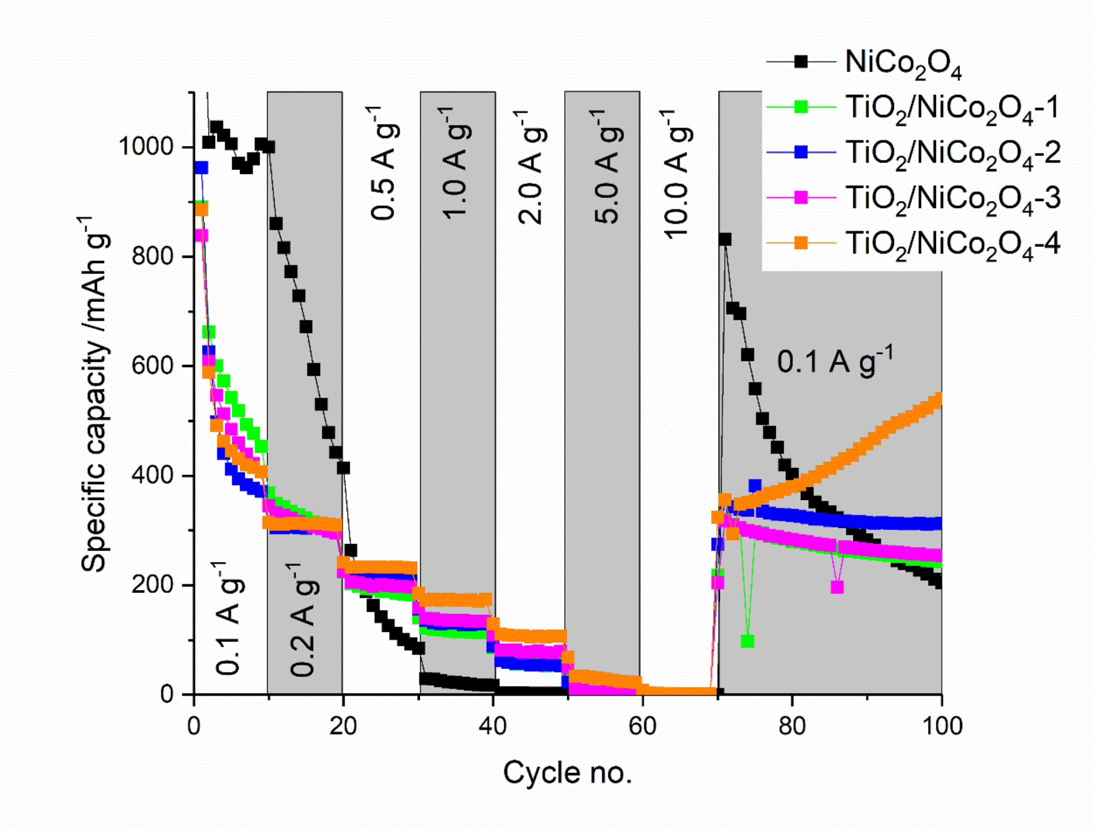

Figure 5-43: Galvanostatic charge/discharge cycling for $TiO_2/NiCo_2O_4$-1, $TiO_2/NiCo_2O_4$-2, $TiO_2/NiCo_2O_4$-3, and $TiO_2/NiCo_2O_4$-4 compared to that of pure $NiCo_2O_4$.

of pure $NiCo_2O_4$ dropped significantly when the specific current was increased to 0.2 A g^{-1}. This could have been a result of the limited back reaction of lithium superoxide at the increased specific current, which in turn limited the lithiation in the subsequent cycle. Whilst the specific capacity of the composite samples varied in the range ca. 190 to 220 mAh g^{-1} after 10 cycles at 0.5 A g^{-1}, $NiCo_2O_4$ only retained ca. 90 mAh g^{-1}. At a specific current of 1.0 A g^{-1}, $TiO_2/NiCo_2O_4$-1, $TiO_2/NiCo_2O_4$-2, $TiO_2/NiCo_2O_4$-3, and $TiO_2/NiCo_2O_4$-4 showed specific capacities of 110, 115, 130 and 180 mAh g^{-1}, respectively. The higher the loading of TiO_2 in the composite, the better the rate properties of the materials were. In contrast, pure $NiCo_2O_4$ retained only ca. 10 mAh g^{-1} at 1.0 A g^{-1}.

When the specific current was returned to 0.1 A g^{-1} after 70 cycles at varying specific currents, the $NiCo_2O_4$ samples co-precipitated with TiO_2 showed superior cycling stability. Whilst the specific capacity for $NiCo_2O_4$ recovered to the highest value of ca. 800 mAh g^{-1}, it dropped significantly to ca. 200 mAh g^{-1} after another

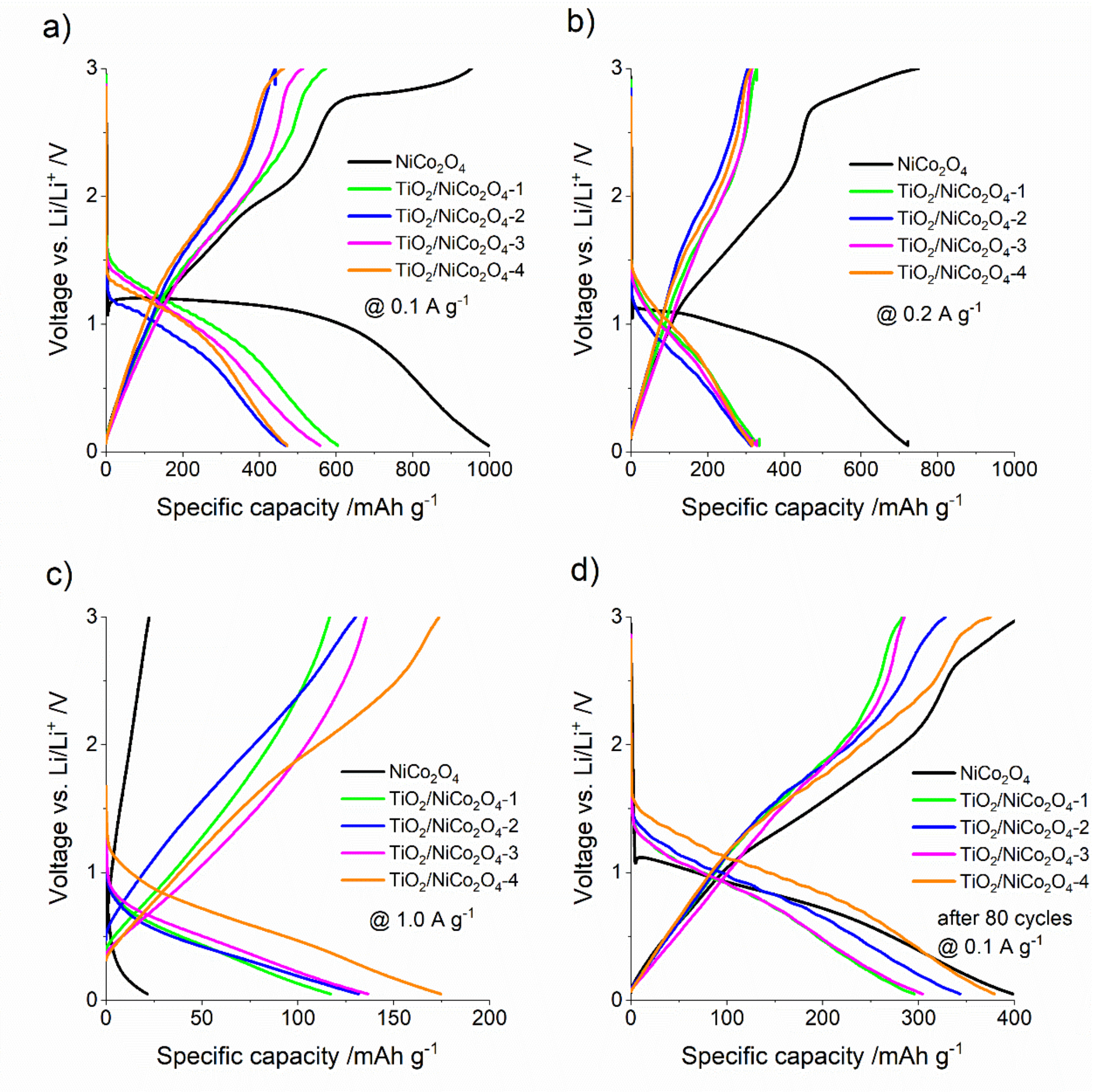

Figure 5-44: Galvanostatic charge/discharge curves for $NiCo_2O_4$, $TiO_2/NiCo_2O_4$-1, $TiO_2/NiCo_2O_4$-2, $TiO_2/NiCo_2O_4$-3, and $TiO_2/NiCo_2O_4$-4 at specific currents of a) 0.1, b) 0.2, and c) 1.0 A g^{-1} and d) 0.1 A g^{-1} after 80 cycles.

30 cycles. In contrast, after the same number of cycles, all composite samples showed higher specific capacities. Interestingly, the specific capacity of $TiO_2/NiCo_2O_4$-4 continued to increase, potentially due to a gradual activation process of the porous electrode.[153,323–326] The specific capacity of $TiO_2/NiCo_2O_4$-4 had climbed to 550 mAh g^{-1} after 100 cycles, far exceeding the performance of pure $NiCo_2O_4$.

A closer inspection of galvanostatic charge/discharge curves at various specific currents revealed further differences in the lithiation and delithiation behaviour of the composite materials. Whilst for $NiCo_2O_4$ there were obvious plateaus associated with the conversion reactions of Ni and Co at both 0.1 and 0.2 A g^{-1} (see Figure 5-44a and b), no such plateaus were observed for any of the composite samples. Furthermore, at a specific current of 1.0 A g^{-1}, $NiCo_2O_4$ barely stored any appreciable specific capacity, whereas $TiO_2/NiCo_2O_4$-4 showed the highest capacity of ca. 180 mAh g^{-1}. The charge/discharge profile of $TiO_2/NiCo_2O_4$-4 resembled a straight line previously associated with nanoparticles (see Figure 5-44c).[14,16,58] Upon returning the specific current to 0.1 A g^{-1}, the plateaus for $NiCo_2O_4$ were reduced, but were still observable, whereas for all of the composite samples, there were still no lithiation/delithiation plateaus (see Figure 5-44d). Furthermore, the specific capacity of all samples had decreased compared to the fifth cycle at 0.1 A g^{-1} (see Figure 5-44a), but the decrease was highest for the samples with low (or no) TiO_2 concentration and lowest for the sample with the highest concentration of TiO_2 ($TiO_2/NiCo_2O_4$-4).

5.5. Conclusions

The co-precipitation of TiO_2 with oft-studied conversion materials for anodes in LIBs, such as $NiCo_2O_4$ and MoO_2, significantly improved the cycling stability and rate performance of these conversion materials, which usually suffer from large voltage hysteresis, poor rate performance, and short cycle life.

While nanosized MoO_2 has been shown to exhibit pseudocapacitive charge storage when cycled as an intercalation material in a limited potential range, to achieve the highest specific capacities, an expanded voltage window must be utilized. The co-precipitation of MoO_2 with TiO_2 in CHFS allowed for smaller particle sizes and better cycling stability, leading to higher pseudocapacitive contributions to charge storage and much better performance at high power. The chemical and physical stability of TiO_2 acted as an “anchor” for MoO_2 to improve the cycling stability and acted to increase the surface area to allow higher pseudocapacitive charge storage. The improvements due to co-precipitation allowed for MoO_2 to be used as anode material in Li-HECs, which showed excellent performance when anodes were pre-lithiated.

To further study the effects of co-precipitation of TiO_2 compared to the inclusion of Ti in the crystal lattice, $NiCo_2O_4$, Co_2TiO_4, and various composite $TiO_2/NiCo_2O_4$ samples were compared. The inclusion of Ti in the spinel structure did not improve the performance of the material, because reduction into the constituent parts (Co, TiO_2 and Li_2O) led to massive first cycle losses and poor rate performance.

In contrast, the composite samples showed improved cycling stability and rate performance; increases in TiO_2 concentration in the composites led to improvements in rate performance.

Future work in this area should involve gaining a better understanding of the mechanism by which co-precipitation of conversion materials with a stabilising phase such as TiO_2 worked to improve rate performance and cycle life. Furthermore, the exploration of further conversion materials stabilised by co-precipitation with TiO_2, as well as the stabilisation of conversion/alloying materials with other potential stabilising phases, would be interesting areas to investigate. For example, the electrochemical performance of Si nanoparticles has recently been reported to significantly improve by wrapping in V_2O_5 nanosheets.[327]

In Chapter 6, the synthesis of mixed metal oxides of VO_2 and MoO_2 will be discussed, with the aim to further improving the high-rate performance of MoO_2.

6. Pseudocapacitive Solid Solutions of Monoclinic Mo/V Oxides for High Power Anodes

6.1. Aims

As discussed above in Chapters 3, 4, and 5, both monoclinic VO_2 and monoclinic MoO_2 have been used as anode materials for LIBs. MoO_2 has shown promise both as an insertion material and as a conversion material, whereas VO_2 shows stable cycling as an insertion material. Solid solutions of the two metal oxides $Mo_xV_{x-1}O_{2+y}$ have shown excellent high-power performance. Monoclinic mixed metal oxides were synthesised via CHFS and characterised using a range of physical and electrochemical methods, including as anode material for LIBs.

6.2. Introduction

Insertion materials for anodes in LIBs such as graphite and TiO_2 are advantageous due to their good cycling stability. However, they tend to have limited specific capacities. Molybdenum(IV) oxide (MoO_2) has been studied as both an intercalation (when cycled in the potential window 1 to 3 V vs. Li/Li^+)[57,180,289] and a conversion negative electrode for LIBs.[148,287,288,290–293] As an intercalation material in LIBs, its theoretical specific capacity is only 209 mAh g^{-1},[294] whereas as a conversion material, it has a theoretical specific capacity of 838 mAh g^{-1}.[95]

When cycled as an insertion material, the lithiation of MoO_2 can be described by Equation 6.1, from monoclinic MoO_2 to orthorhombic Li_xMoO_2 and back to monoclinic $Li_{0.98}MoO_2$:[180,293]

$$\mathrm{MoO_2}_{(\mathrm{mono})} \rightleftharpoons \mathrm{Li_xMoO_2}_{(0.45<x<0.78,\mathrm{ortho})} \rightleftharpoons \mathrm{Li_{0.98}MoO_2}_{(\mathrm{mono})} \tag{6.1}$$

When cycled as a conversion material, the lithiation follows Equation 6.2:

$$\mathrm{Li_{0.98}MoO_2}_{(\mathrm{mono})} + 3.02\ \mathrm{Li^+} + 3.02\ \mathrm{e^-} \rightleftharpoons 2\mathrm{Li_2O} + \mathrm{Mo} \tag{6.2}$$

However, the back reaction of this conversion reaction is limited to just one lithium ion per four Mo atoms.[95] Monoclinic MoO_2 has been reported to show specific capacities of 139, 126, and ca. 60 mAh g^{-1} at specific currents of 0.05, 0.1, and

1.0 A g^{-1}, respectively, when cycled as an insertion material.[180] When cycled as a conversion material in a wider potential window (to potentials in the range 1.0 to 0.05 V vs. Li/Li^+), a MoO_2-graphene composite has been reported to show reversible specific capacities of 672 and 445 mAh g^{-1} after 100 cycles at specific currents of ca. 0.05 and 0.5 A g^{-1}, respectively.[148] A different MoO_2-graphene oxide has been reported with a reversible capacity of 600 mAh g^{-1} at a specific current of 0.80 A g^{-1}.[291] Mixed oxidation state molybdenum oxides (MoO_2/MoO_3 hybrids) have been shown to exhibit excellent performance at high power, with a specific capacity of ca. 500 mAh g^{-1} at 2 A g^{-1}.[328]

Monoclinic vanadium(IV) oxide (VO_2) has a theoretical capacity of up to 320 mAh g^{-1}[329,330] and is of interest because of the high abundance and relatively low costs of vanadium.[122,148,288,290,291,293,331,332] It has previously been synthesized via CHFS and was reported to have specific capacities of 255 and 95 mAh g^{-1} at relatively high specific currents of 1 and 10 A g^{-1}, respectively.[331] Monoclinic VO_2 nanowires showed a specific capacity of 200 and 118 mAh g^{-1} at 0.1 and 1.0 A g^{-1}, respectively, whereas hollow microspheres of monoclinic VO_2 have shown a specific capacity of 163 mAh g^{-1} at 1.0 A g^{-1}.[333] VO_2 nanoribbons showed specific capacities of 200 mAh g^{-1} after 200 cycles at a current of 0.1 mA, whereas a VO_2/graphene composite stabilised the performance at 380 mAh g^{-1} after 50 cycles at the same current.[334]

As previously discussed, conversion materials typically have higher specific capacities than insertion materials. They typically suffer from poor cycling performance due to large volume changes and poor performance at high rate.[322,335] Mixed molybdenum and vanadium oxides with mixed valence states have shown excellent performance at high rates, due to the readily available redox couples.[336,337] A mixed molybdenum and vanadium oxide $LiVMoO_6$ has shown specific capacities of 900 and 285 mAh g^{-1} at specific currents of 0.1 and 5.0 A g^{-1}, respectively, indicating excellent high rate performance. This was attributed to the availability of multiple redox couples [V(V) to V(II) and Mo(VI) to Mo(0)].[338] An amorphous 3D hybrid of VO_x, MoO_y, and carbon has also been reported, with reversible capacities of 1705 and 740 mAh g^{-1} at specific currents of 0.1 and 2.0 A g^{-1}, respectively. The authors attributed the excellent performance to the amorphisation and hybridization of the mixed molybdenum and vanadium oxide.[322]

Often, the synthesis of nanomaterials and nanomaterial hybrids can be limited in terms of scalability, long reaction times, and need for multiple steps.[181,287] Herein, a range of mixed Mo/V oxides were synthesized via a continuous hydrothermal flow synthesis (CHFS) process and tested as active materials in negative electrodes for LIBs.

6.3. Materials & Methods

6.3.1. Synthesis of Monoclinic Mo/V Oxides

The synthesis of the nanomaterials was carried out as described in Section 2.1.1. The production rate for all materials was in the range of 20 to 30 g h^{-1}.

6.3.2. Physical Characterisation of Monoclinic Mo/V Oxides

The physical characterisation of the nanomaterials was carried out according to the methods described in Section 2.2. The methods included PXRD, XPS, TEM, BET, XAS, and EDX.

6.3.3. Electrochemical Characterisation of Monoclinic Mo/V Oxides

The electrochemical characterisation of the mixed molybdenum/vanadium oxides was performed using Li-ion CR2032 half-cells, which used lithium metal as reference and counter electrode. The negative electrodes were cast on copper foil, as described in Section 2.3.1. The tests were carried out in the potential range 0.05 to 3.0 V vs. Li/Li^+. The active mass loading of the anodes was in the range 1.5 to 2.5 mg cm^{-2}. All tests were carried out at room temperature, using an Arbin Instrument Model BT2000 battery tester (Caltest Instruments, Guildford, UK).

Galvanostatic charge/discharge cycling was carried out in the range of specific currents 0.1 to 10.0 A g^{-1}. Long-term cycling was performed on selected materials at a specific current of 1.0 A g^{-1} for 150 cycles. Cyclic voltammetries were performed at scan rates in the range 0.1 to 100 mV s^{-1}.

Electrochemical impedance spectroscopy (EIS) was carried out using an Interface 1000 Gamry potentiostat (Gamry Instruments, Pennsylvania, US), in the frequency range 100 kHz to 50 mHz, using an AC voltage of 0.01 V rms. To determine the diffusion coefficient for selected samples, EIS was carried out in the frequency range 100 kHz to 1 mHz. Staircase potentio electrochemical impedance spectroscopy (SPEIS) was performed using Swagelok-type half-cells, using a Bio-Logic VSP-300 potentiostat (Bio-Logic Science Instruments, France) in the potential window 0.1 to 3.0 V vs Li/Li^+. The excitation potential was 0.01 V rms and EIS was conducted in the range of frequencies 100 kHz to 10 mHz. After each potential step, an EIS measurement was conducted once the current fell below 1 mA (due to electrochemical relaxation).

Galvanostatic Intermittent Titration Technique (GITT) measurements were used to determine Li^+ diffusion coefficients. A specific current of 0.1 A g^{-1} was applied for ten minutes for each current pulse. Each pulse was followed by a ten-minute relaxation step.

6.4. Results and Discussion

6.4.1. Physical Characterisation of Monoclinic Mo/V Oxides

All nanomaterials were recovered as black powders after freeze-drying. PXRD patterns showed sharp peaks, especially for MoO_{2+x}, $Mo_{0.67}V_{0.33}O_{2+x}$, $Mo_{0.5}V_{0.5}O_{2+x}$, and $Mo_{0.33}V_{0.67}O_{2+x}$. The patterns for $Mo_{0.1}V_{0.9}O_{2+x}$, $Mo_{0.05}V_{0.95}O_{2+x}$, and VO_2 revealed sharp peaks, but also broad amorphous regions, especially at low 2θ (see Figure 6-1).

All patterns were a good match to patterns for monoclinic MoO_2/VO_2: the major peaks corresponded to the (011), (101), and (211) planes of the reference pattern for monoclinic VO_2 (2θ = 12.7, 16.9 and 24.7°, ICDS no. 34033). On the other hand, the major peaks of the reference pattern for monoclinic MoO_2 corresponded to the (011) and (-211) peaks (2θ = 11.9 and 16.7 °, ICDS no. 23722). With increasing molybdenum concentration, the peaks became sharper, which indicated increasing crystallinity. The (011) peak shifted from 12.7 (VO_2) to 11.9 ° (MoO_2) as the molybdenum concentration increased. Similarly, the (211) peaks at 24.7 shifted

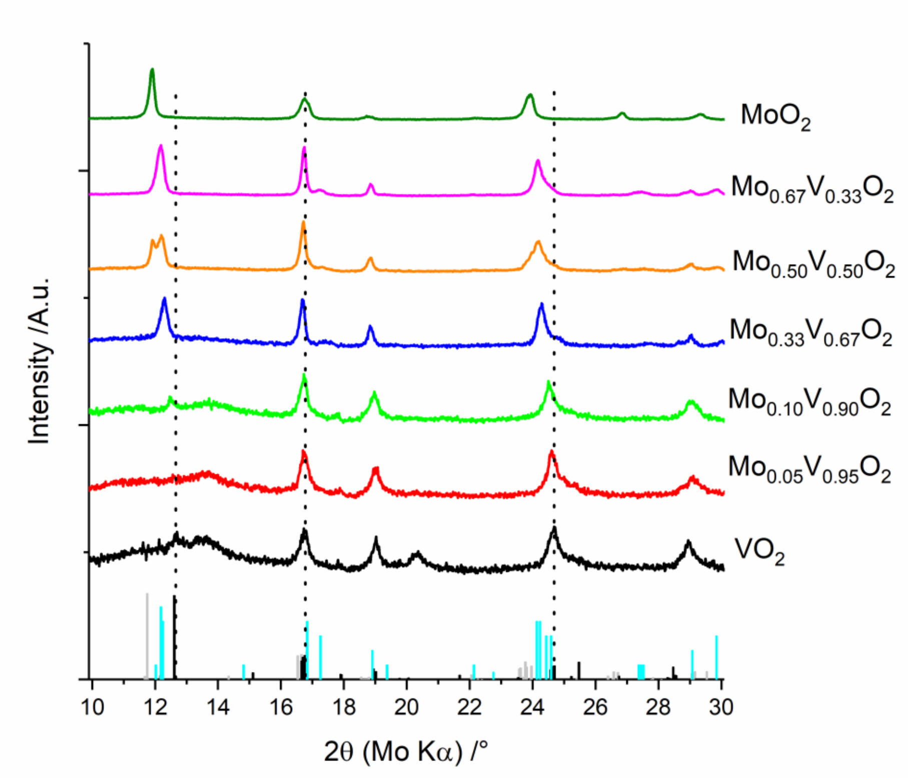

Figure 6-1: X-ray diffraction patterns for the mixed vanadium and molybdenum oxides, along with reference patterns for monoclinic VO_2 (ICDS no. 34033, black bars), monoclinic $V_{0.33}Mo_{0.67}O_2$ (JCPDS no. 030-0849, cyan bars), and monoclinic MoO_2 (ICDS no. 23722, grey bars).

towards 23.5 ° from VO_2 to MoO_2. Other peaks also shifted according to the reference patterns.

The XRD patterns for all mixed samples which contained at least 10 at.% Mo and 33 at.% V were also good matches to the reference pattern of the monoclinic (M_2) phase of a mixed molybdenum vanadium oxide of the composition $V_{0.33}Mo_{0.67}O_2$ (JCPDS no. 030-0849).[339–341] Whilst the authors who originally reported the pattern claimed the M_2 monoclinic phase was only achieved at vanadium concentrations in the range 33 to 55 at.%, the phase was present for a much wider range of vanadium concentrations in this study. The difference between these monoclinic phases is that the metal-metal distances for M_1 are consistent, whereas for the M_2 phase, there is a long and a short metal-metal distance between atoms. The monoclinic crystal structures for MoO_2, VO_2 (M_1), and VO_2 (M_2) are shown in Figure 6-2.

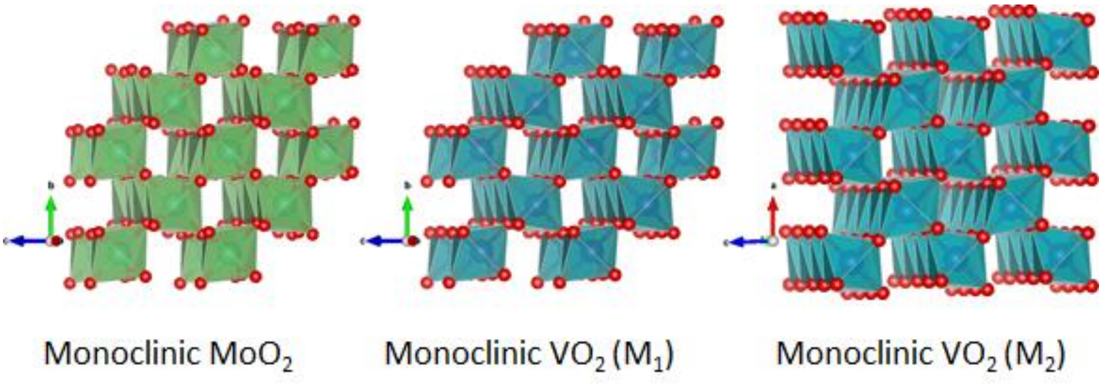

Figure 6-2: Polyhedral representations of the monoclinic crystal structures of MoO_2, VO_2 (M_1) and VO_2 (M_2).

Whilst the PXRD patterns suggested solid solutions of vanadium and molybdenum oxides, the pattern for $Mo_{0.5}V_{0.5}O_{2+x}$ was the only to show splitting of the (011) peak, which suggested a mixture of (V-doped) MoO_2 and (Mo-doped) VO_2. This suggested that the solubility of Mo in the VO_2 structure, and the solubility of V in that of MoO_2, was located around the nominal composition of $Mo_{0.5}V_{0.5}O_{2+x}$.

X-ray photoelectron spectroscopy was used to analyse concentrations and oxidation states of molybdenum and vanadium. The peaks for the V *2p* binding energies were at 517.3 and 524.6 eV. This was in line with the expected positions for the V $2p_{3/2}$ and V $2p_{1/2}$ peaks, respectively. The peak positions and the spin-orbit splitting of 7.3 eV were in line with V(IV).[71] The intensities of the peaks decreased with reducing vanadium concentration (see Figure 6-3a). The centre of the peak for the O *1s* spectra was at ca. 530.6 eV (see Figure 6-3b). This peak position was consistent with metal-oxygen bonds (V-O and Mo-O).[321,322] The Mo *3d* level binding energy spectra showed the peaks which increased in intensity with increasing molybdenum concentration (see Figure 6-3c). The spectra consisted of two peaks, except the pure MoO_2, which showed at least three peaks. The two peaks for the other samples were centred at ca. 232.6 and 235.7 eV, giving a spin-orbit splitting of 3.1 eV. This matched with a Mo (VI) oxidation state.[239] Deconvolution of the peaks in the spectra of pure MoO_2 showed mixed Mo (IV), (V), and (VI) valence states. This was most likely a result of surface oxidation, which has previously been reported for MoO_2 samples.[342,343]

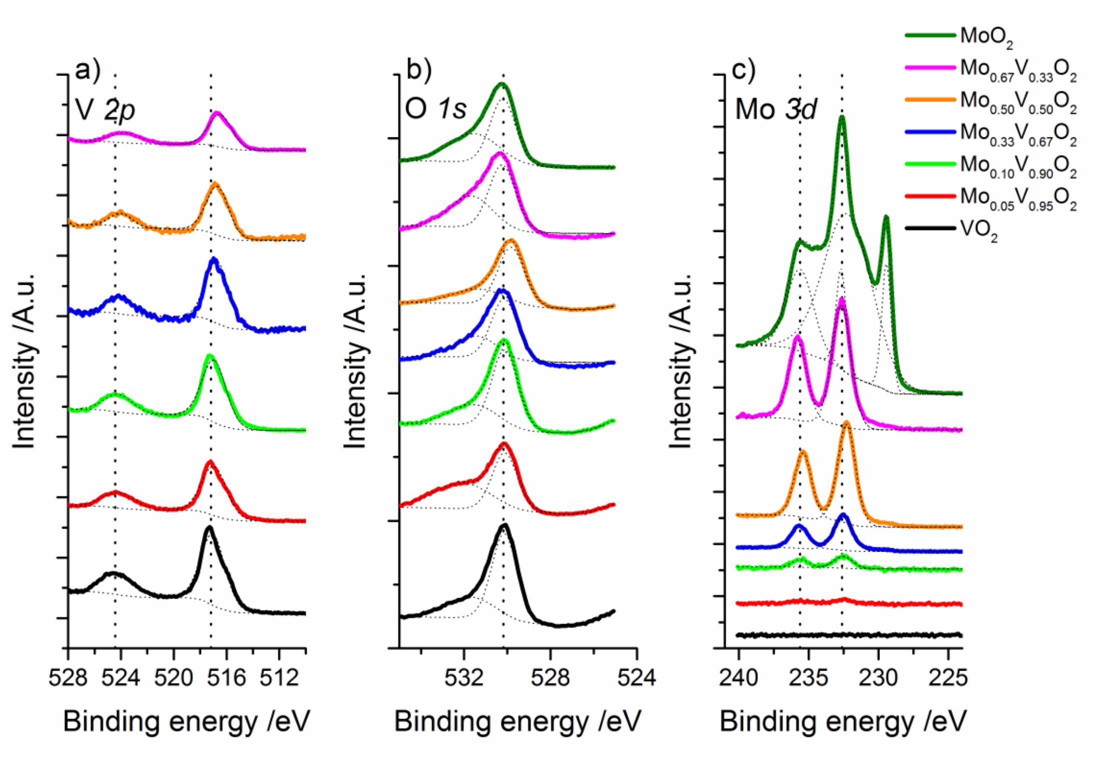

Figure 6-3: High-resolution X-ray photoelectron spectra (XPS) for a) V *2p*, b) O *1s* and c) Mo *3d* for all samples. The dotted lines indicate the peak positions for V(IV), O(II), and Mo(VI) and are only shown to indicate peak shifts.

The XPS spectra were analysed quantitatively to investigate the correlation between nominal concentration of vanadium and molybdenum in the synthesis and that in the resultant oxides. Nominal concentration and experimentally determined concentration from XPS were generally in good alignment (see Figure 6-4). For the samples with nominal concentrations of 5, 10, and 33 at.% molybdenum, the experimental concentrations were slightly lower than expected, whereas for the sample with a nominal concentration of 50 at.%, the experimental concentration of Mo from XPS was slightly higher (see Figure 6-4).

The specific surface areas for all powders were measured using the technique described by Brunauer-Emmett-Teller (see 2.2.8). There were only relatively small differences in the specific surface areas of all samples. The specific surface areas for MoO_2, $Mo_{0.67}V_{0.33}O_{2+x}$, $Mo_{0.5}V_{0.5}O_{2+x}$, $Mo_{0.33}V_{0.67}O_{2+x}$, $Mo_{0.1}V_{0.9}O_{2+x}$, $Mo_{0.05}V_{0.95}O_{2+x}$, and VO_2 were ca. 20, 31, 43, 34, 36, 33 and 40 $m^2\ g^{-1}$, respectively. These surface areas were in line with those previously reported for mixed molybdenum-vanadium oxides by other authors.[322]

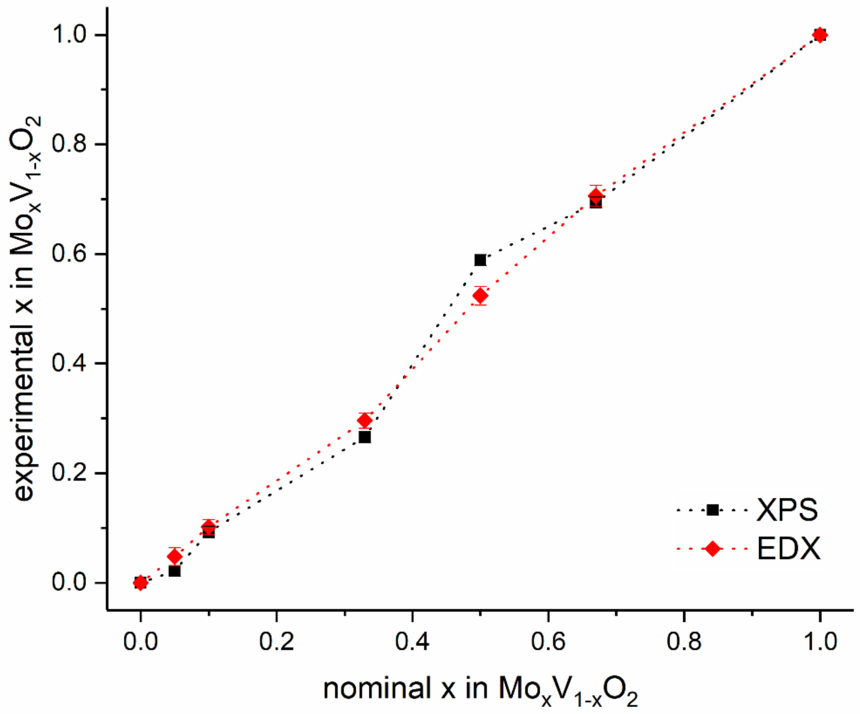

Figure 6-4: Relationship between the nominal concentrations of vanadium and molybdenum in the synthesis and the experimentally determined actual concentrations from XPS and EDX analysis.

Micrographs taken using transmission electron microscopy (TEM) for all samples revealed agglomerated nanoparticles, each with particle sizes below 50 nm. The agglomerates for $Mo_{0.67}V_{0.33}O_{2+x}$ and $Mo_{0.33}V_{0.67}O_{2+x}$ were made up of nanoparticles of varied morphology and size (see Figure 6-5a and b, and Figure 6-5e and f, respectively). Surprisingly, the agglomerates of the sample with the nominal composition $Mo_{0.5}V_{0.5}O_{2+x}$, which was the only sample that showed peak-splitting in XRD, were composed of nanoparticles which were significantly less varied in size and morphology than for the other samples (see Figure 6-5c and d).

Micrographs coupled with energy dispersive X-ray spectroscopy (EDX) mapping for vanadium, molybdenum, and oxygen showed even distributions of all elements throughout the samples (see Figure 6-6). This indicated solid solutions of monoclinic $Mo_zV_yO_{2+x}$ for all samples. As previously discussed for the concentrations determined via XPS, the measured concentrations of molybdenum and vanadium in

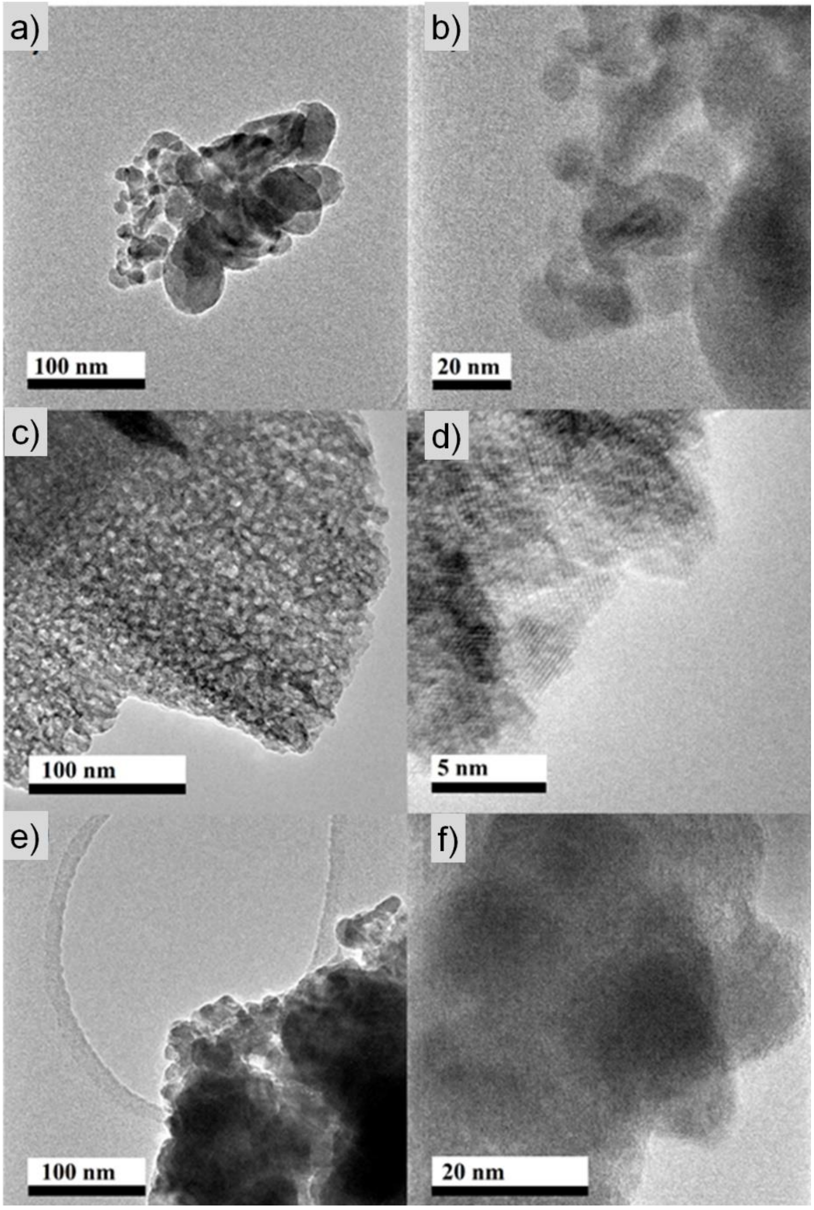

Figure 6-5: Transmission electron micrographs for a and b) $Mo_{0.67}V_{0.33}O_{2+x}$, c and d) $Mo_{0.5}V_{0.5}O_{2+x}$, and e and f) $Mo_{0.33}V_{0.67}O_{2+x}$.

the samples via EDX were in good agreement with nominal values used in the synthesis (see Figure 6-4).

X-ray absorption spectroscopy (XAS) for the V K-edge for $Mo_{0.1}V_{0.9}O_{2+x}$, $Mo_{0.05}V_{0.95}O_{2+x}$, and VO_2 showed a pre-edge feature at 5469.4 eV, whereas the pre-edge feature for $Mo_{0.5}V_{0.5}O_{2+x}$ and $Mo_{0.33}V_{0.67}O_{2+x}$ was at 5468.5 eV, which could indicate some V(V) in the samples with low molybdenum concentration, but only V(IV) in the samples with higher molybdenum concentrations (see Figure 6-7a).[344,345] This was confirmed by a shift of the edge to lower energies for

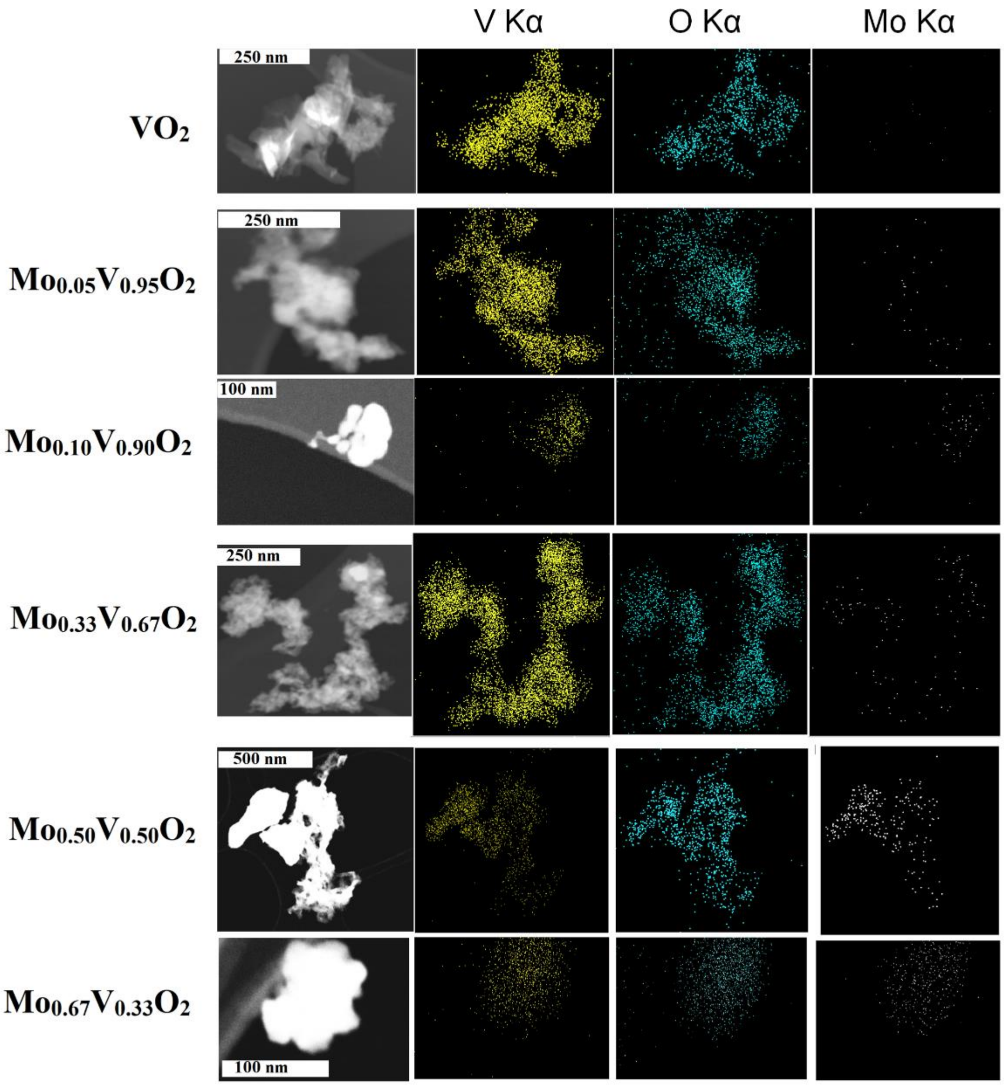

Figure 6-6: Energy dispersive X-ray spectroscopy (EDX) maps for all samples for vanadium (yellow), oxygen (blue), and molybdenum (white).

$Mo_{0.5}V_{0.5}O_{2+x}$ and $Mo_{0.33}V_{0.67}O_{2+x}$ to ca. 5479.6 eV from ca. 5480.9 eV. XAS spectra for the Mo K-edge showed a pre-edge feature at 19995 eV for $Mo_{0.1}V_{0.9}O_{2+x}$ and $Mo_{0.05}V_{0.95}O_{2+x}$ (see Figure 6-7b), which became less evident, but was still present, for $Mo_{0.5}V_{0.5}O_{2+x}$ and $Mo_{0.33}V_{0.67}O_{2+x}$. It was attributed to the 1s-4d transition, associated with tetrahedral geometry. However, it has also been shown to be present in (distorted) octahedral geometries (tetrahedralization).[242,243] There was also a shift of the edge to lower energies for all mixed oxides compared to MoO_2, which was most pronounced in $Mo_{0.1}V_{0.9}O_{2+x}$ and $Mo_{0.05}V_{0.95}O_{2+x}$, potentially indicative of lower valence state molybdenum in these samples.[242]

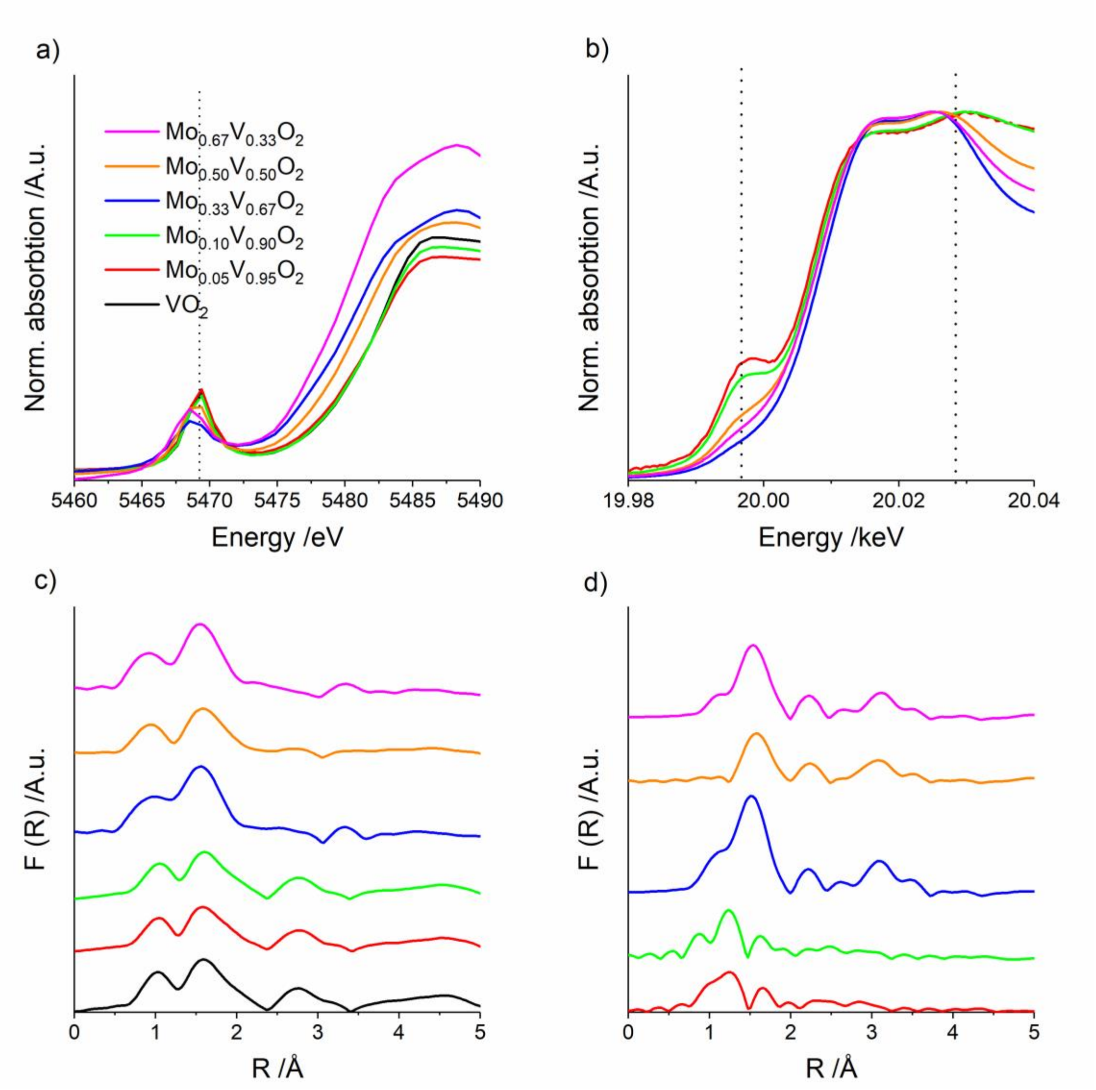

Figure 6-7: X-ray absorption spectra (XAS) for a) V K-edge and b) Mo K-edge. Experimental radial distribution plots for c) V K-edge and d) Mo K-edge.

The Fourier transforms (FT) of the V K-edge data in Figure 6-7c demonstrated similar local environments around V atoms for all samples, which were not in good agreement with a theoretical spectrum for M$_1$ phase. Peaks associated with the V-O coordination of the M$_1$ phase would be expected at ca. 1.35 and 1.75 Å, whilst V-V shells correspond to peaks at ca. 2.15 and 2.95 Å.[346] For the samples with a low concentration of or no molybdenum ($Mo_{0.1}V_{0.9}O_{2+x}$, $Mo_{0.05}V_{0.95}O_{2+x}$ and VO_2), there was a peak at ca. 2.95 Å, which might be correlated to the V-V shells; however, for the samples with higher concentrations of molybdenum ($Mo_{0.67}V_{0.33}O_{2+x}$, $Mo_{0.5}V_{0.5}O_{2+x}$, $Mo_{0.33}V_{0.67}O_{2+x}$), there was a peak at ca. 3.3 Å, which potentially indicated changes in the V-V distances for these samples. The FT of the Mo K-edge

XAS was plotted in Figure 6-7d. The plot for MoO_2 showed the features expected for monoclinic M_1 (MoO_2) with a major peak at ca. 1.4 Å corresponding to the Mo-O coordination and features at ca. 2.0 and 3.2 Å associated with Mo-Mo coordination.[246] For mixed molybdenum/vanadium oxides with a high concentration of molybdenum ($Mo_{0.67}V_{0.33}O_{2+x}$, $Mo_{0.5}V_{0.5}O_{2+x}$, $Mo_{0.33}V_{0.67}O_{2+x}$) the FTs were similar to that of monoclinic (M_1) MoO_2. However, the peak at ca. 3.2 Å was suppressed significantly, which possibly indicated less Mo-Mo coordination.[247] The FTs for the mixed oxides with low concentrations of molybdenum ($Mo_{0.1}V_{0.9}O_{2+x}$, $Mo_{0.05}V_{0.95}O_{2+x}$) were significantly different to the other samples (and especially M_1 MoO_2), indicating a different local environment. This could indicate that the molybdenum in these samples was coordinated with the VO_2, whereas it was not for the samples with higher molybdenum concentrations.

6.4.2. Electrochemical Characterisation of Monoclinic Mo/V Oxides

The materials were investigated via CV in Li-ion half-cells in the potential window 0.05 to 3.00 V vs. Li/Li^+, at a scan rate of 0.05 mV s^{-1}. For VO_2, the reversible peaks were at ca. 2.5 V vs. Li/Li^+, which was similar to previously reported cyclic voltammograms for VO_2 prepared via CHFS.[331] CVs for $Mo_{0.05}V_{0.95}O_{2+x}$ were similar, with reversible peaks at ca. 2.5 V vs. Li/Li^+. On the other hand, the reversible peak for $Mo_{0.1}V_{0.9}O_{2+x}$ was shifted to lower potentials vs. Li/Li^+ (see Figure 6-8a). The cyclic voltammograms of the first two cycles of $Mo_{0.33}V_{0.67}O_{2+x}$ and $Mo_{0.5}V_{0.5}O_{2+x}$ differed significantly from those for VO_2. For $Mo_{0.5}V_{0.5}O_{2+x}$, three distinct reversible peaks could be observed at potentials of ca. 1.4, 1.7, and 2.0 V vs. Li/Li^+ (see Figure 6-8b). Whilst the voltammograms for the first two cycles for $Mo_{0.33}V_{0.67}O_2$ and $Mo_{0.5}V_{0.5}O_{2+x}$ showed relatively small irreversible capacity loss, those for the molybdenum-rich $Mo_{0.67}V_{0.33}O_{2+x}$ showed significant irreversible reactions between 1.0 and 2.0 V vs. Li/Li^+. Generally, the reversibility of $Mo_{0.67}V_{0.33}O_{2+x}$ seemed significantly poorer than for all other materials.

Scan rate testing revealed significant difference between the samples with low and high molybdenum concentrations. At a scan rate of 0.1 V s^{-1}, peaks for $Mo_{0.67}V_{0.33}O_{2+x}$, $Mo_{0.5}V_{0.5}O_{2+x}$, and $Mo_{0.33}V_{0.67}O_{2+x}$ were shifted to lower potentials vs. Li/Li^+ compared to VO_2 (see Figure 6-8c). There were also additional peaks for

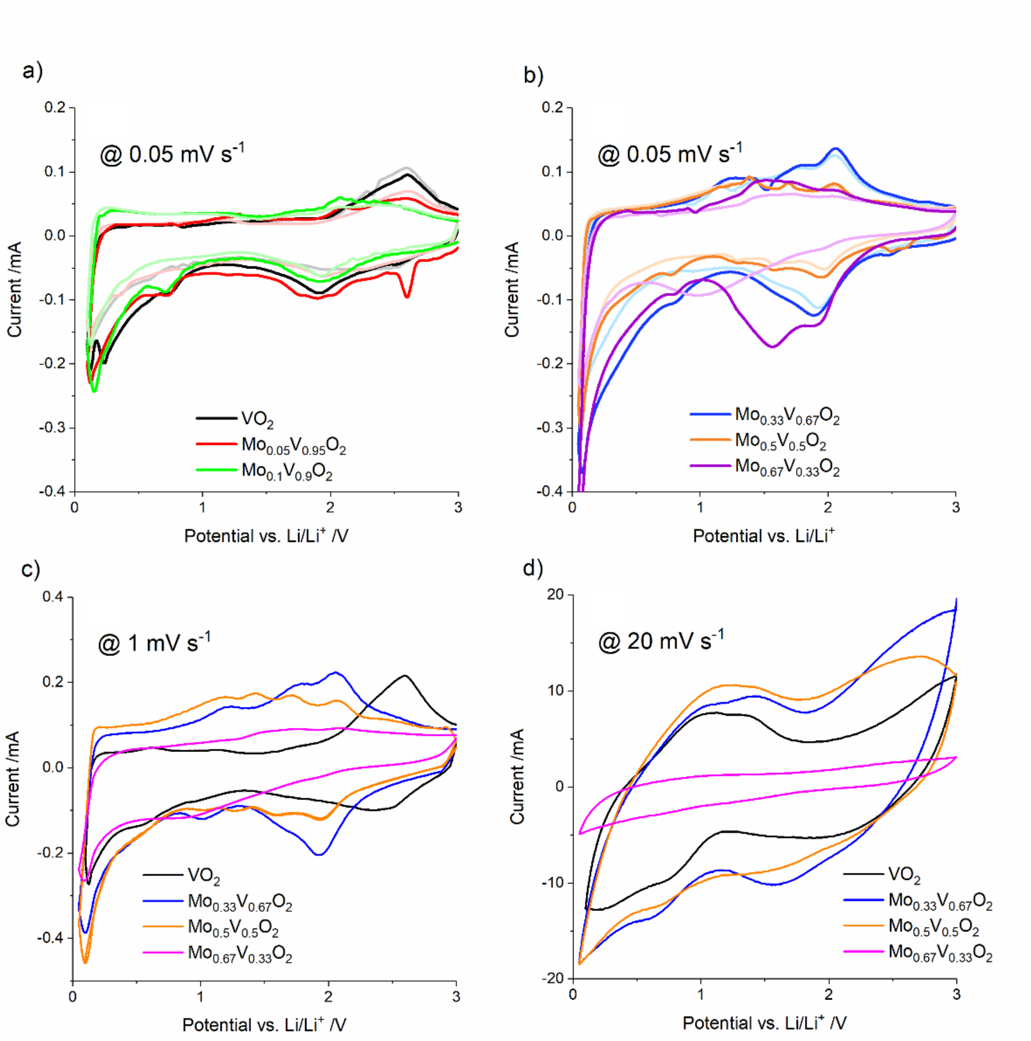

Figure 6-8: a and b) First two CVs for the various samples at scan rates of 0.05 mV s^{-1}. The first cycle for each sample is plotted with a darker colour and the second cycle with lighter colour. CVs for $Mo_{0.67}V_{0.33}O_{2+x}$, $Mo_{0.5}V_{0.5}O_{2+x}$, $Mo_{0.33}V_{0.67}O_{2+x}$, and VO_2 at scan rates of c) 1 and d) 20 mV s^{-1}.

$Mo_{0.5}V_{0.5}O_{2+x}$ and $Mo_{0.33}V_{0.67}O_{2+x}$, which indicated the reversible redox reactions of Mo (VI) to various oxidation states [Mo(V), Mo(IV), Mo(III)]. At higher scan rates, the peaks in the cyclic voltammograms broadened significantly, which indicated increased pseudocapacitive contributions to the overall charge storage (see Figure 6-8d). Whilst the CVs for VO_2 broadened mostly in the potential range 0.05 to 1.00 V vs. Li/Li^+, the cyclic voltammograms of $Mo_{0.5}V_{0.5}O_{2+x}$ and $Mo_{0.33}V_{0.67}O_{2+x}$ broadened over the whole potential range. The CVs for $Mo_{0.67}V_{0.33}O_{2+x}$ showed no broadening and significantly lower currents due to poor lithium-ion diffusion kinetics.

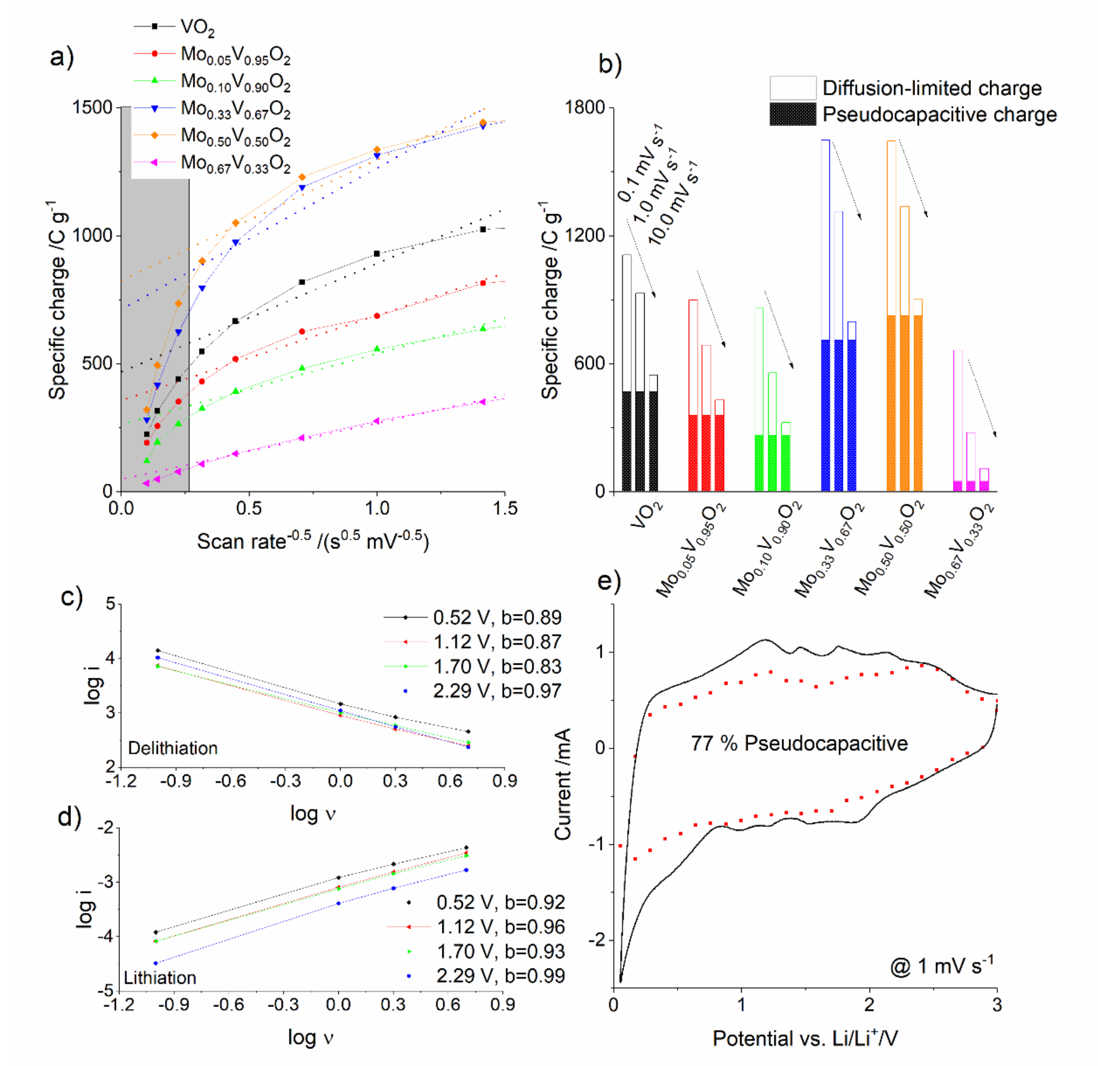

Figure 6-9: a) Specific charge versus reciprocal of the square root of the scan rate for all samples, with the intercept of the lines with the ordinate indicating the charge storage at a theoretical, infinitely fast scan rates. b) Specific charge at various scan rates, separated into diffusion-limited and pseudocapacitive charge (shaded). Plots of the linear relationship between log ν and log i for CVs of c) delithiation and d) lithiation. e) Cyclic voltammogram of $Mo_{0.50}V_{0.50}O_{2+x}$ along with the pseudocapacitive contributions at this scan rate at different potentials.

As described in previous chapters, the pseudocapacitive and diffusion-limited contributions to charge storage were determined from the cyclic voltammograms at various scan rates (see Section 1.5.1.1, Equations 1.28 to 1.30). The total pseudocapacitive contributions (at a theoretical, infinitely fast scan rate) were found to be highest for $Mo_{0.5}V_{0.5}O_{2+x}$ and $Mo_{0.33}V_{0.67}O_{2+x}$ (see Figure 6-9a). The charge stored via pseudocapacitive mechanisms was found to be 468, 357, 263, 712, 825, and

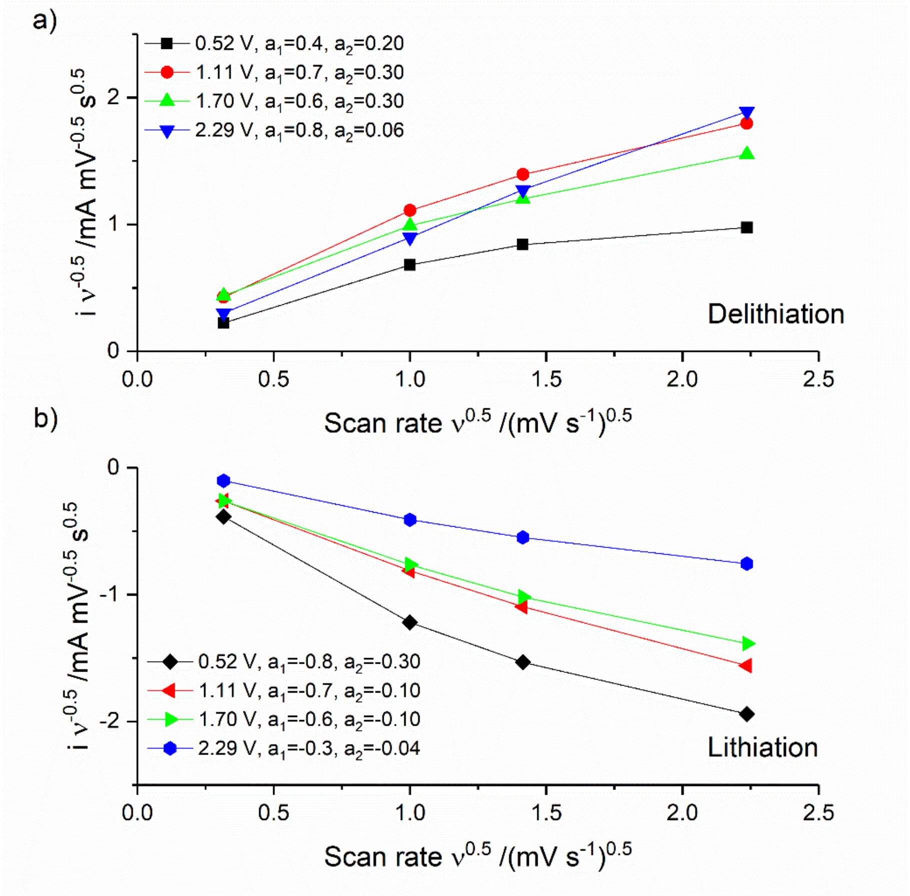

Figure 6-10: Selection of plots of $v^{0.5}$ as a function of $i/v^{0.5}$ to determine parameters a_1 and a_2 at different potentials for $Mo_{0.50}V_{0.50}O_{2+x}$.

50 C g^{-1} for VO_2, $Mo_{0.05}V_{0.95}O_{2+x}$, $Mo_{0.1}V_{0.9}O_{2+x}$, $Mo_{0.33}V_{0.67}O_{2+x}$, $Mo_{0.5}V_{0.5}O_{2+x}$, and $Mo_{0.67}V_{0.33}O_{2+x}$, respectively. Nanosized MoO_2 has previously been reported to show pseudocapacitive charge storage of ca. 300 C g^{-1} (at a scan rate of 10 mV s^{-1}),[57] whereas T-Nb_2O_5, which exhibits intercalation pseudocapacitance, showed capacitive charge storage of ca. 522 C g^{-1} at a theoretical, infinitely fast scan rate.[74]

At a scan rate of 0.1 mV s^{-1}, the pseudocapacitive contributions were 42, 40, 31, 43, 50, and 7 % for VO_2, $Mo_{0.05}V_{0.95}O_{2+x}$, $Mo_{0.1}V_{0.9}O_{2+x}$, $Mo_{0.33}V_{0.67}O_{2+x}$, $Mo_{0.5}V_{0.5}O_{2+x}$, and $Mo_{0.67}V_{0.33}O_{2+x}$, respectively (see Figure 6-9b). At a higher scan rate of 10.0 mV s^{-1}, these pseudocapacitive contributions to charge storage increased to 85, 83, 81, 89, 92, and 45 %, respectively, for the samples.

Furthermore, b-values as described in Section 1.5.1.1 (Equations 1.31 to 1.34) were calculated at various potentials from the slopes of plots such as those in Figure 6-9c and d for delithiation and lithiation, respectively, for $Mo_{0.5}V_{0.5}O_{2+x}$. Values for b near unity indicated the occurrence of mostly pseudocapacitive charge storage processes, whereas values near 0.5 indicated mostly diffusion-limited processes. As can be seen from Figure 6-9e, the charge storage in $Mo_{0.5}V_{0.5}O_{2+x}$ was mostly pseudocapacitive ($b > 0.85$) for both delithiation and lithiation. Only at the lower end of the potential window (< 0.5 V vs. Li/Li^+) were the values indicative of significant contributions from diffusion-limited processes ($b > 0.7$). Additionally, plots showing the scan rate normalised current over the square root of the scan rate, such as those in Figure 6-10, were created for both delithiation and lithiation for $Mo_{0.5}V_{0.5}O_{2+x}$ (see Section 1.5.1.1, Equations 1.35 to 1.37). Parameters a_1 and a_2, which indicate pseudocapacitive and diffusion-limited contributions to charge storage, were determined for a range of potentials. They were used to plot a cyclic voltammogram showing the pseudocapacitive contributions to the current which occurred during the CV at a scan rate of 1.0 mV s^{-1} together with the CV for $Mo_{0.5}V_{0.5}O_{2+x}$ at 1.0 mV s^{-1} (see Figure 6-9d). The charge stored via pseudocapacitive processes was calculated and compared to the total charge. The pseudocapacitive contributions were 77 %, which was in reasonable agreement with the values calculated for Figure 6-9b.

Galvanostatic charge/discharge measurements were conducted in the potential window 0.05 to 3.00 V vs. Li/Li^+ to further investigate the electrochemical performance of the materials. Pure VO_2 showed specific capacities of ca. 350 and 120 mAh g^{-1} at specific currents of 0.1 and 5 A g^{-1}, respectively (see Figure 6-11). This was in good agreement with results previously reported for VO_2 synthesized via CHFS, which showed specific capacities of 350 and 95 mAh g^{-1} at specific currents of 0.1 and 5.0 A g^{-1}.[331] At the same specific currents, the samples with low molybdenum concentration showed decreased performance of 300 and 75 as well as 230 and 45 mAh g^{-1}, respectively, for $Mo_{0.05}V_{0.95}O_{2+x}$ and $Mo_{0.1}V_{0.9}O_{2+x}$, at 0.1 and 5.0 A g^{-1}, respectively.

The samples with a higher molybdenum concentration, $Mo_{0.33}V_{0.67}O_{2+x}$ and $Mo_{0.5}V_{0.5}O_{2+x}$, showed significantly higher specific capacities. At high current rates, the higher pseudocapacitive contributions to charge storage in the samples led to much better charge storage properties; the specific capacities of $Mo_{0.33}V_{0.67}O_{2+x}$ and $Mo_{0.5}V_{0.5}O_{2+x}$ at specific currents of 0.1 and 5 A g^{-1} were 450 and 220 mAh g^{-1} as well as 540 and 255 mAh g^{-1}, respectively. Even at a specific current of 10 A g^{-1}, the

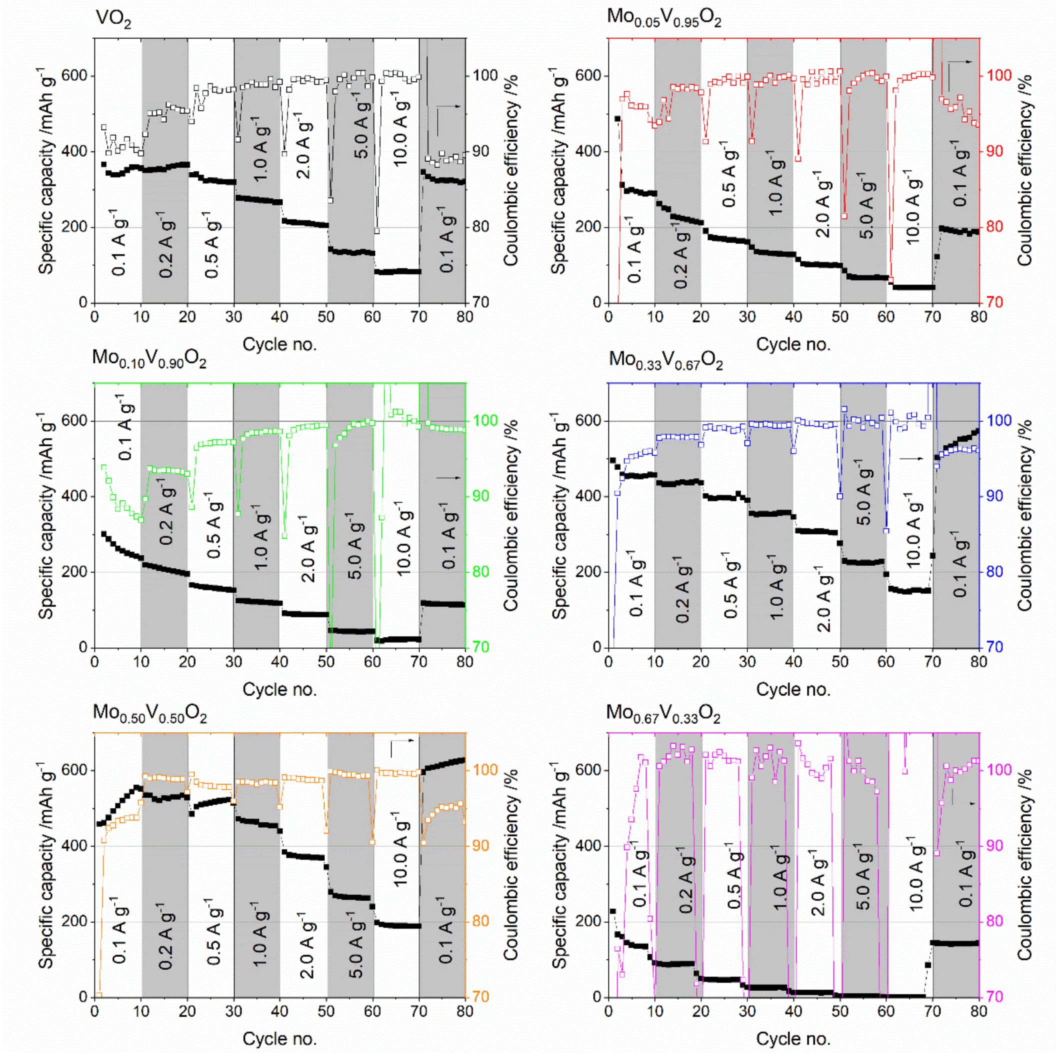

Figure 6-11: Specific capacities from galvanostatic charge/discharge cycling at various specific currents for all samples, along with the respective Coulombic efficiencies.

samples still showed specific capacities of 160 and 200 mAh g^{-1}, respectively. This meant that $Mo_{0.5}V_{0.5}O_{2+x}$ could charge or discharge a specific capacity of 200 mAh g^{-1} within 72 seconds, whilst $Mo_{0.33}V_{0.67}O_{2+x}$ could store 160 mAh g^{-1} in less than one minute. This was significantly better than VO_2 synthesized via CHFS, which showed a capacity of 85 (this work) or 95 mAh g^{-1} (previous reports).[331] The specific capacity of 255 mAh g^{-1} at a specific current of 5 A g^{-1} for $Mo_{0.5}V_{0.5}O_{2+x}$ was comparable to that of a previously reported mixed vanadium-molybdenum oxide ($LiVMoO_6$), which showed a specific capacity of 285 mAh g^{-1}. The synthesis of $LiVMoO_6$, however, required long stirring (12 hr) at 80 °C and sintering at high temperatures.[338]

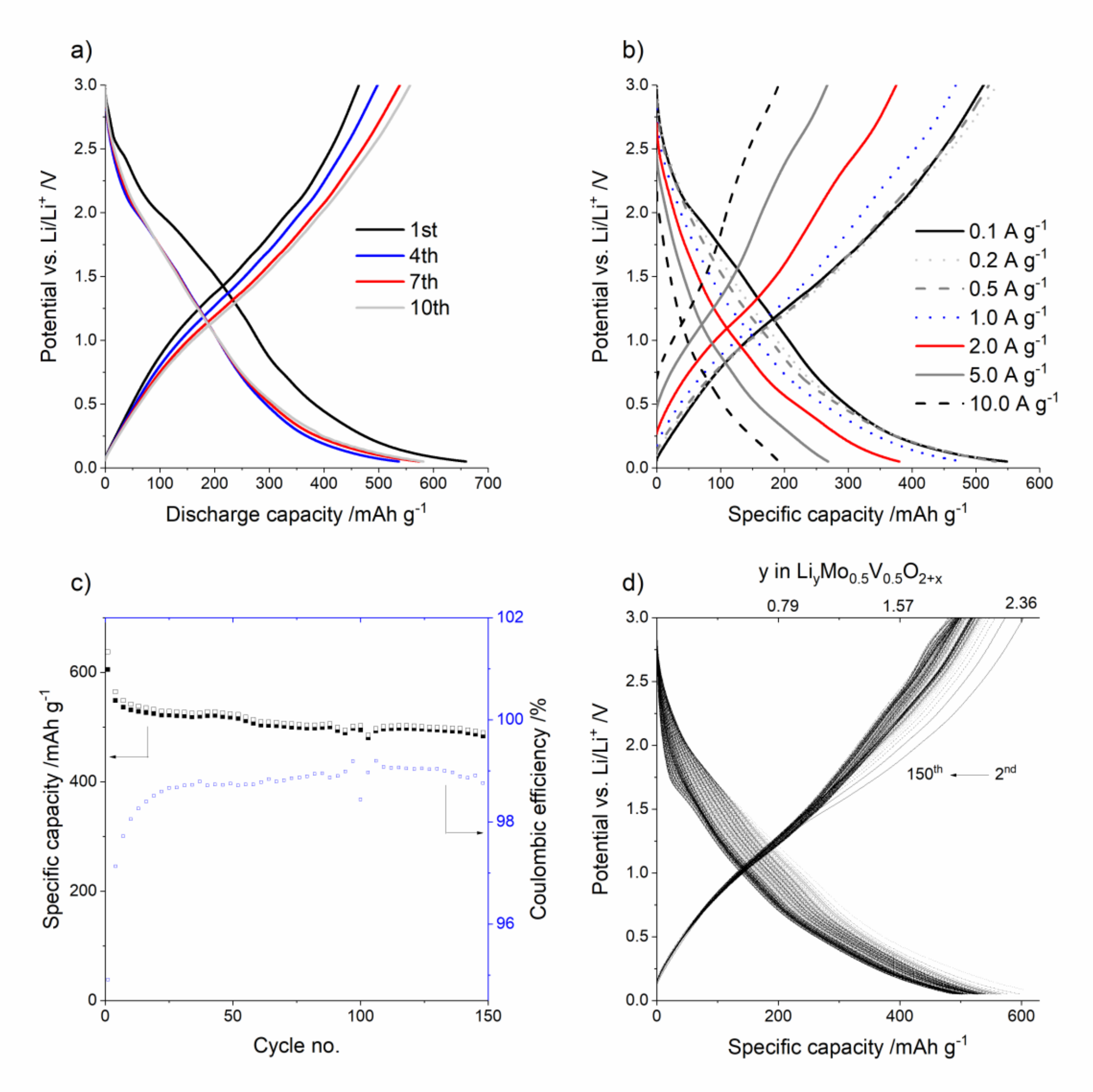

Figure 6-12: a) Galvanostatic charge and discharge curves for the first 10 cycles of $Mo_{0.5}V_{0.5}O_{2+x}$ at 0.1 A g^{-1}. b) Charge and discharge profiles for the 5th cycle at each specific current. c) Cycling stability of $Mo_{0.5}V_{0.5}O_{2+x}$ at 1 A g^{-1}. d) Charge discharge curves for $Mo_{0.5}V_{0.5}O_{2+x}$ at 1.0 A g^{-1}.

For samples with a high molybdenum concentration and for pure MoO_2, the electrochemical properties were poorer. $Mo_{0.67}V_{0.33}O_{2+x}$ showed significant irreversible capacity losses in the first cycle (at 0.1 A g^{-1}), as well as very low Coulombic efficiencies. This indicated the occurrence of irreversible conversion reactions as well as SEI formation, as previously reported for MoO_2 cycled as a conversion material.[335] The first cycle Coulombic efficiencies for $Mo_{0.33}V_{0.67}O_{2+x}$ and $Mo_{0.5}V_{0.5}O_{2+x}$ were 63 and 65 %, respectively, which was presumably because of the formation of SEI and irreversible side reactions.

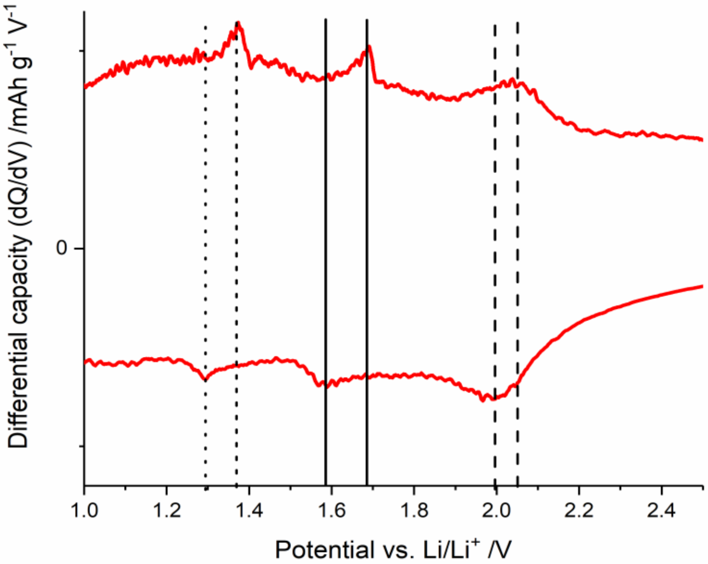

Figure 6-13: Differential capacity (dQ/dV) plot for the third cycle at a specific current of 0.1 A g^{-1} for $Mo_{0.5}V_{0.5}O_{2+x}$ in the potential range 1.0 to 2.5 V vs. Li/Li$^+$.

The charge/discharge plots for $Mo_{0.5}V_{0.5}O_{2+x}$ at a specific current of 0.1 A g^{-1} are shown in Figure 6-12a. There were no significant intercalation plateaus, which indicated that no two-phase lithiation reaction occurred. There appeared to be no (or a very small) miscibility gap for Li$^+$ accommodation. As previously discussed, similar charge/discharge profiles have been observed for a variety of metal oxide nanoparticles. Because this behaviour did not change at higher specific currents (see Figure 6-12b), and because of the relatively low specific surface areas of the materials, it was assumed that intercalation pseudocapacitance rather than extrinsic pseudocapacitance was the dominating charge storage mechanism. As can be seen from Figure 6-12b, as increasing specific current did increase overpotentials, this could be a result of electronic conductivity limitations rather than Li-ion diffusion limitation.

Whilst the lithiation capacity decreased after the first cycle (because SEI formation and other irreversible processes mostly occur then), the delithiation capacity increased with each cycle at a specific current of 0.1 A g^{-1}. Similar behaviour has been observed for a range of porous metal oxide electrodes. The improvement in delithiation capacity can potentially be ascribed to improving lithium diffusion kinetics, increased accessibility of the porous electrode to electrolyte upon cycling, as well as a gradual activation of the conversion reaction for both VO_x and MoO_x.[153,323–326].

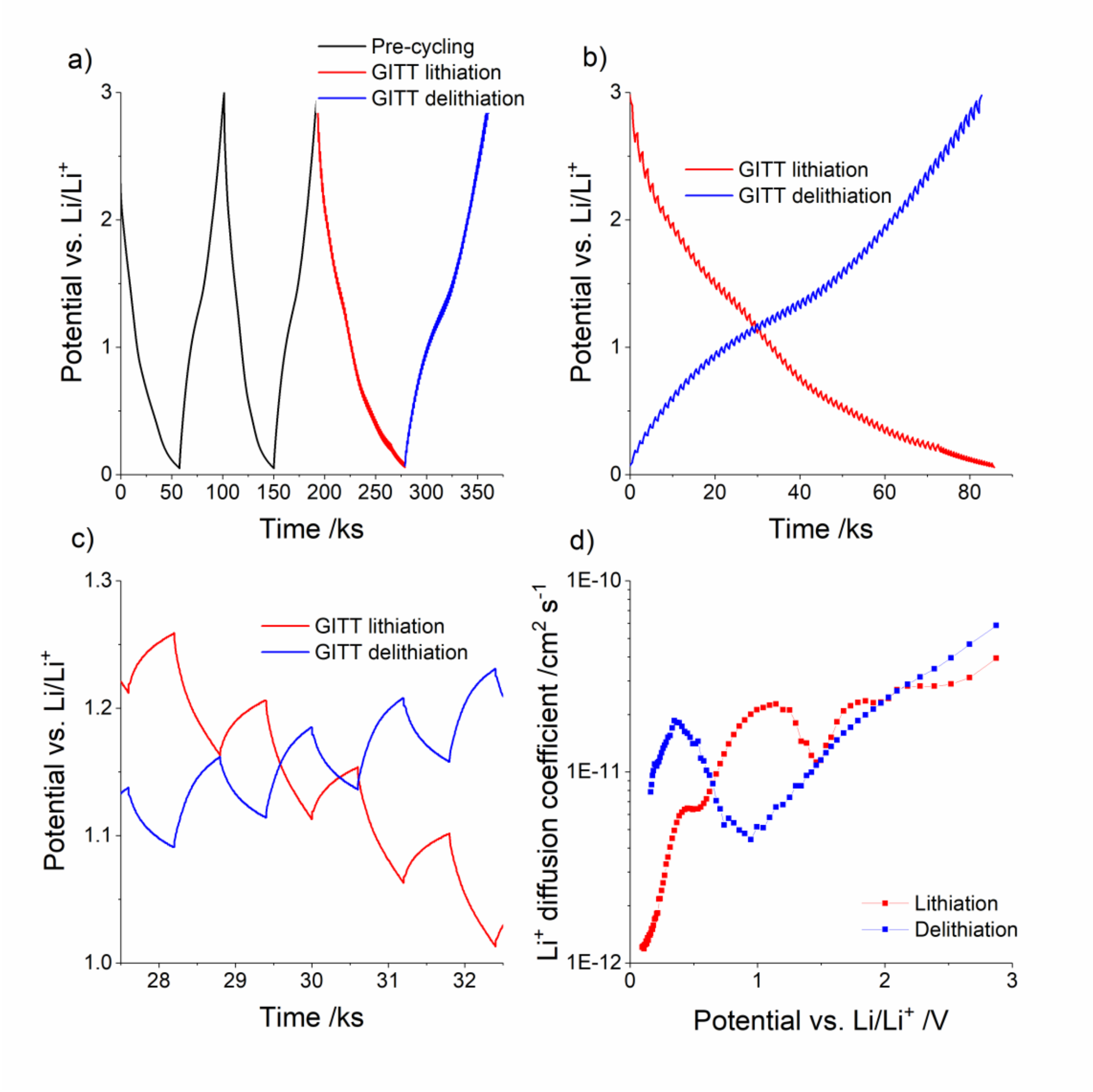

Figure 6-14: a) Galvanostatic pre-cycling for 2 cycles of lithiation and delithiation (black) and Galvanostatic Intermittent Titration Technique (GITT) steps for lithiation (red) and delithiation (blue) of $Mo_{0.5}V_{0.5}O_2$. b) GITT lithiation and delithiation cycling. c) Details of GITT lithiation and delithiation cycling. d) Lithium diffusion coefficients as determined from GITT measurements at different potentials.

Furthermore, the possible formation of vanadium and molybdenum nanoparticles during cycling and their potential catalytic effect on the back reaction of lithium oxides from Li_2O to Li could also have led to the increased capacities.[322]

The differential capacity (dQ/dV) for $Mo_{0.5}V_{0.5}O_{2+x}$ was plotted in Figure 6-13. The differential capacity plot was calculated from the third cycle of galvanostatic charge/discharge cycling at a specific current of 0.1 A g^{-1}. Whilst it was impossible to discern any plateaus from the charge/discharge curves, the differential capacity plot

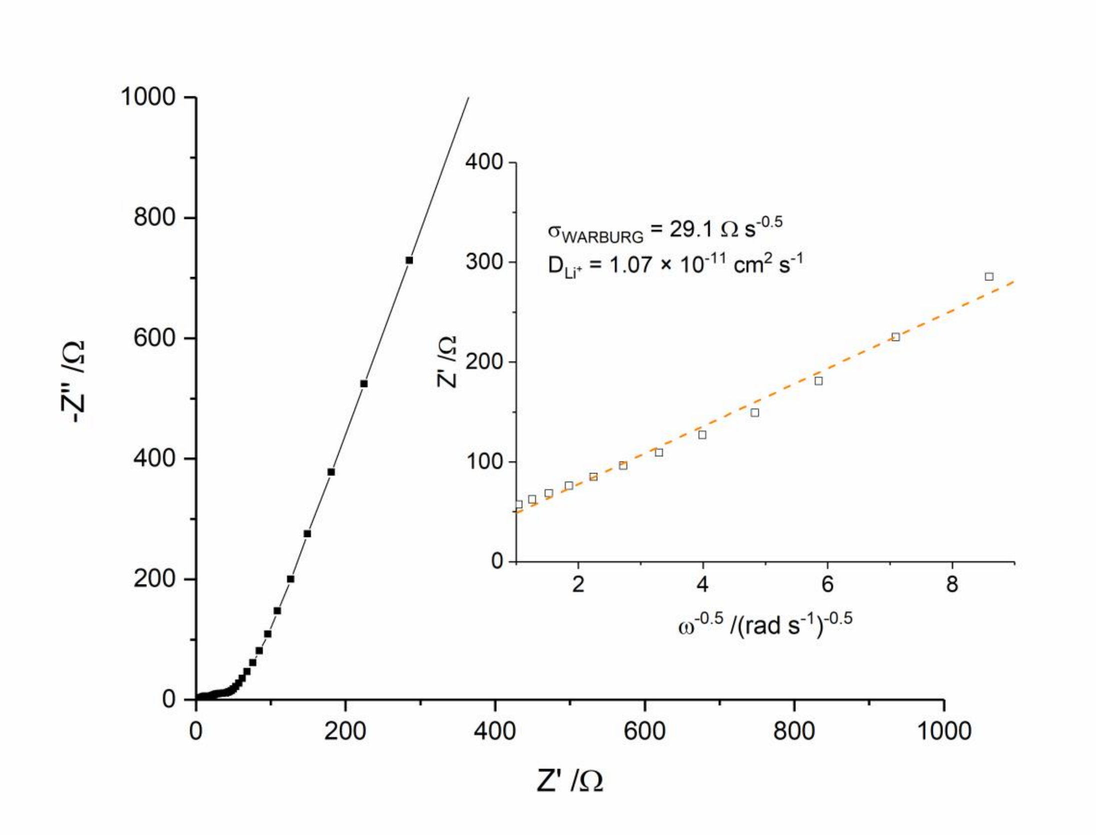

Figure 6-15: Nyquist plot of $Mo_{0.5}V_{0.5}O_{2+x}$ after 20 cycles of galvanostatic cycling along with an inset showing the plot of real impedance vs. the reciprocal square root of the angular frequency, used to determine the Warburg impedance and Li^+ diffusion coefficient.

showed three pairs of small lithiation/delithiation peaks in the potential range 1.0 to 2.5 V vs. Li/Li^+, similar to those for the CVs reported above. This indicated that various redox couples of vanadium and molybdenum ions were available for reversible redox reactions.

Further to the excellent performance at high current rates, $Mo_{0.5}V_{0.5}O_{2+x}$ also showed excellent cycling stability. After 150 cycles at 1.0 A g^{-1}, the specific capacity was 483 mAh g^{-1}. This meant a capacity retention of 84 % (574 mAh g^{-1}, see Figure 6-12c and d), whilst the Coulombic efficiency was above 98 % after the first three cycles. Interestingly, and in contrast to cycling at the lower specific current of 0.1 A g^{-1}, the delithiation capacity did not increase after the first cycle. This was potentially because (with the ten-fold higher current) V and Mo nanoparticle formation and, therefore, the gradual activation processes described above, did not occur.[323,325] On the other hand, the Coulombic efficiency of the first cycle at

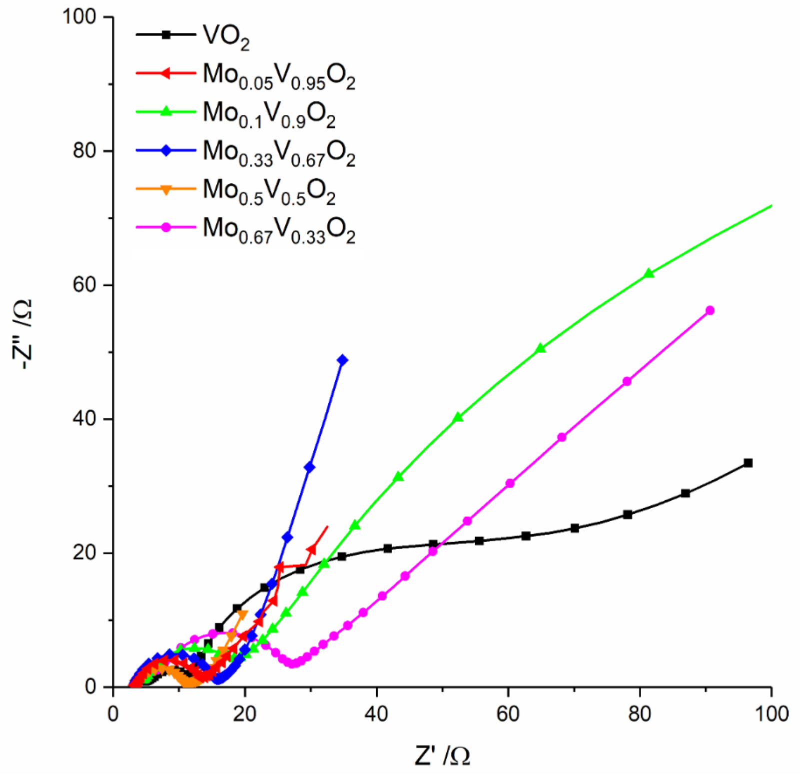

Figure 6-16: Nyquist plots of the various LIB half-cells with mixed Mo/V oxide anodes.

1.0 A g^{-1} was significantly higher than for the first cycle at the lower specific current of 0.1 A g^{-1} (94 and 65 %, respectively). This would indicate that SEI formation and irreversible capacity losses were relatively small and the lower Coulombic efficiency (average of 98.8 % for 150 cycles) could indicate continuous formation of SEI during cycling. Over the 150 cycles, delithiation plots did not change significantly and did not show any discernible plateaus (Figure 6-12b). This performance was excellent compared to similar materials previously reported by other authors. A MoO_2-graphene hybrid showed a capacity fade of 45 % over 100 cycles at a specific current of 0.5 A g^{-1},[148] whereas VO_2 in the literature showed a remaining capacity of only 44 % (460 down to 200 mAh g^{-1}) after 200 cycles at a current of 0.1 mA.[334]

Galvanostatic Intermittent Titration Technique (GITT) was used (see Figure 6-14a to c) to determine the diffusion kinetics of $Mo_{0.5}V_{0.5}O_{2+x}$. It showed that the diffusion coefficients were in the region of 10^{-11} cm^2 s^{-1} over most of the active potential window (see Figure 6-14d). During the lithiation, there was a drop of the diffusion coefficient at ca. 1.5 V vs. Li/Li$^+$ and the diffusion coefficient fell significantly at low potentials. The drop at the middle of the potential window could

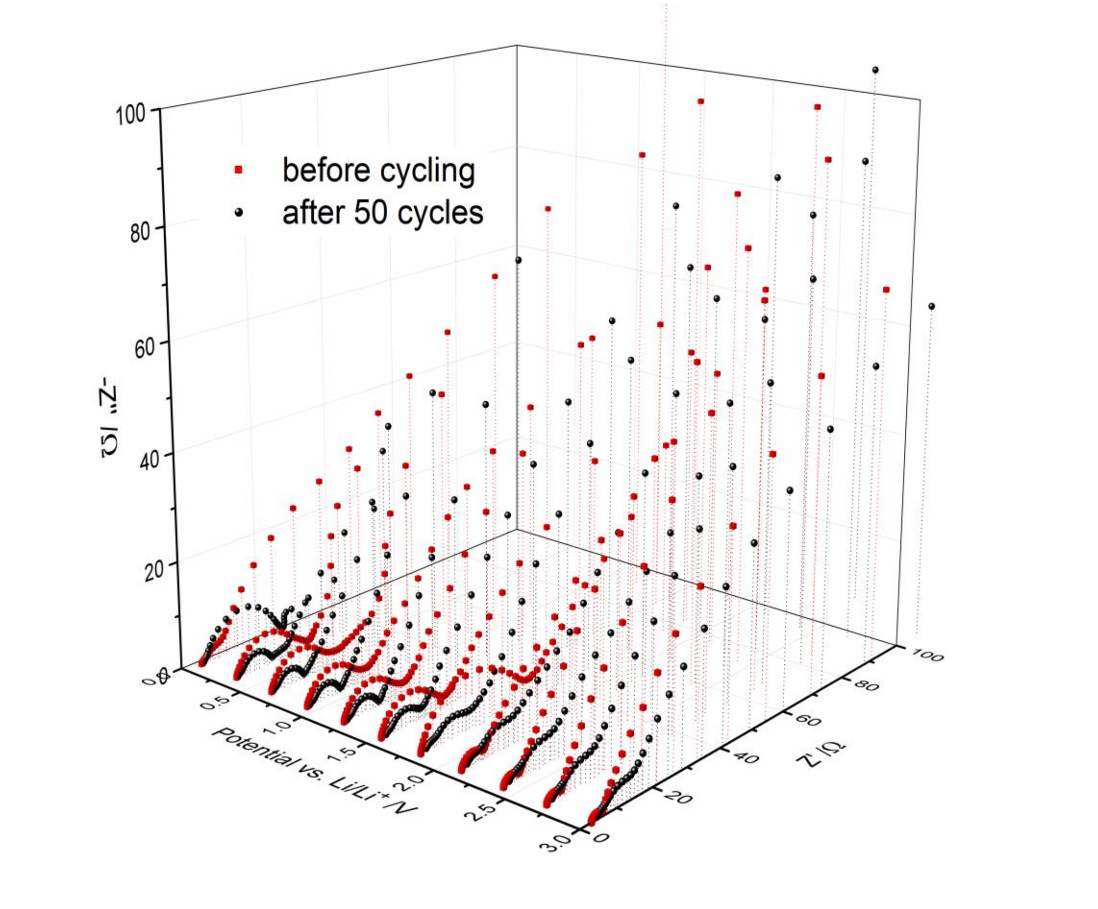

Figure 6-17: Nyquist plots for $Mo_{0.5}V_{0.5}O_{2+x}$ half-cells at various potentials before and after cycling for 50 cycles.

indicate the occurrence of phase transitions which coincide with the peaks in the CVs and the differential capacity. Similar correlations have previously been observed for other electrode materials.[347]

The Li-ion diffusion coefficient for $Mo_{0.5}V_{0.5}O_{2+x}$ was also determined from Electrochemical Impedance Spectroscopy (EIS). After cycling for 20 cycles, the Warburg impedance was determined from the diffusion-limited low frequency region of the Nyquist plot (see Figure 6-15). The Warburg impedance was determined from the slope of the plot of the real impedance versus the reciprocal square root of the angular frequency (as calculated by Equation 1.49, see inset of Figure 6-15). The slope of the potential change with the number of Li-ions in the material was determined to be near unity throughout the galvanostatic charging/discharging via Figure 6-12a. The Warburg impedance was 29.1 Ω $s^{-0.5}$ and the Li-ion diffusion coefficient was

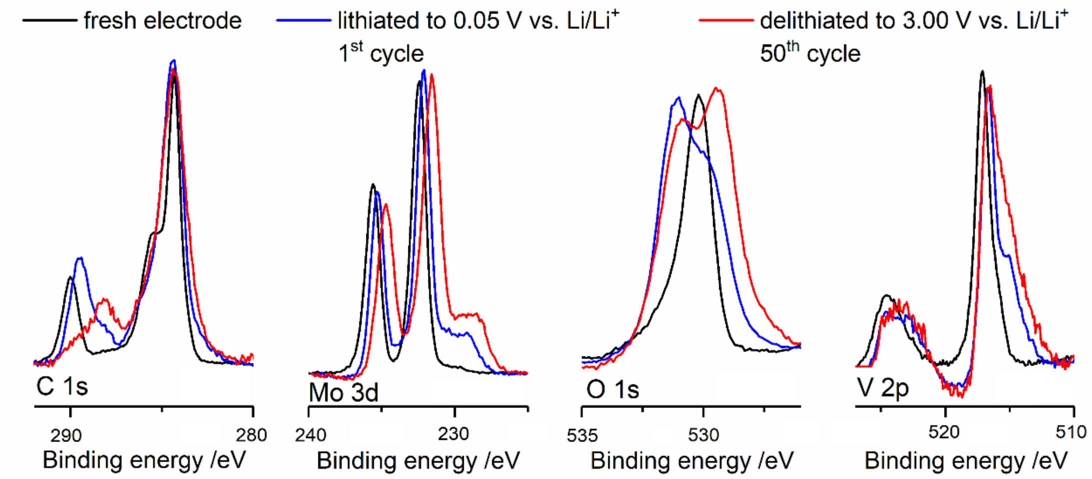

Figure 6-18: X-ray photoelectron spectra of fresh, lithiated, and cycled $Mo_{0.5}V_{0.5}O_{2+x}$ electrodes.

ca. 10^{-11} cm^2 s^{-1}. This was in good agreement with the diffusion coefficients determined from GITT.

To further investigate the electrochemical properties of all samples, EIS was conducted. From the impedance spectra it became apparent that both SEI and charge-transfer resistance for Li-ion half-cells made using $Mo_{0.33}V_{0.67}O_{2+x}$ and $Mo_{0.5}V_{0.5}O_{2+x}$ electrodes were significantly lower than for those made from $Mo_{0.67}V_{0.33}O_{2+x}$ and $Mo_{0.1}V_{0.9}O_{2+x}$ (see Figure 6-16). It was also interesting that $Mo_{0.67}V_{0.33}O_{2+x}$ appeared to possess the highest impedance values, which was surprising considering the near-metallic electronic conductivity of MoO_2. From XRD, $Mo_{0.67}V_{0.33}O_{2+x}$ appeared to have exclusively monoclinic MoO_2 crystal structure.

A Li-ion half-cell of $Mo_{0.5}V_{0.5}O_{2+x}$ was further studied via SPEIS (see Figure 6-17). Charge transfer and SEI resistance, especially in the potential range 0.05 to 2.00 V vs. Li/Li^+ during lithiation, were significantly lower than before cycling. This indicated that resistance to lithiation in the potential range of most interest (considering the peak positions in the CVs) reduced with cycling.

Electrodes of $Mo_{0.5}V_{0.5}O_{2+x}$ were studied ex-situ after cycling. They were examined before cycling, after being fully lithiated to a potential of 0.05 V vs. Li/Li^+ at a specific current of 0.1 A g^{-1}, and after being fully delithiated to a potential of 3.00 V vs. Li/Li^+, after galvanostatic cycling for 50 cycles at a specific current of

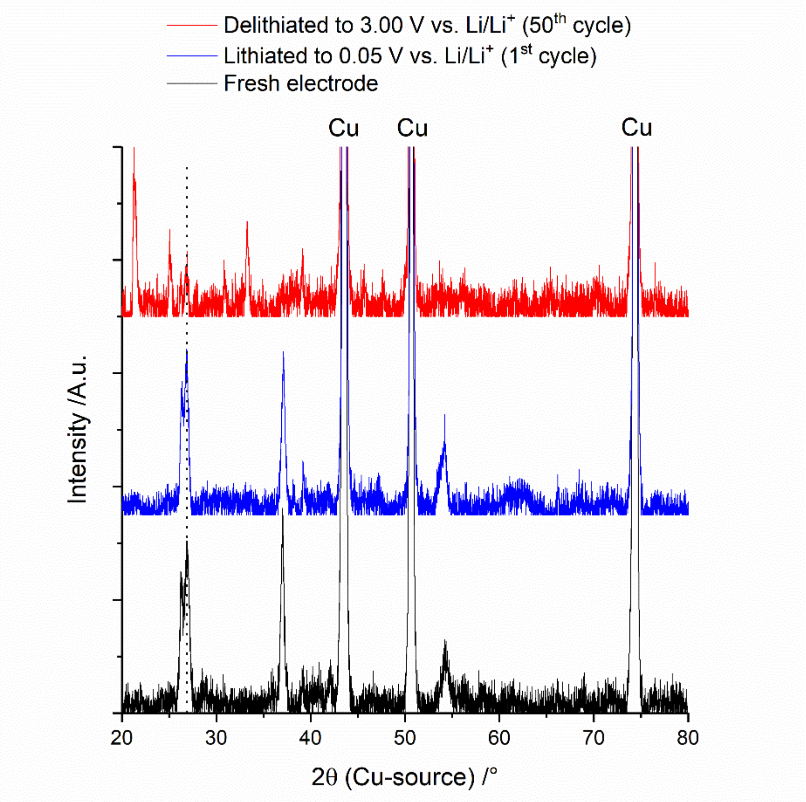

Figure 6-19: XRD patterns of fresh, lithiated, and cycled $Mo_{0.5}V_{0.5}O_{2+x}$ electrodes.

0.1 A g^{-1}. Although some components of both the lithiated and the delithiated electrodes might have been (partially) air-sensitive, XRD and XPS were carried out. As expected, an analysis of XPS spectra for both V *2p* and Mo *3d* of the lithiated electrode revealed a shift of peaks to lower binding energies, which indicated the presence of lower valance-state metal ions compared to the fresh electrode (see Figure 6-18). The “fully” delithiated electrode, after 50 cycles, showed even more significant shifts of the V *2p* and Mo *3d* peaks. Although a return to both V (IV) and Mo (VI) would be expected upon full delithiation, the fact that the Coulombic efficiency was below 100% for each cycle indicated that some irreversible lithiation took place, but was most likely a result of the gradual activation process of porous electrodes, as discussed above.[153,323–326]

In contrast to this, the XRD patterns of the lithiated electrode showed only a minimal shift in peak positions after the first lithiation, which indicated small changes in the lattice parameters due to lithium intercalation (see Figure 6-19). The peak shift was only observable for the (011) peaks for VO_2, not the one for MoO_2. Upon cycling for 50 cycles and delithiation, the peak shifts were still not very pronounced.

Additionally, the XRD pattern showed evidence of crystalline constituents of a SEI along with the original monoclinic phases.

6.5. Conclusions

It was shown that monoclinic, mixed vanadium and molybdenum oxide anode active materials synthesized in a one-step process can show excellent performance in Li-ion half-cells. The mixed oxides formed solid solutions (except for the sample with the experimental and nominal composition $Mo_{0.5}V_{0.5}O_{2+x}$), which suggested a solubility limit of V in MoO_2 and Mo in VO_2 around 50 at.%. Two monoclinic phases were produced, based on Mo and V oxide, respectively.

Pseudocapacitive contributions to charge storage were high for most samples, but especially for $Mo_{0.33}V_{0.67}O_{2+x}$ and $Mo_{0.5}V_{0.5}O_{2+x}$. The pseudocapacitive contributions to the total charge were ca. 90 % at a scan rate of 10 mV s^{-1} for both samples. The theoretical pseudocapacitive charge at an infinitely fast scan rate was 712 and 825 C g^{-1} (equal to 198 and 229 mAh g^{-1}, respectively) for $Mo_{0.33}V_{0.67}O_{2+x}$ and $Mo_{0.5}V_{0.5}O_{2+x}$, respectively.

Because the specific surface areas were not exceedingly high, at least part of the pseudocapacitive contributions was attributed to intercalation pseudocapacitance. Especially for $Mo_{0.33}V_{0.67}O_{2+x}$ and $Mo_{0.5}V_{0.5}O_{2+x}$, this led to excellent charge storage in Li-ion half-cells at high specific currents, e.g. the specific capacities were 160 and 200 mAh g^{-1} for $Mo_{0.33}V_{0.67}O_{2+x}$ and $Mo_{0.5}V_{0.5}O_{2+x}$, respectively, at a specific current of 10 A g^{-1}.

The availability of a large variety of redox couples, nanosizing, and the excellent cyclability due to relatively small geometrical changes upon lithiation and delithiation combined to make the materials reported herein promising materials for Li-ion battery anodes.

Future research could focus on improvements to these materials by adding an addition element to improve specific capacity or lower the average voltage hysteresis (such as Nb or W), as well as further elucidation of the mechanisms that result in the excellent performance for $Mo_{0.5}V_{0.5}O_{2+x}$ and $Mo_{0.33}V_{0.67}O_{2+x}$, but much poorer performance for $Mo_{0.10}V_{0.9}O_{2+x}$ and $Mo_{0.67}V_{0.33}O_{2+x}$. The development of Li-HECs containing these high-power, high-energy negative electrode materials would be rewarding.

7. Overall Conclusions & Future Work

7.1. Summary of Conclusions

A range of materials were synthesised via a continuous hydrothermal flow synthesis (CHFS) process for use as active materials in negative electrodes for Li-ion and Na-ion electrochemical energy storage devices. The materials, which benefited from small particle size, phase purity, and a high synthesis rate, showed excellent properties in electrochemical energy storage devices, especially at high power. This was associated with high pseudocapacitive contributions to charge storage.

In Chapters 3 and 4, molybdenum, vanadium, and niobium doped anatase (TiO_2) samples have been successfully synthesised by varying precursor ratios. Furthermore, synthesis processes for MoO_2, $NiCo_2O_4$, Co_2TiO_4 as well as nanocomposites such as TiO_2/MoO_2 and $TiO_2/NiCo_2O_4$ have been developed in Chapter 5. Finally, the successful synthesis of solid solutions of mixed molybdenum/vanadium oxides and their excellent charge storage properties at high power have been reported in Chapter 6.

In Chapter 3, it was shown that heterometallic doping of TiO_2 with Mo(VI), V(V), or Nb(V) increased the electronic conductivity, Li^+/Na^+ diffusivity, and pseudocapacitive charge storage at high power compared to undoped nanosized TiO_2 (in half-cells). For example, $Mo_{0.1}Ti_{0.9}O_2$ showed a specific capacity of 100 mAh g^{-1} at a specific current of 5 A g^{-1} in Li-ion half-cells, whereas TiO_2 only showed a specific capacity of 75 mAh g^{-1}. All doped samples showed specific capacities of ca. 75 mAh g^{-1} at a specific current of 1 A g^{-1} in Na-ion half-cells, whereas undoped TiO_2 only showed a specific capacity of 30 mAh g^{-1} under the same conditions. The better charge storage at high power in both Li-ion and Na-ion chemistries could be ascribed to the improved electronic conductivity and ion diffusivity due to doping, which improved pseudocapacitive charge storage contributions (that are much faster than diffusion-limited processes).

In Section 3.4.2.2, the improved electrochemical properties shown in half-cell measurements resulted in improved performance of the doped anatase nanomaterials in Li/Na-HECs, compared to undoped TiO_2, versus activated carbon positive electrodes. For example, a $Mo_{0.1}Ti_{0.9}O_2$/AC Li-HEC cycled in the potential window 1 to 3 V demonstrated an energy density of 29 Wh kg^{-1} at a power density of 2000 W kg^{-1}. In contrast, a TiO_2/AC Li-HEC showed an energy density of 14 Wh kg^{-1} at a similar power density (1800 W kg^{-1}). Furthermore, a $Mo_{0.1}Ti_{0.9}O_2$/AC Na-HEC cycled in the potential window 1 to 4 V showed an energy density of 31 Wh kg^{-1} at a power density of 3360 W kg^{-1}, whereas a TiO_2/AC Na-HEC only showed an energy density of 3 Wh kg^{-1} at 2350 W kg^{-1}. The improved performance of the HECs was a result of the improved electrochemical properties of the negative electrode materials. The higher pseudocapacitive contributions, which result in the ability for very fast charge storage, significantly benefitted the energy and power densities of the HECs. This was the first time that Mo- or V-doped anatase (TiO_2) has been used in negative electrodes for NIBs, Na-HECs, and Li-HECs.

In Section 3.4.2.3, it was shown that pre-lithiation/pre-sodiation of the (doped) TiO_2 anodes significantly improved the performance of Li/Na-HECs. A pre-lithiated $Mo_{0.1}Ti_{0.9}O_2$/AC Li-HEC cycled in the potential window 1 to 3 V showed an energy density of 28 Wh kg^{-1} at a power density of 3900 W kg^{-1}, compared to a non-pre-lithiated Li-HEC, which demonstrated an energy density of only 21 Wh kg^{-1} at a power density of 3600 W kg^{-1}. For a $Mo_{0.1}Ti_{0.9}O_2$/AC Na-HEC cycled in the potential window 1 to 4 V, pre-sodiation led to an increase in energy densities to 73 and 42 Wh kg^{-1} (at power densities of 570 and 2630 W kg^{-1}) from 60 and 31 Wh kg^{-1} (at comparable power densities of 340 and 3360 W kg^{-1}) for a $Mo_{0.1}Ti_{0.9}O_2$/AC Na-HEC that was not pre-sodiated.

In Chapter 4, the co-doping of TiO_2 with molybdenum, vanadium, and niobium showed that different combinations of co-dopants can have antagonistic or synergetic effects on the electrochemical properties. For example, molybdenum and vanadium co-doping resulted in significantly lower specific capacities at each specific current, whereas niobium co-doping with either vanadium and molybdenum resulted in improved specific capacities. Furthermore, co-doping with all three dopants could show additional synergetic effects, so that $Nb_{0.08}Mo_{0.04}V_{0.04}Ti_{0.85}O_2$ showed good cycling stability and performance at high specific current rates. These antagonistic and synergistic effects of co-doping were expected to be the result of interactions between dopants. For the first time, CHFS was used for a compositional study of negative electrode materials for LIBs and the antagonistic and synergistic effects of doping were studied.

In Chapter 5, the co-precipitation of conversion active materials for anodes such as MoO_2 and $NiCo_2O_4$ with TiO_2 showed that the inclusion of an electrochemically and physically stable phase such as TiO_2 could significantly improve the cycling stability and rate performance of these conversion materials. Large volume changes during cycling (often resulting in poor cycle life), large voltage hysteresis, and poor rate properties are the concerns usually quoted when discussing conversion materials for anodes in LIBs. The synthesis of composites containing a stabilising phase could reduce some of these issues, potentially by acting as an "anchor" for the back-reaction of the conversion, by increasing the available surface area, and by reducing the particle growth of the conversion materials. It was shown that the co-precipitation was essential, as electrodes made using a mixture of TiO_2 and MoO_2 synthesised separately showed inferior cycling performance than electrodes of the composite with equal molar concentrations. The intimate mixing of the materials during the synthesis was essential to the anchoring function and to increase surface area. This chapter offered a fresh approach to the synthesis of composite materials for negative electrodes for LIBs and Li-HECs, by co-precipitation using a CHFS process.

In Chapter 6, mixed molybdenum/vanadium oxides prepared via CHFS showed highly pseudocapacitive charge storage in Li-ion half-cells. A sample with the nominal composition $Mo_{0.5}V_{0.5}O_{2+x}$ showed over 90 % pseudocapacitive charge storage contributions at a scan rate of 10 mV s^{-1} and a pseudocapacitive charge of 825 C g^{-1} at a theoretical, infinitely fast scan rate. Furthermore, at a specific current of 10 A g^{-1}, the specific capacity was 200 mAh g^{-1}, which was by far the highest specific capacity that has been observed for any LIB electrode active material synthesized via CHFS. The availability of various redox couples, the excellent pseudocapacitive charge storage, and nanosizing all combined to allow 200 mAh g^{-1} of capacity to be stored (or discharged) within just 72 seconds. This chapter, for the first time, showed the potential of mixed metal oxides synthesized via CHFS as highly pseudocapacitive negative electrodes for LIBs.

7.2. Outlook and Future Work

The research presented in this thesis opens a variety of possible opportunities for future studies. The evidence in this thesis shows that transition metal oxide nanoparticles synthesised via CHFS processes can be used effectively as anode materials in a variety of electrochemical energy storage devices, including Li-ion batteries (LIBs), Na-ion batteries (NIBs), Li-ion hybrid electrochemical capacitors (Li-HECs), and Na-ion hybrid electrochemical capacitors (Na-HECs).

Multivalent charge storage offers a huge opportunity for further research, especially for TiO_2 doped with pentavalent or hexavalent transition metal (TM) ions. Computational analysis of Mo-doped TiO_2 has shown that Ti(IV) vacancies created by the introduction of (VI) ions into the lattice can serve as Mg(II) intercalation sites and Mg-ion mobility is significantly increased. Other multivalent storage chemistries, such as Al(III)-ion, could also be an interesting avenue to explore for a variety of dopants explored herein, such as Mo(VI), V(V), and Nb(V), because the improved electronic conductivity and additional Al(III) intercalation sites due to Ti(IV) vacancies could lead to improved multivalent charge storage. Additionally, co-doping of anatase TiO_2 with dopants other than Mo, V, and Nb (such as W, N, or Sn) could be interesting to explore. Dopants such as Sn, which might work to improve the energy density of TiO_2 via introducing alloying reactions to the lithiation process, could significantly enhance performance. Furthermore, exploring the potentially synergetic effects of co-doping on electrochemical energy storage chemistries other than the Li-ion chemistry explored here could be very enlightening.

More energy-dense active anode materials (such as $Mo_{0.5}V_{0.5}O_{2+x}$) offer the opportunity to be explored to further improve energy and power densities of HECs. Besides improvements of the active materials, better conductive networks for highly conductive electrodes offer a key future approach to better performance, due to the limitations of energy densities at high power densities due to limited conductivity. Avenues to explore are three-dimensional, conductive, metallic networks, additives such as carbon nanotubes and graphene, as well as conductive polymeric binders. Furthermore, improved cathode performance by one of these three methods, by using improved activated carbon active materials, or via exploring additives such as transition metal oxide cathode materials could further improve HEC performance significantly.

The exploration of negative electrode materials that showed excellent electrochemical performance in Li-ion chemistries, such as the conversion material composites and the molybdenum/vanadium mixed oxides in Na-ion chemistry, offers an obvious avenue for future studies

Additionally, pre-lithiation/pre-sodiation play an important role not only in Li/Na-HECs, but also in LIBs and NIBs. Extensive research into methods of avoiding a separate pre-lithiation/pre-sodiation step is necessary for the commercialisation of materials such as $Mo_{0.5}V_{0.5}O_{2+x}$ in Li-HECs. For example, sacrificial Li^+/Na^+ donors such as Li_2CuO_2 and $NaCuO_2$, which upon initial charging are delithiated/desodiated and then become conductive (but inert) constituents of the cathode could be further developed. Additionally, pre-doping by inclusion of lithium in either the negative or positive electrode mixtures could be explored.

Finally, exploring the use of stabilising co-precipitates to improve conversion/alloying materials, using a simple one-step synthesis such as CHFS, with different combinations of stabilising material / conversion active materials will enable a better understanding of the mechanisms that lead to improvements in electrochemical performance for these types of composite materials. This could include the combination of stabilising materials such as $Li_4Ti_5O_{12}$, different polymorphs of TiO_2, or Nb_2O_5 with conversion or alloying materials such as SnO_2, Fe_2O_3, Fe_3O_4, Co_3O_4, and others, which have previously been synthesised separately by CHFS.

Bibliography

[1] M.R. Palacín, Recent advances in rechargeable battery materials: a chemist's perspective., Chem. Soc. Rev. 38 (2009) 2565–2575. doi:10.1039/b820555h.

[2] E. Dlugokencky, P. Tans, Averaged monthly mean carbon dioxide levels over global marine surface sites, Natl. Ocean. Atmos. Adm. Earth Syst. Res. Lab. (2017). www.esrl.noaa.gov/gmd/ccgg/trends/.

[3] National Oceanic and Atmospheric Administration, Climate at a Glance: Global Time Series, (2017). http://www.ncdc.noaa.gov/cag/.

[4] B.P. Company, 2016, BP Statistical Review of World Energy, London, (2016) . https://www.bp.com/content/dam/bp/pdf/energy-economics/statistical-review-2016/bp-statistical-review-of-world-energy-2016-full-report.pdf.

[5] B. Scrosati, J. Garche, Lithium batteries: Status, prospects and future, J. Power Sources. 195 (2010) 2419–2430. doi:10.1016/j.jpowsour.2009.11.048.

[6] C. Pillot, Battery Market Development for Consumer Electronics, Automotive, and Industrial: Materials Requirements and Trends, (2015). https://docplayer.net/21143951-Battery-market-development-for-consumer-electronics-automotive-and-industrial-materials-requirements-and-trends.html.

[7] H. Ibrahim, A. Ilinca, J. Perron, Energy storage systems-Characteristics and comparisons, Renew. Sustain. Energy Rev. 12 (2008) 1221–1250. doi:10.1016/j.rser.2007.01.023.

[8] A.S. Aricò, P. Bruce, B. Scrosati, J. Tarascon, W. van Schalkwijk, Nanostructured materials for advanced energy conversion and storage devices, Nat. Mater. 4 (2005) 366–377. doi:10.1038/nmat1368.

[9] I. Plitz, A. DuPasquier, F. Badway, J. Gural, N. Pereira, A. Gmitter, G.G. Amatucci, The design of alternative nonaqueous high power chemistries, Appl. Phys. A. 82 (2006) 615–626. doi:10.1007/s00339-005-3420-0.

[10] H. Berg, The electrochemical cell, in: Batter. Electr. Veh., Cambridge University Press, (2016) 7–46. doi:10.1017/CBO9781316090978.004.

[11] A.J. Bard, L.R. Faulkner, Electrochemical Methods - Fundamentals and Applications, 2nd Ed., John Wiley & Sons, Inc., New York, (2001) . https://goo.gl/1d3SpH.

[12] J.N. Spencer, G.M. Bodner, L.H. Rickard, Electrochemical Cells at Nonstandard Conditions: The Nernst Equation, in: Chem. Struct. Dyn., 5th Ed., John Wiley & Sons, New York, (2010) 563–565.

[13] M.M. Thackeray, C. Wolverton, E.D. Isaacs, Electrical energy storage for transportation—approaching the limits of, and going beyond, lithium-ion batteries, Energy Environ. Sci. 5 (2012) 7854–7863. doi:10.1039/c2ee21892e.

[14] Y. Xu, E. Memarzadeh Lotfabad, H. Wang, B. Farbod, Z. Xu, A. Kohandehghan, D. Mitlin, Nanocrystalline anatase TiO_2: a new anode material for rechargeable sodium ion batteries, Chem. Commun. 49 (2013) 8973. doi:10.1039/c3cc45254a.

[15] H. Usui, S. Yoshioka, K. Wasada, M. Shimizu, H. Sakaguchi, Nb-doped rutile TiO_2: A potential anode material for Na-ion battery, ACS Appl. Mater. Interfaces. 7 (2015) 6567–6573. doi:10.1021/am508670z.

[16] L. Wu, D. Buchholz, D. Bresser, L. Gomes Chagas, S. Passerini, Anatase TiO_2 nanoparticles for high power sodium-ion anodes, J. Power Sources. 251 (2014) 379–385. doi:10.1016/j.jpowsour.2013.11.083.

[17] T. Nagaura, K. Tazawa, Lithium ion rechargeable battery, Prog. Batter. Sol.

Cells. 9 (1990) 209–217.

[18] Y.R. Ahn, C.R. Park, S.M. Jo, D.Y. Kim, Enhanced charge-discharge characteristics of RuO_2 supercapacitors on heat-treated TiO_2 nanorods, Appl. Phys. Lett. 90 (2007) 122106. doi:10.1063/1.2715038.

[19] J.B. Goodenough, General Concepts, in: Lithium Ion Batter., M. Wakihara, O. Yamamoto (Eds.), 1st Ed., Wiley-VCH Verlag GmbH, Weinheim, Germany, (2007) 1–25. doi:10.1002/9783527612000.ch1.

[20] D. Deng, Li-ion batteries: basics, progress, and challenges, Energy Sci. Eng. 3 (2015) 385–418. doi:10.1002/ese3.95.

[21] M. Park, X. Zhang, M. Chung, G.B. Less, A.M. Sastry, A review of conduction phenomena in Li-ion batteries, J. Power Sources. 195 (2010) 7904–7929. doi:10.1016/j.jpowsour.2010.06.060.

[22] E. Peled, The Electrochemical Behavior of Alkali and Alkaline Earth Metals in Nonaqueous Battery Systems—The Solid Electrolyte Interphase Model, J. Electrochem. Soc. 126 (1979) 2047. doi:10.1149/1.2128859.

[23] J.B. Goodenough, K.S. Park, The Li-ion rechargeable battery: A perspective, J. Am. Chem. Soc. 135 (2013) 1167–1176. doi:10.1021/ja3091438.

[24] J.B. Goodenough, Y. Kim, Challenges for rechargeable Li batteries, Chem. Mater. 22 (2010) 587–603. doi:10.1021/cm901452z.

[25] C. Julien, A. Mauger, A. Vijh, K. Zaghib, Lithium Batteries, in: Lithium Batter., M. Wakihara, O. Yamamoto (Eds.), 1st Ed., Springer International Publishing, Cham, (2016) 29–68. doi:10.1007/978-3-319-19108-9_2.

[26] M.A. Muñoz-Márquez, M. Zarrabeitia, E. Castillo-Martínez, A. Eguía-Barrio, T. Rojo, M. Casas-Cabanas, Composition and evolution of the solid-electrolyte interphase in $Na_2Ti_3O_7$ electrodes for Na-Ion batteries: XPS and auger parameter analysis, ACS Appl. Mater. Interfaces. 7 (2015) 7801–7808. doi:10.1021/acsami.5b01375.

[27] R. Mogensen, D. Brandell, R. Younesi, Solubility of the Solid Electrolyte Interphase (SEI) in Sodium Ion Batteries, ACS Energy Lett. 1 (2016) 1173–1178. doi:10.1021/acsenergylett.6b00491.

[28] M.D. Slater, D. Kim, E. Lee, C.S. Johnson, Sodium-Ion Batteries, Adv. Funct. Mater. 23 (2013) 947–958. doi:10.1002/adfm.201200691.

[29] H. Kang, Y. Liu, K. Cao, Y. Zhao, L. Jiao, Y. Wang, H. Yuan, Update on anode materials for Na-ion batteries, J. Mater. Chem. A. 3 (2015) 17899–17913. doi:10.1039/C5TA03181H.

[30] M. Reich, P.M. Vasconcelos, Geological and economic significance of supergene metal deposits, Elements. 11 (2015) 305–310. doi:10.2113/gselements.11.5.305.

[31] D.A. Stevens, J.R. Dahn, High Capacity Anode Materials for Rechargeable Sodium-Ion Batteries, J. Electrochem. Soc. 147 (2000) 1271–1273. doi:10.1149/1.1393348.

[32] N. Yabuuchi, M. Kajiyama, J. Iwatate, H. Nishikawa, S. Hitomi, R. Okuyama, R. Usui, Y. Yamada, S. Komaba, P2-type $Na_x[Fe_{1/2}Mn_{1/2}]O_2$ made from earth-abundant elements for rechargeable Na batteries, Nat. Mater. 11 (2012) 512–517. doi:10.1038/nmat3309.

[33] J. Yin, L. Qi, H. Wang, Sodium titanate nanotubes as negative electrode materials for sodium-ion capacitors, ACS Appl. Mater. Interfaces. 4 (2012) 2762–2768. doi:10.1021/am300385r.

[34] S.W. Kim, D.H. Seo, X. Ma, G. Ceder, K. Kang, Electrode materials for

rechargeable sodium-ion batteries: Potential alternatives to current lithium-ion batteries, Adv. Energy Mater. 2 (2012) 710–721. doi:10.1002/aenm.201200026.

[35] C.K. Alexander, M.N.O. Sadiku, Fundamentals of Electric Circuits, 4th Ed., McGraw Hill Higher Education, New York, US, (2009) .

[36] A. Yu, A. Davies, Z. Chen, Electrochemical Supercapacitors, Electrochem. Technol. Energy Storage Convers. 1 (2012) 317–382. doi:10.1002/9783527639496.ch8.

[37] B.E. Conway, V. Birss, J. Wojtowicz, The role and utilization of pseudocapacitance for energy storage by supercapacitors, J. Power Sources. 66 (1997) 1–14. doi:10.1016/S0378-7753(96)02474-3.

[38] C.-M. Wang, C.-Y. Wen, Y.-C. Chen, J.-Y. Chang, C.-W. Ho, K.-S. Kao, W.-C. Shih, C.-M. Chiu, Y.-A. Shen, The Influence of Specific Surface Area on the Capacitance of the Carbon Electrodes Supercapacitor, in: Proc. 2nd Int. Conf. Ind. Appl. Eng. 2015, The Institute of Industrial Applications Engineers, (2015) 439–442. doi:10.12792/iciae2015.077.

[39] H.I. Becker, Low Voltage Electrolytic Capacitor, US 2800616, 1957.

[40] O. Stern, Zur Theorie der Elektrolytischen Doppelschicht, Zeitschrift Fur Elektrochemie. 30 (1924) 508–516. doi:10.1002/bbpc.192400182.

[41] J.M. Griffin, A.C. Forse, W.Y. Tsai, P.L. Taberna, P. Simon, C.P. Grey, *In situ* NMR and electrochemical quartz crystal microbalance techniques reveal the structure of the electrical double layer in supercapacitors, Nat. Mater. 14 (2015) 812–819. doi:10.1038/nmat4318.

[42] J. Gamby, P.L. Taberna, P. Simon, J.F. Fauvarque, M. Chesneau, Studies and characterisations of various activated carbons used for carbon/carbon supercapacitors, J. Power Sources. 101 (2001) 109–116. doi:10.1016/S0378-7753(01)00707-8.

[43] M. Galinski, K. Babeł, K. Jurewicz, Performance of an Electrochemical double layer capacitor based on coconut shell active material and ionic liquid as an electrolyte, J. Power Sources. 228 (2013) 83–88. doi:10.1016/j.jpowsour.2012.11.048.

[44] K. Naoi, P. Simon, New materials and new confgurations for advanced electrochemical capacitors, J. Electrochem. Soc. 17 (2008) 34–37.

[45] B.E. Conway, Electrochemical Supercapacitors - Scientific Fundamentals and Technological Applications, 1st Ed., Springer Science+Business Media, LLC, New York, (1999) . http://www.springer.com/cn/book/9780306457364.

[46] S. Dsoke, X. Tian, C. Täubert, S. Schlüter, M. Wohlfahrt-Mehrens, Strategies to reduce the resistance sources on Electrochemical Double Layer Capacitor electrodes, J. Power Sources. 238 (2013) 422–429. doi:10.1016/j.jpowsour.2013.04.031.

[47] K. Kim, M.-S. Kim, T. Yeu, The preparation of non-aqueous supercapacitors with lithium transition-metal oxide/activated carbon composite positive electrodes, Bull. Korean Chem. Soc. 31 (2010) 3183–3189. doi:10.5012/bkcs.2010.31.11.3183.

[48] G. Arunabha, Y. Lee, A review of electrode materials for electrochemical supercapacitors, ChemsucChem. 5 (2012) 797. doi:10.1039/c1cs15060j.

[49] J.W. Long, D. Bélanger, T. Brousse, W. Sugimoto, M.B. Sassin, O. Crosnier, Asymmetric electrochemical capacitors—Stretching the limits of aqueous electrolytes, Mater. Res. Bull. 36 (2011) 513–522. doi:10.1557/mrs.2011.137.

[50] T. Pandolfo, V. Ruiz, S. Sivakkumar, J. Nerkar, General Properties of Electrochemical Capacitors, in: Supercapacitors, F. Béguin, E. Frąckowiak (Eds.), 1st Ed., Wiley-VCH Verlag GmbH & Co. KGaA, Weinheim, Germany, (2013) 69–109. doi:10.1002/9783527646661.ch2.

[51] J.P. Zheng, Hydrous Ruthenium Oxide as an Electrode Material for Electrochemical Capacitors, J. Electrochem. Soc. 142 (1995) 2699–2703. doi:10.1149/1.2050077.

[52] J. Wang, J. Polleux, J. Lim, B. Dunn, Pseudocapacitive Contributions to Electrochemical Energy Storage in TiO_2 (Anatase) Nanoparticles, J. Phys. Chem. C. 111 (2007) 14925–14931. doi:10.1021/jp074464w.

[53] M. Lübke, J. Shin, P. Marchand, D. Brett, P. Shearing, Z. Liu, J.A. Darr, D. Brett, Z. Liu, J.A. Darr, Highly pseudocapacitive Nb-doped TiO_2 high power anodes for lithium-ion batteries, J. Mater. Chem. A. 3 (2015) 22908–22914. doi:10.1039/C5TA07554H.

[54] D. Bauer, A.J. Roberts, N. Matsumi, J.A. Darr, Nano-sized Mo- and Nb-doped TiO_2 as anode materials for high energy and high power hybrid Li-ion capacitors, Nanotechnology. 28 (2017) 195403. doi:10.1088/1361-6528/aa69df.

[55] A.G. Dylla, G. Henkelman, K.J. Stevenson, Lithium insertion in nanostructured TiO_2(B) architectures, Acc. Chem. Res. 46 (2013) 1104–1112. doi:10.1021/ar300176y.

[56] H. Liu, Z. Bi, X.-G. Sun, R.R. Unocic, M.P. Paranthaman, S. Dai, G.M. Brown, Mesoporous TiO_2-B Microspheres with Superior Rate Performance for Lithium Ion Batteries, Adv. Mater. 23 (2011) 3450–3454. doi:10.1002/adma.201100599.

[57] H.-S. Kim, J.B. Cook, S.H. Tolbert, B. Dunn, The Development of Pseudocapacitive Properties in Nanosized-MoO_2, J. Electrochem. Soc. 162 (2015) A5083–A5090. doi:10.1149/2.0141505jes.

[58] H. Xiong, M.D. Slater, M. Balasubramanian, C.S. Johnson, T. Rajh, Amorphous TiO_2 Nanotube anode for rechargeable sodium ion batteries, J. Phys. Chem. Lett. 2 (2011) 2560–2565. doi:10.1021/jz2012066.

[59] C. Chen, Y. Wen, X. Hu, X. Ji, M. Yan, L. Mai, P. Hu, B. Shan, Y. Huang, Na^+ intercalation pseudocapacitance in graphene-coupled titanium oxide enabling ultra-fast sodium storage and long-term cycling, Nat. Commun. 6 (2015) 6929–6936. doi:10.1038/ncomms7929.

[60] Z. Hong, K. Zhou, Z. Huang, M. Wei, Iso-Oriented Anatase TiO_2 Mesocages as a High Performance Anode Material for Sodium-Ion Storage, Sci. Rep. 5 (2015) 11960–11971. doi:10.1038/srep11960.

[61] X. Wu, Y. Zeng, H. Gao, J. Su, J. Liu, Z. Zhu, Template synthesis of hollow fusiform $RuO_2 \cdot xH_2O$ nanostructure and its supercapacitor performance, J. Mater. Chem. A. 1 (2013) 469–472. doi:10.1039/c2ta00622g.

[62] W. Yong-gang, Z. Xiao-gang, Preparation and electrochemical capacitance of RuO_2/TiO_2 nanotubes composites, Electrochim. Acta. 49 (2004) 1957–1962. doi:10.1016/j.electacta.2003.12.023.

[63] C.C. Hu, K.H. Chang, M.C. Lin, Y.T. Wu, Design and tailoring of the nanotubular arrayed architecture of hydrous RuO_2 for next generation supercapacitors, Nano Lett. 6 (2006) 2690–2695. doi:10.1021/nl061576a.

[64] S. Ardizzone, G. Fregonara, S. Trasatti, “Inner” and “outer” active surface of RuO_2 electrodes, Electrochim. Acta. 35 (1990) 263–267. doi:10.1016/0013-

4686(90)85068-X.

[65] C.-Y. Lee, A.M. Bond, Revelation of multiple underlying RuO_2 redox processes associated with pseudocapacitance and electrocatalysis., Langmuir. 26 (2010) 16155–16162. doi:10.1021/la102495t.

[66] T. Brousse, D. Belanger, J.W. Long, To Be or Not To Be Pseudocapacitive?, J. Electrochem. Soc. 162 (2015) A5185–A5189. doi:10.1149/2.0201505jes.

[67] P. Simon, Y. Gogotsi, B. Dunn, Where Do Batteries End and Supercapacitors Begin?, Science (80-.). 343 (2014) 1210–1211. doi:10.1126/science.1249625.

[68] V. Augustyn, P. Simon, B. Dunn, Pseudocapacitive oxide materials for high-rate electrochemical energy storage, Energy Environ. Sci. 7 (2014) 1597–1614. doi:10.1039/c3ee44164d.

[69] J. Come, V. Augustyn, J.W. Kim, P. Rozier, P.-L. Taberna, P. Gogotsi, J.W. Long, B. Dunn, P. Simon, Electrochemical Kinetics of Nanostructured Nb_2O_5 Electrodes, J. Electrochem. Soc. 161 (2014) A718–A725. doi:10.1149/2.040405jes.

[70] T.J. Patey, R. Büchel, M. Nakayama, P. Novák, Electrochemistry of $LiMn_2O_4$ nanoparticles made by flame spray pyrolysis, Phys. Chem. Chem. Phys. 11 (2009) 3756. doi:10.1039/b821572n.

[71] M. Sathiya, A.S. Prakash, K. Ramesha, J.M. Tarascon, A.K. Shukla, V_2O_5-anchored carbon nanotubes for enhanced electrochemical energy storage, J. Am. Chem. Soc. 133 (2011) 16291–16299. doi:10.1021/ja207285b.

[72] M. Okubo, E. Hosono, J. Kim, M. Enomoto, N. Kojima, T. Kudo, H. Zhou, I. Honma, Nanosize effect on high rate Li-ion intercalation in $LiCoO_2$ electrode, J. Am. Chem. Soc. 129 (2007) 7444–7452.

[73] V. Augustyn, J. Come, M.A. Lowe, J.W. Kim, P.-L. Taberna, S.H. Tolbert, H.D. Abruña, P. Simon, B. Dunn, High-rate electrochemical energy storage through Li^+ intercalation pseudocapacitance, Nat. Mater. 12 (2013) 518–522. doi:10.1038/nmat3601.

[74] J. Zhang, H. Chen, X. Sun, X. Kang, Y. Zhang, C. Xu, Y. Zhang, High Intercalation Pseudocapacitance of Free-Standing T-Nb_2O_5 Nanowires@carbon Cloth Hybrid Supercapacitor Electrodes, J. Electrochem. Soc. 164 (2017) A820–A825. doi:10.1149/2.1351704jes.

[75] A.A. Lubimtsev, P.R.C. Kent, B.G. Sumpter, P. Ganesh, Understanding the origin of high-rate intercalation pseudocapacitance in Nb_2O_5 crystals, J. Mater. Chem. A. 1 (2013) 14951. doi:10.1039/c3ta13316h.

[76] Y. Wang, Z. Hong, M. Wei, Y. Xia, Layered $H_2Ti_6O_{13}$-nanowires: A new promising pseudocapacitive material in non-aqueous electrolyte, Adv. Funct. Mater. 22 (2012) 5185–5193. doi:10.1002/adfm.201200766.

[77] Y. Wang, Y. Song, Y. Xia, Electrochemical capacitors: mechanism, materials, systems, characterization and applications, Chem. Soc. Rev. 45 (2016) 5925–5950. doi:10.1039/C5CS00580A.

[78] Y. Zhu, L. Peng, D. Chen, G. Yu, Intercalation Pseudocapacitance in Ultrathin $VOPO_4$ Nanosheets: Toward High-Rate Alkali-Ion-Based Electrochemical Energy Storage, Nano Lett. 16 (2016) 742–747. doi:10.1021/acs.nanolett.5b04610.

[79] D. Li, H. Zhou, Two-phase transition of Li-intercalation compounds in Li-ion batteries, Mater. Today. 17 (2014) 451–463. doi:10.1016/j.mattod.2014.06.002.

[80] Z. Chen, V. Augustyn, X. Jia, Q. Xiao, B. Dunn, Y. Lu, High-Performance Sodium-Ion Pseudocapacitors Based on Hierarchically Porous Nanowire

Composites, ACS Nano. 6 (2012) 4319–4327. doi:10.1021/nn300920e.

[81] W. Zuo, R. Li, C. Zhou, Y. Li, J. Xia, J. Liu, Battery-Supercapacitor Hybrid Devices: Recent Progress and Future Prospects, Adv. Sci. 4 (2017) 1600539. doi:10.1002/advs.201600539.

[82] V. Aravindan, J. Gnanaraj, Y.-S. Lee, S. Madhavi, Insertion-Type Electrodes for Nonaqueous Li-Ion Capacitors, Chem. Rev. 114 (2014) 11619–11635.

[83] K. Naoi, "Nanohybrid capacitor": The next generation electrochemical capacitors, Fuel Cells. 10 (2010) 825–833. doi:10.1002/fuce.201000041.

[84] K. Naoi, S. Ishimoto, Y. Isobe, S. Aoyagi, High-rate nano-crystalline $Li_4Ti_5O_{12}$ attached on carbon nano-fibers for hybrid supercapacitors, J. Power Sources. 195 (2010) 6250–6254. doi:10.1016/j.jpowsour.2009.12.104.

[85] J. Yan, Z. Fan, T. Wei, W. Qian, M. Zhang, F. Wei, Fast and reversible surface redox reaction of graphene–MnO_2 composites as supercapacitor electrodes, Carbon N. Y. 48 (2010) 3825–3833. doi:10.1016/j.carbon.2010.06.047.

[86] R. Li, Z. Lin, X. Ba, Y. Li, R. Ding, J. Liu, Integrated copper–nickel oxide mesoporous nanowire arrays for high energy density aqueous asymmetric supercapacitors, Nanoscale Horizons. 1 (2016) 150–155. doi:10.1039/C5NH00100E.

[87] R. Li, Y. Wang, C. Zhou, C. Wang, X. Ba, Y. Li, X. Huang, J. Liu, Carbon-Stabilized High-Capacity Ferroferric Oxide Nanorod Array for Flexible Solid-State Alkaline Battery-Supercapacitor Hybrid Device with High Environmental Suitability, Adv. Funct. Mater. 25 (2015) 5384–5394. doi:10.1002/adfm.201502265.

[88] T. Zhai, X. Lu, H. Wang, G. Wang, T. Mathis, T. Liu, C. Li, Y. Tong, Y. Li, An electrochemical capacitor with applicable energy density of 7.4 Wh/kg at average power density of 3000 W/kg, Nano Lett. 15 (2015) 3189–3194. doi:10.1021/acs.nanolett.5b00321.

[89] C. Han, H. Li, R. Shi, L. Xu, J. Li, F. Kang, B. Li, Nanostructured Anode Materials for Non-aqueous Lithium Ion Hybrid Capacitors, Energy Environ. Mater. 1 (2018) 75–87. doi:10.1002/eem2.12009.

[90] A. Manthiram, Materials Challenges and Opportunities of Lithium Ion Batteries, J. Phys. Chem. Lett. 2 (2011) 176–184. doi:10.1021/jz1015422.

[91] J.M. Tarascon, M. Armand, Issues and challenges facing rechargeable lithium batteries., Nature. 414 (2001) 359–67. doi:10.1038/35104644.

[92] C.M. Hayner, X. Zhao, H.H. Kung, Materials for Rechargeable Lithium-Ion Batteries, Annu. Rev. Chem. Biomol. Eng. 3 (2012) 445–471. doi:10.1146/annurev-chembioeng-062011-081024.

[93] M. Ge, J. Rong, X. Fang, C. Zhou, Porous doped silicon nanowires for lithium ion battery anode with long cycle life, Nano Lett. 12 (2012) 2318–2323. doi:10.1021/nl300206e.

[94] S. Goriparti, E. Miele, F. De Angelis, E. Di Fabrizio, R. Proietti Zaccaria, C. Capiglia, Review on recent progress of nanostructured anode materials for Li-ion batteries, J. Power Sources. 257 (2014) 421–443. doi:10.1016/j.jpowsour.2013.11.103.

[95] J.H. Ku, Y.S. Jung, K.T. Lee, C.H. Kim, S.M. Oh, Thermoelectrochemically Activated MoO_2 Powder Electrode for Lithium Secondary Batteries, J. Electrochem. Soc. 156 (2009) A688. doi:10.1149/1.3141670.

[96] R.A. Huggins, Lithium alloy negative electrodes, J. Power Sources. 81–82 (1999) 13–19. doi:10.1016/S0378-7753(99)00124-X.

[97] W.J. Zhang, Lithium insertion/extraction mechanism in alloy anodes for lithium-ion batteries, J. Power Sources. 196 (2011) 877–885. doi:10.1016/j.jpowsour.2010.08.114.

[98] P. V. Braun, J. Cho, J.H. Pikul, W.P. King, H. Zhang, High power rechargeable batteries, Curr. Opin. Solid State Mater. Sci. 16 (2012) 186–198. doi:10.1016/j.cossms.2012.05.002.

[99] D. Bresser, E. Paillard, M. Copley, P. Bishop, M. Winter, S. Passerini, The importance of “going nano” for high power battery materials, J. Power Sources. 219 (2012) 217–222. doi:10.1016/j.jpowsour.2012.07.035.

[100] F. Jiao, P.G. Bruce, Mesoporous crystalline β-MnO_2 - A reversible positive electrode for rechargeable lithium batteries, Adv. Mater. 19 (2007) 657–660. doi:10.1002/adma.200602499.

[101] G. Bystrzejewska-Piotrowska, J. Golimowski, P.L. Urban, Nanoparticles: Their potential toxicity, waste and environmental management, Waste Manag. 29 (2009) 2587–2595. doi:10.1016/j.wasman.2009.04.001.

[102] E. Navarro, A. Baun, R. Behra, N.B. Hartmann, J. Filser, A.J. Miao, A. Quigg, P.H. Santschi, L. Sigg, Environmental behavior and ecotoxicity of engineered nanoparticles to algae, plants, and fungi, Ecotoxicology. 17 (2008) 372–386. doi:10.1007/s10646-008-0214-0.

[103] C. Levard, E.M. Hotze, G. V. Lowry, G.E. Brown, Environmental Transformations of Silver Nanoparticles: Impact on Stability and Toxicity, Environ. Sci. Technol. 46 (2012) 6900–6914. doi:10.1021/es2037405.

[104] W. Lin, Y. Huang, X.-D. Zhou, Y. Ma, In vitro toxicity of silica nanoparticles in human lung cancer cells, Toxicol. Appl. Pharmacol. 217 (2006) 252–259. doi:10.1016/j.taap.2006.10.004.

[105] E.E. Connor, J. Mwamuka, A. Gole, C.J. Murphy, M.D. Wyatt, Gold nanoparticles are taken up by human cells but do not cause acute cytotoxicity, Small. 1 (2005) 325–327. doi:10.1002/smll.200400093.

[106] A.M. Alkilany, C.J. Murphy, Toxicity and cellular uptake of gold nanoparticles: What we have learned so far?, J. Nanoparticle Res. 12 (2010) 2313–2333. doi:10.1007/s11051-010-9911-8.

[107] P.S. Aithal, S. Aithal, Nanotechnology Innovations and Commercialization – Opportunities, Challenges & Reasons for Delay, Int. J. Eng. Manuf. 6 (2016) 15–25. doi:10.5281/zenodo.161161.

[108] P.G. Bruce, B. Scrosati, J.-M. Tarascon, Nanomaterials for Rechargeable Lithium Batteries, Angew. Chemie Int. Ed. 47 (2008) 2930–2946. doi:10.1002/anie.200702505.

[109] W.J. Zhang, A review of the electrochemical performance of alloy anodes for lithium-ion batteries, J. Power Sources. 196 (2011) 13–24. doi:10.1016/j.jpowsour.2010.07.020.

[110] C.M. Julien, A. Mauger, K. Zaghib, H. Groult, Comparative Issues of Cathode Materials for Li-Ion Batteries, Inorganics. 2 (2014) 132–154. doi:10.3390/inorganics2020132.

[111] D. Song, M.R. Jo, G.-H. Lee, J. Song, N.-S. Choi, Y.-M. Kang, Bifunctional $Li_4Ti_5O_{12}$ coating layer for the enhanced kinetics and stability of carbon anode for lithium rechargeable batteries, J. Alloys Compd. 615 (2014) 220–226. doi:10.1016/j.jallcom.2014.06.158.

[112] J.H. Kim, J.S. Kim, Y.G. Lim, J.G. Lee, Y.J. Kim, Effect of carbon types on the electrochemical properties of negative electrodes for Li-ion capacitors, J. Power

Sources. 196 (2011) 10490–10495. doi:10.1016/j.jpowsour.2011.08.081.

[113] K. Tang, X. Mu, P. a. van Aken, Y. Yu, J. Maier, “Nano-Pearl-String” $TiNb_2O_7$ as Anodes for Rechargeable Lithium Batteries, Adv. Energy Mater. 3 (2013) 49–53. doi:10.1002/aenm.201200396.

[114] D. Aurbach, E. Zinigrad, Y. Cohen, H. Teller, A short review of failure mechanisms of lithium metal and lithiated graphite anodes in liquid electrolyte solutions, Solid State Ionics. 148 (2002) 405–416. doi:10.1016/S0167-2738(02)00080-2.

[115] Z. Hong, M. Wei, Layered titanate nanostructures and their derivatives as negative electrode materials for lithium-ion batteries, J. Mater. Chem. A. 1 (2013) 4403. doi:10.1039/c2ta01312f.

[116] G.-N. Zhu, Y.-G. Wang, Y.-Y. Xia, Ti-based compounds as anode materials for Li-ion batteries, Energy Environ. Sci. 5 (2012) 6652. doi:10.1039/c2ee03410g.

[117] D. Deng, M.G. Kim, J.Y. Lee, J. Cho, Green energy storage materials: Nanostructured TiO_2 and Sn-based anodes for lithium-ion batteries, Energy Environ. Sci. 2 (2009) 818. doi:10.1039/b823474d.

[118] A. Moretti, G.T. Kim, D. Bresser, K. Renger, E. Paillard, R. Marassi, M. Winter, S. Passerini, Investigation of different binding agents for nanocrystalline anatase TiO_2 anodes and its application in a novel, green lithium-ion battery, J. Power Sources. 221 (2013) 419–426. doi:10.1016/j.jpowsour.2012.07.142.

[119] M. V Reddy, G. V Subba Rao, B.V.R. Chowdari, Metal Oxides and Oxysalts as Anode Materials for Li Ion Batteries, Chem. Rev. 113 (2013) 5364–5457. doi:10.1021/cr3001884.

[120] V. Etacheri, R. Marom, R. Elazari, G. Salitra, D. Aurbach, Challenges in the development of advanced Li-ion batteries: a review, Energy Environ. Sci. 4 (2011) 3243. doi:10.1039/c1ee01598b.

[121] W. Zhang, Y. Gong, N.P. Mellott, D. Liu, J. Li, Synthesis of nickel doped anatase titanate as high performance anode materials for lithium ion batteries, J. Power Sources. 276 (2015) 39–45. doi:10.1016/j.jpowsour.2014.11.098.

[122] K. Zhu, Q. Wang, J.H. Kim, A.A. Pesaran, A.J. Frank, Pseudocapacitive lithium-ion storage in oriented anatase TiO_2 nanotube arrays, J. Phys. Chem. C. 116 (2012) 11895–11899. doi:10.1021/jp301884x.

[123] T.V. Thi, A.K. Rai, J. Gim, S. Kim, J. Kim, Effect of Mo^{6+} doping on electrochemical performance of anatase TiO_2 as a high performance anode material for secondary lithium-ion batteries, J. Alloys Compd. 598 (2014) 16–22. doi:10.1016/j.jallcom.2014.02.019.

[124] D. Bresser, B. Oschmann, M.N. Tahir, F. Mueller, I. Lieberwirth, W. Tremel, R. Zentel, S. Passerini, Carbon-Coated Anatase TiO_2 Nanotubes for Li- and Na-Ion Anodes, J. Electrochem. Soc. 162 (2014) A3013–A3020. doi:10.1149/2.0031502jes.

[125] M. Wagemaker, A.A. Van Well, G.J. Kearley, P.M. Mulder, The life and times of lithium in anatase TiO_2, Solid State Ionics. 175 (2004) 191–193. doi:10.1016/j.ssi.2003.11.030.

[126] C. Jiang, J. Zhang, Nanoengineering Titania for High Rate Lithium Storage: A Review, J. Mater. Sci. Technol. 29 (2013) 97–122. doi:10.1016/j.jmst.2012.11.017.

[127] C.J. Howard, T.M. Sabine, F. Dickson, Structural and thermal parameters for rutile and anatase, Acta Crystallogr. Sect. B. 47 (1991) 462–468. doi:10.1107/S010876819100335X.

[128] W.J.H. Borghols, Lithium insertion in nanostructured titanates, Technical University Delft, 2010.

[129] R.J. Cava, D.W. Murphy, S. Zahurak, A. Santoro, R.S. Roth, The crystal structures of the lithium-inserted metal oxides $Li_{0.5}TiO_2$ anatase, $LiTi_2O_4$ spinel, and $Li_2Ti_2O_4$, J. Solid State Chem. 53 (1984) 64–75. doi:10.1016/0022-4596(84)90228-7.

[130] C. Lin, G. Wang, S. Lin, J. Li, L. Lu, $TiNb_6O_{17}$: a new electrode material for lithium-ion batteries, Chem. Commun. 51 (2015) 8970–8973. doi:10.1039/C5CC01494H.

[131] Q. Cheng, J. Liang, Y. Zhu, L. Si, C. Guo, Y. Qian, Bulk $Ti_2Nb_{10}O_{29}$ as long-life and high-power Li-ion battery anodes, J. Mater. Chem. A. 2 (2014) 17258–17262. doi:10.1039/C4TA04184D.

[132] X. Wu, J. Miao, W. Han, Y.-S. Hu, D. Chen, J.-S. Lee, J. Kim, L. Chen, Investigation on $Ti_2Nb_{10}O_{29}$ anode material for lithium-ion batteries, Electrochem. Commun. 25 (2012) 39–42. doi:10.1016/j.elecom.2012.09.015.

[133] C. Lin, S. Yu, H. Zhao, S. Wu, G. Wang, L. Yu, Y. Li, Z.-Z. Zhu, J. Li, S. Lin, Defective $Ti_2Nb_{10}O_{27.1}$: an advanced anode material for lithium-ion batteries., Sci. Rep. 5 (2015) 17836. doi:10.1038/srep17836.

[134] H. Li, L. Shen, G. Pang, S. Fang, H. Luo, K. Yang, X. Zhang, $TiNb_2O_7$ nanoparticles assembled into hierarchical microspheres as high-rate capability and long-cycle-life anode materials for lithium ion batteries., Nanoscale. 7 (2014) 619–24. doi:10.1039/c4nr04847d.

[135] B. Guoa, X. Yub, X. Suna, M. Chic, Z.-A. Qiaoa, J. Liub, Y.-S. Hu, X.-Q. Yang, J.B. Goodenough, S. Dai, A long-life lithium-ion battery with highly porous $TiNb_2O_7$ anode for large-scale electrical energy storage, Energy Environ. Sci. 7 (2014) 2220. doi:10.1039/c4ee00508b.

[136] C. Jo, Y. Kim, J. Hwang, J. Shim, J. Chun, J. Lee, Block copolymer directed ordered mesostructured $TiNb_2O_7$ multimetallic oxide constructed of nanocrystals as high power li-ion battery anodes, Chem. Mater. 26 (2014) 3508–3514. doi:10.1021/cm501011d.

[137] J.T. Han, Y.H. Huang, J.B. Goodenough, New anode framework for rechargeable lithium batteries, Chem. Mater. 23 (2011) 2027–2029. doi:10.1021/cm200441h.

[138] L. Yan, X. Rui, G. Chen, W. Xu, G. Zou, H. Luo, Recent advances in nanostructured Nb-based oxides for electrochemical energy storage., Nanoscale. 8 (2016) 8443–8465. doi:10.1039/c6nr01340f.

[139] M.M. Doeff, M.M. Doeff, Y. Ma, Y. Ma, S.J. Visco, S.J. Visco, L.C. De Jonghe, L.C. De Jonghe, Electrochemical insertion of sodium into carbon, J. Electrochem. Soc. 140 (1993) 169–170. doi:10.1149/1.2221153.

[140] S. Komaba, W. Murata, T. Ishikawa, N. Yabuuchi, T. Ozeki, T. Nakayama, A. Ogata, K. Gotoh, K. Fujiwara, Electrochemical Na insertion and solid electrolyte interphase for hard-carbon electrodes and application to Na-ion batteries, Adv. Funct. Mater. 21 (2011) 3859–3867. doi:10.1002/adfm.201100854.

[141] N. Yabuuchi, K. Kubota, M. Dahbi, S. Komaba, Research Development on Sodium-Ion Batteries, Chem. Rev. 114 (2014) 11636–11682. doi:10.1021/cr500192f.

[142] S. Lunell, A. Stashans, L. Ojamäe, H. Lindström, A. Hagfeldt, Li and Na Diffusion in TiO_2 from Quantum Chemical Theory versus Electrochemical

Experiment, J. Am. Chem. Soc. 119 (1997) 7374–7380. doi:10.1021/ja9708629.

[143] P. Poizot, S. Laruelle, S. Grugeon, L. Dupont, J. Tarascon, From the Vanadates to 3d-Metal Oxides Negative Electrodes, Ionics (Kiel). 6 (2000) 321–330. doi:https://doi.org/10.1007/BF02374148.

[144] L. Ji, Z. Lin, M. Alcoutlabi, X. Zhang, Recent developments in nanostructured anode materials for rechargeable lithium-ion batteries, Energy Environ. Sci. 4 (2011) 2682. doi:10.1039/c0ee00699h.

[145] J. Cabana, L. Monconduit, D. Larcher, M.R. Palacín, Beyond Intercalation-Based Li-Ion Batteries: The State of the Art and Challenges of Electrode Materials Reacting Through Conversion Reactions, Adv. Mater. 22 (2010) E170–E192. doi:10.1002/adma.201000717.

[146] L. Croguennec, M.R. Palacin, Recent Achievements on Inorganic Electrode Materials for Lithium-Ion Batteries, J. Am. Chem. Soc. 137 (2015) 3140–3156. doi:10.1021/ja507828x.

[147] F. Klein, B. Jache, A. Bhide, P. Adelhelm, Conversion reactions for sodium-ion batteries, Phys. Chem. Chem. Phys. 15 (2013) 15876. doi:10.1039/c3cp52125g.

[148] F. Xia, X. Hu, Y. Sun, W. Luo, Y. Huang, Layer-by-layer assembled MoO_2–graphene thin film as a high-capacity and binder-free anode for lithium-ion batteries, Nanoscale. 4 (2012) 4707. doi:10.1039/c2nr30742a.

[149] J. Li, A.K. Dozier, Y. Li, F. Yang, Y.-T. Cheng, Crack Pattern Formation in Thin Film Lithium-Ion Battery Electrodes, J. Electrochem. Soc. 158 (2011) A689. doi:10.1149/1.3574027.

[150] K. Zhao, M. Pharr, J.J. Vlassak, Z. Suo, Fracture of electrodes in lithium-ion batteries caused by fast charging, J. Appl. Phys. 108 (2010) 1–6. doi:10.1063/1.3492617.

[151] X. Li, Y. Ma, L. Qin, Z. Zhang, Z. Zhang, Y.-Z. Zheng, Y. Qu, A bottom-up synthesis of α-Fe_2O_3 nanoaggregates and their composites with graphene as high performance anodes in lithium-ion batteries, J. Mater. Chem. A. 3 (2015) 2158–2165. doi:10.1039/c4ta05420b.

[152] X. Liu, W. Ji, J. Liang, L. Peng, W. Hou, MoO_2@Carbon Hollow Microspheres with Tunable Interiors and Improved Lithium-ion Battery Anode Properties, Phys. Chem. Chem. Phys. 16 (2014) 20570–20577. doi:10.1039/C4CP02960G.

[153] Y. Luo, J. Luo, J. Jiang, W. Zhou, H. Yang, X. Qi, H. Zhang, H.J. Fan, D.Y.W. Yu, C.M. Li, T. Yu, Seed-assisted synthesis of highly ordered TiO_2@α-Fe_2O_3 core/shell arrays on carbon textiles for lithium-ion battery applications, Energy Environ. Sci. 5 (2012) 6559. doi:10.1039/c2ee03396h.

[154] S.E. Kim, K.W. Kim, S.W. Lee, S.O. Kim, J.S. Kim, J.K. Lee, Synthesis and characterization of TiO_2-coated magnetite clusters (n-Fe_3O_4@TiO_2) as anode materials for li-ion batteries, Curr. Appl. Phys. 13 (2013) 1923–1927. doi:10.1016/j.cap.2013.08.003.

[155] M.N. Obrovac, V.L. Chevrier, Alloy Negative Electrodes for Li-Ion Batteries, Chem. Rev. 114 (2014) 11444–11502. doi:10.1021/cr500207g.

[156] Z.-W. Fu, F. Huang, Y. Zhang, Y. Chu, Q.-Z. Qin, The Electrochemical Reaction of Zinc Oxide Thin Films with Lithium, J. Electrochem. Soc. 150 (2003) A714. doi:10.1149/1.1570410.

[157] M.E. Spahr, T. Palladino, H. Wilhelm, A. Würsig, D. Goers, H. Buqa, M. Holzapfel, P. Novák, Exfoliation of Graphite during Electrochemical Lithium Insertion in Ethylene Carbonate-Containing Electrolytes, J. Electrochem. Soc.

151 (2004) A1383–A1395. doi:10.1149/1.1775224.

[158] K.W. Schroder, H. Celio, L.J. Webb, K.J. Stevenson, Examining Solid Electrolyte Interphase Formation on Crystalline Silicon Electrodes: Influence of Electrochemical Preparation and Ambient Exposure Conditions, J. Phys. Chem. C. 116 (2012) 19737–19747. doi:10.1021/jp307372m.

[159] D. Aurbach, The Study of Electrolyte Solutions Based on Ethylene and Diethyl Carbonates for Rechargeable Li Batteries, J. Electrochem. Soc. 142 (1995) 2882. doi:10.1149/1.2048659.

[160] D. Aurbach, Y. Gofer, The behavior of lithium electrodes in mixtures of alkyl carbonates and ethers, J. Electrochem. Soc. 138 (1991) 3529. doi:10.1149/1.2085454.

[161] K.W. Schroder, A.G. Dylla, S.J. Harris, L.J. Webb, K.J. Stevenson, Role of Surface Oxides in the Formation of Solid–Electrolyte Interphases at Silicon Electrodes for Lithium-Ion Batteries, ACS Appl. Mater. Interfaces. 6 (2014) 21510–21524. doi:10.1021/am506517j.

[162] D. Aurbach, The Surface Chemistry of Lithium Electrodes in Alkyl Carbonate Solutions, J. Electrochem. Soc. 141 (1994) L1. doi:10.1149/1.2054718.

[163] P. Verma, P. Maire, P. Novák, A review of the features and analyses of the solid electrolyte interphase in Li-ion batteries, Electrochim. Acta. 55 (2010) 6332–6341. doi:10.1016/j.electacta.2010.05.072.

[164] E. Peled, Advanced Model for Solid Electrolyte Interphase Electrodes in Liquid and Polymer Electrolytes, J. Electrochem. Soc. 144 (1997) L208. doi:10.1149/1.1837858.

[165] E. Peled, S. Menkin, Review—SEI: Past, Present and Future, J. Electrochem. Soc. 164 (2017) A1703–A1719. doi:10.1149/2.1441707jes.

[166] R. Van De Krol, A. Goossens, J. Schoonman, Spatial Extent of Lithium Intercalation in Anatase TiO_2, J. Phys. Chem. B. 103 (1999) 7151–7159. doi:10.1021/jp9909964.

[167] S.K. Das, M. Gnanavel, M.U.M. Patel, C. Shivakumara, A.J. Bhattacharyya, Anamolously High Lithium Storage in Mesoporous Nanoparticulate Aggregation of Fe^{3+} Doped Anatase Titania, J. Electrochem. Soc. 158 (2011) A1290. doi:10.1149/2.029112jes.

[168] J.E.B. Randles, A cathode ray polarograph. Part II. The current-voltage curves, Trans. Faraday Soc. 44 (1948) 327. doi:10.1039/tf9484400327.

[169] P. Simon, Y. Gogotsi, Materials for electrochemical capacitors., Nat. Mater. 7 (2008) 845–854. doi:10.1038/nmat2297.

[170] M. Winter, R.J. Brodd, What are batteries, fuel cells, and supercapacitors?, Chem. Rev. 104 (2004) 4245–4269. doi:10.1021/cr020730k.

[171] M.J. Loveridge, M.J. Lain, I.D. Johnson, A. Roberts, S.D. Beattie, R. Dashwood, J.A. Darr, R. Bhagat, Towards High Capacity Li-ion Batteries Based on Silicon-Graphene Composite Anodes and Sub-micron V-doped $LiFePO_4$ Cathodes, Sci. Rep. 6 (2016) 1–11. doi:10.1038/srep37787.

[172] Z. Shen, L. Cao, C.D. Rahn, C.-Y. Wang, Least Squares Galvanostatic Intermittent Titration Technique (LS-GITT) for Accurate Solid Phase Diffusivity Measurement, J. Electrochem. Soc. 160 (2013) A1842–A1846. doi:10.1149/2.084310jes.

[173] Y. Chen, L. Wang, T. Anwar, Y. Zhao, N. Piao, X. He, Q. Zhu, Application of Galvanostatic Intermittent Titration Technique to Investigate Phase Transformation of $LiFePO_4$ Nanoparticles, Electrochim. Acta. 241 (2017) 132–

140. doi:10.1016/j.electacta.2017.04.137.

[174] A.P. Nowak, B. Wicikowska, K. Trzciński, A. Lisowska-Oleksiak, Determination of chemical diffusion coefficient of lithium ions in ceramics derived from pyrolysed poly(1,2-dimethylsilazane) and starch, Procedia Eng. 98 (2014) 8–13. doi:10.1016/j.proeng.2014.12.480.

[175] G.K. Lewis Jr, G.K. Lewis Sr, W. Olbricht, Cost-effective broad-band electrical impedance spectroscopy measurement circuit and signal analysis for piezo-materials and ultrasound transducers, Meas. Sci. Technol. Meas. Sci. Technol. 19 (2008) 105102–105109. doi:10.1088/0957-0233/19/10/105102.

[176] J.E.B. Randles, Kinetics of rapid electrode reactions, Discuss. Faraday Soc. 1 (1947) 11. doi:10.1039/df9470100011.

[177] R. Ahmed, K. Reifsnider, Study of Influence of Electrode Geometry on Impedance Spectroscopy, Int. J. Electrochem. Sci. 6 (2011) 1159–1174. doi:10.1115/FuelCell2010-33209.

[178] J. Lee, Y.M. Chen, Y. Zhu, B.D. Vogt, Fabrication of porous carbon/TiO_2 composites through polymerization-induced phase separation and use as an anode for Na-ion batteries, ACS Appl. Mater. Interfaces. 6 (2014) 21011–21018. doi:10.1021/am5058037.

[179] R. Bataller, J.M. Gandía, E. García-Breijo, M. Alcañiz, J. Soto, A study of the importance of the cell geometry in non-Faradaic systems. A new definition of the cell constant for conductivity measurement, Electrochim. Acta. 153 (2015) 263–272. doi:10.1016/j.electacta.2014.12.014.

[180] U. Kumar Sen, A. Shaligram, S. Mitra, Intercalation Anode Material for Lithium Ion Battery Based on Molybdenum Dioxide, ACS Appl. Mater. Interfaces. 6 (2014) 14311–14319. doi:10.1021/am503605u.

[181] J.A. Darr, J. Zhang, N.M. Makwana, X. Weng, Continuous Hydrothermal Synthesis of Inorganic Nanoparticles: Applications and Future Directions, Chem. Rev. 117 (2017) 11125–11238. doi:10.1021/acs.chemrev.6b00417.

[182] K. Lu, Nanoparticle Synthesis, in: Nanoparticulate Mater., John Wiley & Sons, Inc., Hoboken, NJ, USA, (2012) 24–127. doi:10.1002/9781118408995.ch2.

[183] H. Hayashi, Y. Hakuta, Hydrothermal Synthesis of metal oxide nanoparticles in supercritical water, Materials (Basel). 3 (2010) 3794–3817. doi:10.3390/ma3073794.

[184] M. Shandilya, R. Rai, J. Singh, Review: hydrothermal technology for smart materials, Adv. Appl. Ceram. 115 (2016) 354–376. doi:10.1080/17436753.2016.1157131.

[185] J.A. Darr, M. Poliakoff, New Directions in Inorganic and Metal-Organic Coordination Chemistry in Supercritical Fluids, Chem. Rev. 99 (1999) 495–542. doi:10.1021/cr970036i.

[186] K. Byrappa, T. Adschiri, Hydrothermal technology for nanotechnology, Prog. Cryst. Growth Charact. Mater. 53 (2007) 117–166. doi:10.1016/j.pcrysgrow.2007.04.001.

[187] H. Duan, D. Wang, Y. Li, Green chemistry for nanoparticle synthesis, Chem. Soc. Rev. 44 (2015) 5778–5792. doi:10.1039/C4CS00363B.

[188] G. Demazeau, Solvothermal processes: a route to the stabilization of new materials, J. Mater. Chem. 9 (1999) 15–18. doi:10.1039/a805536j.

[189] A. Rabenau, The Role of Hydrothermal Synthesis in Preparative Chemistry, Angew. Chemie Int. Ed. English. 24 (1985) 1026–1040. doi:10.1002/anie.198510261.

[190] P. Pollet, E.A. Davey, E.E. Ureña-Benavides, C.A. Eckert, C.L. Liotta, Solvents for sustainable chemical processes, Green Chem. 16 (2014) 1034–1055. doi:10.1039/C3GC42302F.

[191] K.P. Johnston, P.S. Shah, Making Nanoscale Materials with Supercritical Fluids, Science (80-.). 303 (2004) 482–483. doi:10.1126/science.1093951.

[192] T. Adschiri, Y.-W. Lee, M. Goto, S. Takami, Green materials synthesis with supercritical water, Green Chem. 13 (2011) 1380. doi:10.1039/c1gc15158d.

[193] K. Sue, T. Adschiri, K. Arai, Predictive Model for Equilibrium Constants of Aqueous Inorganic Species at Subcritical and Supercritical Conditions, Ind. Eng. Chem. Res. 41 (2002) 3298–3306. doi:10.1021/ie010956y.

[194] V.K. LaMer, R.H. Dinegar, Theory, Production and Mechanism of Formation of Monodispersed Hydrosols, J. Am. Chem. Soc. 72 (1950) 4847–4854. doi:10.1021/ja01167a001.

[195] W. Ostwald, Studien über die Bildung und Umwandlung fester Körper, Zeitschrift Für Phys. Chemie. 22U (1897) 289–330. doi:10.1515/zpch-1897-2233.

[196] Z. Zhang, S. Brown, J.B.M. Goodall, X. Weng, K. Thompson, K. Gong, S. Kellici, R.J.H. Clark, J.R.G. Evans, J.A. Darr, Direct continuous hydrothermal synthesis of high surface area nanosized titania, J. Alloys Compd. 476 (2009) 451–456. doi:10.1016/j.jallcom.2008.09.036.

[197] R.I. Gruar, C.J. Tighe, J.A. Darr, Scaling-up a confined jet reactor for the continuous hydrothermal manufacture of nanomaterials, Ind. Eng. Chem. Res. 52 (2013) 5270–5281. doi:10.1021/ie302567d.

[198] C.J. Tighe, R.Q. Cabrera, R.I. Gruar, J.A. Darr, Scale Up Production of Nanoparticles: Continuous Supercritical Water Synthesis of Ce–Zn Oxides, Ind. Eng. Chem. Res. 52 (2013) 5522–5528. doi:10.1021/ie3025642.

[199] I.D. Johnson, M. Loveridge, R. Bhagat, J.A. Darr, Mapping Structure-Composition-Property Relationships in V- and Fe-Doped $LiMnPO_4$ Cathodes for Lithium-Ion Batteries, ACS Comb. Sci. 18 (2016) 665–672. doi:10.1021/acscombsci.6b00035.

[200] D.P. Howard, P. Marchand, L. McCafferty, C.J. Carmalt, I.P. Parkin, J.A. Darr, High-Throughput Continuous Hydrothermal Synthesis of Transparent Conducting Aluminum and Gallium Co-doped Zinc Oxides, ACS Comb. Sci. 19 (2017) 239–245. doi:10.1021/acscombsci.6b00118.

[201] O. Yakaboylu, J. Harinck, K.G. Gerton Smit, W. de Jong, Supercritical water gasification of manure: A thermodynamic equilibrium modeling approach, Biomass and Bioenergy. 59 (2013) 253–263. doi:10.1016/j.biombioe.2013.07.011.

[202] A. Cabañas, J.A. Darr, E. Lester, M. Poliakoff, Continuous hydrothermal synthesis of inorganic materials in a near-critical water flow reactor; the one-step synthesis of nano-particulate $Ce_{1-x}Zr_xO_2$ (x = 0–1) solid solutions, J. Mater. Chem. 11 (2001) 561–568. doi:10.1039/b008095k.

[203] M. Lübke, A. Sumboja, I.D. Johnson, D.J.L. Brett, P.R. Shearing, Z. Liu, J.A. Darr, High power nano-Nb_2O_5 negative electrodes for lithium-ion batteries, Electrochim. Acta. 192 (2016) 363–369. doi:10.1016/j.electacta.2016.01.226.

[204] M. Lübke, I. Johnson, N.M. Makwana, D. Brett, P. Shearing, Z. Liu, J.A. Darr, High power TiO_2 and high capacity Sn-doped TiO_2 nanomaterial anodes for lithium-ion batteries, J. Power Sources. 294 (2015) 94–102. doi:10.1016/j.jpowsour.2015.06.039.

[205] C.J. Denis, C.J. Tighe, R.I. Gruar, N.M. Makwana, J.A. Darr, Nucleation and Growth of Cobalt Oxide Nanoparticles in a Continuous Hydrothermal Reactor under Laminar and Turbulent Flow, Cryst. Growth Des. 15 (2015) 4256–4265. doi:10.1021/acs.cgd.5b00551.

[206] E. Lester, P.J. Blood, J.P. Denyer, B.J. Azzopardi, J. Li, M. Poliakoff, Impact of reactor geometry on continuous hydrothermal synthesis mixing, Mater. Res. Innov. 14 (2010) 19–26. doi:10.1179/143307510X12599329343042.

[207] J.A. Darr, C.J. Tighe, R.I. Gruar, Co-current mixer, apparatus, reactor and method for precipitating nanoparticles, US2013/0136687 A1, 2013. doi:US20130136687.

[208] C.Y. Ma, J.J. Liu, Y. Zhang, X.Z. Wang, Simulation for scale-up of a confined jet mixer for continuous hydrothermal flow synthesis of nanomaterials, J. Supercrit. Fluids. 98 (2015) 211–221. doi:10.1016/j.supflu.2014.12.016.

[209] G.W. Oetjen, Metal Oxides, Ceramic Powders, in: Freeze-Drying, Wiley-VCH Verlag GmbH & Co. KGaA, Weinheim, Germany, (2004) 359–365. doi:10.1002/9783527612482.ch5.

[210] G.-W. Oetjen, P. Haseley, Foundations and Process Engineering: Section 1.1 (Freezing), in: Freeze-Drying, Wiley-VCH Verlag GmbH & Co. KGaA, Weinheim, Germany, (2003) 1–75. doi:10.1002/9783527612482.ch1a.

[211] W. Abdelwahed, G. Degobert, S. Stainmesse, H. Fessi, Freeze-drying of nanoparticles: Formulation, process and storage considerations, Adv. Drug Deliv. Rev. 58 (2006) 1688–1713. doi:10.1016/j.addr.2006.09.017.

[212] W.H. Bragg, W.L. Bragg, The Reflection of X-rays by Crystals, Proc. R. Soc. A Math. Phys. Eng. Sci. 88 (1913) 428–438. doi:10.1098/rspa.1913.0040.

[213] P. Scherrer, Bestimmung der inneren Struktur und der Größe von Kolloidteilchen mittels Röntgenstrahlen, in: Kolloidchem. Ein Lehrb., Springer Berlin Heidelberg, Berlin, Heidelberg, (1912) 387–409. doi:10.1007/978-3-662-33915-2_7.

[214] U. Holzwarth, N. Gibson, The Scherrer equation versus the "Debye-Scherrer equation," Nat. Nanotechnol. 6 (2011) 534–534. doi:10.1038/nnano.2011.145.

[215] A. Jablonski, Universal energy dependence of the inelastic mean free path, Surf. Interface Anal. 20 (1993) 317–321. doi:10.1002/sia.740200409.

[216] B.S. Mitchell, An Introduction to Materials Engineering and Science, (2003) . doi:10.1002/0471473359.

[217] E.E. Alp, G.L. Goodman, L. Soderholm, S.M. Mini, M. Ramanathan, G.K. Shenoy, A.S. Bommannavar, A new approach to determining the charge distribution in copper compounds, J. Phys. Condens. Matter. 1 (1989) 6463–6468. doi:10.1088/0953-8984/1/36/014.

[218] S. Brunauer, P.H. Emmett, E. Teller, Adsorption of Gases in Multimolecular Layers, J. Am. Chem. Soc. 60 (1938) 309–319. doi:citeulike-article-id:4074706\rdoi: 10.1021/ja01269a023.

[219] J.B. Condon, An Overview of Physisorption, in: Surf. Area Porosity Determ. by Physisorption, 1st Ed., Elsevier, (2006) 1–27. doi:10.1016/B978-044451964-1/50003-0.

[220] S.M. Oh, J.Y. Hwang, C.S. Yoon, J. Lu, K. Amine, I. Belharouak, Y.K. Sun, High electrochemical performances of microsphere C-TiO_2 anode for sodium-ion battery, ACS Appl. Mater. Interfaces. 6 (2014) 11295–11301. doi:10.1021/am501772a.

[221] F. La Mantia, C.D. Wessells, H.D. Deshazer, Y. Cui, Reliable reference

electrodes for lithium-ion batteries, Electrochem. Commun. 31 (2013) 141–144. doi:10.1016/j.elecom.2013.03.015.

[222] J. Costard, M. Ender, M. Weiss, E. Ivers-Tiffée, Three-Electrode Setups for Lithium-Ion Batteries, J. Electrochem. Soc. 164 (2017) A80–A87. doi:10.1149/2.0241702jes.

[223] Z. Hong, K. Zhou, J. Zhang, Z. Huang, M. Wei, Facile synthesis of rutile TiO_2 mesocrystals with enhanced sodium storage properties, J. Mater. Chem. A. 3 (2015) 17412–17416. doi:10.1039/C5TA04232A.

[224] D. Su, S. Dou, G. Wang, Anatase TiO_2: Better Anode Material Than Amorphous and Rutile Phases of TiO_2 for Na-Ion Batteries, Chem. Mater. 27 (2015) 6022–6029. doi:10.1021/acs.chemmater.5b02348.

[225] W. Wang, Y. Liu, X. Wu, J. Wang, L. Fu, Y. Zhu, Y. Wu, X. Liu, Advances of TiO_2 as Negative Electrode Materials for Sodium-Ion Batteries, Adv. Mater. Technol. 1800004 (2018) 1–20. doi:10.1002/admt.201800004.

[226] Y.-C. Nah, I. Paramasivam, P. Schmuki, Doped TiO_2 and TiO_2 Nanotubes: Synthesis and Applications, ChemPhysChem. 11 (2010) 2698–2713. doi:10.1002/cphc.201000276.

[227] H. Liao, L. Xie, Y. Zhang, X. Qiu, S. Li, Z. Huang, H. Hou, X. Ji, Mo-doped Gray Anatase TiO_2: Lattice Expansion for Enhanced Sodium Storage, Electrochim. Acta. 219 (2016) 227–234. doi:10.1016/j.electacta.2016.10.016.

[228] T. Wang, T. Xu, Effects of vanadium doping on microstructures and optical properties of TiO_2, Ceram. Int. 43 (2017) 1558–1564. doi:10.1016/j.ceramint.2016.10.132.

[229] Y. Furubayashi, T. Hitosugi, Y. Yamamoto, K. Inaba, G. Kinoda, Y. Hirose, T. Shimada, T. Hasegawa, A transparent metal: Nb-doped anatase TiO_2, Appl. Phys. Lett. 86 (2005) 1–3. doi:10.1063/1.1949728.

[230] L. Sun, J. Wang, K. Jiang, S. Fan, Mesoporous $Li_4Ti_5O_{12}$ nanoclusters as high performance negative electrodes for lithium ion batteries, J. Power Sources. 248 (2014) 265–272. doi:10.1016/j.jpowsour.2013.09.041.

[231] L.G. Devi, B.N. Murthy, Characterization of Mo doped TiO_2 and its enhanced photo catalytic activity under visible light, Catal. Letters. 125 (2008) 320–330. doi:10.1007/s10562-008-9568-4.

[232] J. Zhang, T. Huang, L. Zhang, A. Yu, Molybdenum-Doped Titanium Dioxide and Its Superior Lithium Storage Performance, J. Phys. Chem. C. 118 (2014) 25300–25309. doi:10.1021/jp506401q.

[233] L.T. Anh, A.K. Rai, T.V. Thi, J. Gim, S. Kim, E.C. Shin, J.S. Lee, J. Kim, Improving the electrochemical performance of anatase titanium dioxide by vanadium doping as an anode material for lithium-ion batteries, J. Power Sources. 243 (2013) 891–898. doi:10.1016/j.jpowsour.2013.06.080.

[234] S. Sharma, S. Chaudhary, S.C. Kashyap, S.K. Sharma, Room temperature ferromagnetism in Mn doped TiO_2 thin films: Electronic structure and Raman investigations, J. Appl. Phys. 109 (2011). doi:10.1063/1.3567938.

[235] M. Pal, U. Pal, J.M.G.Y. Jiménez, F. Pérez-Rodríguez, Effects of crystallization and dopant concentration on the emission behavior of TiO_2:Eu nanophosphors, Nanoscale Res. Lett. 7 (2012) 1. doi:10.1186/1556-276X-7-1.

[236] S. Sathasivam, D.S. Bhachu, Y. Lu, N. Chadwick, S.A. Althabaiti, A.O. Alyoubi, S.N. Basahel, C.J. Carmalt, I.P. Parkin, Tungsten Doped TiO_2 with Enhanced Photocatalytic and Optoelectrical Properties via Aerosol Assisted Chemical Vapor Deposition., Sci. Rep. 5 (2015) 10952. doi:10.1038/srep10952.

[237] H. Su, Y.T. Huang, Y.H. Chang, P. Zhai, N.Y. Hau, P.C.H. Cheung, W.T. Yeh, T.C. Wei, S.P. Feng, The Synthesis of Nb-doped TiO_2 Nanoparticles for Improved-Performance Dye Sensitized Solar Cells, Electrochim. Acta. 182 (2015) 230–237. doi:10.1016/j.electacta.2015.09.072.

[238] E.S. Agorku, B.B. Mamba, A.C. Pandey, A.K. Mishra, Sulfur/Gadolinium-Codoped TiO_2 Nanoparticles for Enhanced Visible-Light Photocatalytic Performance, J. Nanomater. 4 (2014) 1–11. doi:10.1155/2014/289150.

[239] W. Ji, R. Shen, R. Yang, G. Yu, X. Guo, L. Peng, W. Ding, Partially nitrided molybdenum trioxide with promoted performance as an anode material for lithium-ion batteries, J. Mater. Chem. A. 2 (2014) 699–704. doi:10.1039/C3TA13708B.

[240] Z. Li, Q. Zhu, S. Huang, S. Jiang, S. Lu, W. Chen, G.S. Zakharova, Interpenetrating network V_2O_5 nanosheets/carbon nanotubes nanocomposite for fast lithium storage, RSC Adv. 4 (2014) 46624–46630. doi:10.1039/C4RA07937J.

[241] D. Mardare, A. Yildiz, R. Apetrei, P. Rambu, D. Florea, N.G. Gheorghe, D. MacOvei, C.M. Teodorescu, D. Luca, The Meyer-Neldel rule in amorphous TiO_2 films with different Fe content, J. Mater. Res. 27 (2012) 2271–2277. doi:10.1557/jmr.2012.193.

[242] C. Brookes, M. Bowker, P. Wells, Catalysts for the Selective Oxidation of Methanol, Catalysts. 6 (2016) 92. doi:10.3390/catal6070092.

[243] C. Brookes, M. Bowker, E.K. Gibson, D. Gianolio, K.M.H. Mohammed, S. Parry, S.M. Rogers, I.P. Silverwood, P.P. Wells, In situ spectroscopic investigations of MoO_x/Fe_2O_3 catalysts for the selective oxidation of methanol, Catal. Sci. Technol. 6 (2016) 722–730. doi:10.1039/C5CY01175B.

[244] Y.J. Feng, C. Wang, W.R. Cheng, J.H. Huang, T.X. Zhao, Q.H. Liu, Z. Xie, Z.Y. Pan, S.Q. Wei, Local structure of Mo-doped TiO_2 photocatalysts investigated by X-ray absorption fine structure, J. Phys. Conf. Ser. 430 (2013) 012090. doi:10.1088/1742-6596/430/1/012090.

[245] T. Ressler, J. Wienold, R.E. Jentoft, T. Neisius, Bulk structural investigation of the reduction of MoO_3 with propene and the oxidation of MoO_2 with oxygen, J. Catal. 210 (2002) 67–83. doi:10.1006/jcat.2002.3659.

[246] M. Lv, W. Xie, S. Sun, G. Wu, L. Zheng, S. Chu, C. Gao, J. Bao, Activated-carbon-supported K–Co–Mo catalysts for synthesis of higher alcohols from syngas, Catal. Sci. Technol. 5 (2015) 2925–2934. doi:10.1039/C5CY00083A.

[247] J. Majeed, C. Nayak, S.N. Jha, K. Bhattacharyya, D. Bhattacharyya, A.K. Tripathi, Correlation of Mo dopant and photocatalytic properties of Mo incorporated TiO_2: an EXAFS and photocatalytic study, RSC Adv. 5 (2015) 90932–90940. doi:10.1039/C5RA14613E.

[248] K. Brezesinski, J. Wang, J. Haetge, C. Reitz, S.O. Steinmueller, S.H. Tolbert, B.M. Smarsly, B. Dunn, T. Brezesinski, Pseudocapacitive contributions to charge storage in highly ordered mesoporous group v transition metal oxides with iso-oriented layered nanocrystalline domains, J. Am. Chem. Soc. 132 (2010) 6982–6990. doi:10.1021/ja9106385.

[249] J.-Y. Shin, J.H. Joo, K.K. Adepalli, D. Samuelis, J. Maier, The effects of n-type doping on lithium storage in TiO_2, Phys. Chem. Chem. Phys. 18 (2016) 8963–8970. doi:10.1039/C5CP07907A.

[250] L. Wu, D. Bresser, D. Buchholz, G.A. Giffin, C.R. Castro, A. Ochel, S. Passerini, Unfolding the Mechanism of Sodium Insertion in Anatase TiO_2

Nanoparticles, Adv. Energy Mater. 5 (2015) 1–11. doi:10.1002/aenm.201401142.

[251] F. Zhao, B. Wang, Y. Tang, Z. Huang, H. Ge, H. Liu, Niobium doped anatase TiO_2 as an effective anode material for sodium-ion batteries, J. Mater. Chem. A. 3 (2015) 22969–22974. doi:10.1039/C5TA04876A.

[252] B. Tian, H. Xiang, L. Zhang, Z. Li, H. Wang, Niobium doped lithium titanate as a high rate anode material for Li-ion batteries, Electrochim. Acta. 55 (2010) 5453–5458. doi:10.1016/j.electacta.2010.04.068.

[253] H. Kim, M.-Y. Cho, M.-H. Kim, K.-Y. Park, H. Gwon, Y. Lee, K.C. Roh, K. Kang, A Novel High-Energy Hybrid Supercapacitor with an Anatase TiO_2-Reduced Graphene Oxide Anode and an Activated Carbon Cathode, Adv. Energy Mater. 3 (2013) 1500–1506. doi:10.1002/aenm.201300467.

[254] E. Lim, H. Kim, C. Jo, J. Chun, K. Ku, S. Kim, H. Lee, I.-S. Nam, S. Yoon, K. Kang, J. Lee, Advanced Hybrid Supercapacitor Based on a Mesoporous Niobium Pentoxide/Carbon as High-Performance Anode., ACS Nano. 8 (2014) 8968–8978.

[255] S.H. Lee, H.K. Kim, Y.S. Yun, J.R. Yoon, S.G. Lee, Y.H. Lee, A novel high-performance cylindrical hybrid supercapacitor with $Li_{4-x}Na_xTi_5O_{12}$/activated carbon electrodes, Int. J. Hydrogen Energy. 39 (2014) 16569–16575. doi:10.1016/j.ijhydene.2014.05.072.

[256] S.H. Lee, S.G. Lee, J.R. Yoon, H.K. Kim, Novel performance of ultrathin $AlPO_4$ coated $H_2Ti_{12}O_{25}$ Exceeding $Li_4Ti_5O_{12}$ in cylindrical hybrid supercapacitor, J. Power Sources. 273 (2015) 839–843. doi:10.1016/j.jpowsour.2014.09.090.

[257] H.K. Kim, D. Mhamane, M.S. Kim, H.K. Roh, V. Aravindan, S. Madhavi, K.C. Roh, K.B. Kim, TiO_2-reduced graphene oxide nanocomposites by microwave-assisted forced hydrolysis as excellent insertion anode for Li-ion battery and capacitor, J. Power Sources. 327 (2016) 171–177. doi:10.1016/j.jpowsour.2016.07.053.

[258] J. Ni, L. Yang, H. Wang, L. Gao, A high-performance hybrid supercapacitor with $Li_4Ti_5O_{12}$-C nano-composite prepared by in situ and ex situ carbon modification, J. Solid State Electrochem. 16 (2012) 2791–2796. doi:10.1007/s10008-012-1704-9.

[259] Q. Wang, Z. Wen, J. Li, A hybrid supercapacitor fabricated with a carbon nanotube cathode and a TiO_2-B nanowire anode, Adv. Funct. Mater. 16 (2006) 2141–2146. doi:10.1002/adfm.200500937.

[260] V. Aravindan, N. Shubha, W.C. Ling, S. Madhavi, Constructing high energy density non-aqueous Li-ion capacitors using monoclinic TiO_2-B nanorods as insertion host, J. Mater. Chem. A. 1 (2013) 6145–6151. doi:10.1039/C3TA11103B.

[261] V. Aravindan, W. Chuiling, S. Madhavi, High power lithium-ion hybrid electrochemical capacitors using spinel $LiCrTiO_4$ as insertion electrode, J. Mater. Chem. 22 (2012) 16026–16031. doi:10.1039/c2jm32970k.

[262] W.-Q. Han, X.-L. Wang, Carbon-coated Magnéli-phase Ti_nO_{2n-1} nanobelts as anodes for Li-ion batteries and hybrid electrochemical cells, Appl. Phys. Lett. 97 (2010) 2431041–2431043. doi:10.1063/1.3525369.

[263] F. Wang, C. Wang, Y. Zhao, Z. Liu, Z. Chang, L. Fu, Y. Zhu, Y. Wu, D. Zhao, A Quasi-Solid-State Li-Ion Capacitor Based on Porous TiO_2 Hollow Microspheres Wrapped with Graphene Nanosheets, Small. 12 (2016) 6207–

6213. doi:10.1002/smll.201602331.

[264] S. Liu, Z. Cai, J. Zhou, A. Pan, S. Liang, Nitrogen-doped TiO_2 nanospheres for advanced sodium-ion battery and sodium-ion capacitor applications, J. Mater. Chem. A. 4 (2016) 18278–18283. doi:10.1039/C6TA08472A.

[265] R. Ding, L. Qi, H. Wang, An investigation of spinel $NiCo_2O_4$ as anode for Na-ion capacitors, Electrochim. Acta. 114 (2013) 726–732. doi:10.1016/j.electacta.2013.10.113.

[266] X. Liu, N. Zhang, J. Ni, L. Gao, Improved electrochemical performance of sol-gel method prepared $Na_4Mn_9O_{18}$ in aqueous hybrid Na-ion supercapacitor, J. Solid State Electrochem. 17 (2013) 1939–1944. doi:10.1007/s10008-013-2044-0.

[267] D. Cericola, P. Novák, A. Wokaun, R. Kötz, Hybridization of electrochemical capacitors and rechargeable batteries: An experimental analysis of the different possible approaches utilizing activated carbon, $Li_4Ti_5O_{12}$ and $LiMn_2O_4$, J. Power Sources. 196 (2011) 10305–10313. doi:10.1016/j.jpowsour.2011.07.032.

[268] N. Arun, A. Jain, V. Aravindan, S. Jayaraman, W. Chui Ling, M.P. Srinivasan, S. Madhavi, Nanostructured spinel $LiNi_{0.5}Mn_{1.5}O_4$ as new insertion anode for advanced Li-ion capacitors with high power capability, Nano Energy. 12 (2015) 69–75. doi:10.1016/j.nanoen.2014.12.006.

[269] E. Lim, C. Jo, M.S. Kim, M.-H. Kim, J. Chun, H. Kim, J. Park, K.C. Roh, K. Kang, S. Yoon, J. Lee, High-Performance Sodium-Ion Hybrid Supercapacitor Based on Nb_2O_5@Carbon Core-Shell Nanoparticles and Reduced Graphene Oxide Nanocomposites, Adv. Funct. Mater. 26 (2016) 3711–3719. doi:10.1002/adfm.201505548.

[270] L. Zhao, L. Qi, H. Wang, Sodium titanate nanotube/graphite, an electric energy storage device using Na^+-based organic electrolytes, J. Power Sources. 242 (2013) 597–603. doi:10.1016/j.jpowsour.2013.05.132.

[271] B. Babu, M.M. Shaijumon, High performance sodium-ion hybrid capacitor based on $Na_2Ti_2O_4(OH)_2$ nanostructures, J. Power Sources. 353 (2017) 85–94. doi:10.1016/j.jpowsour.2017.03.143.

[272] S.S. Zhang, Eliminating pre-lithiation step for making high energy density hybrid Li-ion capacitor, J. Power Sources. 343 (2017) 322–328. doi:10.1016/j.jpowsour.2017.01.061.

[273] N. Xu, X. Sun, F. Zhao, X. Jin, X. Zhang, K. Wang, K. Huang, Y. Ma, The Role of Pre-Lithiation in Activated Carbon/$Li_4Ti_5O_{12}$ Asymmetric Capacitors, Electrochim. Acta. 236 (2017) 443–450. doi:10.1016/j.electacta.2017.03.189.

[274] F. Holtstiege, P. Bärmann, R. Nölle, M. Winter, T. Placke, Pre-Lithiation Strategies for Rechargeable Energy Storage Technologies: Concepts, Promises and Challenges, Batteries. 4 (2018) 1–39. doi:10.3390/batteries4010004.

[275] N. Kurra, M. Alhabeb, K. Maleski, C.-H. Wang, H.N. Alshareef, Y. Gogotsi, Bistacked Titanium Carbide (MXene) Anodes for Hybrid Sodium-Ion Capacitors, ACS Energy Lett. (2018) 2094–2100. doi:10.1021/acsenergylett.8b01062.

[276] N.A.M. Barakat, A.H. Zaki, E. Ahmed, A.A. Farghali, F.S. Al-Mubaddel, Fe_xCo_{1-x}-doped titanium oxide nanotubes as effective photocatalysts for hydrogen extraction from ammonium phosphate, Int. J. Hydrogen Energy. 43 (2018) 7990–7997. doi:10.1016/j.ijhydene.2018.03.055.

[277] D. Chen, Z. Jiang, J. Geng, Q. Wang, D. Yang, Carbon and Nitrogen Co-doped

TiO_2 with Enhanced Visible-Light Photocatalytic Activity, Ind. Eng. Chem. Res. 46 (2007) 2741–2746. doi:10.1021/ie061491k.

[278] Y.F. Jiang, Y.Y. Chen, B. Zhang, Y.Q. Feng, N, La Co-Doped TiO_2 for Use in Low-Temperature-Based Dye-Sensitized Solar Cells, J. Electrochem. Soc. 163 (2016) F1133–F1138. doi:10.1149/2.0141610jes.

[279] J. Fang, W. Liu, F. Yu, F. Qin, M. Wang, K. Zhang, Y. Lai, Fe, S co-doped anatase TiO_2 nanotubes as anodes with improved electrochemical performance for lithium ion batteries, RSC Adv. 6 (2016) 70133–70140. doi:10.1039/C6RA13850K.

[280] X. Weng, J.K. Cockcroft, G. Hyett, M. Vickers, P. Boldrin, C.C. Tang, S.P. Thompson, J.E. Parker, J.C. Knowles, I. Rehman, I. Parkin, J.R.G.G. Evans, J.A. Darr, High-throughput continuous hydrothermal synthesis of an entire nanoceramic phase diagram, J. Comb. Chem. 11 (2009) 829–834. doi:10.1021/cc900041a.

[281] P. Marchand, N.M. Makwana, C.J. Tighe, R.I. Gruar, I.P. Parkin, C.J. Carmalt, J.A. Darr, High-Throughput Synthesis, Screening, and Scale-Up of Optimized Conducting Indium Tin Oxides, ACS Comb. Sci. 18 (2016) 130–137. doi:10.1021/acscombsci.5b00166.

[282] S. Kellici, K. Gong, T. Lin, S. Brown, R.J.H. Clark, M. Vickers, J.K. Cockcroft, V. Middelkoop, P. Barnes, J.M. Perkins, C.J. Tighe, J.A. Darr, High-throughput continuous hydrothermal flow synthesis of Zn-Ce oxides: Unprecedented solubility of Zn in the nanoparticle fluorite lattice, Philos. Trans. R. Soc. A Math. Phys. Eng. Sci. 368 (2010) 4331–4349. doi:10.1098/rsta.2010.0135.

[283] X. Zhu, C. Yang, F. Xiao, J. Wang, X. Su, Synthesis of nano-TiO_2-decorated MoS_2 nanosheets for lithium ion batteries, New J. Chem. 39 (2015) 683–688. doi:10.1039/c4nj01451k.

[284] B.G. Lee, S.C. Nam, J. Choi, Anodic TiO_2 nanotubes as anode electrode in Li-air and Li-ion batteries, Curr. Appl. Phys. 12 (2012) 1580–1585. doi:10.1016/j.cap.2012.05.004.

[285] D. Wang, D. Choi, Z. Yang, V. V Viswanathan, Z. Nie, C. Wang, Y. Song, J. Zhang, J. Liu, Synthesis and Li-Ion Insertion Properties of Highly Crystalline Mesoporous Rutile TiO_2, Chem. Mater. (2008) 3435–3442. doi:10.1021/cm8002589.

[286] X. Zhu, X. Liang, X. Fan, X. Su, Fabrication of flower-like MoS_2/TiO_2 hybrid as an anode material for lithium ion batteries, RSC Adv. 7 (2017) 38119–38124. doi:10.1039/C7RA06294J.

[287] Y. Liang, Z. Yi, S. Yang, L. Zhou, J. Sun, Y. Zhou, Hydrothermal synthesis and lithium-intercalation properties of MoO_2 nano-particles with different morphologies, Solid State Ion. 177 (2006) 501–505. http://linkinghub.elsevier.com/retrieve/pii/S0167273805006065.

[288] Y. Sun, X. Hu, W. Luo, Y. Huang, Ultrafine MoO_2 nanoparticles embedded in a carbon matrix as a high-capacity and long-life anode for lithium-ion batteries, J. Mater. Chem. 22 (2012) 425–431. doi:10.1039/c1jm14701c.

[289] D. Yuan, W. Yang, J. Ni, L. Gao, Sandwich structured MoO_2@TiO_2@CNT nanocomposites with high-rate performance for lithium ion batteries, Electrochim. Acta. 163 (2015) 57–63. doi:10.1016/j.electacta.2015.02.149.

[290] B. Guo, X. Fang, B. Li, Y. Shi, C. Ouyang, Y.S. Hu, Z. Wang, G.D. Stucky, L. Chen, Synthesis and lithium storage mechanism of ultrafine MoO_2 nanorods, Chem. Mater. 24 (2012) 457–463. doi:10.1021/cm202459r.

[291] Y. Xu, R. Yi, B. Yuan, X. Wu, M. Dunwell, Q. Lin, L. Fei, S. Deng, P. Andersen, D. Wang, H. Luo, High Capacity MoO_2/Graphite Oxide Composite Anode for Lithium-Ion Batteries, J. Phys. Chem. Lett. 3 (2012) 309–314. doi:10.1021/jz201619r.

[292] B. Liu, X. Zhao, Y. Tian, D. Zhao, C. Hu, M. Cao, A simple reduction process to synthesize MoO_2/C composites with cage-like structure for high-performance lithium-ion batteries., Phys. Chem. Chem. Phys. 15 (2013) 8831–8837. doi:10.1039/c3cp44707c.

[293] Y. Shi, B. Guo, S.A. Corr, Q. Shi, Y.S. Hu, K.R. Heier, L. Chen, R. Seshadri, G.D. Stucky, Ordered mesoporous metallic MoO_2 materials with highly reversible lithium storage capacity, Nano Lett. 9 (2009) 4215–4220. doi:10.1021/nl902423a.

[294] J.J. Auborn, Y.L. Barberio, Lithium intercalation cells without metallic lithium $MoO_2/LiCoO_2$ and $WO_2/LiCoO_2$, J. Electrochem. Soc. 134 (1987) 638–640. doi:10.1149/1.2100521.

[295] L. Zeng, C. Zheng, C. Deng, X. Ding, M. Wei, MoO_2-ordered mesoporous carbon nanocomposite as an anode material for lithium-ion batteries., ACS Appl. Mater. Interfaces. 5 (2013) 2182–2187. doi:10.1021/am303286n.

[296] Y. Wang, H. Xia, L. Lu, J. Lin, Excellent Performance in Lithium-Ion Battery Anodes: Rational Synthesis of $Co(CO_3)_{0.5}(OH)_{0.11}H_2O$ Nanobelt Array and Its Conversion into Mesoporous and Single-Crystal Co_3O_4, ACS Nano. 4 (2010) 1425–1432. doi:10.1021/nn9012675.

[297] Y.M. Kang, K.T. Kim, J.H. Kim, H.S. Kim, P.S. Lee, J.Y. Lee, H.K. Liu, S.X. Dou, Electrochemical properties of Co_3O_4, Ni-Co_3O_4 mixture and Ni-Co_3O_4 composite as anode materials for Li ion secondary batteries, J. Power Sources. 133 (2004) 252–259. doi:10.1016/j.jpowsour.2004.02.012.

[298] Y. Wang, Z.W. Fu, Q.Z. Qin, A nanocrystalline Co_3O_4 thin film electrode for Li-ion batteries, Thin Solid Films. 441 (2003) 19–24. doi:10.1016/S0040-6090(03)00918-0.

[299] Z. Wu, W. Ren, L. Wen, L. Gao, J. Zhao, Z. Chen, G. Zhou, F. Li, H. Cheng, Graphene Anchored with Co_3O_4 Nanoparticles as Anode of Lithium Ion Capacity and Cyclic Performance, ACS Nano. 4 (2010) 3187–3194. doi:10.1021/nn100740x.

[300] Y. Li, B. Tan, Y. Wu, Mesoporous Co_3O_4 nanowire arrays for lithium ion batteries with high capacity and rate capability, Nano Lett. 8 (2008) 265–270. doi:10.1021/nl0725906.

[301] W.Y. Li, L.N. Xu, J. Chen, Co_3O_4 Nanomaterials in Lithium-Ion Batteries and Gas Sensors, Adv. Funct. Mater. 15 (2005) 851–857. doi:10.1002/adfm.200400429.

[302] N. Yan, L. Hu, Y. Li, Y. Wang, H. Zhong, X. Hu, X. Kong, Q. Chen, Co_3O_4 Nanocages for High-Performance Anode Material in Lithium-Ion Batteries, J. Phys. Chem. C. 116 (2012) 7227–7235. doi:10.1021/jp2126009.

[303] S. Yuvaraj, R.H. Vignesh, L. Vasylechko, Y.S. Lee, R.K. Selvan, Synthesis and electrochemical performance of Co_2TiO_4 and its core–shell structure of Co_2TiO_4@C as negative electrodes for Li-ion batteries, RSC Adv. 6 (2016) 69016–69026. doi:10.1039/C6RA11251J.

[304] J. Li, S. Xiong, Y. Liu, Z. Ju, Y. Qian, High electrochemical performance of monodisperse $NiCo_2O_4$ mesoporous microspheres as an anode material for Li-ion batteries, ACS Appl. Mater. Interfaces. 5 (2013) 981–988.

doi:10.1021/am3026294.

[305] J. Liu, C. Liu, Y. Wan, W. Liu, Z. Ma, S. Ji, J. Wang, Y. Zhou, P. Hodgson, Y. Li, Facile synthesis of $NiCo_2O_4$ nanorod arrays on Cu conductive substrates as superior anode materials for high-rate Li-ion batteries, CrystEngComm. 15 (2013) 1578. doi:10.1039/c2ce26632f.

[306] T. Li, X. Li, Z. Wang, H. Guo, Y. Li, A novel $NiCo_2O_4$ anode morphology for lithium-ion batteries, J. Mater. Chem. A. 3 (2015) 11970–11975. doi:10.1039/C5TA01928A.

[307] Z. Ju, G. Ma, Y. Zhao, Z. Xing, Y. Qiang, Y. Qian, A Facile Method for Synthesis of Porous $NiCo_2O_4$ Nanorods as a High-Performance Anode Material for Li-Ion Batteries, Part. Part. Syst. Charact. 32 (2015) 1012–1019. doi:10.1002/ppsc.201500093.

[308] W. Xu, X. Cui, Z. Xie, G. Dietrich, Y. Wang, Integrated Co_3O_4/TiO_2 Composite Hollow Polyhedrons Prepared via Cation-exchange Metal-Organic Framework for Superior Lithium-ion Batteries, Electrochim. Acta. 222 (2016) 1021–1028. doi:10.1016/j.electacta.2016.11.071.

[309] D. Zhao, Q. Hao, C. Xu, Nanoporous TiO_2/Co_3O_4 Composite as an Anode Material for Lithium-Ion Batteries, Electrochim. Acta. 211 (2016) 83–91. doi:10.1016/j.electacta.2016.06.043.

[310] S. Nayak, K. Dasari, D.C. Joshi, P. Pramanik, R. Palai, A. Waske, R.N. Chauhan, N. Tiwari, T. Sarkar, S. Thota, Low-temperature anomalous magnetic behavior of Co_2TiO_4 and Co_2SnO_4, J. Appl. Phys. 120 (2016) 0–6. doi:10.1063/1.4966172.

[311] S. Ogawa, S. Waki, Specific Heat of Co_2TiO_4 and its Anomaly Associated with Magnetic Transition, J. Phys. Soc. Japan. 20 (1965) 540–545. doi:10.1143/JPSJ.20.540.

[312] W. Lei, W.-Z. Lu, X.-H. Wang, F. Liang, J. Wang, Phase Composition and Microwave Dielectric Properties of $ZnAl_2O_4$–Co_2TiO_4 Low-Permittivity Ceramics with High Quality Factor, J. Am. Ceram. Soc. 94 (2011) 20–23. doi:10.1111/j.1551-2916.2010.04247.x.

[313] S. Khanahmadzadeh, M. Enhessari, Z. Solati, A. Mohebalizadeh, A. Alipouramjad, Synthesis, characterization and optical band gap of the Co_2TiO_4 nanoparticles, Mater. Sci. Semicond. Process. 31 (2015) 599–603. doi:10.1016/j.mssp.2014.12.043.

[314] Y. He, L. Xu, Y. Zhai, A. Li, X. Chen, A hexangular ring-core $NiCo_2O_4$ porous nanosheet/NiO nanoparticle composite as an advanced anode material for LIBs and catalyst for CO oxidation applications, Chem. Commun. 51 (2015) 14768–14771. doi:10.1039/c5cc03801d.

[315] R. Kakavandi, S.-A. Savu, A. Caneschi, T. Chassé, M.B. Casu, At the interface between organic radicals and $TiO_2(110)$ single crystals: electronic structure and paramagnetic character, Chem. Commun. 49 (2013) 10103. doi:10.1039/c3cc45693e.

[316] Y. Chu, J. Feng, Y. Qian, S. Xiong, Enhancing the electrode performance of Co_3O_4 through Co_3O_4@a-TiO_2 core–shell microcubes with controllable pore size, RSC Adv. 5 (2015) 40899–40906. doi:10.1039/C5RA06711A.

[317] S. Jin, G. Yang, H. Song, H. Cui, C. Wang, Ultrathin Hexagonal 2D Co_2GeO_4 Nanosheets: Excellent Li-Storage Performance and ex Situ Investigation of Electrochemical Mechanism, ACS Appl. Mater. Interfaces. 7 (2015) 24932–24943. doi:10.1021/acsami.5b08446.

[318] M.C. Biesinger, B.P. Payne, A.P. Grosvenor, L.W.M. Lau, A.R. Gerson, R.S.C. Smart, Resolving surface chemical states in XPS analysis of first row transition metals, oxides and hydroxides: Cr, Mn, Fe, Co and Ni, Appl. Surf. Sci. 257 (2011) 2717–2730. doi:10.1016/j.apsusc.2010.10.051.

[319] J.W. Niemantsverdriet, Photoemission and Auger Spectroscopy, in: Spectrosc. Catal., Wiley-VCH Verlag GmbH & Co. KGaA, Weinheim, Germany, (2007) 39–83. doi:10.1002/9783527611348.ch3.

[320] D. Bresser, E. Paillard, R. Kloepsch, S. Krueger, M. Fiedler, R.R. Schmitz, D. Baither, M. Winter, S. Passerini, Carbon coated $ZnFe_2O_4$ nanoparticles for advanced lithium-ion anodes, Adv. Energy Mater. 3 (2013) 513–523. doi:10.1002/aenm.201200735.

[321] Y. Sun, X. Hu, W. Luo, Y. Huang, Self-assembled hierarchical MoO_2/graphene nanoarchitectures and their application as a high-performance anode material for lithium-ion batteries, ACS Nano. 5 (2011) 7100–7107. doi:10.1021/nn201802c.

[322] D. Zhao, J. Qin, L. Zheng, M. Cao, Amorphous vanadium oxide/molybdenum oxide hybrid with three-dimensional ordered hierarchically porous structure as a high-performance li-ion battery anode, Chem. Mater. 28 (2016) 4180–4190. doi:10.1021/acs.chemmater.6b00414.

[323] L. Guo, Y. Wang, Standing carbon-coated molybdenum dioxide nanosheets on graphene: morphology evolution and lithium ion storage properties, J. Mater. Chem. A. 3 (2015) 4706–4715. doi:10.1039/C4TA05520A.

[324] X.-Y. Xue, Z.-H. Chen, L.-L. Xing, S. Yuan, Y.-J. Chen, SnO_2/α-MoO_3 core-shell nanobelts and their extraordinarily high reversible capacity as lithium-ion battery anodes, Chem. Commun. 47 (2011) 5205. doi:10.1039/c1cc00076d.

[325] Y. Tang, D. Wu, Y. Mai, H. Pan, J. Cao, C. Yang, F. Zhang, X. Feng, A two-dimensional hybrid with molybdenum disulfide nanocrystals strongly coupled on nitrogen-enriched graphene via mild temperature pyrolysis for high performance lithium storage, Nanoscale. 6 (2014) 14679–14685. doi:10.1039/C4NR05519E.

[326] D. Zhao, L. Zheng, Y. Xiao, X. Wang, M. Cao, Lithium storage in microstructures of amorphous mixed-valence vanadium oxide as anode materials, ChemSusChem. 8 (2015) 2212–2222. doi:10.1002/cssc.201500256.

[327] G. Carbonari, F. Maroni, A. Birrozzi, R. Tossici, F. Croce, F. Nobili, Synthesis and characterization of Si nanoparticles wrapped by V_2O_5 nanosheets as a composite anode material for lithium-ion batteries, Electrochim. Acta. 281 (2018) 676–683. doi:10.1016/j.electacta.2018.05.094.

[328] D. Wu, R. Shen, R. Yang, W. Ji, M. Jiang, W. Ding, L. Peng, Mixed Molybdenum Oxides with Superior Performances as an Advanced Anode Material for Lithium-Ion Batteries, Sci. Rep. 7 (2017) 44697. doi:10.1038/srep44697.

[329] N.A. Chernova, M. Roppolo, A.C. Dillon, M.S. Whittingham, Layered vanadium and molybdenum oxides: batteries and electrochromics, J. Mater. Chem. 19 (2009) 2526. doi:10.1039/b819629j.

[330] L. Mai, L. Xu, C. Han, X. Xu, Y. Luo, S. Zhao, Y. Zhao, Electrospun ultralong hierarchical vanadium oxide nanowires with high performance for lithium ion batteries, Nano Lett. 10 (2010) 4750–4755. doi:10.1021/nl103343w.

[331] M. Lübke, N. Ding, M.J. Powell, D.J.L. Brett, P.R. Shearing, Z. Liu, J.A. Darr, VO_2 nano-sheet negative electrodes for lithium-ion batteries, Electrochem.

Commun. 64 (2016) 56–60. doi:10.1016/j.elecom.2016.01.013.

[332] B. Paul, J. Kishor, S.P. Chakraborty, A.K. Suri, Thermal analysis on conversion of MoO_3 to MoO_2 and its silicothermic reduction, J. Therm. Anal. Calorim. 112 (2013) 31–36. doi:10.1007/s10973-012-2828-y.

[333] C. Niu, J. Meng, C. Han, K. Zhao, M. Yan, L. Mai, VO_2 nanowires assembled into hollow microspheres for high-rate and long-life lithium batteries, Nano Lett. 14 (2014) 2873–2878. doi:10.1021/nl500915b.

[334] Y. Shi, S.L. Chou, J.Z. Wang, H.Z. Li, H.K. Liu, Y.P. Wu, In-situ hydrothermal synthesis of graphene woven VO_2 nanoribbons with improved cycling performance, J. Power Sources. 244 (2013) 684–689. doi:10.1016/j.jpowsour.2012.11.151.

[335] S. Li, Hierarchical MoO_2/rGO Composite as a High-Performance Anode Material for Lithium-Ion Batteries, Int. J. Electrochem. Sci. 13 (2018) 23–28. doi:10.20964/2018.01.41.

[336] T. Zhai, X. Lu, Y. Ling, M. Yu, G. Wang, T. Liu, C. Liang, Y. Tong, Y. Li, A new benchmark capacitance for supercapacitor anodes by mixed-valence sulfur-doped V_6O_{13-x}, Adv. Mater. 26 (2014) 5869–5875. doi:10.1002/adma.201402041.

[337] S.D. Perera, B. Patel, N. Nijem, K. Roodenko, O. Seitz, J.P. Ferraris, Y.J. Chabal, K.J. Balkus, Vanadium oxide nanowire-carbon nanotube binder-free flexible electrodes for supercapacitors, Adv. Energy Mater. 1 (2011) 936–945. doi:10.1002/aenm.201100221.

[338] N. Chen, C. Wang, F. Hu, X. Bie, Y. Wei, G. Chen, F. Du, Brannerite-Type Vanadium–Molybdenum Oxide $LiVMoO_6$ as a Promising Anode Material for Lithium-Ion Batteries with High Capacity and Rate Capability, ACS Appl. Mater. Interfaces. 7 (2015) 16117–16123. doi:10.1021/acsami.5b05030.

[339] B. Solsona, M.I. Vázquez, F. Ivars, A. Dejoz, P. Concepción, J.M. López Nieto, Selective oxidation of propane and ethane on diluted Mo-V-Nb-Te mixed-oxide catalysts, J. Catal. 252 (2007) 271–280. doi:10.1016/j.jcat.2007.09.019.

[340] F. Ivars, B. Solsona, S. Hernández, J.M. López Nieto, Influence of gel composition in the synthesis of MoVTeNb catalysts over their catalytic performance in partial propane and propylene oxidation, Catal. Today. 149 (2010) 260–266. doi:10.1016/j.cattod.2009.09.018.

[341] B.O. Marinder, On the phase relations in the $V_xMo_{1-x}O_2$ system ($0 \leq x \leq 0.55$), Mater. Res. Bull. 10 (1975) 909–914. doi:10.1016/0025-5408(75)90070-7.

[342] A. Katrib, J.W. Sobczak, M. Krawczyk, L. Zommer, A. Benadda, A. Jablonski, G. Maire, Surface studies and catalytic properties of the bifunctional bulk MoO_2 system, Surf. Interface Anal. 34 (2002) 225–229. doi:10.1002/sia.1288.

[343] J. Baltrusaitis, B. Mendoza-Sanchez, V. Fernandez, R. Veenstra, N. Dukstiene, A. Roberts, N. Fairley, Generalized molybdenum oxide surface chemical state XPS determination via informed amorphous sample model, Appl. Surf. Sci. 326 (2015) 151–161. doi:10.1016/j.apsusc.2014.11.077.

[344] A.N. Mansour, P.H. Smith, W.M. Baker, M. Balasubramanian, J. McBreen, In situ XAS investigation of the oxidation state and local structure of vanadium in discharged and charged V_2O_5 aerogel cathodes, Electrochim. Acta. 47 (2002) 3151–3161. doi:10.1016/S0013-4686(02)00234-7.

[345] T.E. Ashton, D. Hevia Borrás, A. Iadecola, K.M. Wiaderek, P.J. Chupas, K.W. Chapman, S.A. Corr, Microwave-assisted synthesis and electrochemical evaluation of VO 2 (B) nanostructures, Acta Crystallogr. Sect. B Struct. Sci.

Cryst. Eng. Mater. 71 (2015) 722–726. doi:10.1107/S2052520615021289.

[346] Y. Wu, L. Fan, Q. Liu, S. Chen, W. Huang, F. Chen, G. Liao, C. Zou, Z. Wu, Decoupling the lattice distortion and charge doping effects on the phase transition behavior of VO_2 by titanium (Ti^{4+}) doping, Sci. Rep. 5 (2015) 1–8. doi:10.1038/srep09328.

[347] X.H. Rui, N. Yesibolati, S.R. Li, C.C. Yuan, C.H. Chen, Determination of the chemical diffusion coefficient of Li^+ in intercalation-type $Li_3V_2(PO_4)_3$ anode material, Solid State Ionics. 187 (2011) 58–63. doi:10.1016/j.ssi.2011.02.013.

[348] D. Bauer, A.J. Roberts, C.L. Starkey, R. Vedarajan, D.J.L. Brett, P.R. Shearing, N. Matsumi, J.A. Darr, TiO_2/MoO_2 Nanocomposite as Anode Materials for High Power Li-ion Batteries with Exceptional Capacity, Int. J. Electrochem. Sci. 13 (2018) 5120–5140. doi:10.20964/2018.05.37.

[349] D. Bauer, A.J. Roberts, S.G. Patnaik, D.J.L. Brett, P.R. Shearing, E. Kendrick, N. Matsumi, J.A. Darr, High Power Sodium-Ion Batteries and Hybrid Electrochemical Capacitors Using Mo or Nb-Doped Nano-Titania Anodes, J. Electrochem. Soc. 165 (2018) A1662–A1670. doi:10.1149/2.0341809jes.

[350] G.P. Evans, M.J. Powell, I.D. Johnson, D.P. Howard, D. Bauer, J.A. Darr, I.P. Parkin, Room temperature vanadium dioxide–carbon nanotube gas sensors made via continuous hydrothermal flow synthesis, Sensors Actuators, B Chem. 255 (2018). doi:10.1016/j.snb.2017.07.152.

List of Publications

Publications this thesis is based upon:

- **Bauer, D.**, Roberts, A. J., Matsumi, N. and Darr, J. A.: Nanosized Mo- and Nb-doped TiO_2 as anode materials for high energy and high power hybrid Li-ion capacitors[54], *Nanotechnology*. 28 (2017) 195403-195413. doi: 10.1088/1361-6528/aa69df.
- **Bauer, D.**, Roberts, A. J., Starkey, C. L., Vedarajan, R., Brett, D. J. L., Shearing, P. R., Matsumi, M. and Darr, J. A.: TiO_2/MoO_2 Nanocomposite as Anode Materials for High Power Li-ion Batteries with Exceptional Capacity[348], *International Journal of Electrochemical Science*. 13 (2018) 5120-5140. doi: 10.20964/2018.05.37
- **Bauer, D.**, Roberts, A. J., Patnaik, S. G., Brett, D. J. L., Shearing, P. R., Kendrick, E., Matsumi, N. and Darr, J. A.: High Power Sodium-Ion Batteries and Hybrid Electrochemical Capacitors Using Mo or Nb-Doped Nano-Titania Anodes[349], *Journal of the Electrochemical Society*. 165 (2018) A1662–A1670. doi: 10.1149/2.0341809jes
- **Bauer, D.**, Ashton, T. E., Brett, D. J. L., Shearing, P. R., Matsumi, N. and Darr, J. A.: Mixed Molybdenum Vanadium Oxide Nanoparticles with Excellent High-Power Performance as Li-ion Battery Negative Electrodes, *Journal of Power Sources* (under review).
- **Bauer, D.**, Ashton, T. E., Matsumi, N. and Darr, J. A.: Combinatorial Synthesis of Mo/V/Nb (co-)doped TiO_2 for High Power Li-ion Battery Anodes, (in preparation).

Other work:

- **Bauer, D.**, Ashton, T. E., Groves, A. R., Matsumi, N. and Darr, J. A.: Continuous Hydrothermal Synthesis of Metal Germanates (M_2GeO_4; M = Co, Mn, Zn) for High Capacity Negative Electrodes in Li-ion Batteries, (under review)
- Xu, Y., **Bauer, D.**, Luebke, M., Ashton, T. E., Zong, Y., Darr, J. A.: High-Power Sodium Titanate Anodes; A Comparison of Lithium vs. Sodium-ion

Batteries, *Journal of Power Sources*. 408 (2018) 28-37. doi: 10.1016/j.jpowsour.2018.10.038

- Evans, G. P., Powell, M. J., Johnson, I. D., Howard, D. P., **Bauer, D.**, Darr, J. A., & Parkin, I. P.: Room temperature vanadium dioxide–carbon nanotube gas sensors made via continuous hydrothermal flow synthesis[350], *Sensors and Actuators B: Chemical*. 255 (2018) 1119-1129. doi: 10.1016/j.snb.2017.07.152
- Ashton, T. E., McCafferty, L., **Bauer, D.**, Darr, J. A.: Continuous Hydrothermal Synthesis of MnO_2 polymorphs: Structural Dependence on Electrochemical Activity in Li-ion Batteries, (in preparation)
- Ashton, T. E., Sotelo-Vazquez, C., **Bauer, D.**, Darr, J. A.: Scalable Continuous Hydrothermal Flow Assisted Synthesis and Diffusion Studies of High-Nickel NMC LIB cathodes, (in preparation)

List of Figures

List of Abbreviations

AC	Alternating Current/Activate Carbon
Ar	Argon
BET	Brunauer, Emmet and Teller
CE	Counter Electrode
CHFS	Continuous Hydrothermal Flow Synthesis
CJM	Confined Jet Mixer
CV	Cyclic Voltammetry/Voltammogram
DEC	Diethyl Carbonate
DMC	Dimethyl Carbonate
EC	Ethylene Carbonate
EIS	Electrochemical Impedance Spectroscopy
EDLC	Electric Double Layer Capacitor
EDX	Energy Dispersive X-ray
EMC	Ethylmethyl Carbonate
GITT	Galvanostatic Intermittent Titration Technique
HOMO	Highest Occupied Molecular Orbital
ICE	Internal Combustion Engine
ICSD	International Crystal Structure Database
IL	Ionic Liquid
JCPDS	Joint Committee on Powder Diffraction Standards
LIB	Li-Ion Battery
LCO/$LiCoO_2$	Lithium Cobalt Oxide
Li-HEC	Li-ion Hybrid Electrochemical Capacitor
LUMO	Lowest Unoccupied Molecular Orbital
LTO	Lithium Titanium 0xide: $Li_4Ti_5O_{12}$

Na-HEC	Na-ion Hybrid Electrochemical Capacitor
NAB/NIB	Na-Ion Battery
NCA	Lithium Nickel Cobalt Aluminium Oxide
Ni-MH	Nickel-Metal Hydride battery
NMC	Lithium Nickel Manganese Cobalt Oxide
NMP	N-Methyl-2-Pyrrolidone
OCV	Open Circuit Voltage
Pb-acid	Lead-acid battery
PC	Polycarbonate
PEO	Polyethylene Oxide
(P)HEV	(Plug-in) Hybrid Electric Vehicle
PVDF	Polyvinylidene Fluoride
RE	Reference Electrode
SEI	Solid Electrolyte Interphase
SHE	Standard Hydrogen Electrode
SPEIS	Step-Potentio Electrochemical Impedance Spectroscopy
SSA	Specific Surface Area
TEM	Transmission Electron Microscopy
TiBALD	Titanium(IV) bis(ammonium lactato)dihydroxide
TMO	TiO_2/MoO_2 composite
VC	Vinylene Carbonate
WE	Working Electrode
XAS	X-ray Absorption Spectroscopy
XPS	X-ray Photoelectron Spectroscopy
XRD	X-ray Diffraction

List of Tables

Appendices

Appendix Chapter 4

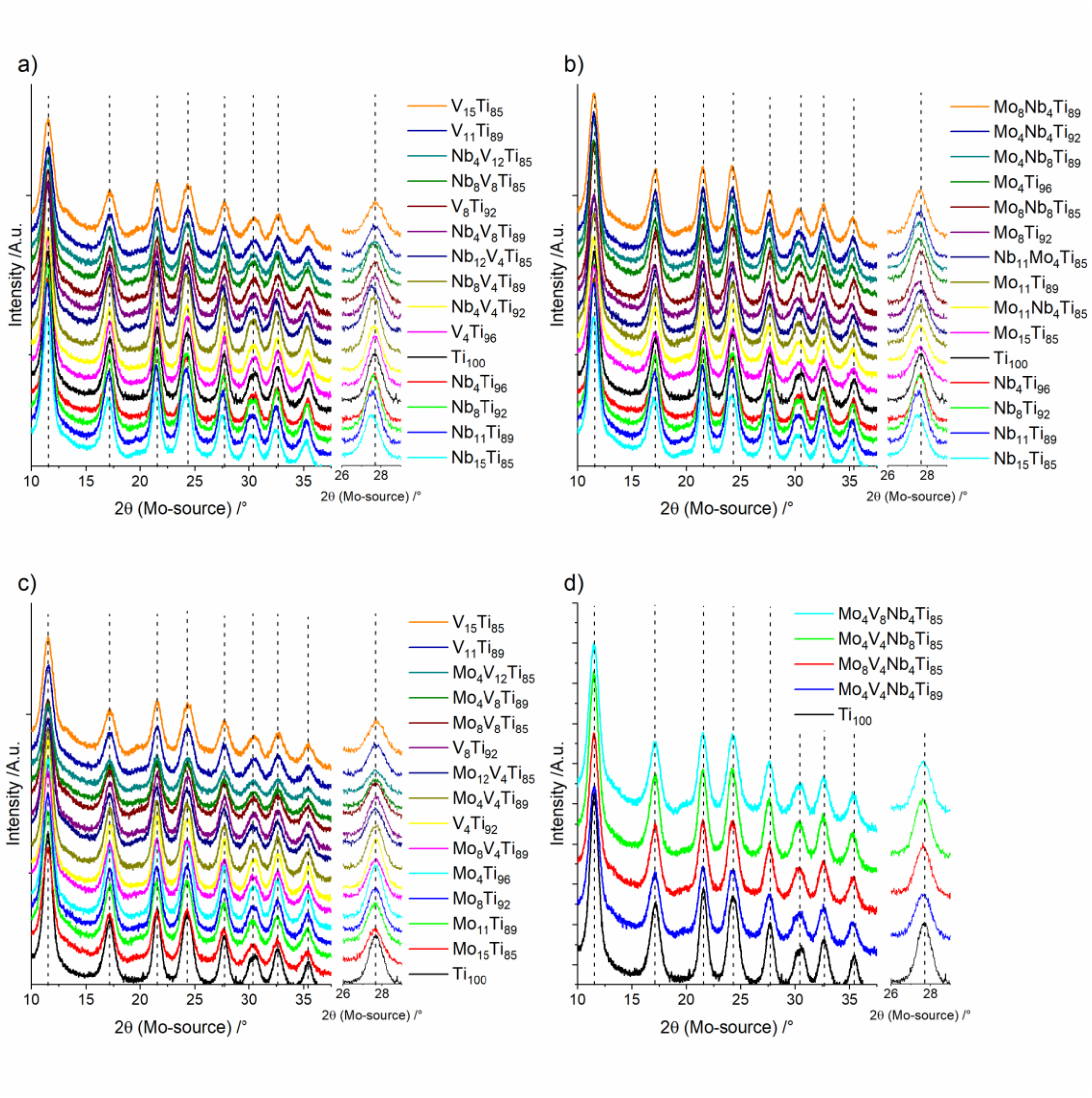

Figure A1: PXRD patterns for the TiO_2 (anatase) samples co-doped with a) Nb/V, b) Mo/Nb, c) Mo/V, and d) Mo/V/Nb.

Table A1: Full width at half maximum (FWHM) and positions of the three peaks for anatase TiO_2 used to analyse the estimated crystallite domain size via Scherrer equation.

	FWHM1	Position1	FWHM2	Position2	FWHM3	Position3	Size [/nm]
Nb15	0.8487	11.46981	0.7793	21.461228	1.06482	24.205172	4.215336
Nb11	0.7978	11.481358	0.74642	21.490669	0.95375	24.219233	4.514666
Nb8	0.7613	11.501645	0.70778	21.515189	0.92033	24.26984	4.727272
Nb4	0.7351	11.510432	0.68146	21.543341	0.93344	24.292544	4.833693
TiO2	0.7636	11.524104	0.67538	21.559276	0.96127	24.329648	4.749147
Mo15	0.9033	11.503766	0.83482	21.500662	1.03763	24.293608	4.052912
Mo11Nb4	0.897	11.492394	0.80673	21.48269	0.95643	24.270472	4.216452
Mo11	0.915	11.502784	0.85293	21.503601	0.96286	24.295982	4.097485
Mo8	0.8776	11.510921	0.79756	21.518438	0.96072	24.31609	4.258928
Nb11Mo4	0.8567	11.47005	0.77827	21.458359	0.9622	24.220951	4.329246
Mo4	0.8127	11.524133	0.74061	21.545447	0.94408	24.322086	4.513406
Mo8Nb8	0.8779	11.485416	0.7663	21.466377	0.935	24.25876	4.35751
Mo4Nb8	0.8276	11.487481	0.73939	21.485894	0.95225	24.243511	4.477238
Mo4Nb4	0.798	11.504072	0.72727	21.518198	0.9232	24.282851	4.601805
Mo8Nb4	0.8676	11.497602	0.80402	21.498823	0.9316	24.277576	4.30297
Mo8Nb4V4	0.8654	11.500255	0.81069	21.503484	0.92937	24.284788	4.29712
Mo8V4	0.8914	11.515119	0.81847	21.526152	0.97101	24.322516	4.183607
V4	0.7928	11.532666	0.71041	21.56051	0.95443	24.345751	4.608497
Nb4V4	0.7757	11.513151	0.71927	21.545519	0.95005	24.306763	4.627001
Mo4V4	0.8445	11.525842	0.76119	21.526409	0.9583	24.321345	4.391523
Nb8Mo4V4	0.8258	11.49356	0.76767	21.495781	0.96512	24.265495	4.401138
Nb8V4	0.744	11.495664	0.69971	21.513555	0.94096	24.268355	4.755191

Mo12V4	0.9501	11.520145	0.86562	21.520209	1.04627	24.329827	3.923234
Mo4V4Mo4	0.9028	11.501964	0.80253	21.509624	0.99659	24.287427	4.163222
Nb12V4	0.8389	11.483847	0.79459	21.491087	0.96384	24.237144	4.324634
Nb4V8	0.8688	11.522304	0.77971	21.538639	0.98923	24.317926	4.27134
V8	0.882	11.536581	0.80001	21.547431	0.99616	24.358032	4.200956
V8Mo8	0.9741	11.520313	0.87965	21.523095	1.05898	24.341515	3.854176
V8Mo4	0.9258	11.537251	0.82831	21.525188	1.07305	24.351375	3.992114
V8Mo4Nb4	0.9228	11.509945	0.83353	21.5086	1.0155	24.29343	4.052744
V8Nb8	0.8386	11.503057	0.76772	21.514653	0.99259	24.292119	4.34263
V12Mo4	0.9877	11.518262	0.8999	21.511224	1.09815	24.359993	3.762947
V12Nb4	0.8926	11.522024	0.80867	21.536862	1.03144	24.341049	4.124902
V12	0.9179	11.533361	0.8306	21.544796	1.06463	24.369663	4.008675
V15	0.9688	11.542335	0.85552	21.548583	1.07411	24.389178	3.884501

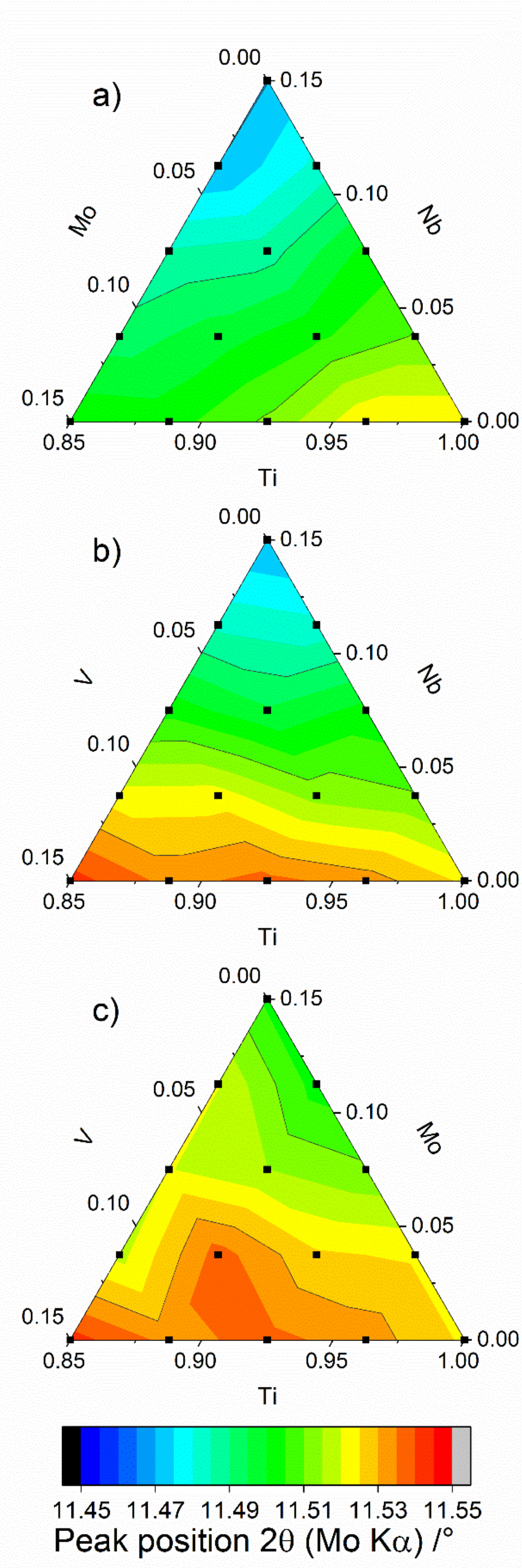

Figure A2: Ternary plots of the (101) peak positions for a) Mo/Nb, b) Nb/V, and c) Mo/V (co-)doped TiO_2 samples.

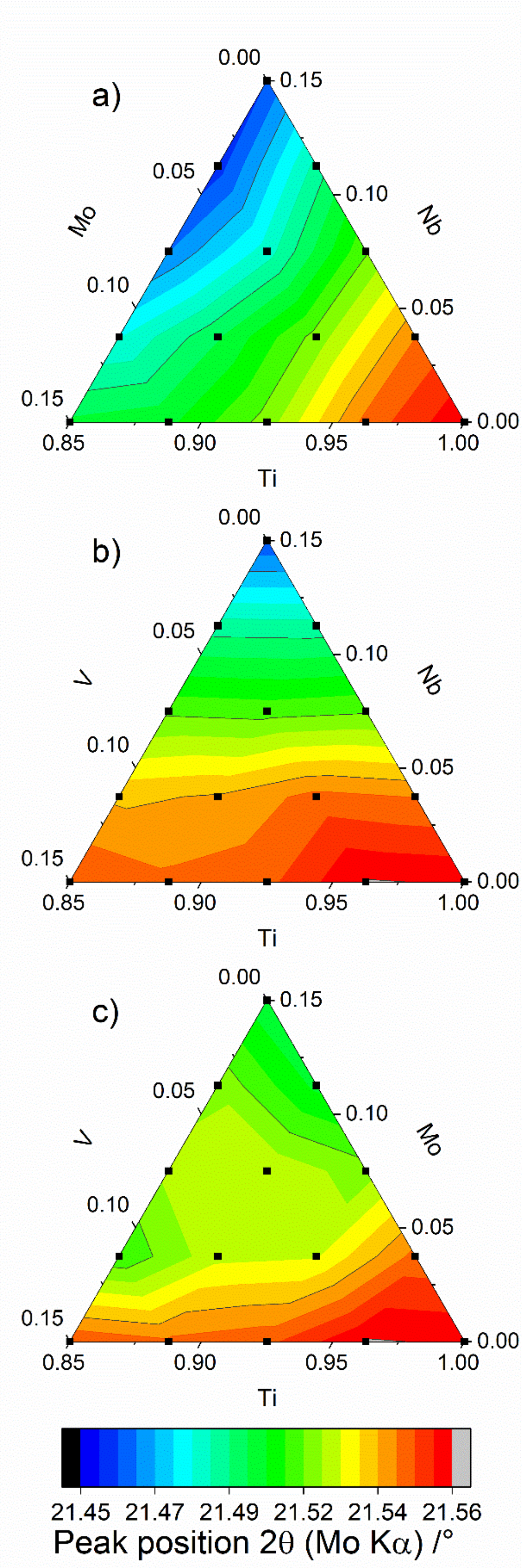

Figure A3: Ternary plots of the (020) peak positions for a) Mo/Nb, b) Nb/V, and c) Mo/V (co-)doped TiO_2 samples.

Appendix Chapter 5

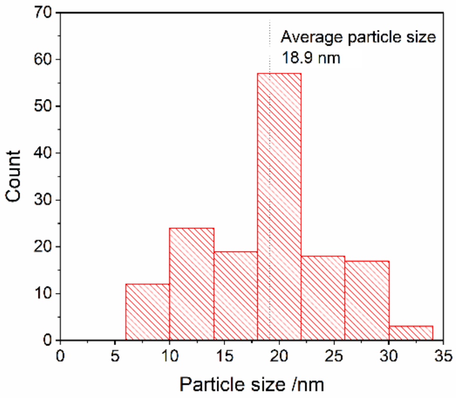

Figure A4: Particle size analysis for samples MoO_2 and TiO_2/MoO_2-3 using transmission electron micrographs.

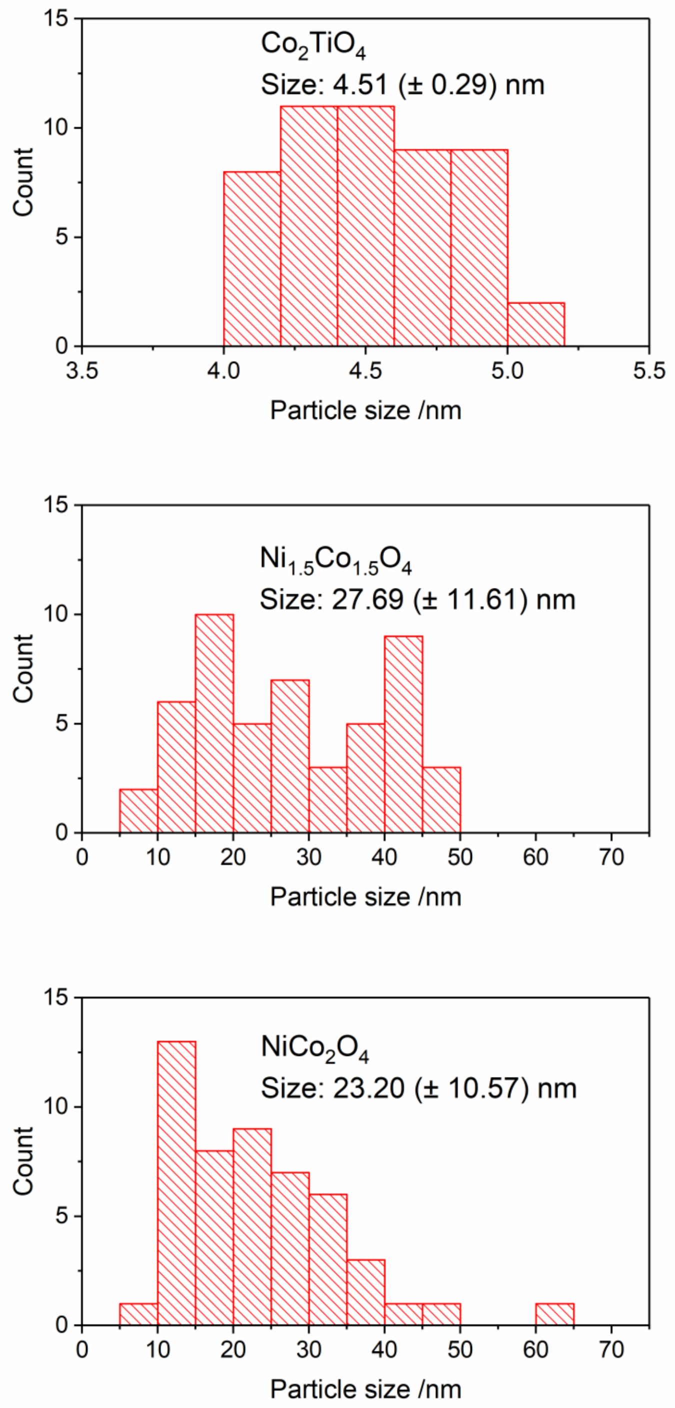

Figure A5: Particle size analysis for Co_2TiO_4, $Ni_{1.5}Co_{1.5}O_4$, and $NiCo_2O_4$.

Appendix Chapter 6

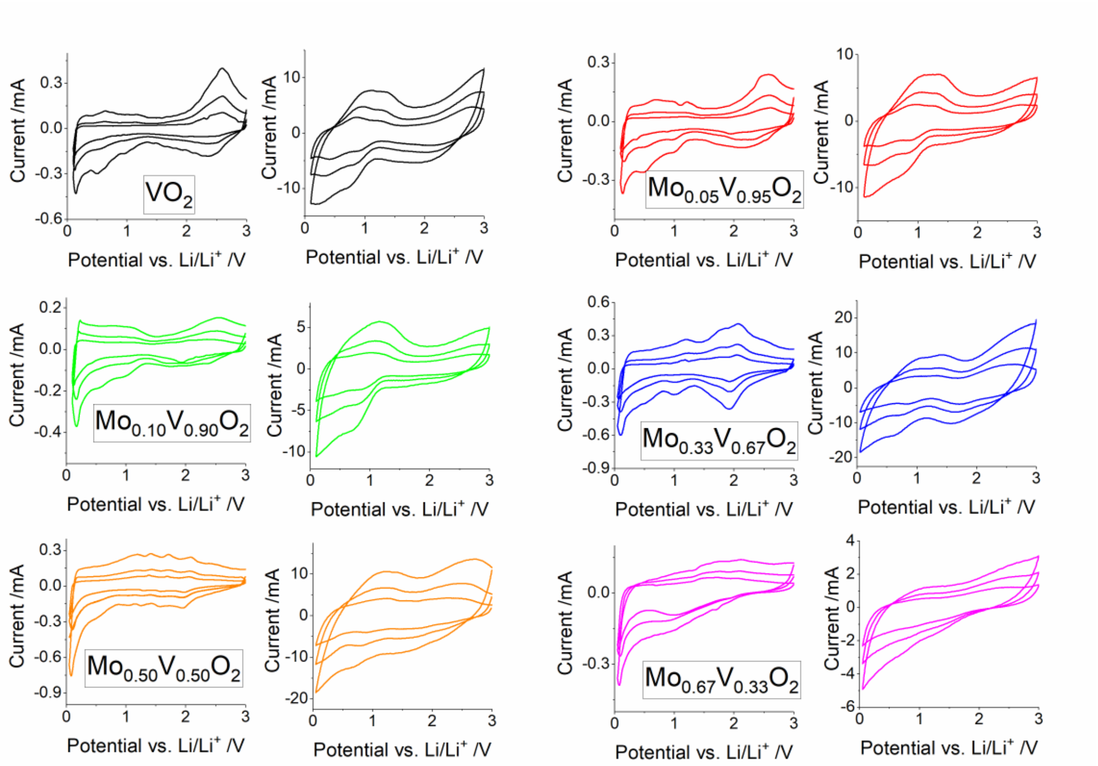

Figure A6: Cyclic voltammograms for all samples at scan rates of 0.5, 1, and 2 mV s^{-1} and 5, 10, and 20 mV s^{-1} on the left and right for each sample, respectively.